Volume 2 · Issue 4
December 2023
ISSN: 2810-9635 (Online)

Materials Science in Additive Manufacturing

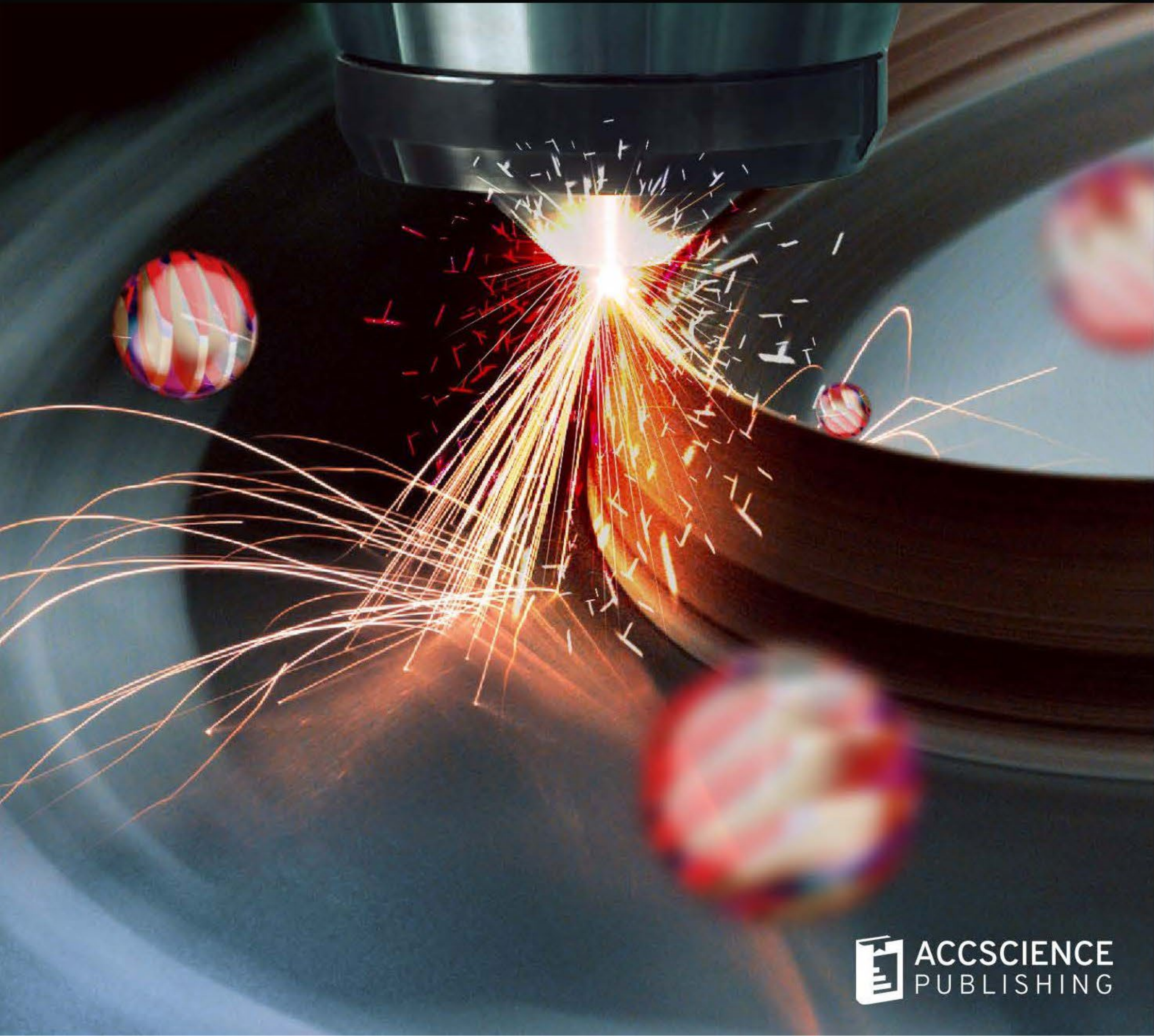

ACCSCIENCE
PUBLISHING

ACCSCIENCE
PUBLISHING

Materials Science in Additive Manufacturing

Online ISSN: 2810-9635

Materials Science in Additive Manufacturing aims to bridge the cutting-edge research between additive manufacturing and the entire spectrum of materials science. The journal covers all applied and fundamentals of processing, synthesis, structure, composition, properties and performance of materials designed or manipulated for additive manufacturing. The journal covers a wide scope of innovative techniques, processes, methods, and applications.

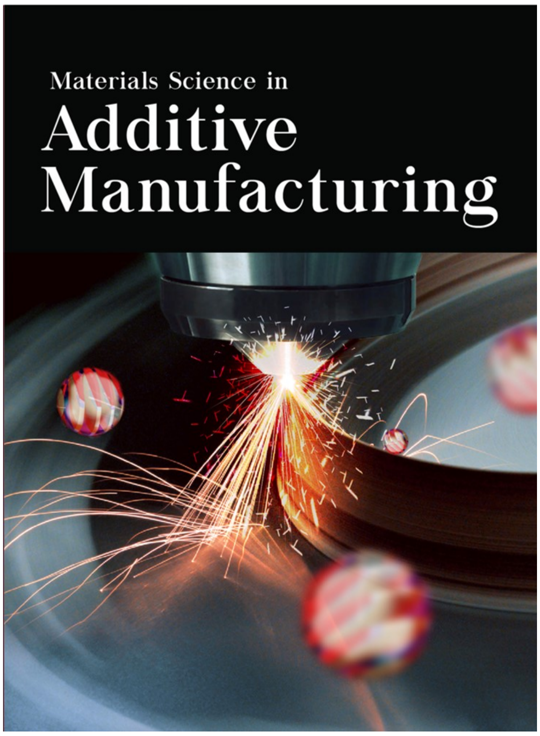

About the Publisher

AccScience Publishing is a publishing company based in Singapore. We publish a range of high-quality, open-access, peer-reviewed journals and books from a broad spectrum of disciplines.

Contact Us

Managing Editor
msam.office@accscience.sg

AccScience Publishing
8 Burn Road, #15-03 Trivex, Singapore 369977.

Volume 2 • Issue 4 • December 2023
ISSN 2810-9635 (online)

MATERIALS SCIENCE IN ADDITIVE MANUFACTURING

Editor-in-Chief

Chee Kai Chua

Singapore University of Technology and Design, Singapore

ACCSCIENCE PUBLISHING

Full issue copyright © 2023 AccScience Publishing
All rights reserved. Without permission in writing from the publisher, this full issue publication in its entirety may not be reproduced or transmitted for commercial purposes in any form or by any means, electronic or mechanical, including photocopying, recording, or any information storage and retrieval system. Permissions may be sought from msam.office@accscience.sg.

Article copyright © Respective Author(s)
See articles for copyright year. All articles in this full issue publication are open-access. There are no restrictions in the distribution and reproduction of individual articles, provided the original work is properly cited. However, permission to reuse copyrighted materials of an article for commercial purposes is applicable if the article is licensed under Creative Commons Attribution-NonCommercial License. Check the specific license before reusing.

MATERIALS SCIENCE IN ADDITIVE MANUFACTURING

ISSN: 2810-9635 (online)

Editorial and Production Credits

Publisher: AccScience Publishing
Managing Editor: Ginger Lv
Editorial Assistant: Flora Kang
Production Editor: Chi Tat Poon
Article Layout and Typeset: Sinjore Technologies (India)
Cover Design: BUTTON GRAPHIC DESIGN STUDIO (Malaysia)

For all advertising queries, contact msam.office@accscience.sg.

Supplementary file

Supplementary files of articles can be obtained at https://accscience.com/journal/MSAM/2/4.

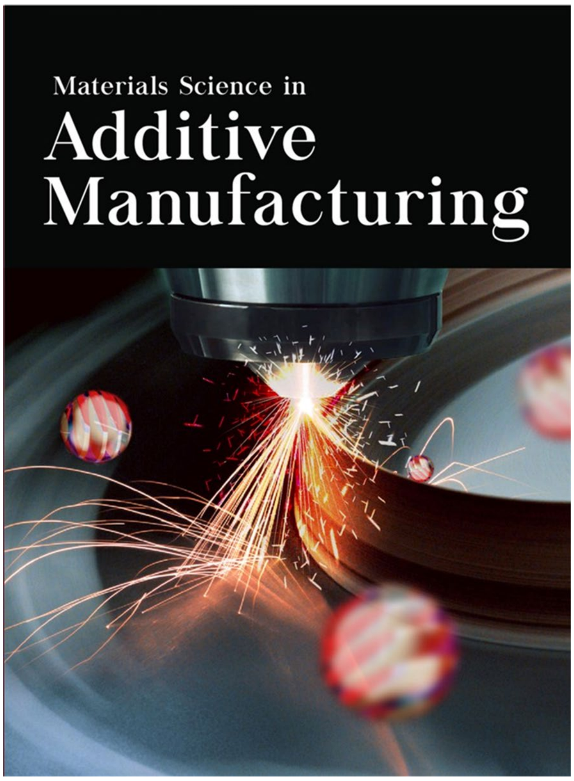

About the Cover

Directed energy deposition in progress

Disclaimer

AccScience Publishing is not liable to the statements, perspectives, and opinions contained in the publications. The appearance of advertisements in the journal shall not be construed as a warranty, endorsement, or approval of the products or services advertised and/or the safety thereof. AccScience Publishing disclaims responsibility for any injury to persons or property resulting from any ideas or products referred to in the publications or advertisements. AccScience Publishing remains neutral with regard to jurisdictional claims in published maps and institutional affiliations.

Materials Science in Additive Manufacturing

Editorial Board

Editor-in-Chief

Associate Editor

Editorial Board Members*

ACCSCIENCE PUBLISHING

Volume 2 | Issue 4 | December 2023 |

Materials Science in Additive Manufacturing

https://accscience.com/journal/msam

CONTENTS

REVIEW ARTICLES

ORIGINAL RESEARCH ARTICLES

ACCSCIENCE PUBLISHING

Materials Science in Additive Manufacturing

REVIEW ARTICLE

Emerging 3D-printed zeolitic gas adsorbents

Jiazhao Huang[1], Rocky Gipson[2], Chengcheng Wang[2], Su Xia Zhang[1], Subhash Guddati[2], and Sharon Mui Ling Nai[1]*

[1]Additive Manufacturing Division, Singapore Institute of Manufacturing Technology (SIMTech), Agency for Science, Technology and Research (A*STAR), Singapore, 636732, Republic of Singapore

[2]Entegris Inc., Billerica, Massachusetts, 01821, United States of America

Abstract

The development of zeolitic adsorbents is an essential subject of interest in the realm of green chemistry, especially in the aspect of gas adsorption. The intrinsic molecular sieving capacity of zeolites allows them to be widely adopted as effective gas adsorbents. As a layer-by-layer deposition technology, three-dimensional (3D) printing can achieve more complex zeolitic gas adsorbent structures than conventional manufacturing methods by offering flexible freeform construction and controllable 3D structural design. This review article focuses on the recent development of 3D-printed zeolitic gas adsorbents, which integrate advanced zeolitic structures and emerging additive manufacturing technologies for gas absorption. A description of zeolites and their conventional fabrication methods is given for a basic understanding of zeolitic gas adsorbents. 3D printing technologies are also introduced and discussed for the fabrication of zeolitic adsorbents such as monoliths. Next, the recent progress in the fabrication of zeolitic gas adsorbents using 3D printing is illustrated and summarized, which boosts the application of 3D-printed zeolite absorbents in different fields of gas adsorption. Conclusions are given with an outlook on opportunities ahead for future research. It is expected that the development of advanced zeolitic materials and structures for gas adsorption purposes will be significantly accelerated through 3D printing technologies.

Keywords: Additive manufacturing; 3D printing; Zeolites; Gas adsorption

***Corresponding author:**
Sharon Mui Ling Nai
(mlnai@simtech.a-star.edu.sg)

Citation: Huang J, Gipson R, Wang C, Zhang SX, Guddati S, Nai SML, 2023, Emerging 3D-printed zeolitic gas adsorbents. *Mater Sci Add Manuf*, 2(4): 1880. https://doi.org/10.36922/msam.1880

Received: September 20, 2023

Accepted: November 7, 2023

1. Introduction

With growing global sustainability issues, substantial efforts have been made to develop new materials and technologies for green chemistry over decades. Green chemistry aims at limiting or eliminating the usage and production of hazardous substances through a good design of chemical synthesis and processing[1,2]. Gas adsorption is vital in green chemistry as a promising technology for air pollution prevention and utilization of carbon oxide (CO_2) resources[3-5]. Zeolite absorbents are widely applied for gas adsorption because of their unique microporous structures and substantial active sites[6]. Zeolites are generally described as a class of aluminosilicate materials that have open microporous crystalline structures[7,8]. Among those micropores, the relatively large cavities generated by the $[Si_{1-x}Al_xO_2]^{x-}$ negatively charged frameworks provide sufficient sites for the storage of balancing cations. There are also numerous microchannels linking the cavities, thus forming a complex network of microporous structures[9]. Such structures can achieve the desired molecular sieving phenomena for gas separation technologies by selectively allowing the penetration of molecules under a specific size[10]. Figure 1 illustrates the forms and structures of zeolite A, a commonly used gas adsorbent, at different length scales. Silica-alumina ratio, crystal structure, surface area, pore structure, and pore volume are important physio-chemical factors that affect the adsorption efficiency of zeolite absorbent[11].

Although multiple approaches have been developed for the fabrication of zeolite materials and structures, new scientific technologies are still expected to achieve cost-effective production[14-16]. As a novel manufacturing technology, it is believed that three-dimensional (3D) printing can give rise to robust zeolite absorbent for gas separation[17,18]. 3D printing, also referred to as additive manufacturing (AM), is a cutting-edge technology for manufacturing products with required customization, intricate geometry, and high flexibility[19-21]. Therefore, 3D printing enables the fabrication of complex objects which are generally challenging to be produced by conventional manufacturing methods[22,23]. The printing process typically starts with creating a 3D model through digital design or scanning, followed by generating sliced layers within special software. The fabrication of the targeted model is then accomplished by adding each individual two-dimensional (2D) layer over the prior one[24-26]. Due to this unique building process, 3D printing has been proven to be a promising method for producing natural materials and synthetic materials in various fields, including aerospace, petrochemical, and environment industries[27-29]. For the fabrication of zeolite absorbents, 3D printing possesses some distinct advantages when compared to traditional manufacturing approaches:

- 3D printing enables customized configurations of zeolitic absorbent to be effectively achieved by freeform production[30].
- 3D printing also allows a complex zeolitic absorbent interior channel system with desired surface chemistry, shape, and porosity[31].
- 3D printing further offers a convenient and straightforward fabrication of zeolitic composites for gas adsorption[32].

This review article focuses on the development of 3D-printed zeolite absorbents for gas adsorption purposes, where the current stage, fabrication strategies, and future opportunities are outlined and discussed. After a brief introduction in Section 1, Section 2 provides a general description of zeolite and its conventional shaping and structuring methods. The same section also discusses the basic concepts of different 3D printing processes to reveal their potential for zeolitic absorbents. Section 3 further gives a summary of the most recent developments in 3D-printed zeolite absorbent, followed by an elaboration on its different applications as gas adsorbent in Section 4. The article ends with conclusions and prospects in Section 5.

2. Fabrication of zeolite absorbents

The major benefit that 3D printing can bring for the fabrication of zeolitic gas adsorbents is the high design flexibility, which allows the production of geometries with more efficient adsorbent rate[33,34]. This section illustrates the basic aspects of zeolite absorbents and their conventional shaping and structuring methods, followed by a brief description of 3D printing technologies.

2.1. Basic aspects of zeolites

Together with good chemical and thermal stability, zeolite absorbents have demonstrated outstanding potential for gas adsorption. This section gives a general description of zeolites and the influencing factors for the adsorption of gases on zeolites.

2.1.1. Structure and type

Zeolites are a class of aluminosilicate materials with a general chemical formula of $M^{n+}_{x/n}[Al_xSi_yO_{2x+2y}]^{2+}\cdot wH_2O$, where M represents alkali or alkaline earth cation of valency n, w is the number of water molecules attached with the zeolite unit. Subscripts x and y represent the

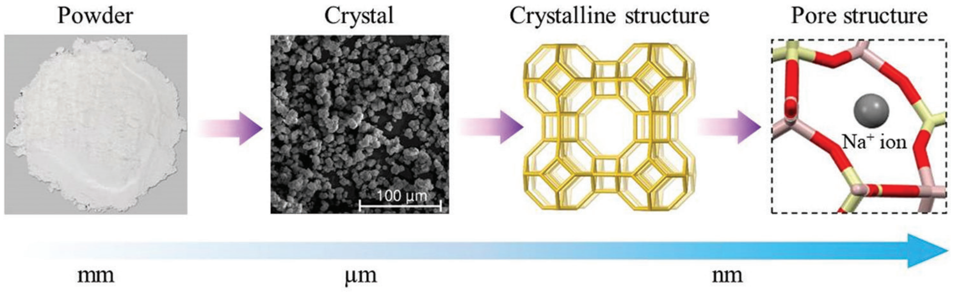

Figure 1. Forms and structures of zeolite A across different length scales. Adapted with permissions from Oheix *et al.*[12] (crystalline structure and pore structure) and Praipipat *et al.*[13] (powder and crystal).

number of their corresponding element groups[35]. As shown in Figure 2, building blocks of zeolites are formed based on the $[SiO4]^{4-}$ and $[AlO_4]^{5-}$ tetrahedral units, defined as primary building units. Each tetrahedron unit is linked to its four neighbors through their shared vertex oxygen atoms. This leads to a spatial arrangement of simple geometric forms, such as rings, prisms, and polyhedrals, also known as secondary building units[36,37]. Within such an interconnecting framework, voids and pores are produced in the form of cages and channels between the adjacent tetrahedra[38].

The International Zeolite Association has established a three-code system to differentiate zeolites based on their crystal frameworks[39]. There are over 200 types of zeolites according to their silica-alumina ratios. These various zeolites can be categorized into two major groups: Nature and synthetic. Nature zeolites are typically of basalt or volcanic origin. They often appear as crystals in igneous and metamorphic rocks, while also as small grains embedded within sedimentary rocks[40]. Natural zeolites sometimes suffer from contamination by other minerals, limiting their potential applications in fields where uniformity and purity are critical[41].

Compared to their natural forms, synthetic zeolites are more likely to be uniform and pure in terms of frameworks, lattice structures, and pore sizes for industrial applications. However, professional equipment and clean substrates are usually required for the synthesis reaction of zeolites, leading to a higher fabrication cost than the price of natural zeolites. Natural and waste raw materials are widely used for the synthesis because they are both cheap substrates. Due to the high contents of silicon and aluminum, clay minerals such as kaolin are regarded as the natural material source for zeolite synthesis. By-products of industries such as coal flying ashes are waste material sources to produce synthetic zeolites[42,43]. Some well-known synthetic zeolite Linda type A (LTA), X and Y, mainly differ in their silica-alumina ratios, leading to various crystal structures and molecular sieving properties. Table 1 lists some selected typical zeolites for gas adsorption applications.

2.1.2. Influencing factors for gas adsorption

Zeolites exhibit remarkable gas adsorption properties, making them highly sought-after materials for various applications. As described in the previous section, these crystalline aluminosilicates possess a unique porous structure with well-defined channels and cavities, allowing for efficient gas adsorption. The adsorption of gases on zeolites is mainly driven by the adsorbent-adsorbate interaction, where the structural characteristics of zeolites play a crucial role. The number of exchangeable cations in zeolites affects the adsorption capacity, as a higher number of cations provides more sites for interaction with gas molecules. The size of the pores in zeolites is also essential, as it determines the accessibility and penetration of gas molecules into the zeolite structure. The appropriate pore size allows for effective adsorption, while larger or smaller pore sizes may limit the adsorption capacity and rate. The silica-alumina ratio is another structural characteristic of zeolites which has a significant impact on the electric field within zeolite structure for gas adsorption. A higher silica-alumina ratio generally leads to lower electric field strength and polarity within the zeolite pores. This is because Al atoms have a higher charge density than Si atoms, resulting

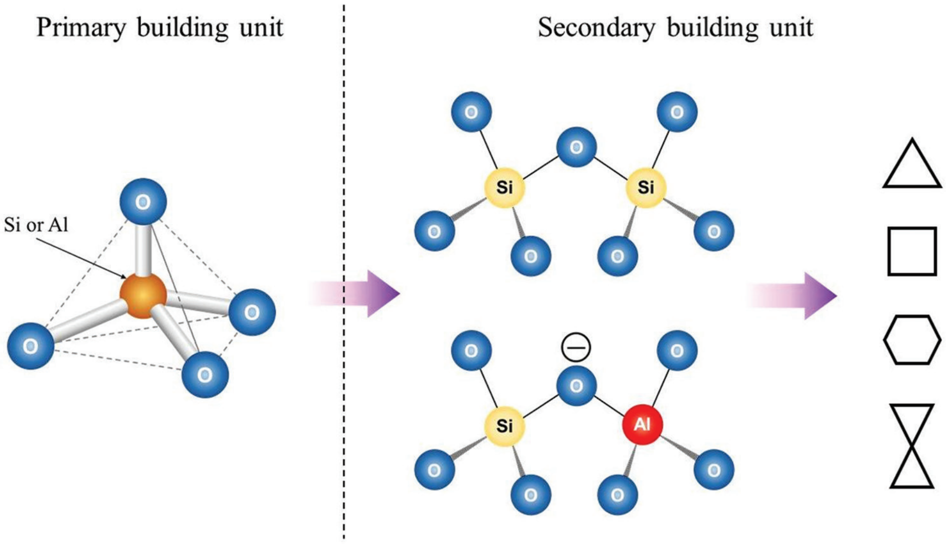

Figure 2. Primary and secondary building units of zeolites.

Table 1. Properties of selected typical zeolites for gas adsorption

Zeolite	Group	Silica-alumina ratio[44-46]	Application for gas adsorption
Chabazite	Natural	1 – 4	Separation of CO_2 from natural/landfill gas; removal of NH_3 gas[47,48]
Clinoptilolite	Natural	6	Removal of CO_2, H_2S, N_2, and H_2O from natural gas; removal of SO_2 from flue gas; removal of NH3 gas[49,50]
Mordenite	Natural	5.5	Adsorption of CO_2, SO_2 and xylene[51,52]
LTA	Synthetic	0.7 – 1.2	Storage and separation of CO_2; dehydration agent[53]
X	Synthetic	1 – 1.5	Storage and separation of CO_2 and H_2[54]
Y	Synthetic	1.5 – 7.9	Storage and separation of CO_2, H_2O, and CH_4[55]

in a stronger electric field when Al is present. Therefore, zeolites with high alumina content, such as zeolite A and X, generally have higher adsorption capacities when compared to zeolite Y[56,57].

Besides the structural characteristics of zeolitic gas adsorbents, the adsorbent-adsorbate interaction is also affected by the adsorbates. Adsorbates with a greater polarity, such as CO_2, tend to have stronger interactions with the electric field within zeolites. This favors their adsorption, as they can effectively interact with the surface and pores of zeolites. On the other hand, less polar adsorbates may have weaker interactions and lower adsorption capacities. Dimension of adsorbates also affects their ability to access the available pore space in zeolites. Zeolite structures usually consist of interconnected pores of specific sizes and shapes. Smaller adsorbate molecules that are even smaller than the pore size can easily enter and occupy the available pore space, leading to efficient adsorption. In addition, environmental conditions, such as pressure and temperature, also influence the adsorbent-adsorbate interaction in zeolites. Pressure can affect adsorption capacity by limiting the available pore space, while temperature can affect the strength of the adsorbent-adsorbate interaction by increasing the mobility of the adsorbate molecules. Table 2 summarizes the relation between the above-mentioned factors and the gas adsorption performance of zeolites.

2.2. Conventional shaping and structuring methods

Zeolites, in their natural form, are typically synthesized in powder form. However, it is necessary to transform them into structured materials for their industrial applications as gas adsorbents. A general introduction to conventional shaping and structuring methods for zeolitic gas adsorbents is given in this section.

2.2.1. Pelletization and granulation

Pelletization and granulation are traditional methods used for adsorbent geometric processing. In pelletization, the process involves compressing and shaping a powder mixture into small, spherical particles. This is typically achieved by applying pressure to the powder mixture using a pellet press or extruder. The pressure helps to bind the particles together, forming cohesive pellets[60]. Granulation, on the other hand, involves the formation of larger, irregularly shaped particles by agglomerating powder particles with a binder. The powder mixture is typically mixed with a liquid binder, such as water or a solvent, to create a wet mass. This wet mass is then subjected to drying or spray drying processes to remove the liquid and form granules[61]. These methods offer simplicity and versatility in material incorporation, allowing for the inclusion of various components or additives in the pellet or granule structure.

2.2.2. Die-based extrusion

Compared to granulation and pelletization, extrusion has been developed for the fabrication of structured adsorbents with open channels[60-63]. Such open channeling can reduce resistance to gas flow, resulting in an improved gas transfer rate and more efficient adsorption. Unlike the extrusion-based 3D printing technology, a die is required for conventional extrusion manufacturing. The die-based extrusion usually starts with mixing zeolite with binder materials and water. The mixture is then extruded into green monoliths in different shapes using corresponding dies. The final products can be obtained after drying and firing[64]. However, the usage of binders could weaken the support strength and block the pores of zeolites[65]. Although hydraulic extrusion is applied to fabricate binderless zeolites, a marginal amount of binding agent is still required, leading to a zeolite loading lower than 100 wt%[66-68]. Besides the direct forming of zeolite monoliths, extrusion is commonly adopted for fabricating microporous alumina supports where zeolite monoliths or membranes can be grown through the coating.

2.2.3. Coating

Slurry coating and in situ synthesis are two widely used methods for coating zeolite monolith onto the monolith

Table 2. Factors that influence the adsorption of gases on zeolites[58,59].

Factors	Influence on the adsorption of gases on zeolites
Basicity	Zeolites with higher basicity exhibit a greater capacity for gas adsorption due to the enhanced electron density of the framework oxygen.
Exchangeable cations	• Polarizing power: Zeolites with smaller exchangeable cations have higher polarizing power and stronger interactions with polar gas molecules such as CO_2. • Distribution: The distribution of exchangeable cations within zeolites contributes to the heterogeneous character of the adsorption process. Different sites within the zeolite structure result in the selectivity of the gas adsorption. • Size: The energy of interaction between the gas molecules and exchangeable cations is inversely proportional to the size of cations, influencing the overall adsorption capacity and selectivity. • Number: A higher number of exchangeable cations can provide more sites for interaction with gas molecules, leading to an increase in the gas adsorption capacity and selectivity of zeolites
Silica-alumina ratio	A lower silica-alumina ratio increases the electric field within the zeolite pores, enhancing the adsorption of polar molecules and resulting in improved gas adsorption properties.
Size of pores	The size of pores within zeolites determines the accessibility and penetration of gas molecules into the structure. The appropriate pore size allows for effective adsorption, while larger or smaller pore sizes may limit the adsorption capacity and rate.
Polarity of adsorbates	The polarity of adsorbates influences their interaction with the electric field within zeolites, which in turn affects gas adsorption. Adsorbates with a greater polarity tend to have stronger interactions with the electric field of zeolites, leading to enhanced adsorption capabilities.
Dimension of adsorbates	The dimensions of adsorbates, such as the size and shape of molecules, play a role in their adsorption on zeolites. The porosity of zeolite cavities is a selective factor for adsorbed molecules, with specific dimensions being more favorable for effective adsorption.
Pressure	At low pressures, the amount of gas adsorbed is directly proportional to the cationic density in the zeolite pores. In contrast, at high pressures, the volume of the pores becomes more significant.
Temperature	An increase in temperature can decrease the adsorbent-adsorbate interactions, leading to a decrease in gas adsorption of zeolites.

support surfaces. The slurry coating is often applied for the fabrication of zeolite monoliths because it is easy to apply the wash coat. Zeolite crystals and precursors of the binder are carried by the wash-coat solutions. The bonding between the crystallites and support is then obtained through the calcination of coatings[69]. In contrast to slurry coating, zeolite crystals are directly coated on the support surfaces through *in situ* coating. Such a coating process requires the support to be immersed in a clear solution such as the synthesis gel. The nucleation and growth of zeolite crystals are intended to occur on the support than in the solution, leading to the fabrication of monoliths with higher mechanical strength than those produced by slurry coating. In this way, dense and homogeneous zeolite coatings can be achieved for the fabrication of monolith[70]. Zeolite membrane can also be made through the growth of zeolite crystals over the support surfaces to form polycrystalline film[71].

2.2.4. Drawbacks of conventional methods

Pellets and granules are easier to produce and have a faster production rate, but they have some disadvantages compared to extruded structures, such as honeycombs. These drawbacks include millimeter-sized particles, leading to a reduced external surface area. Therefore, pellets and granules are packed into a fixed bed to increase the bed voidage for gas adsorption. However, the fixed bed can experience a significant pressure drop as the gas flows through the bed. This pressure drop can affect the overall efficiency of the adsorption process and may require additional energy for gas flow. Furthermore, there is a possibility that the gas preferentially flows through certain pathways or channels, bypassing some of the adsorbent material. This can result in reduced contact between the gas and the adsorbent, leading to lower adsorption efficiency.

Die-based extrusion lacks the ability to fabricate zeolite absorbents with very complex geometries rather than continuous channels or other simple structures. Stuecker *et al.* performed a simulation study on the flow velocities of gas passing through an extruded honeycomb-structured zeolite monolith and a 3D-printed one[72]. As shown in Figure 3, the maximum gas flow velocity achieved by the straight continuous channel system is found to be over 4 times less than that offered by the interlocking channel system fabricated through 3D printing. Such a complex interlocking channel system cannot be manufactured by extrusion. This is because the nature of this conventional fabrication method is to create a continuous shape with a consistent cross-section.

Coating of structured zeolitic gas adsorbents involves applying a thin layer of zeolite materials onto a support structure, which can be fabricated into complex interlocking channel systems through other fabrication approaches, such as 3D printing. However, the coating for synthesizing structured adsorbents has drawbacks that include a relatively low overall capacity per unit mass due to the large weight percentage of the substrate, the potential for nonuniform coating leading to mass transport limitations, and the lack of rigid binding between the adsorbent film and the substrate. In addition, the use of a substrate may introduce additional costs and complexity to the manufacturing process. Figure 4 summarizes and compares the characteristics of the above-mentioned shaping and structuring methods for the zeolitic gas adsorbents.

2.3. 3D printing systems

Compared to conventional shaping and structuring methods, 3D printing has emerged as a promising fabrication approach for zeolite absorbents by offering higher flexibility of geometry and versatility of materials. In general, 3D printing has the potential to achieve high resolution, down to a fraction of a millimeter (microns), and can produce intricate and complex structures. Traditional manufacturing methods, such as die-based extrusion or coating, can also achieve high precision but may have limitations regarding interlocking channel systems. It is critical to achieve gas adsorbent with both high adsorption

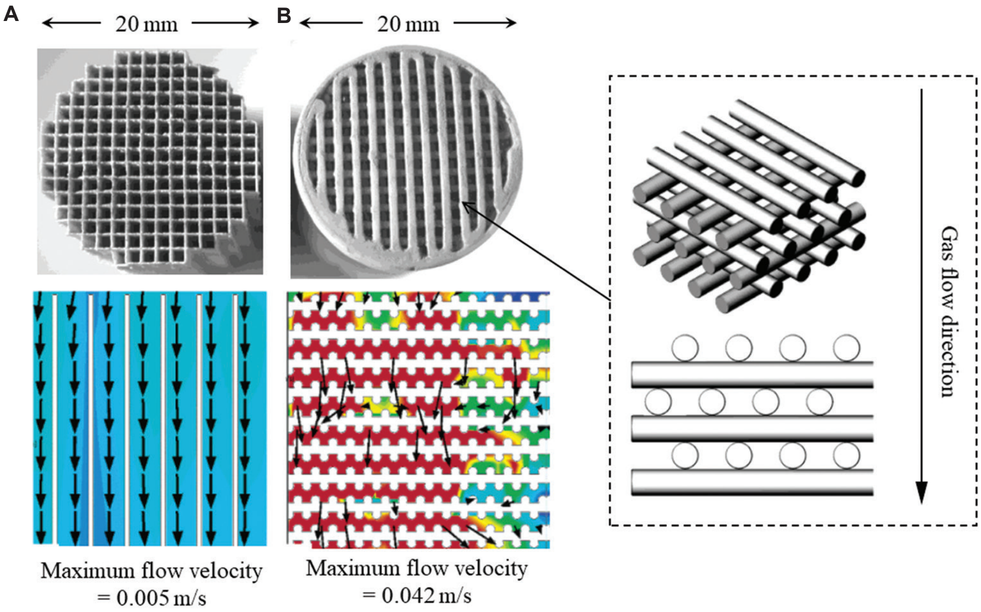

Figure 3. Comparison between the maximum flow velocities for (A) extruded honeycomb and (B) 3D-printed monoliths. Adapted with permission from Stuecker *et al.*[72].

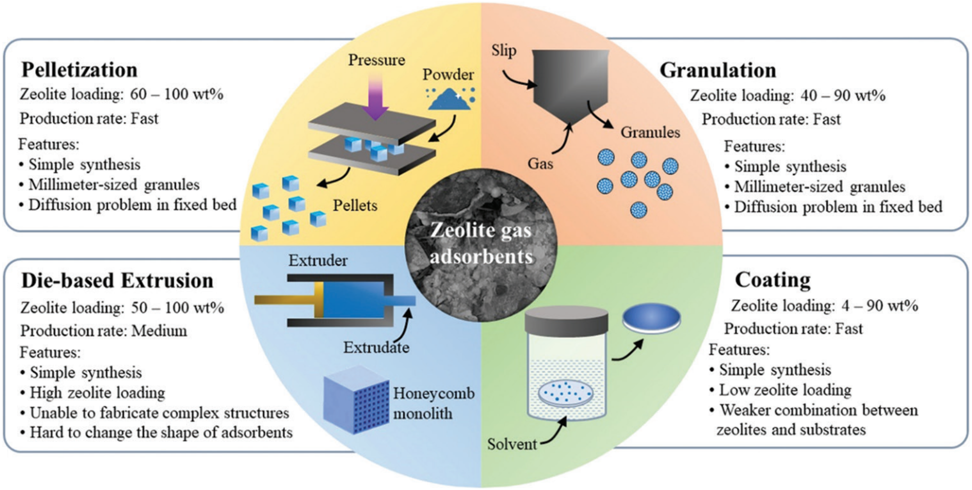

Pelletization
Zeolite loading: 60 – 100 wt%
Production rate: Fast
Features:
- Simple synthesis
- Millimeter-sized granules
- Diffusion problem in fixed bed

Granulation
Zeolite loading: 40 – 90 wt%
Production rate: Fast
Features:
- Simple synthesis
- Millimeter-sized granules
- Diffusion problem in fixed bed

Die-based Extrusion
Zeolite loading: 50 – 100 wt%
Production rate: Medium
Features:
- Simple synthesis
- High zeolite loading
- Unable to fabricate complex structures
- Hard to change the shape of adsorbents

Coating
Zeolite loading: 4 – 90 wt%
Production rate: Fast
Features:
- Simple synthesis
- Low zeolite loading
- Weaker combination between zeolites and substrates

Figure 4. Comparison of characteristics of conventional shaping and structuring methods for zeolite gas adsorbents.

rate and capacity. Since each 3D printing system has its unique manufacturing process, feedstock materials, and final products, a suitable system needs to be selected for specific technical requirements. Therefore, a brief introduction of 3D printing systems, such as photopolymerization, extrusion, powder-based, and lamination, is given below to provide a basic understanding of their applications for zeolitic gas adsorbent manufacturing.

The origin of 3D printing can be traced back to the 1980s when photopolymerization was developed to prototype various materials rapidly. As one of the most commonly adopted photopolymerization processes, stereolithography (SLA) was filed for a patent by Charles W. Hull in 1986 for fabricating products with photopolymers[73]. Other common types of polymerization printing technologies are digital light processing (DLP), two-photon lithography, and continuous digital light processing/continuous liquid interface production[74]. As shown in Figure 5, the printing principle of such a system is based on the polymerization reactions of photopolymers to construct solid 3D objects[75]. Photopolymers are generally made of light-curable resins and stored in a vat for visible or ultraviolet light treatment. The light treatment would then trigger the cross-linking of polymers to achieve the solidification of resins. Photopolymerization has shown the advantages of fabricating porous ceramic materials in terms of high printing speed, good geometry accuracy, and versatile material selections[76,77]. From these perspectives, a polymerization 3D printing system is a competitive candidate for fabricating zeolitic gas adsorbents.

The extrusion-based 3D printing process is another widely applied fabrication technique due to its simple operation and affordable cost. Such a process consists of two main steps: pretreatment of materials and feedstock deposition through nozzles[78-80]. In 1992, Scott Crump invented fused deposition modeling (FDM), the first type of extrusion-based 3D printing process[81]. Thermoplastic filaments are generally utilized for the FDM process in which they are preheated to a semi-molten status. The dispenser nozzle would deposit the materials onto the substrate in a layer-by-layer manner[82]. Figure 6 shows another extrusion-based process, direct ink writing (DIW), which shares a similar printing principle with FDM. However, DIW does not require the drying and solidification of inks to maintain the shapes by using non-Newtonian viscous slurry. This fact enables DIW to print 3D objects from a wide range of various materials, such as plastics, composites, and ceramics. The slurry can be prepared for ceramic printing by a mixture of ceramic materials and binders[78]. Therefore, DIW can be adopted to fabricate structures with complex configurations, especially the porous monolithic components[83,84].

Powder-based 3D printing processes such as binder jetting and selective laser sintering (SLS) are also suitable for printing porous ceramic materials because the powder bed is porous in nature. In the binder jetting process, a layer of powder is recoated over the powder bed before spreading. The liquid binder is then selectively deposited onto the powder bed to glue the powder particles together in the designed shape. The process is repeated until the final product is fabricated, as shown in Figure 7. Binder jetting has been proven to be capable of manufacturing a wide variety of materials, including polymers, metals, and ceramics[85,86]. Various binders can be adopted in binder jetting to create the ceramic-binder composite. The post-processing makes the printed composite form into porous ceramic materials. There are many factors,

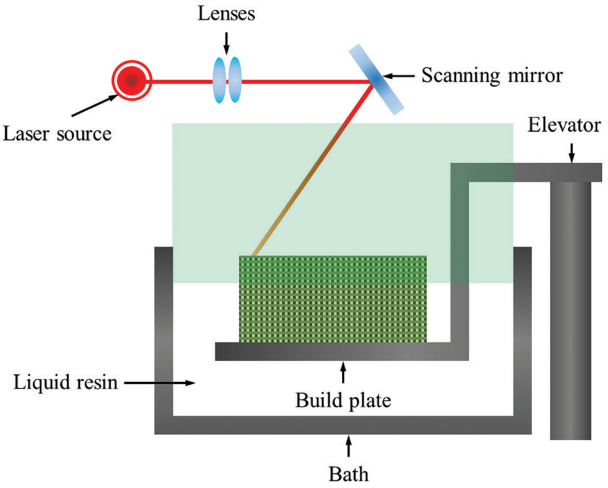

Figure 5. Schematic of stereolithography as a typical polymerization printing process.

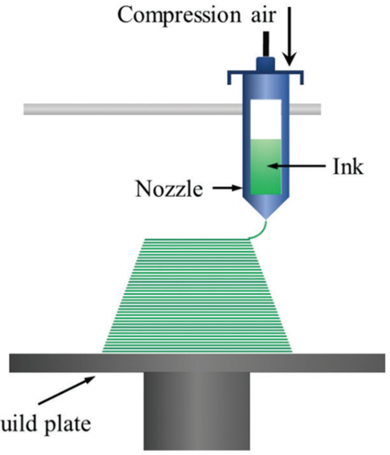

Figure 6. Schematic of direct ink writing as a typical extrusion-based printing process.

such as the binder content, sintering strategy, and powder characteristics, affecting the geometries and mechanical properties of the final products[87]. The feeding process of SLS is similar to that of binder jetting. SLS employs a laser which is only sufficiently strong for the fusion of powder particles. Therefore, the SLS is generally used to print ceramic materials by coating material with a lower melting point onto the matrix powder. The coating materials can be removed later through sintering or left to enhance the mechanical properties[88].

Besides the groups of 3D systems mentioned above, laminated object manufacturing (LOM) is also a standard 3D printing technique. In the LOM process, the top layer cutting is achieved by a blade or laser cutter, followed by the laminate bonding. Additional machining is often required to achieve final products in the desired shape. LOM is also used to produce porous ceramic materials like other 3D printing systems[89].

3. Recent advancements in 3D printing of zeolitic gas adsorbents

As mentioned in the previous sections, 3D printing is a practical approach to fabricating zeolitic adsorbents in customized geometry for gas adsorption usage. Both the gas adsorption performance and fabrication processes of the 3D-printed zeolitic adsorbents are essential to their practical applications. The recent advances in the development of 3D-printed zeolitic adsorbents are reviewed and discussed in this section.

3.1. Material selection and development

3D printing has been applied to fabricate porous ceramic or metal support structures such as scaffolds for the growth of zeolite crystals[90]. However, the non-zeolite layers between the zeolite and the substrate could act as barriers to the reactants, leading to a reduced adsorption rate. Therefore, recent research has focused on developing a self-standing zeolite monolith for gas adsorption through 3D printing.

3.1.1. Self-standing type

In 2016, Thakkar *et al.* first formulated the printable 13X and 5A zeolite paste with binding agents for the fabrication of monoliths through the DIW printing technique. The printed products were found to achieve a CO_2 adsorption capacity comparable to that of their counterparts in powder form[91]. Figure 8 reveals that the 3D-printed zeolite monoliths can preserve a stable porous network for gas adsorption without requiring an additional supporting structure made from a different material.

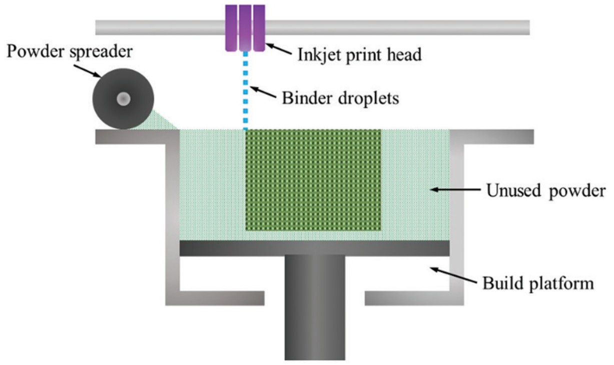

Figure 7. Schematic of binder jetting as a typical powder-based printing process.

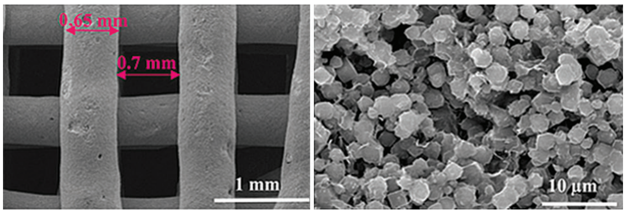

Figure 8. Scanning electron microscopy images of self-standing 3D-printed zeolite structure with different magnifications. Reprinted with permission from Thakkar *et al.*[91].

One critical aspect of material selection for the 3D printing of zeolitic gas adsorbents is the choice of a zeolite framework. It is because that framework determines the structural and chemical properties of zeolites, leading to different selectivity and absorptivity of different gases. Therefore, the selection of the appropriate framework is crucial to the fabrication of zeolitic gas adsorbent for targeted gas through 3D printing. As shown in Figure 9, different zeolite frameworks contain various tiny openings that permit molecules of a specific size to pass through. The size of these pores determines which gas molecules can be absorbed into a zeolitic gas adsorbent. Any molecules that are larger than the pore size will be unable to enter and be absorbed by the pores.

For example, LTA zeolites have a narrow pore size distribution and a high degree of structural order, which makes them ideal for separating small molecules based on size and shape. In contrast, faujasite (FAU) zeolites have a larger pore size and a more disordered structure, which makes them better suited for adsorbing larger molecules. Furthermore, smaller pores tend to have higher selectivity for specific gases, while larger pores tend to have higher adsorption capacity. Table 3 shows some common types of zeolite materials, including mordenite framework inverted (MFI) and chabazite (CHA) zeolites, that have been applied for the 3D printing of gas adsorbent, where the surface area of the printed adsorbent structure is determined by the Brunauer-Emmett-Teller (BET) test.

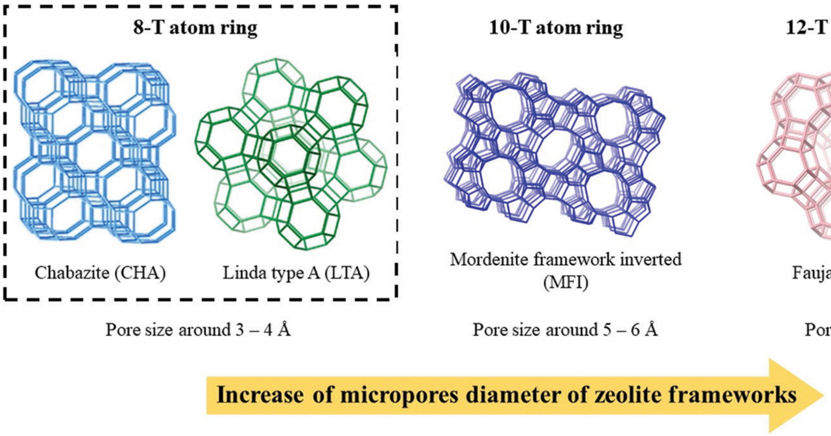

Figure 9. Schematic of zeolite frameworks with different sizes of pores and channels. Adapted with permissions from Liu *et al.*[92] (CHA framework) and Asgar Pour and Sebakhy[93] (LTA, MFI, and FAU frameworks).

Table 3. Selected types of zeolites used for 3D printing of gas adsorbents

Zeolite	Framework	Printing technique	Zeolite loading (wt%)	BET surface area (m^2/g)	Adsorption capacity (mmol/g)	Targeted usage	References
5A	LTA	DIW	80 – 90	395 – 543	1.59	CO_2 removal	[91]
5A	LTA	DIW	92.1	540	3.7	CO_2 adsorption	[94]
5A	LTA	DLP	70	361	1.6	CO_2 adsorption	[95]
ZSM-5*	MFI	DIW	75	390	-	CO_2 adsorption	[94]
ZSM-5	MFI	DIW	65	261	1.08 for N_2 1.41 for CH_4 2.39 for CO_2	CO_2, CH_4, and N_2 separation	[96]
ZSM-5	MFI	DIW	84	330 – 339	45.9 – 47.8 for toluene (humidified) 34.1 – 44.3 for toluene (humidified)	Volatile organic compounds removal	[97]
ZSM-5	MFI	SLA	-	311	-	CO_2 adsorption	[98]
SA*	FAU	DIW	81.6	96	-	CO_2 adsorption	[94]
13X	FAU	DIW	80 – 90	498 – 571	1.6	CO_2 removal	[91]
13X	FAU	DIW	64.5 – 66.7	550 – 640	3.3 – 3.5	CO_2 adsorption	[94]
13X	FAU	DIW	90	767.429	-	CO_2 adsorption	[99]
13X	FAU	DIW	83.3 – 85	550 – 570	0.7 – 1.6 (dry) 0.3 – 0.5 (humidified)	CO_2 capture	[100]
SAPO-34*	CHA	DIW	50	263/357	1.8 – 5.41	CO_2/N_2 separation	[101]

Abbreviations: BET, Brunauer-Emmett-Teller; CHA, chabazite; DIW, direct ink writing; DLP, digital light process; FAU, faujasite; LTA, Linda type A; MFI, mordenite framework inverted; SA: South Asia zeolite; SAPO-34: silicoaluminophosphate-34; SLA, stereolithography; ZSM-5: zeolite Socony mobil-5.

Zeolite powder needs to be made into a paste/slurry for 3D printing because it is difficult to extrude the powder directly. The zeolite-based paste preparation for 3D printing is usually achieved with the aid of additives, such as inorganic and organic binders. Inorganic materials such as bentonite clay, colloidal silica, and aluminophosphate solution have been investigated as primary binders for the 3D printing of zeolite monoliths. Bentonite clay is a natural mineral known for its high swelling properties and colloidal behavior, making it suitable for use as a binder in 3D printing[102]. Colloidal silica, on the other hand, is a synthetic material that has a high surface area and can form strong bonds with zeolite particles, resulting in good mechanical strength of the printed monoliths[103]. Aluminophosphate solution can provide good adhesion between the zeolite particles and improve the mechanical strength of the printed monoliths[104]. Lefevere *et al.* discussed the impact of the above-mentioned inorganic materials on the quality of 3D-printed zeolites. The shrinkage of printed zeolites would be reduced when bentonite was mixed in a 50/50 ratio with aluminophosphate or colloidal silica to form a binary binder system[105].

Organic materials are also utilized as binding agents due to their ability of forming strong bonds between zeolite particles and water solubility, allowing for easy binder removal during calcination. Methylcellulose is a commonly used organic plasticizing binder. It can promote both the gelation and shear thinning behavior of zeolite mixtures because it can form a network of hydrogen bonds in the presence of water. This network can increase the viscosity of the mixture and promote gelation. However, under shear stress, the hydrogen bonds can break, causing the viscosity to decrease and allowing for easier extrusion through the printer nozzle[106]. Another type of organic material, polyvinyl alcohol (PVA), is often added as a co-binder that provides additional binding strength and stability to the printed structure. PVA also has a high degree of flexibility, which can help to reduce the likelihood of cracking or deformation during the printing process. In addition to its binding properties, PVA can act as a pore-forming agent in the printed structure. Controlling the concentration and distribution of PVA in the printed material makes it possible to create specific pore structures within the printed zeolitic gas adsorbents[107].

Recent research has focused on the exploration of alternative additives that can be entirely removed by the post-processing treatment for the fabrication of binderless zeolitic gas adsorbents. It is because that the additives, such as clay binders, cannot be easily removed after printing because they do not decompose at low temperatures. This makes achieving 100% pure zeolite structures difficult, which is necessary for many applications. Wang *et al.* adopted a solvothermal bridging technique to create binderless NaX zeolite monoliths. However, this technique was time-consuming and required extensive optimization to coordinate the various components, as shown in Figure 10. In addition, it only resulted in a single binderless zeolite and has not been applied to other zeolite families[27].

Lawson *et al.* developed a novel 3D printing approach for producing binderless zeolite monoliths with sacrificial biopolymers gelatin and pectin. Those biopolymers were found to be fully removed by calcination at high temperatures, resulting in 100% pure zeolite structures without any residual binder material. Moreover, calcining zeolites alongside gelatin and pectin led to the narrowing of the pore windows and gave rise to enhanced adsorption capacities. The resulting binderless zeolite monoliths demonstrate a versatile means of 3D printing binderless zeolites for the first time, with several advantages over traditional methods, such as greater geometric control during 3D printing and lower manufacturing costs compared to hydraulic extrusion[94].

3.1.2. Polymer-based type

Polymer-zeolitic gas adsorbents are composed of a polymer matrix with dispersed zeolite particles. Such hybrid materials combine the properties of both polymers and zeolites, resulting in materials that have enhanced mechanical strength. This is because incorporating zeolite particles into the polymer matrix gives the composite adsorbents a higher surface area for gas adsorption compared to traditional zeolite monoliths[108]. In addition, the polymer matrix provides a synergistic effect that enhances the adsorption properties of the zeolite particles. This is

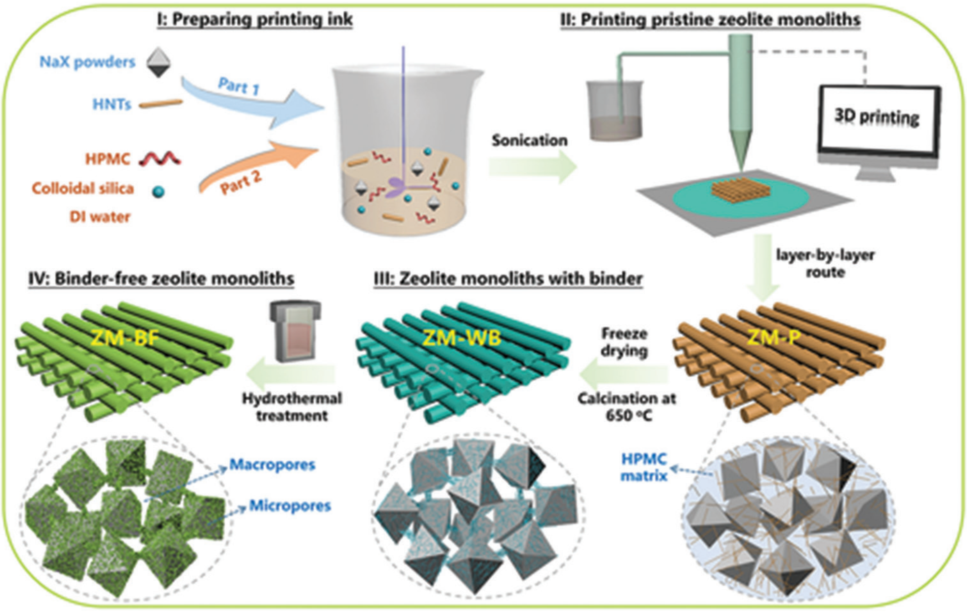

Figure 10. Schematic of 3D printing procedure of binderless zeolite. Reprinted with permission from Wang *et al.*[27].

because the polymer matrix can act as a support structure for the zeolite particles, preventing them from collapsing or agglomerating during use. Thakkar *et al.* fabricated the zeolite-embedded polymer monoliths through the DIW technique[109]. The printed monoliths consisted of Torlon polymer and zeolites 13X and 5A, with around 31 wt% zeolite particles incorporated into the polymer matrix. The composite monoliths demonstrated a compressive strength of approximately 210 MPa. This compressive strength was notably higher than that of 3D-printed zeolite monoliths developed in the previous work, which is below 1 MPa[109]. The improved compressive strength of the polymer-zeolite composite monoliths makes them highly robust structures with outstanding mechanical integrity. This enhanced strength allows for better resistance to deformation and attrition during handling and adsorption processes.

In 2017, Wudy *et al.* investigated using the SLS technique to manufacture zeolite-filled polypropylene composites. The properties of printed composite materials are comparable to those manufactured through extrusion processes, with the added benefit of improved water adsorption properties. The addition of 20 wt% zeolite resulted in a 50% increase in water uptake compared to unfilled polypropylene. It was anticipated that the addition of thermally conductive fillers could enhance the thermal conductivity of the composite, which might have implications for vapor adsorption. Furthermore, SLS-manufactured composite is expected to have improved mechanical properties than its extruded counterpart due to better interfacial bonding between polymer matrix and zeolite fillers. The authors stated that the detailed mechanical strength performance of the printed composite would be evaluated in their future study[110].

Zhang *et al.* explored the fabrication of polymer-zeolite composite with up to 75 wt% zeolite filler contents through direct laser writing (DLW), a type of photopolymerization-based 3D printing. The printed composite can absorb water and expand, causing the 3D object to change shape. When the water is removed, the composite returns to its original shape due to the shape memory effect of the polymer, resulting in 4D behavior. The storage modulus of the composites increased by 10-fold compared to that of a pure polymer. The tensile strength and elongation at the break of the composites were slightly lower than those of the pure polymer[111]. Table 4 summarizes the composition, mechanical strength, and gas adsorption properties of the above-mentioned polymer-zeolite composites.

3.1.3. Metal-organic frameworks-based type

Metal-organic frameworks (MOFs) are a class of porous materials consisting of metal ions or clusters linked together by organic molecules, creating a highly ordered network with a large surface area and high porosity[112]. As shown in Figure 11, zeolitic imidazolate framework-8 (ZIF-8) is a type of commercialized MOF material that has garnered significant attention in recent years due to its excellent gas adsorption properties and affordable price for large quantities. As a type of MOFs being topologically isomorphic with zeolites, ZIF-8 has a regular arrangement of pores and channels that allow for efficient gas transport, making it attractive for various gas adsorption applications[113].

Evans *et al.* adopted FDM for the 3D printing of ZIF-8 in thermoplastic polymer composites. The MOF-thermoplastic polymer composites were produced by incorporating ZIF-8 homogeneously into both polylactic acid and thermoplastic polyurethane matrices at high loadings of up to 50% by mass. The BET surface area of the printed ZIF-8 was not high initially, but it increased after CH_3OH solvent exchange and evacuation, yielding a BET surface area of 105 m^2/g. The specific surface area increased to 141 ± 27 m^2/g after printing the filament with the ZIF-8 to PLA weight ratio of 1.5[114].

Bible et *al.* developed composite materials by incorporating ZIF-8 into acrylonitrile butadiene styrene (ABS) through FDM[115]. The authors previously determined gas adsorption kinetics for 3D-printed pure ABS, which had a BET surface area of 0.6 m^2/g and a total pore volume of 0.002 cm^3/g. In contrast, the printed ABS-ZIF-8 composite had a BET surface area of 1.5 m^2/g and a total pore volume of 0.005 cm^3/g, indicating that the incorporation of ZIF-8 MOFs significantly increased the porosity and surface area of the composite material. The printed MOFs also maintained their N_2 adsorption capacities within the composites even after soaking in water[115].

Lefevere *et al.* reported the use of the DIW technique to synthesize ZIF-8 monoliths with open flow-through channels. The MOF structures were fabricated layer-by-layer using a binder recipe containing methylcellulose and bentonite binder, and thermally treated to remove the organic binder without destroying the ZIF-8 structure. The resulting ZIF-8 monoliths exhibited high mechanical stability with compressive strengths ranging from 0.6 to 1.4 MPa and high adsorption capacities for CO_2, CH_4, and N_2 gases, with maximum uptakes of 1.5, 0.5, and 0.3 mmol/g, respectively[116].

3.2. Structural design

The design of the zeolite structures can influence the diffusion, adsorption, and desorption properties of the adsorbent. Even zeolite materials with identical compositions can display distinct structural characteristics for gas adsorption. Table 5 summarizes some structures which are commonly adopted for the fabrication of

Table 4. Comparison of 3D-printed zeolite and polymer-zeolite composite for gas adsorption

Material	Printing technique	Mechanical strength	Gas adsorption properties	References
Zeolite 5A	DIW	• Compression strength: 0.05 – 0.35 MPa • Young's modulus: 1.65 – 9.45 MPa	• BET surface area: 395 – 543 m^2/g • CO_2 adsorption capacities: 1.59 mmol/g using 5000 ppm (0.5%) CO_2 in nitrogen at room temperature	[91]
Zeolite 5A + Torlon	DIW	Compression strength: around 210 MPa	• BET surface area: 59 m^2/g • CO_2 adsorption isotherms: CO_2 uptake=1.83 mmol/g at 35°C and 1 bar	[109]
Zeolite 5A + PEG-diacrylate	DLW	• Maximum storage modulus: 67.3 MPa (75% zeolite filler) • Maximum loss modulus: 5.5 MPa (75% zeolite filler)	BET surface area: 626 m^2/g	[111]
Zeolite 13X	DIW	• Compression strength: 0.3 – 0.69 MPa • Young's modulus: 7.5 – 15 MPa	• BET surface area: 498 – 571 m^2/g • CO_2 adsorption capacities: 1.6 mmol/g using 5000 ppm (0.5%) CO_2 in nitrogen at room temperature	[91]
Zeolite 13X + Torlon	DIW	Compression strength: around 210 MPa	• BET surface area: 93 m^2/g • CO_2 adsorption isotherms: CO_2 uptake=1.51 mmol/g at 35°C and 1 bar	[109]
Zeolite 13X + PEG-diacrylate	DLW	• Maximum storage modulus: Around 18.5 MPa (50% zeolite filler) • Maximum loss modulus: 2.48 MPa (60% zeolite filler)	BET surface area: 834 m^2/g	[111]

Abbreviations: BET: Brunauer-Emmett-Teller; DIW: Direct ink writing; DLW: Direct laser writing; PEG: Polyethylene glycol.

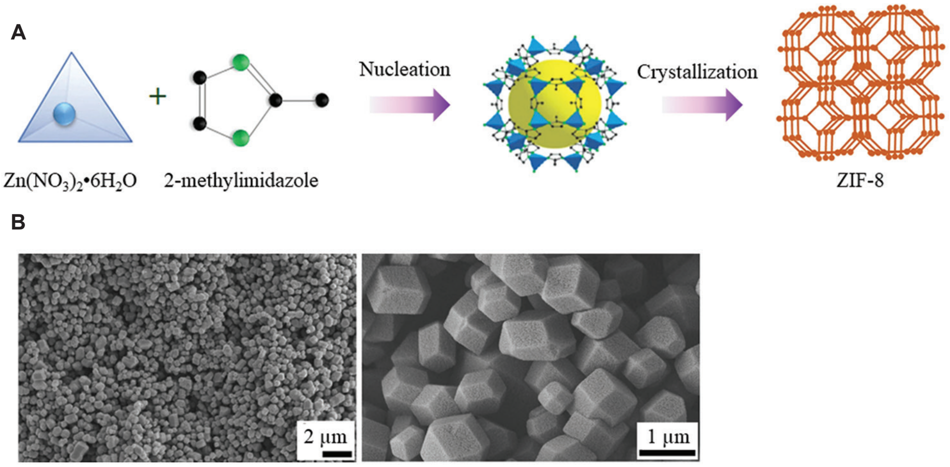

Figure 11. (A) The synthetic procedure of zeolitic imidazolate framework-8 (ZIF-8) catalyst, where zinc nitrate hexahydrate (chemical formula: $Zn(NO_3)_2{\cdot}6H_2O$) reacts with 2-methylimidazole (chemical formula: $C_4H_6N_2$) to yield ZIF-8 basic structural units; (B) Scanning electron microscopy (SEM) images of hexagonal synthetic ZIF-8 particles with an average particle size was about 500 nm. Adapted with permission from Bragina *et al.*[112].

zeolitic gas adsorbents through traditional or 3D printing methods. Researchers have explored various porous structural designs to optimize the adsorption capacity and selectivity of the printed zeolitic adsorbents[117,118]. Compared to traditional manufacturing methods, 3D printing enables the fabrication of zeolitic gas adsorbent with complex and intrinsic geometry. The wall thickness, channel diameter, and channel shape of a zeolite monolith have a direct impact on mass transfer within the monolith. Consequently, these factors have a significant effect on the adsorption performance of the monolith.

In the study by Couck *et al.*, the authors employed DIW with a fiber diameter of 400 μm and an inter-fiber distance of 500 μm to fabricate zeolite monolith for gas adsorption[96]. The monolithic structure was characterized by a scanning electron microscope (SEM) with a CO_2 adsorption capacity of 1.6 mmol/g at room temperature and atmospheric pressure[96]. The same group of authors used thinner fibers

Table 5. Comparison of commonly used structured gas absorbents

Feature	Structure			
	Pellet	Granule	Monolith	Membrane
Manufacturing method	Die-based extrusion; pelletization	Granulation	Die-based extrusion; coating; 3D printing	Coating; 3D printing
Common shape	Spherical or cylindrical	Irregular	Honeycomb, cylinder, and cuboid	Flat or tubular
Size	0.5 – 5 mm	0.5 – 5 mm	1 – 10 cm	0.1 – 1 mm
Porosity	Low to medium	Low to medium	High	Low to medium
Surface area	Low to medium	Low to medium	High	High
Zeolite loading	Low to medium	Low to medium	High	Low to medium
Durability	Moderate	Moderate	High	Moderate

with a thickness of around 300 μm for the 3D printing of zeolite monolith with an average channel width of 650 μm. The monolith was tested for adsorption and separation of CO_2 and N_2 through isotherms and breakthrough experiments. The resulting materials showed CO_2 adsorption properties similar to the parent powder SAPO-34, with a moderate decrease in capacity due to the presence of binder in the monolithic structures[101]. For extrusion-based 3D printing, the precision of the structure of zeolite monoliths is mainly dependent on the size of the nozzle, which limits the ability to design the structure with finer details. By utilizing the DLP 3D printing technique, Zhang *et al.* reduced the wall thickness of the zeolite monolith to 250 μm, resulting in improved dynamic adsorption performance[95]. The breakthrough width of the printed monolith reached 5.6 min, which was shorter than 6.8 min for commercial pellets, indicating that the refinement of the structure improved the dynamic adsorption rate of the zeolite monolith and showed fast adsorption kinetics[95]. Lawson *et al.* discussed the effects of cell density and intrinsic porosity on structural properties and adsorption kinetics in 3D-printed zeolite monoliths[100]. The monoliths were printed with three cell densities of 200, 400, and 600 cpsi, while their wall porosities were in the range from 0.23 to 0.46 based on the mercury intrusion porosimetry measurements. The study found that monoliths made from a macroporous binder had a faster CO_2 mass transfer rate, while those with increased cell density had a reduced CO_2 mass transfer rate[100].

Recent research has also focused on the 3D printing of zeolites with hierarchical porosity structures, which have larger pore sizes and higher surface areas compared to conventional structures such as honeycombs. Honeycomb structures typically have a uniform pore size distribution, limiting their ability to selectively adsorb gases based on size and shape. In contrast, hierarchical porosity gas adsorbents have a range of pore sizes, including both micro- and meso-pores, which allow them to capture a broader range of gas molecules more effectively. The hierarchical structure also provides a larger surface area for gas adsorption, which improves the overall adsorption capacity of the material. In addition, hierarchical porosity gas adsorbents have the potential to be more durable and stable under high-pressure conditions compared to traditional honeycomb structures. 3D printing has been utilized to create mesoporous zeolite monoliths with oriented hierarchical mesopores, which exhibit high adsorption capacity and selectivity. The incorporation of hierarchical porosity, which consists of both micro- and meso-pores, can improve the adsorption properties of the printed zeolitic adsorbents. For the extrusion-based 3D printing technique, the zeolite monoliths printed through DIW in the study by Li *et al.* exhibited hierarchical porosity with pore sizes ranging from 1.5 nm to 1 μm. The BET surface area of the samples ranged from 17 to 326 m^2/g, while the micropore area and micropore volume were determined using the t-plot method. The total pore volume of the samples ranged from 0.27 to 1.02 cm^3/g, with micropore volume ranging from 0.01 to 0.13 cm^3/g and mesopore volume ranging from 0.17 to 1.01 cm^3/g[119]. As an alternative to DIW, SLA has high resolution and superior forming capability, which allows for the creation of intricate geometries with high accuracy and precision. Merilaita *et al.* found that SLA can create hierarchically porous zeolite structures with porosity on three scales: printed flow channels for rapid gas transportation, porosity between primary particles allowing gas to flow into the structure, and micropores characteristic to the material itself, where adsorption finally occurs[98].

3.3. Influence of printing process parameters

Besides material development, recent research has focused on optimizing the process parameters to improve the performance of the 3D-printed zeolitic gas adsorbents. By controlling the process parameters, not only can the quality and precision of the printed adsorbent can be enhanced, but its utilization efficiency can also be improved.

Chu *et al.* conducted a study on the extrusion-based 3D printing of zeolite monolith to optimize the printing resolution and mechanical stability of the printed structures[120]. The study investigated the effects of several parameters, including nozzle diameter, nozzle height, printing speed, and ink viscosity, on the printing process. A variety of zeolite catalysts with different heights were prepared and analyzed for their morphology and mechanical strength. It was found that lower solid content in the ink resulted in easier extrusion from the nozzle. The size and morphology of ink deposition were controlled by adjusting the ratio of extrusion speed to printing speed and the height of the nozzle. It was found that the ink deflection was proportional to the span, which was defined as the distance between two supporting points of the printed structure. Specifically, the influence of span on deflection was studied by printing structures whose spans were 1800, 1300, and 950 µm, respectively. The measurement revealed that fine ink deposition without deflection could be ensured when the span was < 920 µm. The printed zeolite monolith experienced roughly a 53% volume shrinkage and displayed a surface fluctuation of about 100 µm, while the sidewalls fluctuated around 200 µm, indicating a high level of precision in its formation. The mechanical strength of the structure reached up to 11 MPa but decreased as the layer height increased[120]. As for the other printing techniques, most of the existing research has been performed on the material development for the zeolitic gas adsorbents, whereas few studies have focused on the optimization of printing process parameters.

3.4. Post-processing of 3D-printed zeolites

Calcination is another crucial post-processing step in fabricating 3D-printed zeolitic gas adsorbents, as it can affect their morphology, crystallinity, and surface chemistry. Calcination helps remove the organic additives used in the 3D printing process, leaving behind only the inorganic zeolite framework. This is important because the presence of organic materials in the zeolite can significantly compromise its porosity and adsorption performance[121]. Calcination helps to activate the zeolite framework and remove any residual water molecules or impurities trapped within it. This process results in an increase in the surface area and pore volume of the zeolite, which is vital for achieving high adsorption capacity and selectivity toward the target gas molecules[99-101]. Calcination also improves the mechanical strength and stability of the 3D-printed zeolite structure, making it more robust and resistant to deformation or cracking during subsequent handling[27,105]. Calcination time and duration for 3D-printed zeolite monoliths depend on several factors, such as the type of zeolite, the type of binder, and the desired properties and performance of the final product. Typically, calcination is performed at temperatures between 400°C and 800°C for several hours in the presence of air or another oxidizing agent. However, the specific conditions and duration of calcination may need to be optimized to ensure that the desired properties and performance of the 3D-printed zeolite monoliths are achieved. It is recommended to consult the literature for more specific guidance on the calcination process for a given zeolite system. Thakkar *et al.* made the printed zeolite calcinated at 700°C for 2 – 4 h to remove the organic content, leading to an increase in both the mesoporosity and mechanical strength of the final product[91]. Couck *et al.* adopted a calcination condition of 823 K for 3 h to ensure that the printed ZSM-5 monolith retained its crystalline nature[96].

4. Applications of 3D-printed zeolitic gas absorbents

Recent advancements in 3D printing technology have enabled the fabrication of complex zeolite structures with precise control over their pore size and geometry. This has opened new possibilities for designing and optimizing zeolitic adsorbents for specific gas separation, purification, and storage applications.

4.1. Gas separation

3D-printed zeolite monoliths have shown significant potential for use in gas separation. One typical application of 3D-printed zeolite structures for gas separation is the selective removal of CO_2 from CH_4 in natural gas streams. It is because that the existence of CO_2 would lower the heating value of gas, leading to corrosion when water is also present in pipelines[122,123]. Lawson *et al.* measured the adsorption isotherms for CO_2 and CH_4 at 25°C from 0 to 1 bar for four different 3D-printed zeolite structures that made of 13X, 5A, ZSM-5, and South Asia (SA)[94]. It was found that the South Asia zeolite monolith exhibited a CO_2/CH_4 selectivity of approximately 50 with a corresponding uptake capacity of approximately 3 mmol/g at a pressure of 0.15 bar[94]. In the study by Wang *et al.*, 3D-printed NaX zeolite monoliths were shown to be highly effective in separating CO_2 and CH_4 gases in fuel gas purification. Dynamic adsorption breakthrough tests demonstrated the superiority of 3D-printed zeolites over commercial benchmark ones for flue gas purification and natural gas upgrading. The equilibrium CO_2 uptake of the 3D-printed zeolite monoliths reached up to 5.58 mmol/g at a temperature of 298 K and pressure of 1 bar. The 3D-printed gas adsorbents displayed an ultra-strong CO_2 affinity compared to the parental NaX zeolite powders, particularly at low partial pressure[27].

One promising approach for the removal of CO_2 from natural gas streams is the use of electric swing adsorption (ESA) technology. In the traditional temperature swing adsorption process, the adsorbent is regenerated by increasing the temperature, which causes the adsorbed gas to desorb from the surface of the adsorbent. In contrast, the energy expended is delivered directly to the adsorbent during the ESA process, which implies a higher efficiency and minimization of lost heat[124]. Regufe *et al.* used DIW to print an electrically conductive 3D-printed zeolitic gas adsorbent for CO_2 capture in the ESA process[125]. Zeolite 13X was mixed with activated carbon and carboxymethylcellulose to formulate printing ink. At a pressure of 0.15 bar, the CO_2 adsorption capacity of the 3D-printed gas adsorbent is 3.49 mol/kg, an increase of about 40% from its counterpart fabricated by the traditional die-based extrusion process.

4.2. Gas purification

There are several high-value purification applications for 3D-printed zeolite form factors. Specialty gases are one such area. Contaminant signatures are unique to many specialty gases, mainly due to production methods. Still, these signatures can also be influenced and even determined by other factors such as geography and raw materials supply. Purification across this gas landscape involves dozens, perhaps hundreds of separations, which are complicated by the inherent reactivity of the gas itself and competition of contaminants for adsorbent active sites. The semiconductor industry is a large consumer of ultra-high purity specialty gases, where sensitivity to contamination often drives purity needs to 99.999% (5N) or better. Gas-phase processes such as deposition, etch, epitaxy, and annealing all consume specialty gases through the use of sophisticated process tools. Often, these tools employ many different gases in their operation, and most include small point-of-use purifiers to ensure both stable process yield and protection of critical components. Considering the physical space constraints, gas velocities, and lifetimes required in these ultra-high purity applications, the purification of specialty gases represents considerable challenges. For the gas purification technologist, gaining access to the large variety of zeolite structural motifs and other sorbents through 3D printing is a significant solution enabler.

Although contaminant signatures can be specific to many process gases, many long-standing purification targets are common across the industry. Atmospherics such as moisture, CO, CO_2, and NO_x compounds are ubiquitous contaminants, usually present due to intrusions in handling and transportation. Other common contaminants include the class of volatile organic compounds (VOCs), which can be attributed to the atmosphere, lubricants used in various processes, or even cleaning residue. Adsorption of VOCs is an essential application of 3D-printed zeolite structures for gas purification. VOCs are a group of organic chemicals that are emitted as gases from certain solids or liquids. They can cause a variety of health and environmental problems, including respiratory issues and the formation of smog[126,127]. As shown in Figure 12, Wang *et al.* proposed a design of the core-shell structure in the 3D-printed zeolite monoliths to enhance their adsorption and separation performance. The core of the monolith was a ZSM-5 honeycomb structure with high selectivity for VOCs. After the ZSM-5 core was printed, a hydrophobic silicalite-1 shell was grown on the surface of individual ZSM-5 crystals by introducing colloidal silica into the printing inks. The breakthrough time for toluene removal over one printed sample under dry conditions is reported as 357 s/g, while under humid conditions, it is slightly longer at 442 s/g[97].

As a typical zeolite-like structure, 3D-printed ZIF-8 monoliths have also been adopted for the removal of VOCs. Pellejero *et al.* formulated the ZIF-8 on ABS filament to adopt dimethyl methylphosphonate (DMMP), a type of VOC used as a simulant for nerve agents in research and testing[128]. The formulation involved low-temperature atomic layer deposition of ZnO on the ABS matrix and subsequent hydrothermal conversion of ZnO to ZIF-8 on the ABS support to prepare the filament. The printed ABS/ZIF-8 fillers were found to have an adsorption capacity of 20.4 mg of DMMP per gram of ZIF-8[128].

4.3. Gas storage

The storage of gases such as CH_4 for energy sources is a key application for 3D-printed ZIF-8 gas adsorbents that possess MOFs and zeolites properties. The high porosity and stability of 3D-printed ZIF-8 gas adsorbents make them suitable for gas storage, as they can provide high storage capacity and stability under a wide range of operating conditions. Dhainaut *et al.* studied the formulation of several types of MOF inks, including ZIF-8, for 3D printing and the creation of robust microporous solids for high-pressure gas storage. The SEM examination in Figure 13A showed that the 3D-printed ZIF-8 monoliths contain numerous pores induced by the rapid drying process, leading to a compressive strength slightly lower than that of dense ZIF-8 pellets by a factor of 10–100 times. Figure 13B shows that high-pressure CH_4 adsorption/desorption isotherms were measured at ambient temperature on 3D-printed ZIF-8 monoliths up to 55 bars. The results revealed that 3D-printed monoliths were able to store 59 g/kg of ZIF-8 at 298 K and 30 bars. Such capacity was close to that of commercial ZIF-8 powder, which was reported to store 68 g/kg at the same temperature and pressure level. It was pointed out that further optimization of printing parameters and MOF crystal loadings was required to improve mechanical properties and prevent partial sagging on the edges of the printed monolith for gas storage application[129].

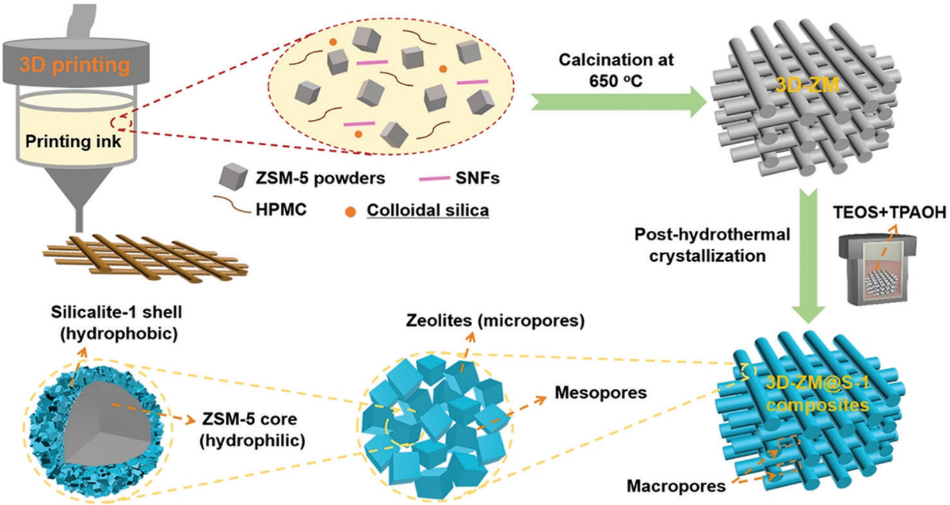

Figure 12. Schematic diagram for the additive manufacturing of core-shell structure zeolite composites for gas purification which consists of four major steps: ink formulation, 3D printing, high-temperature calcination, and post-hydrothermal treatment. Reprinted with permission from Wang *et al.*[97].

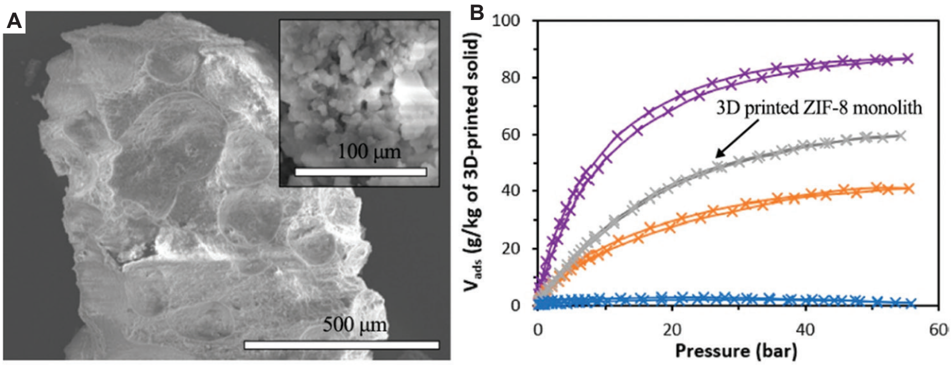

Figure 13. (A) Fragment and (B) high-pressure methane physisorption isotherms at 298 K of 3D-printed ZIF-8 monoliths. Reprinted with permission from Dhainaut *et al.*[129].

5. Conclusions and outlooks

In conclusion, 3D-printed zeolite monoliths have proved to be promising for gas adsorption, storage, and separation applications. They have several advantages over traditional methods of synthesizing zeolites, such as precise control over pore size and geometry and the ability to tailor the material for specific applications. Meanwhile, material limitation and production cost are the two major challenges that need to be overcome for the 3D printing of zeolite gas adsorbents. Zeolitic materials can be limited in their suitability for 3D printing methods. Such material limitation also makes 3D printing sometimes more expensive and time-consuming for large-scale production when compared to traditional manufacturing approaches. It is expected that 3D-printed zeolite monoliths can be fabricated with high resolution and precision, leading to improved performance in gas adsorption, storage, and separation applications.

The future research will focus on the development of 3D printing technology for zeolitic gas adsorbents and will continue to focus on producing printed components with improved properties for gas adsorption. This may involve the development of new zeolite materials with optimized pore structures and surface chemistries, as well as improvements in the 3D printing process itself, such as faster printing speeds and the ability to print larger and more complex structures. Such material limitation also makes 3D printing sometimes more expensive and time-consuming for large-scale production when compared to traditional manufacturing methods. Multi-material 3D printing is also a promising approach for fabricating zeolitic gas adsorbents with complex geometries and highly customized material properties. Thompson *et al.* adopted a multi-material DLP technique to create a multi-functional composite for CO_2 adsorption with embedded resistive heating capability by co-printing non-conductive and conductive zeolite sorbent inks together. It can be foreseen that the combination of zeolite with polymers or MOFs enables the fabrication of multi-functional components with enhanced gas adsorption performance[130]. In addition, there is a greater emphasis on using sustainable and environmentally friendly materials for 3D-printed zeolitic monoliths, such as biodegradable polymers and renewable energy sources for printing. With continued research and development, 3D-printed zeolitic gas adsorbents will become an increasingly important component in the transition to a more sustainable and clean energy future.

Acknowledgments

This research/project is supported by A*STAR under RIE2020, industry alignment fund – industry collaboration projects (IAF-ICP) (I2001E0056).

Funding

See Acknowledgments section.

Conflict of interest

The authors declare that they have no competing interests.

Author contributions

Conceptualization: Subhash Guddati, Sharon Mui Ling Nai
Writing – original draft: Jiazhao Huang, Rocky Gipson
Writing – review and editing: Rocky Gipson, Chengcheng Wang, Su Xia Zhang, Subhash Guddati, Sharon Mui Ling Nai

Ethics approval and consent to participate

Not applicable.

Consent for publication

Not applicable.

Availability of data

Not applicable.

References

1. Anastas P, Eghbali N, 2010, Green chemistry: Principles and practice. *Chem Soc Rev*, 39: 301–312.

   https://doi.org/10.1039/B918763B

2. Li Y, Li L, Yu J, 2017, Applications of zeolites in sustainable chemistry. *Chem*, 3: 928–949.

   https://doi.org/10.1016/j.chempr.2017.10.009

3. Min BK, Friend CM, 2007, Heterogeneous gold-based catalysis for green chemistry: Low-temperature CO oxidation and propene oxidation. *Chem Rev*, 107: 2709–2724.

   https://doi.org/10.1021/cr050954d

4. Yue X, Ma NL, Sonne C, *et al.*, 2021, Mitigation of indoor air pollution: A review of recent advances in adsorption materials and catalytic oxidation. *J Hazard Mater*, 405: 124138.

   https://doi.org/10.1016/j.jhazmat.2020.124138

5. Zeng H, Qu X, Xu D, *et al.*, 2022, Porous adsorption materials for carbon dioxide capture in Industrial flue gas. *Front Chem*, 10: 939701.

6. Zagho MM, Hassan MK, Khraisheh M, *et al.*, 2021, A review on recent advances in CO_2 separation using zeolite and zeolite-like materials as adsorbents and fillers in mixed matrix membranes (MMMs). *Chem Eng J Adv*, 6: 100091.

7. Dyer A, 1988, An Introduction to Zeolite Molecular Sieves. New York, United States: John Wiley and Sons Inc. Available from: https://www.osti.gov/biblio/5362126 [Last accessed on 2023 Sep 21].

8. Ozin GA, Kuperman A, Stein A, 1989, Advanced zeolite, materials science. *Angew Chem Int Ed*, 28: 359–376.

   https://doi.org/10.1002/anie.198903591

9. Busca G, (eds), 2014, Zeolites and other structurally microporous solids as acid-base materials. In: Heterogeneous Catalytic Materials. Ch. 7. Amsterdam: Elsevier, p.197–249. Available from: https://www.sciencedirect.com/science/article/pii/B9780444595249000079 [Last accessed on 2023 Sep 21].

10. Sherman JD, 1999, Synthetic zeolites and other microporous oxide molecular sieves. *Proc Natl Acad Sci*, 96: 3471–3478.

    https://doi.org/10.1073/pnas.96.7.3471

11. Combariza AF, Sastre G, 2011, Influence of zeolite surface in the sorption of methane from molecular dynamics. *J Phys Chem C*, 115: 13751–13758.

    https://doi.org/10.1021/jp202043t

12. Oheix E, Reicher C, Nouali H, *et al.*, 2022, Rational design and characterisation of novel mono- and bimetallic antibacterial Linde type A zeolite materials. *J Funct Biomater*, 13: 73.

    https://doi.org/10.3390/jfb13020073

13. Praipipat P, Ngamsurach P, Roopkhan N, 2023, Zeolite A powder and beads from sugarcane bagasse fly ash modified with iron(III) oxide-hydroxide for lead adsorption. *Sci Rep*, 13: 1873.

    https://doi.org/10.1038/s41598-023-29055-4

14. Bingre R, Louis B, Nguyen P, 2018, An overview on zeolite shaping technology and solutions to overcome diffusion limitations. *Catalysts*, 8: 163.

    https://doi.org/10.3390/catal8040163

15. Coronas J, 2010, Present and future synthesis challenges for zeolites. *Chem Eng J*, 156: 236–242.

16. Williams JL, 2001, Monolith structures, materials, properties and uses. *Catal Today*, 69: 3–9.

17. Halevi O, Chen TY, Lee PS, *et al.*, 2020, Nuclear wastewater decontamination by 3D-printed hierarchical zeolite monoliths. *RSC Adv*, 10: 5766–5776.

    https://doi.org/10.1039/C9RA09967K

18. Hawaldar NH, 2018, Slurry Preparation of Zeolite and Metal-organic Framework for Extrusion Based 3D-printing. United States: Purdue University. Available from: https://docs.lib.purdue.edu/dissertations/AAI10809712 [Last accessed 2023 Sep 21].

19. Chua CK, Leong KF, 2016, 3D Printing and Additive Manufacturing. Singapore: World Scientific.

    https://doi.org/10.1142/10200

20. Comroe ML, Kolasinski KW, Saha D, 2022, Direct ink 3D printing of porous carbon monoliths for gas separations. *Molecules*, 27: 5653.

    https://doi.org/10.3390/molecules27175653

21. Middelkoop V, Coenen K, Schalck J, *et al.*, 2019, 3D printed versus spherical adsorbents for gas sweetening. *Chem Eng J*, 357: 309–319.

22. Toh WQ, Wang P, Tan X, *et al.*, 2016, Microstructure and wear properties of electron beam melted Ti-6Al-4V parts: A comparison study against as-cast form. *Metals*, 6: 284.

    https://doi.org/10.3390/met6110284

23. Zhu ZG, Nguyen QB, Ng FL, *et al.*, 2018, Hierarchical microstructure and strengthening mechanisms of a CoCrFeNiMn high entropy alloy additively manufactured by selective laser melting. *Scr Mater*, 154: 20–24.

24. Hon KKB, Li L, Hutchings IM, 2008, Direct writing technology-advances and developments. *CIRP Ann Manuf Technol*, 57: 601–620.

25. Thakkar H, Eastman S, Al-Naddaf Q, *et al.*, 2017, 3D-printed metal-organic framework monoliths for gas adsorption processes. *ACS Appl Mater Interfaces*, 9: 35908–35916.

    https://doi.org/10.1021/acsami.7b11626

26. Yuan S, Bai J, Chua CK, *et al.*, 2016, Material evaluation and process optimization of CNT-coated polymer powders for selective laser sintering. *Polymers* (*Basel*), 8: 370.

    https://doi.org/10.3390/polym8100370

27. Wang S, Bai P, Sun M, *et al.*, 2019, Fabricating mechanically robust binder-free structured zeolites by 3D printing coupled with zeolite soldering: A superior configuration for CO_2 capture. *Adv Sci* (*Weinh*), 6: 1901317.

    https://doi.org/10.1002/advs.201901317

28. Nadagouda MN, Ginn M, Rastogi V, 2020, A review of 3D printing techniques for environmental applications. *Curr Opin Chem Eng*, 28: 173–178.

29. Hubesch R, Mazur M, Föger K, *et al.*, 2021, Zeolites on 3D-printed open metal framework structure: Metal migration into zeolite promoted catalytic cracking of endothermic fuels for flight vehicles. *Chem Commun*, 57: 9586–9589.

    https://doi.org/10.1039/D1CC04246G

30. Low ZX, Chua YT, Ray BM, *et al.*, 2017, Perspective on 3D printing of separation membranes and comparison to related unconventional fabrication techniques. *J Membr Sci*, 523: 596–613.

31. Lawson S, Snarzyk M, Hanify D, *et al.*, 2020, Development of 3D-printed polymer-MOF monoliths for CO_2 adsorption. *Ind Eng Chem Res*, 59: 7151–7160.

    https://doi.org/10.1021/acs.iecr.9b05445

32. Zhakeyev A, Wang P, Zhang L, *et al.*, 2017, Additive manufacturing: Unlocking the evolution of energy materials. *Adv Sci*, 4: 1700187.

    https://doi.org/10.1002/advs.201700187

33. Li X, Rezaei F, Rownaghi AA, 2019, Methanol-to-olefin conversion on 3D-printed ZSM-5 monolith catalysts: Effects of metal doping, mesoporosity and acid strength. *Microporous Mesoporous Mater*, 276: 1–12.

34. Wright PA, Pearce GM, (eds), 2010, Structural chemistry of zeolites. In: Zeolites and Catalysis. Germany: Wiley-VCH, Federal Republic of Germany, p.171–207.

    https://doi.org/10.1002/9783527630295.ch7

35. Derbe T, Temesgen S, Bitew M, 2021, A short review on synthesis, characterization, and applications of zeolites. *Adv Mater Sci Eng*, 2021: 6637898.

    https://doi.org/10.1155/2021/6637898

36. Emami Moghaddam SA, Harun R, Mokhtar MN, *et al.*, 2018, Potential of zeolite and algae in biomass immobilization. *Biomed Res Int*, 2018: 6563196.

    https://doi.org/10.1155/2018/6563196

37. Weckhuysen BM, 2016, Zeolites shine bright. *Nat Mater*, 15: 933–934.

    https://doi.org/10.1038/nmat4730

38. Jha B, Singh DN, (eds), 2016, Basics of zeolites. In: Fly Ash Zeolites: Innovations, Applications, and Directions. Singapore, Berlin: Springer Singapore, p.5–31.

    https://doi.org/10.1007/978-981-10-1404-8_2

39. Baerlocher C, McCusker LB, Olson DH, (eds), 2007, Introduction and explanatory notes. In: Atlas of Zeolite Framework Types. 6th ed. Amsterdam: Elsevier Science B.V, p.3–11. Available from: https://www.sciencedirect.com/science/article/pii/B9780444530646501870 [Last accessed on 2023 Sep 21].

40. Król M, 2020, Natural vs. synthetic zeolites. *Crystals*, 10: 622.

https://doi.org/10.3390/cryst10070622

41. Mijailović NR, Nedić Vasiljević B, Ranković M, *et al*., 2022, Environmental and pharmacokinetic aspects of zeolite/pharmaceuticals systems-Two facets of adsorption ability. *Catalysts*, 12: 837.

    https://doi.org/10.3390/catal12080837

42. Hollman GG, Steenbruggen G, Janssen-Jurkovičová M, 1999, A two-step process for the synthesis of zeolites from coal fly ash. *Fuel*, 78: 1225–1230.

43. Yuna Z, 2016, Review of the natural, modified, and synthetic zeolites for heavy metals removal from wastewater. *Environ Eng Sci*, 33: 443–454.

    https://doi.org/10.1089/ees.2015.0166

44. Sircar S, Myers AL, 2003, Gas separation by zeolites. In: Handbook of Zeolite Science and Technology. Boca Raton: CRC Press, p. 22.

45. Tran YT, Lee J, Kumar P, *et al*., 2019, Natural zeolite and its application in concrete composite production. *Compos B Eng*, 165: 354–364.

46. Li J, Gao M, Yan W, *et al*., 2023, Regulation of the Si/Al ratios and Al distributions of zeolites and their impact on properties. *Chem Sci*, 14: 1935–1959.

    https://doi.org/10.1039/D2SC06010H

47. Bakhtyari A, Mofarahi M, Lee CH, (eds), 2020, CO2 adsorption by conventional and nanosized zeolites. In: Advances in Carbon Capture. Ch. 9. United Kingdom: Woodhead Publishing, p.193–228. Available from: https://www.sciencedirect.com/science/article/pii/B9780128196571000098 [Last accessed 2023 Sep 21].

48. Langwaldt J, 2008, Ammonium removal from water by eight natural zeolites: A comparative study. *Sep Sci Technol*, 43: 2166–2182.

    https://doi.org/10.1080/01496390802063937

49. Karousos DS, Sapalidis AA, Kouvelos EP, *et al*., 2016, A study on natural clinoptilolite for CO_2/N_2 gas separation. *Sep Sci Technol*, 51: 83–95.

    https://doi.org/10.1080/01496395.2015.1085880

50. Kraljević Pavelić S, Simović Medica J, Gumbarević D, *et al*., 2018, Critical review on zeolite clinoptilolite safety and medical applications *in vivo*. *Front Pharmacol*, 9: 01350.

51. Bandura L, Woszuk A, Kołodyńska D, *et al*., 2017, Application of mineral sorbents for removal of petroleum substances: A review. *Minerals*, 7: 37.

    https://doi.org/10.3390/min7030037

52. Villarreal A, Garbarino G, Riani P, *et al*., 2017, Adsorption and separation of CO_2 from N_2-rich gas on zeolites: Na-X faujasite vs Na-mordenite. *J CO2 Util*, 19: 266–275.

53. Shukla P, Dong K, Rudolph V, *et al*., 2019, Adsorptive dehydration of ethanol using 3A zeolite: An evaluation of transport behaviour in a two-phase zeolite pellet. *Adsorption*, 25: 1611–1623.

    https://doi.org/10.1007/s10450-019-00145-y

54. Larasati ZS, Widiastuti N, 2018, Adsorption-desorption of CO_2 and H_2 gases on zeolite-X supported on glass fiber. *AIP Conf Proc*, 2049: 020083.

    https://doi.org/10.1063/1.5082488

55. Guo X, Zhang P, Navrotsky A, 2020, The thermodynamics of gas absorption and guest-induced flexibility in zeolite Y. *Microporous Mesoporous Mater*, 294: 109893.

56. Bradley SA, Broach RW, Mezza TM, *et al*., (eds), 2010, Zeolite characterization. In: Zeolites in Industrial Separation and Catalysis. Great Britain: Wiley-VCH, p.85–171.

    https://doi.org/10.1002/9783527629565.ch4

57. Stelzer J, Paulus M, Hunger M, *et al*., 1998, Hydrophobic properties of all-silica zeolite beta1Dedicated to Professor Lovat V.C. Rees in recognition and appreciation of his lifelong devotion to zeolite science and his outstanding achievements in this field.1. *Microporous Mesoporous Mater*, 22: 1–8.

58. Feng C, Jiaqiang E, Han W, *et al*., 2021, Key technology and application analysis of zeolite adsorption for energy storage and heat-mass transfer process: A review. *Renew Sustain Energy Rev*, 144: 110954.

59. Pérez-Pellitero J, Pirngruber GD, (eds), 2020, Industrial zeolite applications for gas adsorption and separation processes. In: New Developments in Adsorption/Separation of Small Molecules by Zeolites. Cham: Springer International Publishing, p.195–225.

    https://doi.org/10.1007/430_2020_75

60. Rezaei F, Webley P, 2010, Structured adsorbents in gas separation processes. *Sep Purif Technol*, 70: 243–256.

61. Wu J, Zhu X, Yang F, *et al*., 2022, Shaping techniques of adsorbents and their applications in gas separation: A review. *J Mater Chem A*, 10: 22853–22895.

    https://doi.org/10.1039/D2TA04352A

62. Boer DG, Langerak J, Pescarmona PP, 2023, Zeolites as selective adsorbents for CO_2 separation. *ACS Appl Energy Mater*, 6: 2634–2656.

    https://doi.org/10.1021/acsaem.2c03605

63. Tomašić V, Jović F, 2006, State-of-the-art in the monolithic catalysts/reactors. *Appl Catal A Gen*, 311: 112–121.

64. Li YY, Perera SP, Crittenden BD, 1998, Zeolite monoliths for air separation: Part 1: Manufacture and characterization. *Chem Eng Res Des*, 76: 921–930.

65. Aranzabal A, Iturbe D, Romero-Sáez M, *et al*., 2010, Optimization of process parameters on the extrusion of honeycomb shaped monolith of H-ZSM-5 zeolite. *Chem*

Eng J, 162: 415–423.

66. Fedosov DA, Smirnov AV, Knyazeva EE, *et al.*, 2011, Zeolite membranes: Synthesis, properties, and application. *Pet Chem*, 51: 657–667.

    https://doi.org/10.1134/S0965544111080032

67. Mette B, Kerskes H, Drück H, *et al.*, 2014, Experimental and numerical investigations on the water vapor adsorption isotherms and kinetics of binderless zeolite 13X. *Int J Heat Mass Transf*, 71: 555–561.

68. Silva JAC, Schumann K, Rodrigues AE, 2012, Sorption and kinetics of CO_2 and CH_4 in binderless beads of 13X zeolite. *Microporous Mesoporous Mater*, 158: 219–228.

69. Scheffler M, Scheffler F, 2006, Zeolite coatings on porous monoliths. *Adv Sci Technol*, 45: 1260–1267.

70. Li L, Xue B, Chen J, *et al.*, 2005, Direct synthesis of zeolite coatings on cordierite supports by *in situ* hydrothermal method. *Appl Catal A Gen*, 292: 312–321.

71. Aimen Isa M, Hanif Halim M, Chew TL, *et al.*, 2020, Formation of NaY zeolite membrane: Influence of intermediate layer and its characterization. *IOP Conf Ser Mater Sci Eng*, 736: 052019.

    https://doi.org/10.1088/1757-899X/736/5/052019

72. Stuecker JN, Miller JE, Ferrizz RE, *et al.*, 2004, Advanced support structures for enhanced catalytic activity. *Ind Eng Chem Res*, 43: 51–55.

    https://doi.org/10.1021/ie030291v

73. Liu J, Huo W, Ren B, *et al.*, 2018, A novel approach to fabricate porous alumina ceramics with excellent properties via pore-forming agent combined with sol impregnation technique. *Ceram Int*, 44: 16751–16757.

74. Hull CW, 1984, Apparatus for Production of Three-dimensional Objects by Stereolithography. United States Patent, Application, No. 638905, Filed. Avialable from: https://pubchem.ncbi.nlm.nih.gov/patent/US-6027324-A [Last accessed on 2023 Sep 21].

75. Pagac M, Hajnys J, Ma QP, *et al.*, 2021, A review of vat photopolymerization technology: Materials, applications, challenges, and future trends of 3D printing. *Polymers* (*Basel*), 13: 598.

    https://doi.org/10.3390/polym13040598

76. Nohut S, Schwentenwein M, 2022, Vat photopolymerization additive manufacturing of functionally graded materials: A review. *J Manuf Mater Process*, 6: 17.

77. Zhang F, Li Z, Xu M, *et al.*, 2022, A review of 3D printed porous ceramics. *J Eur Ceram Soc*, 42: 3351–3373.

78. Shahzad A, Lazoglu I, 2021, Direct ink writing (DIW) of structural and functional ceramics: Recent achievements and future challenges. *Compos B Eng*, 225: 109249.

79. Pan Y, Zhu P, Wang R, *et al.*, 2019, Direct ink writing of porous cordierite honeycomb ceramic. *Ceram Int*, 45: 15230–15236.

80. Solís Pinargote NW, Smirnov A, Peretyagin N, *et al.*, 2020, Direct ink writing technology (3D printing) of graphene-based ceramic nanocomposites: A review. *Nanomater*, 10: 1300.

    https://doi.org/10.3390/nano10071300

81. Crump SS, 1992, Apparatus and Method for Creating Three-dimensional Objects. United States Patent, Application, No. 5,121,329, Filed. Available from: https://patents.google.com/patent/US5121329/en [Last accessed on 2023 Sep 21].

82. Lakhdar Y, Tuck C, Binner J, *et al.*, 2021, Additive manufacturing of advanced ceramic materials. *Prog Mater Sci*, 116: 100736.

83. Smay JE, Gratson GM, Shepherd RF, *et al.*, 2002, Directed colloidal assembly of 3D periodic structures. *Adv Mater*, 14: 1279–1283.

    https://doi.org/10.1002/1521-4095(20020916)14:18<1279::AID-ADMA1279>3.0.CO;2-A

84. Schlordt T, Schwanke S, Keppner F, *et al.*, 2013, Robocasting of alumina hollow filament lattice structures. *J Eur Ceram Soc*, 33: 3243–3248.

85. Ziaee M, Crane NB, 2019, Binder jetting: A review of process, materials, and methods. *Addit Manuf*, 28: 781–801.

86. Mirzababaei S, Pasebani S, 2019, A review on binder jet additive manufacturing of 316L stainless steel. *J Manuf Mater Process*, 3: 82.

    https://doi.org/10.3390/jmmp3030082

87. Bose S, Vahabzadeh S, Bandyopadhyay A, 2013, Bone tissue engineering using 3D printing. *Mater Today*, 16: 496–504.

88. Chung H, Das S, 2008, Functionally graded Nylon-11/silica nanocomposites produced by selective laser sintering. *Mater Sci Eng A*, 487: 251–257.

89. Zhang G, Chen H, Yang S, *et al.*, 2018, Frozen slurry-based laminated object manufacturing to fabricate porous ceramic with oriented lamellar structure. *J Eur Ceram Soc*, 38: 4014–4019.

90. Van Noyen J, De Wilde A, Schroeven M, *et al.*, 2012, Ceramic processing techniques for catalyst design: Formation, properties, and catalytic example of ZSM-5 on 3-dimensional fiber deposition support structures. *Int J Appl Ceram Technol*, 9: 902–910.

    https://doi.org/10.1111/j.1744-7402.2012.02781.x

91. Thakkar H, Eastman S, Hajari A, *et al.*, 2016, 3D-printed zeolite monoliths for CO_2 removal from enclosed environments. *ACS Appl Mater Interfaces*, 8: 27753–27761.

    https://doi.org/10.1021/acsami.6b09647

92. Liu X, He J, Li R, 2012, High-pressure hydrogen adsorption in the zeolites: A grand canonical Monte Carlo study. *ISRN Renew Energy*, 2012: 491396.

https://doi.org/10.5402/2012/491396

93. Asgar Pour Z, Sebakhy KO, 2022, A review on the effects of organic structure-directing agents on the hydrothermal synthesis and physicochemical properties of zeolites. *Chemistry*, 4: 431–446.

94. Lawson S, Newport K, Al-Naddaf Q, *et al.*, 2021, Binderless zeolite monoliths production with sacrificial biopolymers. *Chem Eng J*, 407: 128011.

95. Zhang H, Wang P, Zhang H, *et al.*, 2020, Structured zeolite monoliths with ultrathin framework for fast CO_2 adsorption enabled by 3D printing. *Ind Eng Chem Res*, 59: 8223–8229.

https://doi.org/10.1021/acs.iecr.9b07060

96. Couck S, Lefevere J, Mullens S, *et al.*, 2017, CO_2, CH_4 and N_2 separation with a 3DFD-printed ZSM-5 monolith. *Chem Eng J*, 308: 719–726.

97. Wang S, Bai P, Wei Y, *et al.*, 2019, Three-dimensional-printed core-shell structured MFI-type zeolite monoliths for volatile organic compound capture under humid conditions. *ACS Appl Mater Interfaces*, 11: 38955–38963.

https://doi.org/10.1021/acsami.9b13819

98. Merilaita N, Vastamäki T, Ismailov A, *et al.*, 2021, Stereolithography as a manufacturing method for a hierarchically porous ZSM-5 zeolite structure with adsorption capabilities. *Ceram Int*, 47: 10742–10748.

99. Hawaldar N, Park HY, Jung YG, *et al.*, 2018, Extrusion-based 3D printing of molecular sieve zeolite for gas adsorption applications. *Mater Sci Technol*, 33–40.

https://doi.org/10.7449/2018mst/2018/mst_2018_33_40

100. Lawson S, Adebayo B, Robinson C, *et al.*, 2020, The effects of cell density and intrinsic porosity on structural properties and adsorption kinetics in 3D-printed zeolite monoliths. *Chem Eng Sci*, 218: 115564.

101. Couck S, Cousin-Saint-Remi J, Van der Perre S, *et al.*, 2018, 3D-printed SAPO-34 monoliths for gas separation. *Microporous Mesoporous Mater*, 255: 185–191.

102. Feilden E, Blanca EGT, Giuliani F, *et al.*, 2016, Robocasting of structural ceramic parts with hydrogel inks. *J Eur Ceram Soc*, 36: 2525–2533.

103. Liu G, Guo J, Meng F, *et al.*, 2014, Effects of colloidal silica binder on catalytic activity and adhesion of HZSM-5 coatings for structured reactors. *Chin J Chem Eng*, 22: 875–881.

104. Lee KY, Lee HK, Ihm SK, 2010, Influence of catalyst binders on the acidity and catalytic performance of HZSM-5 zeolites for methanol-to-propylene (MTP) process: Single and binary binder system. *Top Catal*, 53: 247–253.

https://doi.org/10.1007/s11244-009-9412-0

105. Lefevere J, Protasova L, Mullens S, *et al.*, 2017, 3D-printing of hierarchical porous ZSM-5: The importance of the binder system. *Mater Des*, 134: 331–341.

106. Yang Y, Zhou Z, Chu X, *et al.*, 2022, 3D-printed zeolite with combined structure for xylene isomerization. *Mater Des*, 219: 110744.

107. Shukrun Farrell E, Schilt Y, Moshkovitz MY, *et al.*, 2020, 3D printing of ordered mesoporous silica complex structures. *Nano Lett*, 20: 6598–6605.

https://doi.org/10.1021/acs.nanolett.0c02364

108. Bastani D, Esmaeili N, Asadollahi M, 2013, Polymeric mixed matrix membranes containing zeolites as a filler for gas separation applications: A review. *J Ind Eng Chem*, 19: 375–393.

109. Thakkar H, Lawson S, Rownaghi AA, *et al.*, 2018, Development of 3D-printed polymer-zeolite composite monoliths for gas separation. *Chem Eng J*, 348: 109–116.

110. Wudy K, Hinze M, Ranft F, *et al.*, 2017, Selective laser sintering of zeolite filled polypropylene composites: Processing and properties of bulk adsorbents. *J Mater Process Tech*, 246: 136–143.

111. Zhang Y, Josien L, Salomon JP, *et al.*, 2021, Photopolymerization of zeolite/polymer-based composites: Toward 3D and 4D printing applications. *ACS Appl Polym Mater*, 3: 400–409.

https://doi.org/10.1021/acsapm.0c01170

112. Liu J, He J, Wang L, *et al.*, 2016, NiO-PTA supported on ZIF-8 as a highly effective catalyst for hydrocracking of Jatropha oil. *Sci Rep*, 6: 23667.

https://doi.org/10.1038/srep23667

113. Huang H, Zhang W, Liu D, *et al.*, 2011, Effect of temperature on gas adsorption and separation in ZIF-8: A combined experimental and molecular simulation study. *Chem Eng Sci*, 66: 6297–6305.

114. Evans KA, Kennedy ZC, Arey BW, *et al.*, 2018, Chemically active, porous 3D-printed thermoplastic composites. *ACS Appl Mater Interfaces*, 10: 15112–15121.

https://doi.org/10.1021/acsami.7b17565

115. Bible M, Sefa M, Fedchak JA, *et al.*, 2018, 3D-printed acrylonitrile butadiene styrene-metal organic framework composite materials and their gas storage properties. *3D Print Addit Manuf*, 5: 63–72.

https://doi.org/10.1089/3dp.2017.0067

116. Lefevere J, Claessens B, Mullens S, *et al.*, 2019, 3D-printed zeolitic imidazolate framework structures for adsorptive separations. *ACS Appl Nano Mater*, 2: 4991–4999.

https://doi.org/10.1021/acsanm.9b00934

117. Magzoub F, Li X, Lawson S, *et al.*, 2020, 3D-printed HZSM-5 and 3D-HZM5@SAPO-34 structured monoliths with controlled acidity and porosity for conversion of methanol to dimethyl either. *Fuel*, 280: 118628.

118. Lee J, Chuah CY, Tan WS, *et al.*, 2022, 3D-printed monolithic porous adsorbents from a solution-processible, hypercrosslinkable, functionalizable polymer. *Chem Eng J*, 427: 130883.

119. Li X, Rezaei F, Rownaghi AA, 2018, 3D-printed zeolite monoliths with hierarchical porosity for selective methanol to light olefin reaction. *React Chem Eng*, 3: 733–746.

https://doi.org/10.1039/C8RE00095F

120. Chu X, Tang X, Chen W, *et al.*, 2023, Direct-ink-write printing performance of zeolite catalysts with porous structures. *Ceram Int*, 49: 13531–13541.

121. Bragina AA, Lysikov AI, Parkhomchuk EV, 2022, Forming of block zeolites using 3D printing technology. *Pet Chem*, 62: 853–861.

https://doi.org/10.1134/S0965544122070088

122. Morishige K, 2011, Adsorption and separation of CO_2/CH_4 on amorphous silica molecular sieve. *J Phys Chem C*, 115: 9713–9718.

https://doi.org/10.1021/jp202572w

123. Li Y, Yi H, Tang X, *et al.*, 2013, Adsorption separation of CO_2/CH_4 gas mixture on the commercial zeolites at atmospheric pressure. *Chem Eng J*, 229: 50–56.

124. Zhao R, Liu L, Zhao L, *et al.*, 2018, Thermodynamic analysis on carbon dioxide capture by electric swing adsorption (ESA) technology. *J CO2 Util*, 26: 388–396.

125. Regufe MJ, Ferreira AFP, Loureiro JM, *et al.*, 2019, Electrical conductive 3D-printed monolith adsorbent for CO_2 capture. *Microporous Mesoporous Mater*, 278: 403–413.

126. Gelles T, Krishnamurthy A, Adebayo B, *et al.*, 2020, Abatement of gaseous volatile organic compounds: A material perspective. *Catal Today*, 350: 3–18.

127. Krishnamurthy A, Adebayo B, Gelles T, *et al.*, 2020, Abatement of gaseous volatile organic compounds: A process perspective. *Catal Today*, 350: 100–119.

128. Pellejero I, Almazán F, Lafuente M, *et al.*, 2020, Functionalization of 3D printed ABS filters with MOF for toxic gas removal. *J Ind Eng Chem*, 89: 194–203.

129. Dhainaut J, Bonneau M, Ueoka R, *et al.*, 2020, Formulation of metal-organic framework inks for the 3D Printing of robust microporous solids toward high-pressure gas storage and separation. *ACS Appl Mater Interfaces*, 12: 10983–10992.

https://doi.org/10.1021/acsami.9b22257

130. Thompson JF, Bellerjeau C, Marinick G, *et al.*, 2019, Intrinsic thermal desorption in a 3D printed multifunctional composite CO_2 sorbent with embedded heating capability. *ACS Appl Mater Interfaces*, 11: 43337–43343.

https://doi.org/10.1021/acsami.9b14111

ACCSCIENCE PUBLISHING

Materials Science in Additive Manufacturing

REVIEW ARTICLE

Metal additive manufacturing of orthopedic bone plates: An overview

Weiting Xu, Aydin Nassehi, and Fengyuan Liu*

School of Electrical, Electronic and Mechanical Engineering, University of Bristol, Bristol, United Kingdom

Abstract

Orthopedic bone plates, traditionally made from materials such as stainless steel or titanium alloy, have been pivotal in treating fractures. However, the disparity in modulus between these metals and natural bone leads to challenges, especially stress shielding, which can hinder optimal healing and cause issues such as bone resorption. In addition, the increase in complex fractures due to osteoporosis and demographic changes also points to the limitations of standard bone plates. This evolving landscape underscores the growing need for patient-specific solutions. This review delves into the advantages and challenges concerning the material choice, design, and production processes for the additive manufacturing (AM) of bone plates. AM offers the potential to customize bone plates using detailed computerized tomography scans or topology optimization, paving the way for unparalleled customization and potentially more effective bone regeneration. However, the intricacies of AM, from choosing the right materials to final production, add layers of complexity. An innovative methodology in the field of laser-metal Additive Manufacturing, known as Material-Structure-Performance Integrated AM (MSPI-AM), is at the forefront of tackling existing challenges, with the goal of enhancing the overall process in this domain. This strategy seamlessly blends material properties, structural components, and functional performance. Enriched by the analytical capabilities of artificial intelligence, this comprehensive method aims to enhance the AM process. It envisions a future where orthopedic treatments are not just functional but also are personalized masterpieces that reflect individual patient needs and address a variety of fracture scenarios.

Keywords: Orthopedic bone plate; Additive manufacturing; Biomaterial; Patient-specific implant; Stress shielding

***Corresponding author:**
Fengyuan Liu
(fengyuan.liu@bristol.ac.uk)

Citation: Xu W, Nassehi A, Liu F, 2023, Metal additive manufacturing of orthopedic bone plates: An overview. *Mater Sci Add Manuf,* 2(4): 2113. https://doi.org/10.36922/msam.2113

Received: October 25, 2023

Accepted: November 22, 2023

1. Introduction

Bone fractures represent a significant concern in orthopedics, stemming from various causes such as injuries, osteoporosis, and overuse[1]. Remarkably, the natural regenerative capacity of bone tissues allows for a high success rate in fracture healing, with approximately 90 – 95% of fractures achieving successful recovery[2]. Nevertheless, the healing process is complex as it involves a series of interconnected cellular events over a prolonged time[3-5].

Two primary mechanisms underpin fracture healing are the primary and secondary healing processes[6]. Primary healing is a direct, although rare, and self-repair process where mesenchymal cells transition into bone-forming osteoblasts in a stable post-fracture environment[6]. In contrast, secondary healing is a more common and efficient mechanism, encompassing a series of stages, namely, hematoma formation, granulation tissue formation, callus formation, and finally, bone remodeling[7,8]. These stages are graphically depicted in Figure 1.

When a fracture occurs, the immediate response in the vicinity is inflammation of the soft tissues, which leads to the formation of a hematoma[8]. This hematoma serves as a hub where immune-related cells release bioactive factors, setting in motion the fracture healing process[9]. As days progress, a transformation occurs: chondrocytes and a subset of osteoblasts, derived from osteoprogenitor cells and bone mesenchymal stem cells, begin to differentiate. Their collective action results in the formation of a cartilaginous callus, replacing the earlier hematoma[10]. This soft callus is temporary. As the differentiated osteoblasts work to fill the fracture gap with woven bone, they also lay down a hard bone callus within the periosteum. Over time, this leads to the emergence of a hard callus tissue, taking the place of the cartilaginous callus[3,11]. The healing journey concludes with the coordinated actions of osteoclasts and osteoblasts, ushering in the phase of bone remodeling[12]. This phase is characterized by the transformation of the callus tissue into the more structured lamellar bone. The intrinsic healing capabilities of bone are impressive, but they do not operate in isolation. For optimal bone regeneration, specific external stimuli are crucial. The cells involved in bone healing thrive in a specific environment marked by biomechanical load, stiffness, topography, and controlled movement of bone fragments[7,13].

With the recognition of the critical role external stimuli play in bone healing, the research community has shifted its focus. Current investigations are centered on the transduction mechanisms of mechanical stimuli and how they influence cellular behavior[6,13]. This interest stems partly from the extensive use of external implants in medical treatments. The choice of implant materials and design is pivotal as they shape the mechanical microenvironment at the fracture site[7,14]. Through tailored implants, one can modulate cellular activities, influencing the trajectory of bone fracture healing[15].

Bone plates, integral to fracture treatment, have an illustrious history dating back to the late 19th century[16]. However, the initial designs faced considerable challenges, notably their limited mechanical strength and a pronounced vulnerability to corrosion[17]. A pivotal moment in the evolution of bone plate design came in 1956, when Bagby and Janes introduced the concept of elliptical screw holes[18]. This seminal innovation enabled the screws to apply axial pressure upon tightening, thereby ensuring effective compression of the fractured bone fragments. This marked the advent of what came to be known as "compression plates"[18]. Over time, the category of compression plates has diversified, encompassing variants such as fusion plates, tension plates, and dynamic compression plates[19]. The primary objective of these plates remains consistent: to compress fractured fragments, limit movement, and facilitate primary bone healing. However, as with many medical innovations, compression plates present their own set of challenges. Among the most significant are an extended healing duration and the potential risk of bone resorption beneath the plate[20].

Modern research has pinpointed excessive plate-to-bone contact as a key contributor to bone loss under traditional compression plates[20,21]. In response, the design ethos shifted to minimize this contact area. The limited contact plate and point-contact fixation plate emerged as embodiments of this philosophy, offering benefits such as easier insertion and reduced post-operative complications[22]. However, the specter of osteoporosis due to prolonged implantation remained.

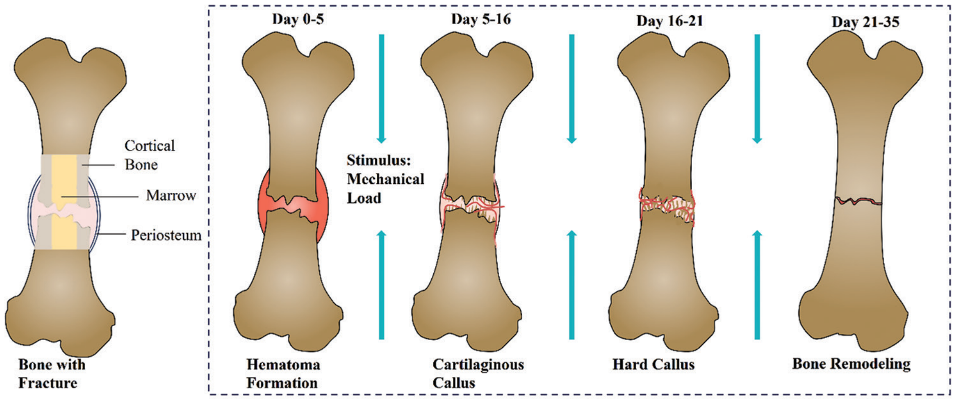

Figure 1. Stages of bone healing: from hematoma formation to complete remodeling. Modified from Einhorn and Gerstenfeld[106].

The revelation of the role of inter-fragmentary motion in fracture healing ushered in a new design paradigm. Bone plates with elliptical screw holes, allowing slight axial movement, were crafted to encourage secondary healing and minimize fibrous tissue formation[14,23]. Locking plates, with their design promoting a gap between bone and plate, further advanced this cause, preserving blood supply, and ensuring secondary healing[24].

However, a significant challenge – stress shielding – persisted. The stiffness of traditional bone plates far exceeded that of natural bone, inhibiting the transfer of biomechanical stimuli and potentially leading to bone resorption near the fracture[25]. Addressing stress shielding has been at the forefront of contemporary bone plate development. Strategies span novel materials, refined structural designs, and cutting-edge fabrication techniques[26,27]. With the challenges of secondary surgeries and long-term fatigue in mind, ongoing research is zeroing in on materials and designs that biodegrade post-healing[7,28].

Additive manufacturing (AM) is an advanced manufacturing technology that creates parts from three-dimensional (3D) model data by layering materials, a process outlined by ISO/ASTM standards 52900:2021[29]. Metal AM (MAM) extends this principle, using metal powder or wire as feedstock, to fabricate parts with complex geometries that are often challenging for conventional subtractive and formative manufacturing methods. In the medical industry, MAM has become crucial for producing medical implants, particularly those aimed at repairing or replacing diseased or damaged components of the bone musculoskeletal system[30-32]. MAM facilitates the realization of innovative bone plate designs, employing advanced design strategies such as topology optimization, lattice design, and generative design[33-35]. This approach not only enhances processing accuracy and efficiency but also effectively addresses critical issues like stress shielding. Moreover, advancements in MAM technology have significantly expanded the range of bone plate designs, catering to highly specialized medical procedures, including mandibular reconstructions and patient-specific osteotomies[36-38].

In summary, the evolution of bone plate development can be delineated into three significant phases, as illustrated in Figure 2. The introduction of locked compression plates marked a transformative phase, transitioning from primary to secondary healing. This change resulted in expedited healing processes and diminished post-healing defects. At present, the emphasis is on identifying materials that align more aptly with clinical requirements, paired with the adoption of advanced manufacturing techniques to produce customized, intricate bone plates. This review delves not only into the contemporary advancements in bone plate development using AM across all stages but also highlights potential challenges that may emerge. The content is

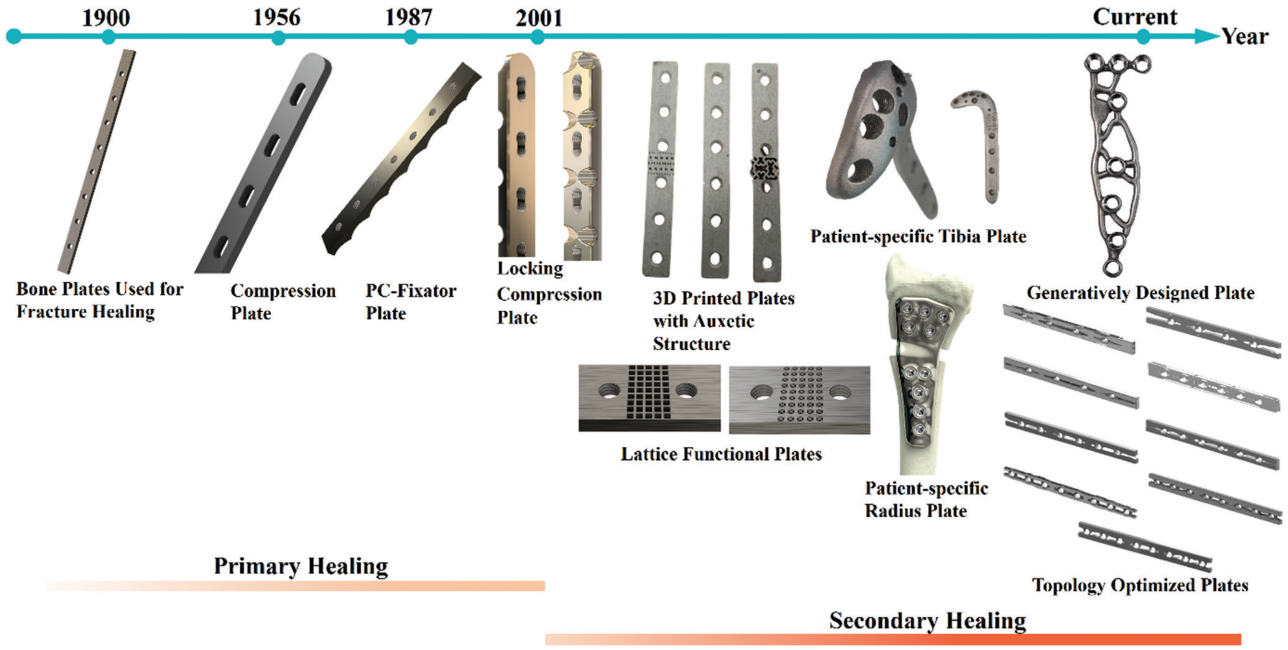

Figure 2. Evolution and diversity of bone plate designs. Adapted from Al-Tamimi *et al.*, Vijayavenkataraman *et al.*, Kanagalingam *et al.*, Dobbe *et al.*, and Teo *et al.*[33-37].

organized to cover the entire spectrum of manufacturing phases through AM, from material evolution and bone plate design to prevailing technologies and post-processing methodologies for the additive manufactured bone plates. Furthermore, insights into potential future directions associated with AM in bone plate development are provided.

2. Essentials of bone plate integration

Bones are fundamental to the structural integrity and mobility of vertebrates. Among them, long bones, such as the femur, tibia, fibula, metatarsals, humerus, ulna, radius, metacarpals, and phalanges, play a crucial role in providing support and facilitating movement[39]. Due to their prominence and function, these bones are often susceptible to injuries, commonly resulting from accidents or physical trauma.

To address such injuries, medical professionals resort to a range of treatments. One prevalent method involves the use of internal implants to stabilize fractured bone fragments. Depending on the specific location and function of the injured bone, various implants ranging from bone plates and intramedullary nails to K-wires and screws are employed[7]. Among these, osteosynthesis plates, which facilitate the healing process, are particularly significant. Their vital role in ensuring the proper fusion of fractured bone segments has made them an indispensable tool in orthopedic treatments[15].

Orthopedic plates play a pivotal role in the healing process of fractures, but their design and material composition are crucial for optimal patient outcomes. The ideal materials for these implants should be non-toxic, biocompatible, non-immunogenic, and bioactive, ensuring both effective healing and patient comfort[40]. As outlined by the Arbeitsgemeinschaft für Osteosynthesefragen, the key principles of internal fixation include meticulous alignment of fractured fragments, secure stabilization, preservation of blood supply, and early initiation of functional movement[41].

However, a significant challenge in the realm of orthopedic plates is the discrepancy in stiffness between metal plates and natural cortical bones. Metal plates, commonly used in medical applications, often possess a stiffness much higher than that of bones. This differential can lead to undesirable consequences, such as stress shielding, manifesting as bone loss beneath the plate, or osteoporosis in the regenerated bones[42,43]. To circumvent this issue, the design focus has shifted toward creating bone plates with materials that mimic the stiffness of natural bones. Such designs foster a conducive mechanical environment, promoting effective bone fracture healing[44-46].

The process of fracture healing is protracted, typically spanning 3 – 6 months. Recognizing this, some bone plates are engineered as permanent fixtures, obviating the need for subsequent removal surgeries[47,48]. These plates, especially those for load-bearing bones, must be resilient to endure the healing process and accommodate the specific biomechanical loads[49].

When designing or selecting bone plates for medical applications, it is crucial to address a multifaceted set of requirements. These encompass not only the choice of material composition, ensuring compatibility, and durability but also the mechanical and biomechanical properties that guarantee optimal performance under physiological conditions. In addition, the biomedical implications, including biocompatibility, potential inflammatory responses, and long-term outcomes for the patient, are equally significant in determining the success of the bone plate.

3. Overview of MAM

AM, often referred to as 3D printing or rapid prototyping, has transformed the landscape of manufacturing since its pioneering introduction in 1984[50]. Unlike traditional manufacturing methods that subtract material, AM adds material layer by layer, hence its nomenclature. This method not only optimizes material usage but also offers unparalleled design freedom.

The journey of an additive manufactured product begins in the digital realm. A product design is first conceptualized and then rendered into a digital 3D model using computer-aided design software or through 3D scanning of an existing object. This digital model is saved in the.stl format. Before printing can commence, this model is processed using slicing software. The software breaks down the model into hundreds or thousands of horizontal layers, creating a G-code file. This G-code serves as the instruction manual for the AM machine, dictating every precise movement it must undertake. Guided by this code, the printer systematically deposits or solidifies the chosen material layer upon layer, gradually giving shape to the desired object.

While the foundational concept of AM remains consistent, the technologies driving it have proliferated into diverse paths. At present, over 20 distinct AM technologies have been acknowledged[32]. Standardizing bodies such as ASTM and ISO classify them into seven primary categories: Binder jetting (BJT), directed energy deposition (DED), material extrusion (MEX), material jetting, powder bed fusion (PBF), sheet lamination, and vat photopolymerization (VPP)[29,32]. These categories encompass various techniques, materials, and applications, with certain methods such as BJT, DED, MEX, and PBF specialized in fabricating metallic products. The MAM sector prominently features two technologies: DED and PBF. Their market presence is substantial, with DED accounting for 16% and PBF a dominant 54% of the 2020 market share[31].

The DED and PBF techniques, as depicted in Table 1, have distinct methodologies and parameters. DED stands out for its adaptability, offering a range of feedstock options, including powders and wires. Moreover, its versatility extends to energy sources, encompassing lasers, electric arcs, and electron beams. This flexibility results in accelerated printing speeds, but often at the expense of finer layer resolution.

PBF, in contrast, is distinguished by its precision. While it primarily utilizes powders and has a more constrained set of energy sources, it excels in delivering superior layer resolutions. A noteworthy advantage of PBF is its integral powder bed. This not only provides the material base but also serves as an intrinsic support structure. This dual functionality facilitates the creation of complex designs, eliminating the need for supplementary, and sometimes cumbersome, support structures. Such an attribute endows PBF with a design adaptability that often surpasses that of DED[51].

4. The comprehensive journey of AM-based bone plate production

4.1. Selecting materials for orthopedic implants

Orthopedic implants play a crucial role in addressing bone defects. Over the years, they have undergone significant evolution, especially in terms of their constitutive materials. Conventionally, these materials are grouped into metals, bioceramics, and polymers[52]. Metals, due to their robust fixation capabilities and their resilience against daily mechanical loads, particularly in long bones, have become the primary choice for bone plates. For a detailed comparison of these metallic materials in orthopedic contexts, refer to Table 2.

Initially, vanadium steel was the preferred material for orthopedic implants. However, its limitations, particularly its subpar corrosion resistance and inadequate load-bearing capacity, led to a search for better alternatives[17]. This search culminated in the adoption of stainless steel (316L SS) and titanium alloy (Ti-6Al-4V). Characterized by improved corrosion resistance, mechanical strength, stiffness, and biocompatibility, these materials have since become staples in the orthopedic implant domain[53]. Furthermore, their versatility is evident in their compatibility with modern AM techniques. Both can be processed as powder or wire feedstock, aligning well with PBF and DED methodologies[54].

While these materials have revolutionized orthopedic treatments, the biomechanics of bone healing introduces new challenges. Mechanical stimulation and microinter fragmentary motion play pivotal roles in optimal bone regeneration. However, materials such as stainless steel and titanium alloy have a stiffness considerably surpassing

Table 1. Comparative analysis of key parameters for DED and PBF

Techniques	General process	Subcategory	Feedstock form	Thermal energy type	Typical layer thickness (μm)	Deposition rate (kg/h)	References
DED	Metal powder or wire is consistently introduced into the nozzle and subjected to a heat source (laser, electric arc or electron beam). This results in the material being melted to create a molten pool, which conforms to the designated layer configuration, and subsequently solidifies onto the substrate. This iterative process is reiterated to generate successive molten pools layer upon layer until the printing procedure reaches its culmination	Laser additive manufacturing DED	Powders	Laser	200 – 500	<0.50	[107,108]
		Wire and arc additive manufacturing	Wires	Electric arc	1000 – 2000	1.0 – 4.00	[107,109]
		Wire and laser additive manufacturing	Wires	Laser	>1000	0.10 – 2.88	[107,109-111]
		Wire and electron beam additive manufacturing	Wires	Electron beam	<3000	<19.80	[107,112]
PBF	A roller uniformly applies metallic powder onto a substrate, followed by controlled melting using a laser or electron beam. Subsequent layers are added using the roller, leading to the gradual fabrication of the product. This iterative process continues until the final desired structure is achieved with integrity	Selective laser melting	Powders	Laser	25 – 75	0.10 – 0.30	[37,43,47,93,113]
		Selective laser sintering	Powders	Laser	80 – 500	0.10 – 0.20	[79,114]
		Electron beam melting	Powders	Electron beam	50 – 100	0.10 – 0.20	[7,35]

DED: Directed energy deposition, PBF: Powder bed fusion

Table 2. Summary of orthopedic bone plate materials

Material category	Specific materials	Pros	Cons	References
Practical plate material	• Stainless steel 316L • Titanium alloy Ti-6Al-4V	• High mechanical strength • Corrosion resistance • Biocompatibility	• Stiffness mismatch with bone • Low fatigue life	[52-54,60]
Low-modulus alloy (β-Ti alloys)	• Ti–35Nb–7Zr–5Ta • Ti-35Zr-28Nb	• Resembles cortical bone modulus • Low toxicity • Good mechanical attributes • Corrosion resistance	• Inconsistency in the fabrication process • Mechanical property deviations	[7,61]
Smart alloy	• Ni-Ti	• Low stiffness • Biocompatibility • Super-elasticity	• Not mechanically superior • Nickel release concerns	[43,48,60]
Biodegradable metal	• Iron-based • Magnesium-based • Zinc-based	• Good mechanical strength • Enhances bone formation	• Uncontrollable degradation rate • Hydrogen gas formation (magnesium)	[28,64-71]
Bioceramic and polymer	• Nano-hydroxyapatite • Polyetheretherketone	• Biocompatibility • Biodegradability • Drug loading capability	• Insufficient bone healing support • Low mechanical strength	[15,27,52,72,73]

that of cortical bones. For instance, Young's modulus for 316L SS ranges between 190 and 205 GPa and for Ti6Al4V between 110 and 112 GPa, while cortical bone has a much lower modulus ranging between 11.6 and 20.8 GPa. Similarly, while 316L SS has a yield strength of 343 – 535 MPa and an ultimate tensile strength of 557 – 661 MPa, Ti6Al4V displays higher values, with a yield strength of 795 – 1051 MPa and an ultimate tensile strength of 860 – 1116 MPa. In comparison, the cortical bone's yield strength is between 53.4 and 132.4 MPa, and its ultimate tensile strength is between 72.8 and 175.2 MPa[55-59]. This disparity can hinder beneficial mechanical cues, potentially affecting the healing process or even leading to conditions like osteoporosis[27]. Notably, due to to the superior strength and reduced stiffness of Ti6Al4V bone plates compared to 316 L SS, they are becoming a popular alternative to traditional plates. However, they still faced challenges like poor fatigue properties, which can result in plate loosening or fractures[60].

Addressing the stiffness mismatch in orthopedic implants calls for exploring materials with a more appropriate modulus. A promising avenue has been the development of biocompatible β-Ti alloys, especially with the incorporation of β stabilizing alloy elements such as molybdenum (Mo), niobium (Nb), silicon (Si), tantalum (Ta), tin (Sn), and zirconium (Zr). The alloys, Ti–35Nb–7Zr–5Ta (TNZT) and Ti-35Zr-28Nb (TZN), have garnered particular attention due to their modulus being akin to that of cortical bone[61]. A study by Li *et al.*[62] illustrated the potential of TZN for bone scaffolds using selective laser melting (SLM). Although the mechanical properties varied based on the employed porosity structures, the scaffolds showcased promising biocompatibility and corrosion resistance. However, a notable challenge in this domain is the sensitivity of these alloys to AM parameters. For instance, variations in energy density can lead to significant changes in the mechanical properties of TNZT samples[61]. Similarly, scanning strategies during the AM process have been observed to influence the porosity and modulus of the resultant implants[63].

Another intriguing development is the incorporation of titanium into the nickel-titanium (NiTi) shape memory alloy. Boasting low stiffness, superior biocompatibility, and superelastic properties, NiTi alloys present a strong case for orthopedic applications, especially in fracture plates. Recent studies have underscored the potential of these alloys, highlighting their consistency and mechanical appropriateness for bone plate manufacturing[43,48]. However, there are concerns regarding the release of nickel (Ni) elements into the human body[60].

It is evident that while metals such as stainless steel and titanium-based alloys offer robust mechanical support for bone healing, their finite lifespan poses another challenge. These materials often necessitate subsequent removal surgeries. Consequently, the spotlight is shifting toward biodegradable or smart materials, which not only support bone healing but also degrade over time, obviating the need for removal.

The evolution of materials for orthopedic implants now emphasizes biodegradable options. Such materials should ideally exhibit adequate mechanical strength without inducing stress shielding. They should also degrade at a rate that aligns with the bone healing process, ensuring continuous mechanical support[64]. In addition, it is imperative that these materials avoid elements such as Al, V, Cr, and Ni to mitigate risks associated with allergies or inflammation due to degradation by-products[65,66].

Current explorations primarily revolve around three metallic categories: iron-based, magnesium-based, and zinc-based materials[67]. Magnesium alloys, for instance, have been proposed as potential substitutes for permanent metals. Chaya *et al.*[68] noted their beneficial role in fracture healing and bone formation. However, concerns arise from their swift degradation, sometimes resulting in inadequate support during crucial healing stages. Moreover, by-products like hydrogen gas from their degradation can potentially hinder bone formation[28,69,70]. Solutions like the ZX11 magnesium alloy have been explored to tackle these challenges[71].

Zinc-based materials, with their moderate degradation rate, have emerged as potential alternatives to their magnesium-based counterparts[67]. Their strength lies in the absence of hydrogen gas in their degradation products and complete absorbability. He *et al.*[65] showcased an innovative biodegradable iron scaffold coated with zinc that demonstrated promising bone formation and controlled degradation.

The exploration is not confined to metals. Non-metallic materials, particularly bioceramics and specific polymers, have garnered interest due to their superior biocompatibility and biodegradability[15,27]. Mo *et al.*[72] highlighted the potential of nanohydroxyapatite (n-HAp) orthopedic implants, emphasizing their role in drug delivery and healing enhancement. However, materials like polyetheretherketone, despite their promise in reducing imaging artifacts, face challenges in ensuring adequate support during bone healing[73].

To recapitulate, while strides have been made in the evolution of materials for orthopedic implants, challenges persist. The quest continues for materials that can provide robust, biocompatible, and timely degrading solutions for bone healing[52].

4.2. Crafting ideal bone plates with AM

AM has spurred a design revolution, enabling the fabrication of intricate structures that traditional manufacturing once deemed challenging. With the manufacturing constraints diminished, designers are now empowered to prioritize product functionality and structural robustness. This shift in design philosophy has profoundly impacted multiple sectors, such as aerospace, mobile technology, and notably, biomedical engineering. Specifically, in orthopedics, the potential of AM to craft innovative and optimized orthopedic implants has attracted significant research attention, aiming to address prevalent issues like stress shielding seen with conventional metallic implants.

A notable advancement in orthopedics, highlighted by AM, is the emphasis on bone plate design, with topology optimization at the forefront. Pioneering work by Al-Tamimi *et al.*[33] initiated this exploration, delving into patient-specific bone plates tailored for distal tibia fractures. Building on this foundation, subsequent research sought to alleviate stress shielding, a recurrent challenge in bone fracture interventions[46]. The complexity of the design process was further accentuated by Wu *et al.*[74], who integrated a time-dependent TO approach to accommodate bone remodeling dynamics. Notwithstanding the promising outcomes of these studies in curbing stress shielding and enhancing graft longevity, they often hinge on intricate algorithms necessitating considerable computational prowess. In a significant stride toward practical application, Zhang *et al.*[75] showcased the practicality of SLM in producing bespoke biological fixation plates, underscoring the potential of SLM in advancing high-performance biological fixation plates.

Despite the transformative potential of AM and TO in bone plate design, it is crucial to acknowledge the existing challenges. The computationally intensive nature of TO, as pointed out by Wu *et al.*[74], may hinder its broad-scale adoption. Zhang *et al.*[75] provided promising insights into the viability of SLM-produced plates, but the long-term clinical implications remain underexplored. Moreover, the seemingly boundless design freedom granted by AM and TO is often tethered by practicalities, like screw placement constraints, as elucidated by Park *et al.*[76] Hence, while the horizons of bone plate design have expanded, realizing the full potential of these technologies necessitates addressing these limitations.

Pivoting to recent innovations, AM has catalyzed the advent of unique design structures targeting stress shielding mitigation. Subasi *et al.*[77] pioneered a finite element (FE)-rooted design of experiments to discern the mechanical nuances of lattice-augmented bone plates. Their manipulation of design variables achieved a substantial stiffness reduction, hinting at better osteosynthesis outcomes. Emphasizing biomechanics, Xu *et al.*[78] showcased AM lattice bone plates, reinforcing the need for biomechanical synchronization for optimal healing. Diverging from conventional designs, Vijayavenkataraman *et al.*[34] delved into auxetic structures in bone plates, highlighting their potential in attenuating stress shielding. Finally, the generative design approach of Kanagalingam *et al.*[35] for patient-specific high tibial osteotomy plates stands as a testament to the adaptability of AM in orthopedics. However, amidst these advancements lies a significant lacuna: the absence of comprehensive biomedical testing for cellular compatibility. While these designs display mechanical prowess, their biocompatibility remains a question, underscoring the need for a holistic evaluation.

The emergence of patient-specific bone plates through AM, driven by 3D imaging-based models from technologies such as computed tomography, magnetic resonance imaging, and 3D scanners[79], has marked a transformative era. Such plates promise greater precision in screw placements, decreased surgical durations, and enhanced patient outcomes. For instance, studies like those from Steffen *et al.*[38] and Dobbe *et al.*[36] testify to the mechanical robustness and superior pain alleviation associated with these plates. Despite these benefits, challenges persist. Advanced imaging, while improving accuracy, can inflate time and financial costs[79]. The manufacturing timeline, as highlighted by Teo *et al.*[37], could introduce surgical delays. Moreover, a conspicuous gap in the literature pertains to the long-term efficacy and biocompatibility of these plates.

Transitioning from the fully patient-specific realm, semi-patient-specific bone plate designs offer a harmonious blend of mechanical optimization and time and cost efficiency. This approach, which involves tweaking features of a foundational design, synergizes well with AM. Jabran *et al.*[80] exemplify this by optimizing features like screw distribution. Yet, many studies in this domain, such as those by Yan *et al.*[81], often eschew clinical validation for mechanical assessments. The introduction of mechanobiological elements, highlighted by works like Subasi *et al.*[77], brings added intricacy. While AM has undoubtedly expanded the horizons of bone plate design, realizing its full potential mandates a more integrated research approach. Holistic studies that amalgamate mechanical, clinical, and biocompatibility aspects are the need of the hour.

4.3. Technological innovations in bone plate fabrication

Commercially available bone plates predominantly utilize subtractive manufacturing techniques. This method encompasses various stages, beginning with raw material formation, and culminating in finishing tasks such as hole drilling and surface polishing[82,83]. The integration of computer numerical control (CNC) technology into the machining phase offers notable advantages, including accelerated production, minimized tolerances, and enhanced repeatability – qualities that align well with mass production objectives.

However, the rigidity of subtractive manufacturing becomes evident when confronted with the need for nuanced alterations in bone plate geometry. Specifically, it falls short in addressing the diverse and intricate design requirements tailored to individual patients or specific fracture types. As a result, this traditional approach struggles to truly realize patient-specific solutions, underscoring the need for innovative manufacturing strategies.

In the dynamic landscape of orthopedic manufacturing, AM techniques, especially PBF, have emerged as a transformative force. They offer both design flexibility and the potential for tailored solutions. For instance, Kim *et al.*[47] leveraged a metal laser melting system to craft a unique fixation plate tailored for distal radial fractures. In biomechanical assessments, these AM plates outperformed conventional volar locking plates, showcasing their potential to better match individual anatomical requirements and reduce stress shielding. A comparative study by Xie *et al.*[84] revealed the biomechanical edge of plates produced through direct metal laser sintering (DMLS) over CNC-manufactured plates. Although there was a slight compromise in fatigue performance, DMLS plates comfortably met clinical standards.

From an economic perspective, Ballard *et al.*[85] shed light on the potential cost-efficiencies of AM models. Their findings underscored the benefits of reduced surgical time and fewer revision surgeries, translating to substantial savings for healthcare institutions and patients. Yet, as Teo *et al.*[37] pointed out, the real-world feasibility of these AM techniques often hinges on the availability of both sophisticated infrastructure and skilled personnel. In a bid to innovate further, Vijayavenkataraman *et al.*[34] unveiled an orthopedic bone plate incorporating auxetic structures. This design innovation not only curtails the stress-shielding effect but also offers the flexibility of intraoperative bending.

The realm of bone plate manufacturing is witnessing transformative changes, particularly with the melding of additive and subtractive manufacturing techniques. AM brings to the table its prowess in crafting intricate geometries, although often with subpar surface finishes. This necessitates post-manufacturing processes to enhance surface quality, such as drilling and surface modifications[86,87]. On the other hand, subtractive methods like CNC machining excel in achieving superior surface finishes but grapple with the complexities of detailed structures.

To harness the strengths of both worlds, the fusion of AM and subtractive manufacturing has gained traction[88]. For instance, Da Cruz Gomes *et al.*[48] employed AM-assisted investment casting to fabricate NiTi shape memory alloy bone plates, unveiling notable enhancements in mechanical properties and biocompatibility. Another leap in this hybrid domain is the work by Lu *et al.*[89], where the synergy of laser- DED with laser shock peening was shown to markedly bolster the microstructural and mechanical attributes of Ti6Al4V alloy samples.

Hybrid manufacturing presents a constellation of advantages, including elevated efficiency, improved product quality, and a marked reduction in material wastage[90]. Yet, as a nascent technology, it grapples with hurdles. Limited accessibility to specialized machines, intricate integration demands, and an augmented necessity for rigorous quality assurance stand out as prominent challenges.

In the domain of bone plate manufacturing, the evolution from traditional subtractive methods to revolutionary AM techniques, and ultimately to hybrid approaches, showcases the industry's relentless pursuit of innovation. Subtractive manufacturing, while proficient in mass production, often encounters limitations in crafting patient-specific solutions. AM techniques, especially PBF, introduce unparalleled flexibility in crafting intricate, customized designs, although with its own set of challenges, such as high costs and post-processing demands. The most recent stride in this journey is the advent of hybrid manufacturing, which marries the strengths of both subtractive and additive processes. This synergistic approach aims to produce bone plates that boast the structural complexity enabled by AM, while retaining the superior surface finish typical of subtractive methods. However, the nascent state of hybrid manufacturing means that its full potential is yet to be realized, necessitating further research and optimization, particularly given the critical nature of bone plate applications where structural integrity and biocompatibility are of paramount importance.

4.4. Perfecting additive manufactured bone plates with post-processing

AM has substantially expanded the horizons of medical device production. However, the creation of a bone plate does not end with the completion of the printing process. Post-processing – the series of operations performed after the initial AM process – plays a pivotal role in ensuring that the bone plates are not only structurally sound but also biocompatible.

As the initial phase of AM often leaves parts with surface roughness or residual stresses, post-processing techniques such as heat treatment and surface modification become indispensable. These treatments can profoundly impact the mechanical properties of the printed parts, enhancing their strength and fatigue resistance, which are paramount for bone plates subjected to significant mechanical loads during their life cycle[86].

Equally significant is the impact of these treatments on the biomedical properties of the bone plates. Surface integrity, which can be tailored through post-processing, determines how a bone plate will interact with the biological environment. An optimized surface can reduce corrosion, minimize bacterial adhesion, and promote osseointegration, ensuring the long-term success of the implant[91]. On the other hand, a compromised surface can have severe repercussions, including implant failure[92].

Research findings emphasize the nuanced role of post-processing. Jahadakbar *et al.*'s work[43] on porous nitinol bone fixation plates illustrates the efficacy of chemical polishing in removing unmelted powder residues while preserving intricate geometries. The scanning electron microscopy analysis of their study specifically found that an etching solution composed of 10% HF, 40% HNO_3, and 50% H_2O, applied for an effective time of 4 min, was optimal for removing unmelted powder particles. Such meticulous post-processing is essential, especially when catering to patient-specific needs that require high precision.

Heat treatment plays a pivotal role in refining the mechanical attributes of AM components. Research by Gupta *et al.*[93] showcased the potential of this method, focusing on Ti-6Al-4V plates produced through SLM. When juxtaposed with plates machined from wrought sheets, the value-add of AM in orthopedics becomes evident. Nonetheless, while the immediate benefits are clear, queries regarding the long-term stability and dependability of such treatments persist. These concerns become especially pertinent when AM techniques are compared with traditional manufacturing methods.

Furthermore, heat treatment can significantly enhance material properties, making them more suitable for biomedical applications. As elucidated by Hou *et al.*[71], materials like the ZX11 magnesium alloy, although promising, are subjected to rapid degradation. This raises concerns about the longevity and stability of such implants. Their study compared the degradation rates of the alloy in two states: as-rolled and annealed at 400°C. Their findings revealed that while the annealed alloy exhibited relatively lower strength, it benefited from a significantly reduced degradation rate and demonstrated stable elongation in the initial weeks of immersion, underscoring the importance of heat treatment in optimizing material performance for biomedical implants.

Another significant facet of post-processing is surface modification, which has been thoroughly studied concerning its impact on biocompatibility and cellular interactions. Surface characteristics, from roughness to chemical composition, can profoundly influence cell adhesion, proliferation, and differentiation, as highlighted by Gittens *et al.*[94] and Stepanovska *et al.*[87]. While these alterations can bolster implant performance, they simultaneously introduce challenges related to quality control and standardization.

Post-processing techniques, while offering potential enhancements for AM bone plates, bring forth a series of variables that necessitate rigorous oversight. Current literature, while illuminating, underscores the need for more nuanced research. The objective remains clear: optimizing these processes, especially when the stakes involve critical applications like bone plates where mechanical robustness and biocompatibility are of paramount importance.

5. Navigating challenges in AM-based bone plate creation

5.1. Material challenges

In AM for orthopedics, selecting the right materials is crucial but challenging. The limited availability of materials specifically tailored for orthopedic applications like bone plates is a significant concern[60,95]. These materials need to balance critical properties, such as biocompatibility, mechanical strength, and controlled degradation rates, which are essential for successful orthopedic applications[7,68].

5.2. Design challenges

Designing bone plates for AM involves computational and clinical challenges. The complexity and computational intensity of topology optimization algorithms can hinder their adoption[74]. Moreover, the lack of long-term clinical data for AM-based bone plate designs raises questions about their clinical validity[36,38,75]. Practical design constraints, such as the number and positioning of screws, also impact the flexibility and functionality of the final products[76].

5.3. Manufacturing challenges

The manufacturing process of AM bone plates faces several hurdles. High costs, particularly for techniques like PBF, are a primary concern[85]. In addition, post-processing steps essential for achieving desired product quality are often time-consuming and complex[86,87,91]. Hybrid manufacturing, which combines additive and subtractive methods, introduces further complexities[90].

5.4. Other challenges

Beyond material, design, and manufacturing, there are additional hurdles in AM-based bone plate creation. Many advanced AM designs have not undergone comprehensive biomedical testing, a critical step to ensure efficacy and safety[34,77,78]. Patient-specific plates, while offering customization, may lead to increased surgery costs and duration, and necessitate specialized equipment and expertise[36-38,79,96]. Moreover, research in this field often focuses narrowly on specific parameters or aspects, limiting broader applications[80,81,97-99].

6. The road ahead in additive manufactured bone plates

6.1. Emerging biomaterials for orthopedics

Future advancements in orthopedic implants, especially bone plates, hinge on the expansion of suitable biomaterials tailored for AM. The current material palette for commercial metallic AM – comprising options such as stainless steel, mild steel, and titanium alloy – is notably restricted. Even among these, only a handful meet the stringent demands of biomedical applications. Challenges with existing materials, such as the potential screw detachment or the release of undesirable elements during prolonged use, underscore the urgent need for innovative solutions.

Machine learning (ML) emerges as a transformative tool in this quest. By assisting in the discovery and optimization of nanobiomaterials, ML can significantly expedite the material development process. This data-driven approach, as outlined by Suwardi *et al.*[27], offers a streamlined methodology for biomaterial design optimization, harnessing ML's capacity to analyze vast datasets and unveil intricate patterns. The ML-driven biomaterial development typically encompasses three pivotal phases: (i) Analysis of synthesis, structure, and properties; (ii) optimization of surface and interfaces; and (iii) comprehensive material screening coupled with integrated manufacturing.

The merits of integrating ML into biomaterial development are manifold, promising accelerated development timelines, enhanced material performance, cost reductions, and heightened efficiency. In essence, by leveraging ML, the future of orthopedics could witness the emergence of biodegradable materials that expertly balance mechanical robustness with controlled degradation rates, heralding a new era of safer, more effective bone plates.

6.2. Future design strategies for bone plates

The horizon of bone plate design, particularly within the realm of AM, is being reshaped by the material-structure-performance integrated AM (MSPI-AM) concept. This integrated approach seeks to revolutionize the AM landscape, prioritizing concurrent optimization of material selection, structural design, and manufacturing methodologies. Such an approach stands in stark contrast to the traditional "series mode" AM, which frequently grapples with a time-intensive, trial-and-error process[100].

A particularly intriguing facet of MSPI-AM is its facilitation of parametric design. This enables agile customization of generic bone plate features, paving the way for the creation of semi-patient-specific plates with remarkable efficiency[97]. The transformative potential of this approach is further amplified when integrated with artificial intelligence algorithms, which can swiftly analyze patient-specific data to guide design alterations.

Beyond mere design benefits, MSPI-AM extends its promise to the domain of multi-material printing. This capability heralds the prospect of functionally graded material design for bone plates. Lima *et al.*[101], through their pioneering work using laser-engineered net shaping (LENS), showcased the feasibility of orthopedic implants designed with graded stiffness. Such an approach directly addresses the long-standing challenge of stress shielding, promising to enhance the longevity and efficacy of orthopedic implants. The ripple effect of such innovations could resonate beyond the medical sphere, influencing sectors such as aerospace and automotive engineering.

In essence, the MSPI-AM framework is set to revolutionize AM design, presenting a more cohesive, efficient, and tailored pathway to the development of high-caliber, bespoke bone plates.

6.3. Optimizing bone plate manufacturing processes

The future of bone plate manufacturing in the realm of AM is increasingly leaning toward the integration of ML techniques for process optimization. One of the most pressing challenges in MAM is the management of complex thermal fields generated during the printing process. These thermal fields can significantly vary depending on the geometry of the part, leading to inconsistent mechanical properties even when using the same machine and material[102]. Traditional mathematical modeling approaches often fall short of capturing these complexities and can be time-consuming. In contrast, ML can offer a more efficient and accurate solution by learning from prior experimental data to find correlations between input process parameters and output geometrical parameters[103].

A study by Le *et al.*[104] utilized an ML algorithm in conjunction with the Gurson-Tvergaard porous plasticity model to predict the flexural strength of fused deposition modeling bone plates made of PLA. The study found that ML algorithms could accurately predict mechanical behavior, thereby reducing the time and cost associated with experimental testing. This not only reduces the time and cost associated with traditional trial-and-error methods but also improves the accuracy of predicting mechanical properties at a macro scale[105].

However, the integration of ML in the AM is not without challenges. The development of advanced ML algorithms requires large, accurate datasets, and significant computational power. The training data, often obtained from high-fidelity simulations, must be reliable and account for all influential factors at specific levels of resolution[102]. These challenges highlight the need for further research to ensure the robustness and transferability of ML algorithms in AM.

7. Conclusion

Bone fractures are a leading type of traumatic injury in humans and frequently necessitate the use of bone plates for optimal recovery. The evolution of these plates has been remarkable, encompassing improvements in the principles of healing, selection of materials, and design advancements. Modern bone plates not only facilitate secondary healing but also effectively relay mechanical stimuli to fracture segments, thereby reducing complications such as non-union, infections, and secondary reduction loss. Nonetheless, certain issues remain. A prominent concern is that the rigidity of metallic bone plates often surpasses that of natural bones, initiating a process known as stress shielding. This can lead to bone thinning and eventual osteoporosis. This article probes the latest progress in the fabrication of metallic bone plates, with a specific emphasis on AM techniques. These methods have been instrumental in overcoming hurdles related to material selection, design, manufacturing, and post-processing.

Recent advancements in biocompatible materials, including β-Ti and smart alloys, have improved the crafting of bone plates, although challenges like implant loosening persist. The exploration of biodegradable materials that align with bone recovery phases is ongoing, but ensuring their decomposition rate matches natural bone healing is complex. AI might provide insights into designing materials that degrade appropriately and support healing. AM offers enhanced design flexibility, with techniques such as TO and FEA enabling the production of bone plates with sophisticated, less rigid structures. Conventionally, bone plate manufacturing relied on subtractive methods for mass production, but the shift to AM allows for more intricate, customizable structures. Despite the challenges in optimizing AM settings for diverse designs, AI's analytical capabilities could help in fine-tuning these parameters to create plates with balanced rigidity and strength, addressing issues like stress shielding.

The primary objective of current metallic bone plate research is to reduce stress shielding and potential risks linked to permanent fixtures. AM has risen as a pivotal tool, enabling the creation of intricate designs tailored to individual patients. As the field advances, AI appears well-positioned to further refine material and design choices and fine-tune AM procedures.

Acknowledgments

The authors would like to thank the China Scholarship Council (CSC) and the University of Bristol (UoB) for the awarded CSC-UoB scholarship.

Funding

None.

Conflict of interest

The authors declare that they have no competing interests

Author contributions

Conceptualization: Fengyuan Liu, Weiting Xu
Writing – original draft: Weiting Xu
Writing – review & editing: Fengyuan Liu, Aydin Nassehi

Ethics approval and consent to participate

Not applicable.

Consent for publication

Not applicable.

Availability of data

Not applicable.

References

1. Zhou J, Zhang Z, Joseph J, *et al.*, 2021, Biomaterials and nanomedicine for bone regeneration: Progress and future prospects. *Exploration*, 1: 20210011.

   https://doi.org/10.1002/EXP.20210011

2. Wildemann B, Ignatius A, Leung F, *et al.*, 2021, Non-union bone fractures. *Nat Rev Dis Primers*, 7: 57.

   https://doi.org/10.1038/s41572-021-00289-8

3. Phillips AM, 2005, Overview of the fracture healing cascade. *Injury*, 36: S5–S7.

   https://doi.org/10.1016/j.injury.2005.07.027

4. Ghiasi MS, Chen J, Vaziri A, *et al.*, 2017, Bone fracture healing in mechanobiological modeling: A review of principles and methods. *Bone Rep*, 6: 87–100.

   https://doi.org/10.1016/j.bonr.2017.03.002

5. Salhotra A, Shah HN, Levi B, *et al.*, 2020, Mechanisms of bone development and repair. *Nat Rev Mol Cell Biol*, 21: 696–711.

   https://doi.org/10.1038/s41580-020-00279-w

6. Bahney CS, Zondervan RL, Allison P, *et al.*, 2019, Cellular biology of fracture healing. *J Orthop Res*, 37: 35–50.

   https://doi.org/10.1002/jor.24170

7. Li J, Qin L, Yang K, *et al.*, 2020, Materials evolution of bone plates for internal fixation of bone fractures: A review. *J Mater Sci Technol*, 36: 190–208.

   https://doi.org/10.1016/j.jmst.2019.07.024

8. Sheen JR, Mabrouk A, Garla VV, 2023, Fracture healing overview. In: *StatPearls*, Treasure Island, FL: StatPearls Publishing.

9. Ito H, 2011, Chemokines in mesenchymal stem cell therapy for bone repair: A novel concept of recruiting mesenchymal stem cells and the possible cell sources. *Mod Rheumatol*, 21: 113–121.

   https://doi.org/10.1007/s10165-010-0357-8

10. Pivonka P, Dunstan CR, 2012, Role of mathematical modeling in bone fracture healing. *Bonekey Rep*, 1: 221.

    https://doi.org/10.1038/bonekey.2012.221

11. Duan ZW, Lu H, 2021, Effect of mechanical strain on cells involved in fracture healing. *Orthop Surg*, 13: 369–375.

    https://doi.org/10.1111/os.12885

12. Alias MA, Buenzli PR, 2018, Osteoblasts infill irregular pores under curvature and porosity controls: A hypothesis-testing analysis of cell behaviours. *Biomech Model Mechanobiol*, 17: 1357–1371.

    https://doi.org/10.1007/s10237-018-1031-x

13. Rajendran AK, Sankar D, Amirthalingam S, *et al.*, 2023, Trends in mechanobiology guided tissue engineering and tools to study cell-substrate interactions: A brief review. *Biomater Res*, 27: 55.

    https://doi.org/10.1186/s40824-023-00393-8

14. Zaheer MU, Mehboob H, Mehboob A, *et al.*, 2022, Evaluation of the effect of bone plate modulus on the early bone healing of fractured tibia. *Compos B Eng*, 233: 109668.

    https://doi.org/10.1016/j.compositesb.2022.109668

15. Kim T, See CW, Li X, *et al.*, 2020, Orthopedic implants and devices for bone fractures and defects: Past, present and perspective. *Eng Regen*, 1: 6–18.

    https://doi.org/10.1016/j.engreg.2020.05.003

16. Bartonícek J, 2010, Early history of operative treatment of fractures. *Arch Orthop Trauma Surg*, 130: 1385–1396.

    https://doi.org/10.1007/s00402-010-1082-7

17. Lane WA, 1895, Some remarks on the treatment of fractures. *Br Med J*, 1: 861–863.

18. Bagby GW, Janes JM, 1958, The effect of compression on the rate of fracture healing using a special plate. *Am J Surg*, 95: 761–771.

    https://doi.org/10.1016/0002-9610(58)90625-1

19. Uhthoff HK, Poitras P, Backman DS, 2006, Internal plate fixation of fractures: Short history and recent developments.

J Orthop Sci, 11: 118–126.

https://doi.org/10.1007/s00776-005-0984-7

20. Perren SM, 2002, Evolution of the internal fixation of long bone fractures. The scientific basis of biological internal fixation: Choosing a new balance between stability and biology. *J Bone Joint Surg Br*, 84: 1093–1110.

    https://doi.org/10.1302/0301-620x.84b8.13752

21. Egol KA, Kubiak EN, Fulkerson E, *et al.*, 2004, Biomechanics of locked plates and screws. *J Orthop Trauma*, 18: 488–493.

    https://doi.org/10.1097/00005131-200409000-00003

22. Haas N, Hauke C, Schütz M, *et al.*, 2001, Treatment of diaphyseal fractures of the forearm using the Point Contact Fixator (PC-Fix): results of 387 fractures of a prospective multicentric study (PC-Fix II). *Injury*, 32 Suppl 2: B51–B62.

    https://doi.org/10.1016/s0020-1383(01)00126-7

23. Mehboob A, Chang SH, 2019, Effect of initial micro-movement of a fracture gap fastened by composite prosthesis on bone healing. *Compos Struct*, 226: 111213.

    https://doi.org/10.1016/j.compstruct.2019.111213

24. Wagner M, 2003, General principles for the clinical use of the LCP. *Injury*, 34 Suppl 2: B31–B42.

    https://doi.org/10.1016/j.injury.2003.09.023

25. Huiskes R, Weinans H, van Rietbergen B, 1992, The relationship between stress shielding and bone resorption around total hip stems and the effects of flexible materials. *Clin Orthop Relat Res*, 274: 124–134.

26. Feng YJ, Lin KP, Tsai CL, *et al.*, 2021, Influence of gap distance between bone and plate on structural stiffness and parallel interfragmental movement in far-cortical locking technique - a biomechanical study. *Comput Methods Biomech Biomed Engin*, 24: 1206–1211.

    https://doi.org/10.1080/10255842.2020.1870964

27. Suwardi A, Wang F, Xue K, *et al.*, 2022, Machine learning-driven biomaterials evolution. *Adv Mater*, 34: 2102703.

    https://doi.org/10.1002/adma.202102703

28. Yang Y, He C, Dianyu E, *et al.*, 2020, Mg bone implant: Features, developments and perspectives. *Mater Des*, 185: 108259.

    https://doi.org/10.1016/j.matdes.2019.108259

29. ISO/ASTM, 2021, ISO/ASTM 52900:2021(en), Additive Manufacturing - General Principles -Fundamentals and Vocabulary. Available from: https://www.iso.org/obp/ui/#iso: std:iso-astm:52900:ed-2:v1:en [Last accessed on 2023 Aug 07].

30. Salmi M, 2021, Additive manufacturing processes in medical applications. *Materials* (*Basel*), 14: 191.

    https://doi.org/10.3390/ma14010191

31. Vafadar A, Guzzomi F, Rassau A, *et al.*, 2021, Advances in metal additive manufacturing: A review of common processes, industrial applications, and current challenges. *Appl Sci*, 11: 1213.

    https://doi.org/10.3390/app11031213

32. Askari M, Hutchins DA, Thomas PJ, *et al.*, 2020, Additive manufacturing of metamaterials: A review. *Addit Manuf*, 36: 101562.

    https://doi.org/10.1016/j.addma.2020.101562

33. Al-Tamimi AA, Huang B, Vyas C, *et al.*, 2019, Topology optimised metallic bone plates produced by electron beam melting: A mechanical and biological study. *Int J Adv Manuf Technol*, 104: 195–210.

    https://doi.org/10.1007/s00170-019-03866-0

34. Vijayavenkataraman S, Gopinath A, Lu WF, 2020, A new design of 3D-printed orthopedic bone plates with auxetic structures to mitigate stress shielding and improve intra-operative bending. *Bio Des Manuf*, 3: 98–108.

    https://doi.org/10.1007/s42242-020-00066-8

35. Kanagalingam S, Dalton C, Champneys P, *et al.*, 2023, Detailed design for additive manufacturing and post processing of generatively designed high tibial osteotomy fixation plates. *Prog Addit Manuf*, 8: 409–426.

    https://doi.org/10.1007/s40964-022-00342-2

36. Dobbe JGG, Peymani A, Roos HAL, *et al.*, 2021, Patient-specific plate for navigation and fixation of the distal radius: A case series. *Int J CARS*, 16: 515–524.

    https://doi.org/10.1007/s11548-021-02320-5

37. Teo AQA, Ng DQK, Lee P, *et al.*, 2021, Point-of-care 3D printing: A feasibility study of using 3D printing for orthopaedic trauma. *Injury*, 52: 3286–3292.

    https://doi.org/10.1016/j.injury.2021.02.041

38. Steffen C, Sellenschloh K, Willsch M, *et al.*, 2023, Patient-specific miniplates versus patient-specific reconstruction plate: A biomechanical comparison with 3D-printed plates in mandibular reconstruction. *J Mech Behav Biomed Mater*, 140: 105742.

    https://doi.org/10.1016/j.jmbbm.2023.105742

39. Nicholson J, Makaram N, Simpson A, *et al.*, 2021, Fracture nonunion in long bones: A literature review of risk factors and surgical management. *Injury*, 52: S3–S11.

    https://doi.org/10.1016/j.injury.2020.11.029

40. Roseti L, Parisi V, Petretta M, *et al.*, 2017, Scaffolds for Bone Tissue Engineering: State of the art and new perspectives. *Mater Sci Eng C Mater Biol Appl*, 78: 1246–1262.

    https://doi.org/10.1016/j.msec.2017.05.017

41. DePuy Synthes, 2023, Small Fragment Locking Compression Plate System. DePuy Synthes. J&J MedTech. Available

from: https://www.jnjmedtech.com/en-US/product/small-fragment-locking-compression-plate-system [Last accessed on 2023 Jul 24].

42. Millis DL, 2014, Responses of musculoskeletal tissues to disuse and remobilization. In: Levine D, editor. Canine Rehabilitation and Physical Therapy. 2nd ed. St. Louis: W.B. Saunders. p. 92–153.

    https://doi.org/10.1016/B978-1-4377-0309-2.00007-7

43. Jahadakbar A, Nematollahi M, Safaei K, *et al.*, 2020, Design, modeling, additive manufacturing, and polishing of stiffness-modulated porous nitinol bone fixation plates followed by thermomechanical and composition analysis. *Metals*, 10: 151.

    https://doi.org/10.3390/met10010151

44. Son DS, Chang SH, 2013, The simulation of bone healing process of fractured tibia applied with composite bone plates according to the diaphyseal oblique angle and plate modulus. *Compos B Eng*, 45: 1325–1335.

    https://doi.org/10.1016/j.compositesb.2012.07.037

45. Mehboob A, Chang SH, 2018, Effect of composite bone plates on callus generation and healing of fractured tibia with different screw configurations. *Compos Sci Technol*, 167: 96–105.

    https://doi.org/10.1016/j.compscitech.2018.07.039

46. Al-Tamimi AA, 2021, 3D topology optimization and mesh dependency for redesigning locking compression plates aiming to reduce stress shielding. *Int J Bioprint*, 7: 339.

    https://doi.org/10.18063/ijb.v7i3.339

47. Kim S, Jo Y, Choi W, *et al.*, 2017, Biomechanical properties of 3-dimensional printed volar locking distal radius plate: Comparison with conventional volar locking plate. *J Hand Surg*, 42: 747.e1–747.e6.

    https://doi.org/10.1016/j.jhsa.2017.05.009

48. Da Cruz Gomes AA, Grassi END, Da Silva PCS, *et al.*, 2021, Mechanical behavior of a NiTi superelastic bone plate obtained by investment casting assisted by additive manufacturing. *Smart Mater Struct*, 30: 025009.

    https://doi.org/10.1088/1361-665X/abca83

49. Bandyopadhyay A, Ciliveri S, Bose S, 2022, Metal additive manufacturing for load-bearing implants. *J Indian Inst Sci*, 102: 561–584.

    https://doi.org/10.1007/s41745-021-00281-x

50. Ngo TD, Kashani A, Imbalzano G, *et al.*, 2018, Additive manufacturing (3D printing): A review of materials, methods, applications and challenges. *Compos B Eng*, 143: 172–196.

    https://doi.org/10.1016/j.compositesb.2018.02.012

51. Barroqueiro B, Andrade-Campos A, Valente RAF, *et al.*, 2019, Metal additive manufacturing cycle in aerospace industry: A comprehensive review. *J Manuf Mater Process*, 3: 52.

    https://doi.org/10.3390/jmmp3030052

52. Chocholata P, Kulda V, Babuska V, 2019, Fabrication of scaffolds for bone-tissue regeneration. *Materials* (*Basel*), 12: 568.

    https://doi.org/10.3390/ma12040568

53. Hayes JS, Richards RG, 2010, The use of titanium and stainless steel in fracture fixation. *Expert Rev Med Devices*, 7: 843–853.

    https://doi.org/10.1586/erd.10.53

54. Wang D, Yang Y, Han C, 2023, Additive manufacturing of metal implants and surgical plates. In: Additive Manufacturing: Materials, Functionalities and Applications. Cham: Springer International Publishing. pp. 151–203.

    https://doi.org/10.1007/978-3-031-04721-3_5

55. Röttger A, Boes J, Theisen W, *et al.*, 2020, Microstructure and mechanical properties of 316L austenitic stainless steel processed by different SLM devices. *Int J Adv Manuf Technol*, 108: 769–783.

    https://doi.org/10.1007/s00170-020-05371-1

56. Geetha M, Singh AK, Asokamani R, *et al.*, 2009, Ti based biomaterials, the ultimate choice for orthopaedic implants - a review. *Prog Mater Sci*, 54: 397–425.

    https://doi.org/10.1016/j.pmatsci.2008.06.004

57. Liu S, Shin YC, 2019, Additive manufacturing of Ti6Al4V alloy: A review. *Mater Des*, 164: 107552.

    https://doi.org/10.1016/j.matdes.2018.107552

58. Mirzaali MJ, Schwiedrzik JJ, Thaiwichai S, *et al.*, 2016, Mechanical properties of cortical bone and their relationships with age, gender, composition and microindentation properties in the elderly. *Bone*, 93: 196–211.

    https://doi.org/10.1016/j.bone.2015.11.018

59. Katzenberger MJ, Albert DL, Agnew AM, *et al.*, 2020, Effects of sex, age, and two loading rates on the tensile material properties of human rib cortical bone. *J Mech Behav Biomed Mater*, 102: 103410.

    https://doi.org/10.1016/j.jmbbm.2019.103410

60. Chen Q, Thouas GA, 2015, Metallic implant biomaterials. *Mater Sci Eng R Rep*, 87: 1–57.

    https://doi.org/10.1016/j.mser.2014.10.001

61. Nadammal N, Rajput M, Gupta SK, *et al.*, 2022, Laser powder bed fusion additive manufacturing of a low-modulus Ti-35Nb-7Zr-5Ta alloy for orthopedic applications. *ACS Omega*, 7: 8506–8517.

    https://doi.org/10.1021/acsomega.1c06261

62. Li Y, Ding Y, Munir K, *et al.*, 2019, Novel β-Ti35Zr28Nb

alloy scaffolds manufactured using selective laser melting for bone implant applications. *Acta Biomater*, 87: 273–284.

https://doi.org/10.1016/j.actbio.2019.01.051

63. Batalha WC, Batalha RL, Kosiba K, *et al.*, 2023, Effect of scanning strategy on microstructure and mechanical properties of a biocompatible Ti-35Nb-7Zr-5Ta alloy processed by laser-powder bed fusion. *J Mater Res*, 38: 154–164.

https://doi.org/10.1557/s43578-022-00735-7

64. Putra NE, Mirzaali MJ, Apachitei I, *et al.*, 2020, Multi-material additive manufacturing technologies for Ti-, Mg-, and Fe-based biomaterials for bone substitution. *Acta Biomater*, 109: 1–20.

https://doi.org/10.1016/j.actbio.2020.03.037

65. He J, Fang J, Wei P, *et al.*, 2021, Cancellous bone-like porous Fe@Zn scaffolds with core-shell-structured skeletons for biodegradable bone implants. *Acta Biomater*, 121: 665–681.

https://doi.org/10.1016/j.actbio.2020.11.032

66. Manam NS, Harun WSW, Shri DNA, *et al.*, 2017, Study of corrosion in biocompatible metals for implants: A review. *J Alloys Compd*, 701: 698–715.

https://doi.org/10.1016/j.jallcom.2017.01.196

67. Kabir H, Munir K, Wen C, *et al.*, 2021, Recent research and progress of biodegradable zinc alloys and composites for biomedical applications: Biomechanical and biocorrosion perspectives. *Bioact Mater*, 6: 836–879.

https://doi.org/10.1016/j.bioactmat.2020.09.013

68. Chaya A, Yoshizawa S, Verdelis K, *et al.*, 2015, *In vivo* study of magnesium plate and screw degradation and bone fracture healing. *Acta Biomater*, 18: 262–269.

https://doi.org/10.1016/j.actbio.2015.02.010

69. Wang J, Dou J, Wang Z, *et al.*, 2022, Research progress of biodegradable magnesium-based biomedical materials: A review. *J Alloys Compd*, 923: 166377.

https://doi.org/10.1016/j.jallcom.2022.166377

70. Bairagi D, Mandal S, 2022, A comprehensive review on biocompatible Mg-based alloys as temporary orthopaedic implants: Current status, challenges, and future prospects. *J Magnes Alloys*, 10: 627–669.

https://doi.org/10.1016/j.jma.2021.09.005

71. Hou R, Victoria-Hernandez J, Jiang P, *et al.*, 2019, *In vitro* evaluation of the ZX11 magnesium alloy as potential bone plate: Degradability and mechanical integrity. *Acta Biomater*, 97: 608–622.

https://doi.org/10.1016/j.actbio.2019.07.053

72. Mo X, Zhang D, Liu K, *et al.*, 2023, Nano-hydroxyapatite composite scaffolds loaded with bioactive factors and drugs for bone tissue engineering. *Int J Mol Sci*, 24: 1291.

https://doi.org/10.3390/ijms24021291

73. Barth T, Münch M, Seide K, *et al.*, 2022, Additive Manufactured Versus Traditional Osteosynthesis Plates - a Finite Element Analysis. In: Conference Transactions on Additive Manufacturing Meets Medicine. p. 644.

https://doi.org/10.18416/AMMM.2022.2209644

74. Wu C, Zheng K, Fang J, *et al.*, 2020, Time-dependent topology optimization of bone plates considering bone remodeling. *Comput Methods Appl Mech Eng*, 359: 112702.

https://doi.org/10.1016/j.cma.2019.112702

75. Zhang G, Li J, Zhou X, *et al.*, 2023, The design and processing of a 3D-printed high-performance biological fixation plate. *Int J Bioprint*, 9: 658.

https://doi.org/10.18063/ijb.v9i2.658

76. Park S, Park S, Park J, *et al.*, 2021, Design process of patient-specific osteosynthesis plates using topology optimization. *J Computat Des Eng*, 8: 1257–1266.

https://doi.org/10.1093/jcde/qwab047

77. Subasi O, Karaismailoglu B, Ashkani-Esfahani S, *et al.*, 2023, Investigation of lattice infill parameters for additively manufactured bone fracture plates to reduce stress shielding. *Comput Biol Med*, 161: 107062.

https://doi.org/10.1016/j.compbiomed.2023.107062

78. Xu S, Ding X, Xiong M, *et al.*, 2023, The optimal design of 3D-printed lattice bone plate by considering fracture healing mechanism. *Int J Numer Methods Biomed Eng*, 39: e3682.

https://doi.org/10.1002/cnm.3682

79. Javaid M, Haleem A, 2019, Current status and challenges of Additive manufacturing in orthopaedics: An overview. *J Clin Orthop Trauma*, 10: 380–386.

https://doi.org/10.1016/j.jcot.2018.05.008

80. Jabran A, Peach C, Zou Z, *et al.*, 2019, Parametric design optimisation of proximal humerus plates based on finite element method. *Ann Biomed Eng*, 47: 601–614.

https://doi.org/10.1007/s10439-018-02160-6

81. Yan L, Lim JL, Lee JW, *et al.*, 2020, Finite element analysis of bone and implant stresses for customized 3D-printed orthopaedic implants in fracture fixation. *Med Biol Eng Comput*, 58: 921–931.

https://doi.org/10.1007/s11517-019-02104-9

82. Abellán-Nebot JV, Siller HR, Vila C, *et al.*, 2012, An experimental study of process variables in turning operations of Ti-6Al-4V and Cr-Co spherical prostheses. *Int J Adv Manuf Technol*, 63: 887–902.

https://doi.org/10.1007/s00170-012-3955-0

83. Xu M, Zhang LH, Zhang YZ, *et al.*, 2014, Custom-made locked plating for acetabular fracture: A pilot study in 24 consecutive cases. *Orthopedics*, 37: e660–e670.

https://doi.org/10.3928/01477447-20140626-59

84. Xie P, Ouyang H, Deng Y, *et al.*, 2017, Comparison of conventional reconstruction plate versus direct metal laser sintering plate: An *in vitro* mechanical characteristics study. *J Orthop Surg Res*, 12: 128.

https://doi.org/10.1186/s13018-017-0628-6

85. Ballard DH, Mills P, Duszak R Jr., *et al.*, 2020, Medical 3D printing cost-savings in orthopedic and maxillofacial surgery: Cost analysis of operating room time saved with 3D printed anatomic models and surgical guides. *Acad Radiol*, 27: 1103–1113.

https://doi.org/10.1016/j.acra.2019.08.011

86. Davis R, Singh A, Jackson MJ, *et al.*, 2022, A comprehensive review on metallic implant biomaterials and their subtractive manufacturing. *Int J Adv Manuf Technol*, 120: 1473–1530.

https://doi.org/10.1007/s00170-022-08770-8

87. Stepanovska J, Matejka R, Otahal M, *et al.*, 2020, The effect of various surface treatments of Ti6Al4V on the growth and osteogenic differentiation of adipose tissue-derived stem cells. *Coatings*, 10: 762.

https://doi.org/10.3390/coatings10080762

88. Jia Z, Xu X, Zhu D, *et al.*, 2023, Design, printing, and engineering of regenerative biomaterials for personalized bone healthcare. *Prog Mater Sci*, 134: 101072.

https://doi.org/10.1016/j.pmatsci.2023.101072

89. Lu H, Wu L, Wei H, *et al.*, 2022, Microstructural evolution and tensile property enhancement of remanufactured Ti6Al4V using hybrid manufacturing of laser directed energy deposition with laser shock peening. *Addit Manuf*, 55: 102877.

https://doi.org/10.1016/j.addma.2022.102877

90. Lalegani Dezaki M, Serjouei A, Zolfagharian A, *et al.*, 2022, A review on additive/subtractive hybrid manufacturing of directed energy deposition (DED) process. *Adv Powder Mater*, 1: 100054.

https://doi.org/10.1016/j.apmate.2022.100054

91. Shalabi MM, Gortemaker A, Hof MAV, *et al.*, 2006, Implant surface roughness and bone healing: A systematic review. *J Dent Res*, 85: 496–500.

https://doi.org/10.1177/154405910608500603

92. Rønold HJ, Lyngstadaas SP, Ellingsen JE, 2003, Analysing the optimal value for titanium implant roughness in bone attachment using a tensile test. *Biomaterials*, 24: 4559–4564.

https://doi.org/10.1016/S0142-9612(03)00256-4

93. Gupta SK, Shahidsha N, Bahl S, *et al.*, 2021, Enhanced biomechanical performance of additively manufactured Ti-6Al-4V bone plates. *J Mech Behav Biomed Mater*, 119: 104552.

https://doi.org/10.1016/j.jmbbm.2021.104552

94. Gittens RA, McLachlan T, Olivares-Navarrete R, *et al.*, 2011, The effects of combined micron-/submicron-scale surface roughness and nanoscale features on cell proliferation and differentiation. *Biomaterials*, 32: 3395–3403.

https://doi.org/10.1016/j.biomaterials.2011.01.029

95. Haleem A, Javaid M, 2020, 3D printed medical parts with different materials using additive manufacturing. *Clin Epidemiol Glob Health*, 8: 215–223.

https://doi.org/10.1016/j.cegh.2019.08.002

96. Omori S, Murase T, Kataoka T, *et al.*, 2014, Three-dimensional corrective osteotomy using a patient-specific osteotomy guide and bone plate based on a computer simulation system: Accuracy analysis in a cadaver study. *Int J Med Robot*, 10: 196–202.

https://doi.org/10.1002/rcs.1530

97. Chung CY, 2018, A simplified application (APP) for the parametric design of screw-plate fixation of bone fractures. *J Mech Behav Biomed Mater*, 77: 642–648.

https://doi.org/10.1016/j.jmbbm.2017.10.025

98. Mohandes Y, Tahani M, Rouhi G, *et al.*, 2021, A mechanobiological approach to find the optimal thickness for the locking compression plate: Finite element investigations. *Proc Inst Mech Eng H*, 235: 408–418.

https://doi.org/10.1177/0954411920985757

99. Schader JF, Mischler D, Dauwe J, *et al.*, 2022, One size may not fit all: Patient-specific computational optimization of locking plates for improved proximal humerus fracture fixation. *J Shoulder Elbow Surg*, 31: 192–200.

https://doi.org/10.1016/j.jse.2021.06.012

100. Gu D, Shi X, Poprawe R, *et al.*, 2021, Material-structure-performance integrated laser-metal additive manufacturing. *Science*, 372: eabg1487.

https://doi.org/10.1126/science.abg1487

101. Lima DD, Mantri SA, Mikler CV, *et al.*, 2017, Laser additive processing of a functionally graded internal fracture fixation plate. *Mater Des*, 130: 8–15.

https://doi.org/10.1016/j.matdes.2017.05.034

102. Babu SS, Mourad AHI, Harib KH, *et al.*, 2023, Recent developments in the application of machine-learning towards accelerated predictive multiscale design and additive manufacturing. *Virtual Phys Prototyp*, 18: e2141653.

https://doi.org/10.1080/17452759.2022.2141653

103. Caiazzo F, Caggiano A, 2018, Laser direct metal deposition of 2024 Al Alloy: Trace geometry prediction via machine learning. *Materials* (*Basel*), 11: 444.

https://doi.org/10.3390/ma11030444

104. Le C, Kolasangiani K, Nayyeri P, *et al.*, 2023, Experimental and numerical investigation of 3D-Printed bone plates

under four-point bending load utilizing machine learning techniques. *J Mech Behav Biomed Mater*, 143: 105885.

https://doi.org/10.1016/j.jmbbm.2023.105885

105. Wang C, Tan XP, Tor SB, *et al.*, 2020, Machine learning in additive manufacturing: State-of-the-art and perspectives. *Addit Manuf*, 36: 101538.

https://doi.org/10.1016/j.addma.2020.101538

106. Einhorn TA, Gerstenfeld LC, 2015, Fracture healing: Mechanisms and interventions. *Nat Rev Rheumatol*, 11: 45–54.

https://doi.org/10.1038/nrrheum.2014.164

107. Ahn DG, 2021, Directed energy deposition (DED) process: State of the art. *Int J Precis Eng Manuf Green Tech*, 8: 703–742.

https://doi.org/10.1007/s40684-020-00302-7

108. Singh A, Kapil S, Das M, 2020, A comprehensive review of the methods and mechanisms for powder feedstock handling in directed energy deposition. *Addit Manuf*, 35: 101388.

https://doi.org/10.1016/j.addma.2020.101388

109. Casalino G, Karamimoghadam M, Contuzzi N, 2023, Metal wire additive manufacturing: A comparison between arc laser and laser/arc heat sources. *Inventions*, 8: 52.

https://doi.org/10.3390/inventions8020052

110. Bassis M, Ron T, Leon A, *et al.*, 2022, The influence of intralayer porosity and phase transition on corrosion fatigue of additively manufactured 316L stainless steel obtained by direct energy deposition process. *Materials*, 15: 5481.

https://doi.org/10.3390/ma15165481

111. Bambach M, Sizova I, Kies F, *et al.*, 2021, Directed energy deposition of Inconel 718 powder, cold and hot wire using a six-beam direct diode laser set-up. *Addit Manuf*, 47: 102269.

https://doi.org/10.1016/j.addma.2021.102269

112. Negi S, Nambolan AA, Kapil S, *et al.*, 2020, Review on electron beam based additive manufacturing. *Rapid Prototyp J*, 26: 485–498.

113. Tilton M, Lewis GS, Bok Wee H, *et al.*, 2020, Additive manufacturing of fracture fixation implants: Design, material characterization, biomechanical modeling and experimentation. *Addit Manuf*, 33: 101137.

https://doi.org/10.1016/j.addma.2020.101137

114. Schappo H, Giry K, Salmoria G, *et al.*, 2023, Polymer/calcium phosphate biocomposites manufactured by selective laser sintering: An overview. *Prog Addit Manuf*, 8: 285–301.

https://doi.org/10.1007/s40964-022-00332-4

ACCSCIENCE PUBLISHING

Materials Science in Additive Manufacturing

REVIEW ARTICLE

Current materials for 3D-printed flexible medical electrodes

Yiting Huang[1], Qi Zhu[1], Haofan Liu[1], Ya Ren[2], Li Zhang[1], Maling Gou[1]*

[1]Department of Biotherapy, Cancer Center and State Key Laboratory of Biotherapy, West China Hospital, Sichuan University, Chengdu, Sichuan, China

[2]Huahang Microcreate Technology Co., Ltd, Chengdu, Sichuan, China

Abstract

Electrodes serve as essential tools for both acquiring and stimulating electrical signals, pivotal in monitoring human health through electrophysiological signals and playing a significant role in disease management and treatment. Notably, Young's modulus of flexible electrodes is similar to that of tissues and organs, thereby avoiding tissue or organ damage arising from mechanical mismatch. Thus, flexible electrodes become the fundamental devices for ensuring the stable, long-term acquisition of electrical signals and delivering reversed electrical stimulation to guide disease treatment. Reducing the size of flexible electrodes and increasing the number of electrode channels are significant for improving the sensitivity and accuracy of signal acquisition. In comparison to traditional manufacturing methods, 3D printing technology is able to fabricate products with higher resolution at a much faster speed. It is customizable and provides a novel approach for preparing flexible electrodes. Many conductive materials have been developed and applied to prepare flexible electrodes, and some have been integrated into 3D printing techniques, driving forward the development of 3D-printed flexible electrodes in medical fields. This article reviews recent research advances concerning the combination of these materials with 3D printing technology to prepare flexible electrodes and categorizes the materials into four main groups, namely metallic materials, carbon-based materials, conductive polymers, and other materials. In addition, we outline the future directions regarding the application of 3D-printed flexible electrodes in clinical research and medical translation.

Keywords: 3D printing; Biomaterials; Flexible electrodes; Conductive materials

1. Introduction

Electrophysiological signals usually arise concomitantly with human physiological activities. The acquisition and analysis of electrophysiological signals can be used to monitor human body status and guide the treatment of some diseases[1-4]. Given their important roles in extracting electrophysiological information directly from the human-body interface and providing feedback, electrodes are in great demand in the clinical and medical fields[5]. In addition to acquiring electrophysiological signals, external electrical signals can be transmitted to the cerebral cortex or even deeper brain regions through electrodes, assisting in controlling limb movement and other

***Corresponding author:**
Maling Gou
(goumaling@scu.edu.cn)

Citation: Huang Y, Zhu Q, Liu H, Ren Y, Zhang L, Gou M, 2023, Current materials for 3D-printed flexible medical electrodes. *Mater Sci Add Manuf*, 2(4): 2084.
https://doi.org/10.36922/msam.2084

Received: October 22, 2023

Accepted: November 24, 2023

physiological activities and improving human health[6-8]. In traditional rigid electrodes, hard metal materials with good electrical conductivity are mostly used as conductors. However, the shortcomings of these electrodes, such as poor adherence to the human body and propensity to cause skin and tissue contusion, make long-term stable human monitoring a challenging endeavor[9-11]. Thus, it is of utmost importance to develop flexible electrodes with stable electrical conductivity, excellent tissue adhesion, and good biocompatibility, which also possess the ability to prevent mechanical damage to tissues. These flexible electrodes can be utilized in various medical applications, such as brain-computer interface, signal monitoring,[12] and tissue regeneration and repair[13-15]. Nevertheless, the preparation of flexible electrodes with properties such as high sensitivity, high adhesion, small size, high specific capacity, long cycle life, and excellent human compatibility is still a great challenge[16,17].

Compared with traditional manufacturing technologies, 3D printing is an additive manufacturing technology that transforms digital models into physical models with complex shapes[18-21]. With the advantages of high resolution, fast printing speed, and low cost, 3D printing provides a new strategy for preparing personalized, high precision, and multichannel flexible electrodes[22-24]. Several studies have applied 3D printing technology to prepare flexible electrodes for use in medical applications (Figure 1). Light-curing 3D printing is a printing technology that scans photosensitive materials with a specific wavelength of light beams and stacking multiple layers to prepare 3D structures[25]. It can prepare high-precision flexible electrodes with printing accuracy down to the micron level[26,27]. Direct-ink-writing (DIW) can utilize mechanical or pneumatic pressure to extrude and shape highly viscous or solid–liquid mixed ink materials, which is suitable for the preparation of large flexible electrodes *in vitro*[28-31]. Compared to DIW printing or digital light processing (DLP)-based 3D printing, fused deposition modeling (FDM) printing requires lower material fluidity and eliminates the need for post-processing, such as drying or freeze-drying[32-34]. It simplifies the printing process and maintains the mechanical properties of the material, allowing more materials to be used in the manufacture of wearable devices and bionic electronic skin products[35,36]. Electrospinning can obtain nanoscale fibers by applying a voltage to the needle and collector and using static field forces to pull out the polymer-based liquid, which is advantageous for the preparation of multichannel, stretchable, and flexible electrodes[37-39]. Inkjet printing (IJP) creates patterned thin films or stacked 3D structures on media by spraying nano-sized solutions, which can be used to prepare miniature, multichannel flexible electrodes, or arrays for sensitive acquisition of electrical signals[40-42]. The rapid development of different 3D printing technologies in recent years has provided additional strategies for preparing flexible electrodes. However, the lack of advanced materials limit the medical applications of 3D-printed flexible electrodes[43]. Materials used to prepare flexible medical electrodes need to be conductive, biocompatible, ductile, and stable[44,45]. To advance the development of conductive materials in 3D printing, various strategies for the preparation of flexible electrodes have emerged, as shown in Figure 2.

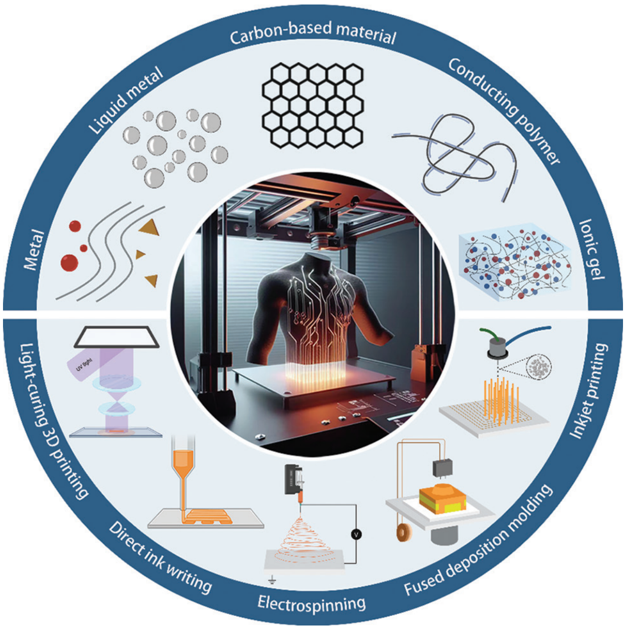

Figure 1. Materials and 3D printing technologies for flexible medical electrodes. (The middle image was generated by an AI tool, while other images were created using BioRender.com.)

This article provides an overview of recent research advances in materials used for 3D-printed flexible electrodes, including metallic materials, carbon-based materials, conductive polymers, and other materials (Figure 1). Through intensive efforts in improving 3D printing technology and material properties, as well as combining multiple materials, a range of flexible medical electrodes with good performance has been created, displaying great application prospects in medicine, such as physiological signal acquisition, biochips, soft robotics, tissue regeneration, and biosensors.

2. Metallic materials

Metallic materials are known for their good ductility, thermal conductivity, and electrical conductivity. Electrodes made with metallic materials, such as gold, silver, and platinum, have a wide range of applications for neural recordings, typically seen in animal studies

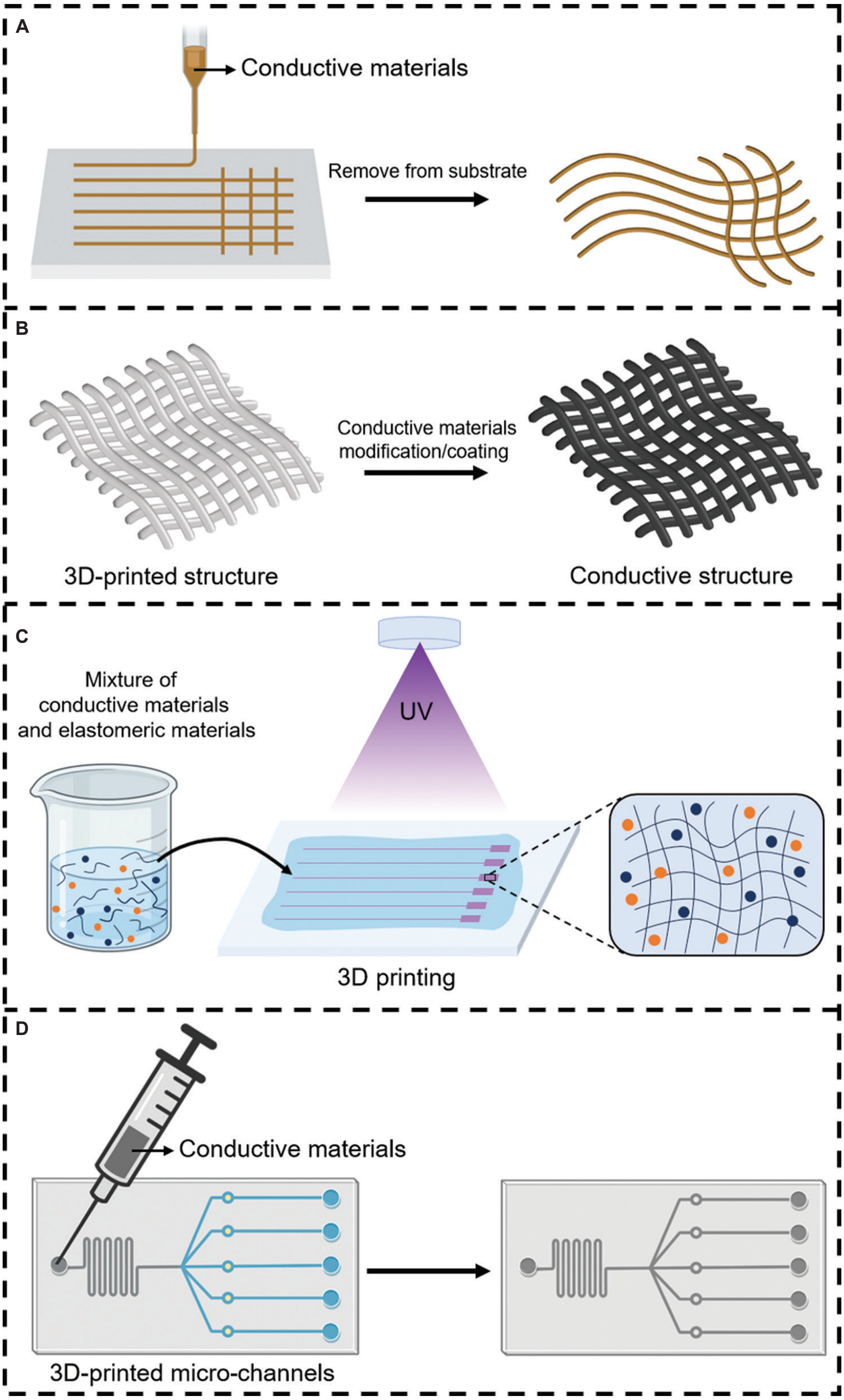

Figure 2. Strategies for preparing flexible electrodes. (A) Direct 3D printing of conductive materials. (B) Modification or coating of conductive materials on the surface of 3D-printed structures. (C) Mixing conductive materials with elastomers for 3D printing. (D) Injecting conductive materials into micro-channels prepared by 3D printing. The images in Figure 2 were created using BioRender.com.

and human clinical devices. For example, Utah electrodes and Michigan electrodes use metal as conductors and are utilized as invasive electrodes for intracranial applications[46,47]. Nevertheless, conventional hard metals are often subjected to mechanical mismatches at biological tissue interfaces, resulting in irreversible damage and inflammatory reactions[48-51]. These issues greatly limit the use of metal electrodes in animal research and human clinical neurological recording devices.

Recent years have seen the emergence of several strategies for combining flexible polymer materials with metallic materials, effectively mitigating the abovementioned problems. Hui et al prepared an Ag-based ink for extruded 3D printing by mixing silver with hydrogel and showed that the ink can be printed in a hydrogel-support matrix to form a 3D conductive structure that can be stretched and compressed[52]. Electronic devices prepared in this way can be used as biomedical electrodes. Ma *et al.* reported the optimization of a drop-on-demand, high-resolution electrohydrodynamic-based jet-printing method for generating 3D gold (Au) micropillar electrode arrays on flexible substrates (Figure 3A)[53]. The electrode array showed mechanical flexibility under planar, concave, and convex conditions, and its sensing capability remained virtually unchanged[53]. Another study conducted by a research team from Carnegie Mellon University reported the formation of shanks with a diameter of only a few tens of micrometers by stacking atomized metal ink as an aerosol on a two-dimensional (2D) substrate. A high-density microarray electrode with 2,600 shanks per square centimeter was obtained. This microarray electrode caused very minimal gross tissue damage and yielded an excellent signal-to-noise ratio given the low impedance of the metal ink[54]. On the other hand, Morgan *et al.* attempted to integrate 3D microarrays on flexible polyimide or parylene C films through two-photon lithography and modify the metallic platinum on arrays to obtain flexible microarray electrodes[55]. The microarray electrode with flexible substrates significantly reduces tissue damage caused by hard metals. This electrode can be used for signal acquisition inside tissues to enhance the spatial resolution of physiological electrical signals and hold immense promise for use as implantable brain-computer interfaces.

Compared to common metals, metal nanoparticles (NPs)/nanowires/nanosheets have relatively small sizes and more interactions between grains[56-58]. A recent study used CuO NP inks for electrospinning, as shown in Figure 3B. After post-processing, a Cu wire with a width of 50 μm, a thickness of 1.48 μm and a resistivity of only 5.46 μΩ·cm was obtained[59]. Moreover, the high surface area to volume ratio of metal nanomaterials allows them to adsorb small molecules to achieve better chemical stability and processability by modification[60-62]. Thus, metal nanomaterials become the preferred materials for 3D printing of flexible electrodes for medical applications. In another study, Im *et al.* added multifunctional thiols to AuNP ink to modulate the cohesion of AuNP by inducing strong interactions between the thiol groups and the gold surface so that microcracks and pores are not easily generated in the AuNP film after heat exposure (Figure 3C)[11]. The modified AuNP ink is more structurally stable during processing and can form stable, flexible conductive devices by IJP onto flexible substrates. These flexible electrodes are stable in high humidity and salt-rich liquids and can maintain stable conductivity after more than 1,000 bending cycle tests[11]. The improvements of the ink properties are made possible only after the tremendous advancements in materials science, which further spawn the development of various flexible and elastomeric materials with mechanical properties equivalent to those of human tissues and organs, and lay solid foundation for preparing flexible medical electrodes based on metal materials.

In addition to the traditional solid metal, room-temperature liquid metals represented by gallium (Ga)-based alloys have good room-temperature mobility and low toxicity. The liquid metals can reach a conductivity of 3.8 × 10^6 S/m, making them ideal materials for manufacturing flexible electrodes[63,64]. However, it is still challenging for liquid metals to form a continuous and stable conductive structure due to their highly oxidizable surface, large surface tension, and low viscosity[65-67]. Wu *et al.* printed liquid metal in an acrylamide/nanoclay support bath with oxidizing properties, forming a viscoelastic oxide skin instantaneously on the extruded liquid metal surface[67]. It allows the formation of continuous liquid metal filaments (150 μm) with tensile strains up to 1400%, as shown in Figure 3D[67]. This flexible electrode can be used as a strain sensor and a passive resonant sensor, which has potential applications in wearable biomonitoring and untethered robotics. In addition, a common method for fabricating flexible electrodes based on liquid metals involves the preparation of liquid metals into nano-sized particles, followed by printing and molding through annealing or other operations[68-70].

This section summarizes the research on metallic materials used in the preparation of 3D-printed flexible medical electrodes. These studies have facilitated flexible metal-based electrodes in implantable neural interfaces, sensors, and wearable devices by improving 3D printing techniques or modifying the materials. The involved methods not only allow better machinability while maintaining the good properties of the metallic material but also increase the mechanical properties of the flexible electrodes, such as tensile and flexibility.

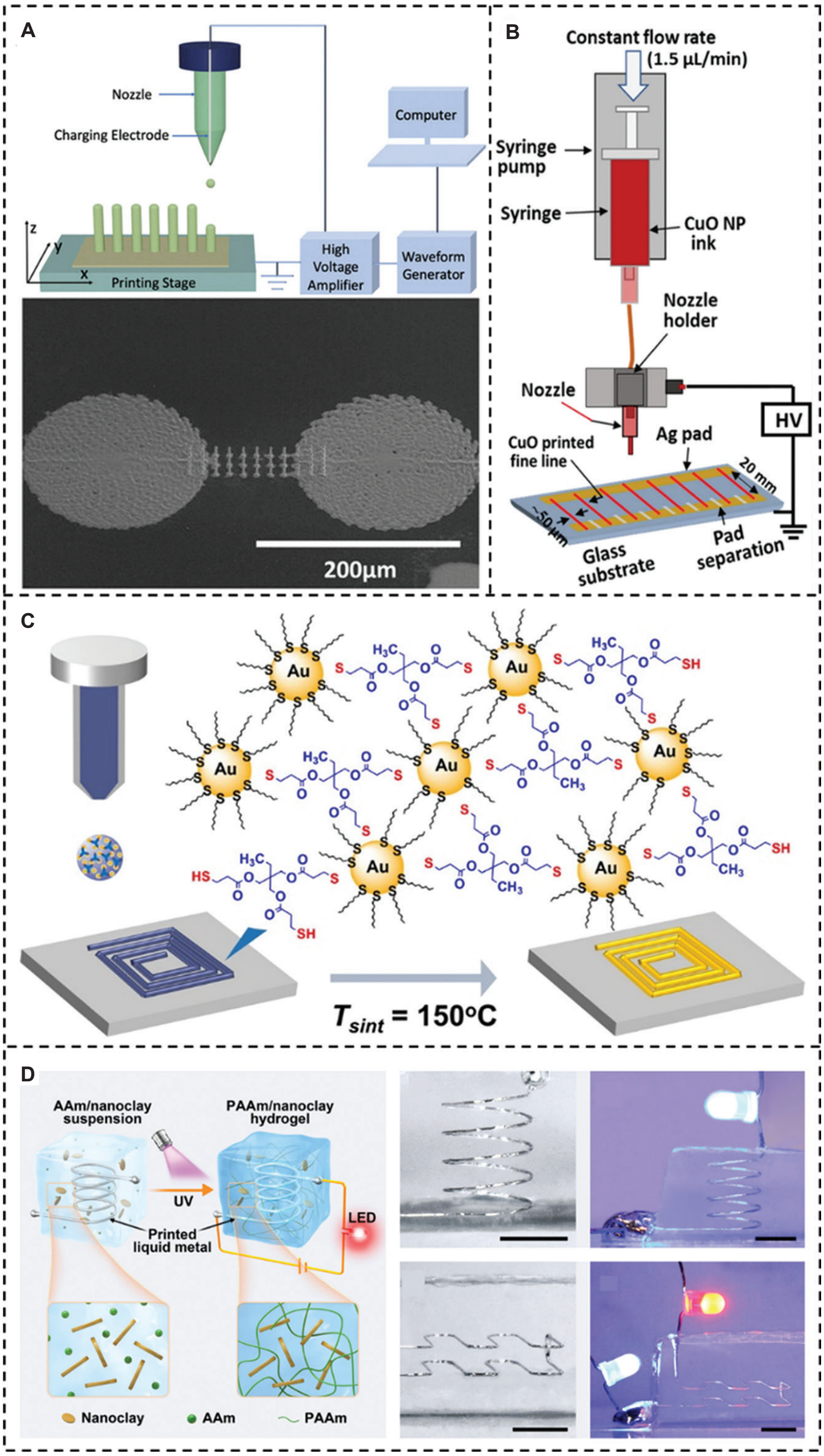

Figure 3. Metallic materials for 3D-printed flexible electrodes. (A) Drop-on-demand and electrohydrodynamic-based jet-printing method for generating 3D Au micro-pillar electrode arrays on flexible substrates[53]. Copyright © 2023 John Wiley and Sons. Reprinted with permission of John Wiley and Sons. (B) CuO NP inks for electrospinning[59]. Copyright © 2023 Springer Nature. Reprinted with permission of Springer Nature. (C) Modified AuNP inks for inkjet printing to form flexible conductive devices[11]. Copyright © 2022 American Chemical Society. Reprinted with permission of American Chemical Society. (D) Suspension printing of liquid metals in an acrylamide/nanoclay support bath[67]. Copyright © 2022 Springer Nature. Reprinted with permission of Springer Nature.

3. Carbon-based materials

In addition to their ductility and stable cycling performance, carbon-based materials are more widely available and less expensive than metal materials, making them attractive topic of research in the domain of flexible electronic devices in recent years[71,72]. Some examples, such as carbon nanotubes (CNTs), graphene, and other polymer-derived carbon materials, are widely used as functional materials for flexible medical electrodes.

CNTs are one-dimensional quantum materials with a special structure consisting of several layers of hexagonally arranged carbon atoms in a coaxial circular tube[73]. The unique structure of CNTs gives them strong physical properties with single-walled CNTs reaching tensile strengths of about 800 GPa and elastic moduli of up to 1 TPa[74,75]. Thus, CNTs not only have a hardness close to that of diamond but also have good flexibility, making them a preferred material for preparing flexible medical electrodes. There are two main strategies for prepare CNTs-based conductive elastomers. The first strategy is to use CNTs as fillers uniformly dispersed in the polymer matrix. For example, Sun *et al.* composited CNTs with polydimethylsiloxane (PDMS) to prepare flexible piezoresistive tactile sensors[76]. However, this approach tends to affect the mechanical properties of the polymers and limits the sensitivity of the sensor devices[77]. The second strategy is to coat the CNTs on the surface of the polymer matrix. Kim *et al.* deposited CNT film onto polystyrene (PS) substrates and transferred CNT film to PDMS to form flexible thin-film pressure sensors[78], which are highly sensitive. Nevertheless, the CNTs may be detached from the surface of the polymer matrix during the deformation of the sensor, which is unfavorable for the long-term monitoring of physiological electrical signals *in vitro*[79]. To overcome these problems, Yu *et al.* adopted a strategy to embed CNTs into the surface of FDM-printed thermoplastic elastomer (TPE), as shown in Figure 4A[80]. The CNTs are encapsulated by the melted TPE on the surface through a high-temperature heating process. This flexible electronic sensor has a sensitivity of up to 136.8 kPa^{-1} at an applied pressure of <200 Pa while compressing and recognizes human facial activity at a thickness of only 2 mm. Its potential application extends to monitoring and recognizing various human physiological signals.

First discovered in 2004 by Andre Geim and Konstantin Novoselov, graphene has a high carrier mobility (~10 000 $\text{cm}^2/\text{V}\cdot\text{s}$) and a high Young's modulus (~1 TPa) at room temperature[81-83]. Some studies have been conducted to apply graphene to prepare conductive devices, such as sensors and supercapacitors. Yang *et al.* integrated patterned graphene on PDMS film to prepare graphene/PDMS electrodes with excellent stability and reusability, which has comparable sensitivity to commercial wet Ag/AgCl electrodes[84]. In another study, Qian *et al.* demonstrated that reduced graphene oxide (rGO) and elastomeric resins formed a composite material that could be prepared as a flexible strain sensor using DLP 3D printing (Figure 4B). This sensor has high mechanical stability of more than 10,000 stretching–relaxing cycles and a sensitivity of 6.723 over a linear strain detection range from 0.01% to 40%[85]. In addition, there are studies on graphene materials to prepare biological scaffolds with conductive properties. For instance, Fang *et al.* mixed rGO with polycaprolactone (PCL) and printed it into an orderly arranged microfiber layer by melt electro-writing technology (Figure 4C)[86]. Incorporating rGO enhances the mechanical properties of the PCL scaffolds while conferring better electrical conductivity on the scaffolds, which is essential for the functional recovery of peripheral nerves. The experimental results showed that the nerve guidance conduits with conductive carbon-based materials could promote nerve regeneration, myelin sheath formation, and functional regeneration of nerve tissues[86].

MXene is a novel 2D carbon nanofiber material, mainly composed of carbon (C), nitrogen (N), titanium (Ti), niobium (Nb), and tantalum (Ta)[87]. MXene was first used as a contact layer for electrochemical biosensors in 2014[88]. The unique layered structure gives MXene a conductivity similar to that of metals, which exhibit good sensitivity in sensors[88-90]. In addition, MXene has other excellent properties, including controllability in elemental composition and structure, as well as favorable optical and mechanical properties (Young's modulus ~0.4TPa, fracture strength ~26 GPa)[91-93]. These properties give MXene materials a significant advantage in sensing elements for flexible sensors. Cui *et al.* prepared a wearable MXene-polyurethane mesh (MPM) electronic skin (e-skin) by embedding or wrapping MXene nanosheets into porous polyurethane (PU) nanogrid scaffolds generated by electrospinning (Figure 4D). With ultra-low electrode-skin contact impedance (4.68 kΩ at 1 kHz) and high signal-to-noise ratio (16.5 dB), MPM e-skin demonstrated good stability and signal acquisition accuracy in long-term electrocardiographic testing. The fiber film produced by electrostatic spinning allows the MPM e-skin to be breathable, minimizing the risk of adverse effects as a result of blocked sweat evaporation[94]. It has also been studied to make composite gels of MXene with conductive polymers, which can be used for DIW 3D printing. The incorporation of MXene nanosheets enables the connection of disconnected structural domains between neighboring conductive polymer molecules, facilitating ion/electron transport in the gel. The composite gel exhibits

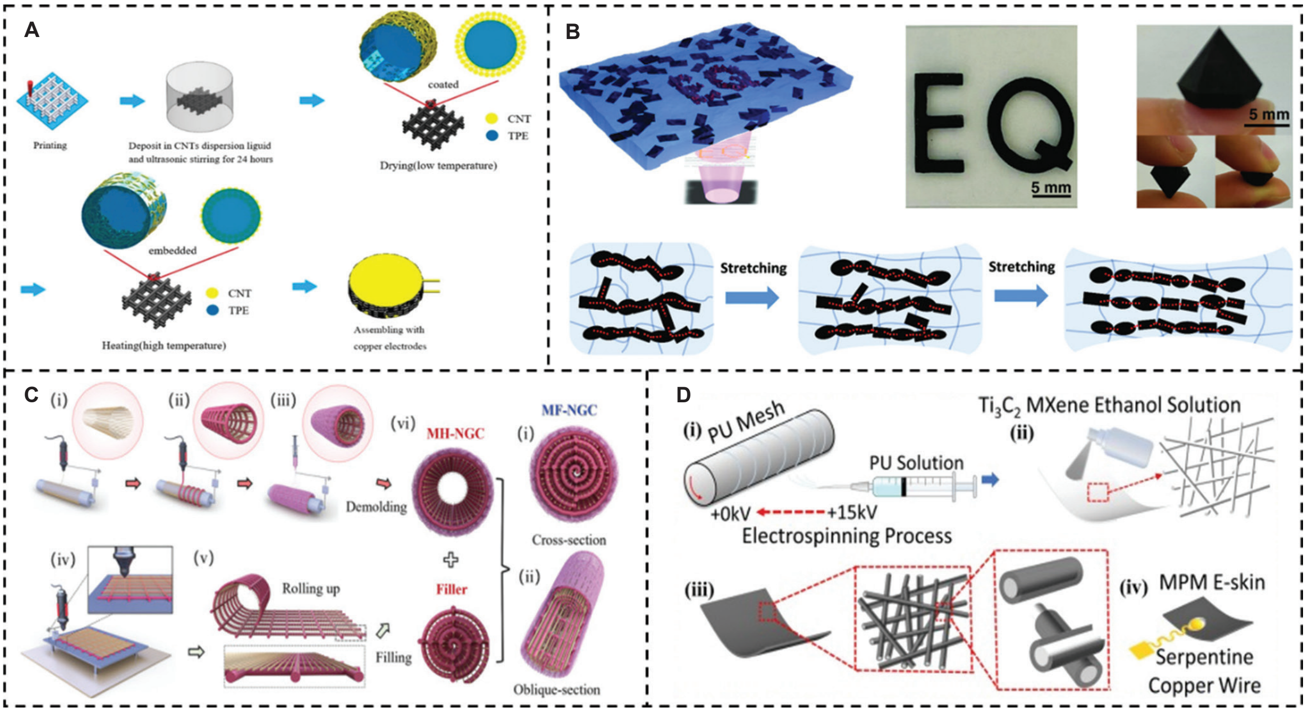

Figure 4. Carbon-based materials for 3D printed flexible electrodes. (A) Preparation of electrically conductive 3D structures by embedding CNTs in thermoplastic elastomer thermoplastic elastomer surfaces using FDM printing[80]. Copyright © 2020 American Chemical Society. Reprinted with permission of American Chemical Society. (B) Composites of rGO and elastomeric for digital light processing 3D printing[85]. Copyright © 2021 Wiley-VCH. Reprinted with permission of Wiley-VCH. (C) Melt electro-writing-prepared rGO/PCL microfiber layer[86]. Copyright © 2023 John Wiley and Sons. Reprinted with permission of John Wiley and Sons. (D) Embedding or wrapping MXene nanosheets into porous PU nanogrid scaffolds produced by electrospinning[94]. Copyright © 2022 ELSEVIER BV. Reprinted with permission of ELSEVIER BV.

excellent energy storage performances and is resistant to deformation and low temperature, making it a good flexible electrode element[95].

Many carbon-based materials have been applied to the preparation of flexible medical electrodes. In these reports, carbon-based materials can be directly used in 3D printing, encapsulated or embedded in structures created by 3D printing, or composited with other materials to form inks that can be used for 3D printing. The combination between carbon-based materials with excellent conductivity and ductility and flexible substrates with great mechanical properties may lead to the creation of conductive materials with high sensitivity. Characterized by low toxicity and thermal conductivity, carbon-based materials are regarded as potential substitutes for metal materials in the preparation of future flexible medical electrodes and have promising application prospects in various facets, such as biosensing, physiological signal detection, and biological scaffolds.

4. Conductive polymers

The conductivity of conductive polymers lies within the range between semiconductors and conductors and is achieved through methods such as doping[96,97]. Conductive polymer materials offer the advantages of easy processing and production, low density, and corrosion resistance compared to traditional metal conductors[98-100]. Meanwhile, the conductivity of the conductive polymer can be adjusted by tinkering with the electrochemical reversible reaction[101-103], offering flexibility to practical applications. Polyaniline (PANI) was the first-discovered conductive polymer, whose electrical conductivity could change with the degree of hydration and acid-base parameters of different derivatives[104,105]. The application of PANI to IJP for the preparation of flexible and patterned electrochromic devices (ECDs) has been reported[106]. In the wake of the serendipitous synthesis of polyacetylene with a metallic luster, a wave of studies aiming to enhance the electrical conductivity of polyacetylene has emerged[107-109]. Subsequently, a series of conductive polymers, including polypyrrole (PPy)[110-112], polythiophene[113-115], and PEDOT:PSS[116-118] were developed, significantly expanding the selection of materials available for the preparation of flexible medical electrodes.

PEDOT:PSS has good electrical conductivity, biocompatibility, and water solubility. With the help of

3D printing technology, PEDOT:PSS with 3D microscale structure finds diverse applications in wearable and implantable electrodes, biochips, and other similar fields[102,119,120]. Yuk *et al.* developed a paste-like PEDOT:PSS ink by altering the rheological properties of PEDOT:PSS to enable direct use in 3D printing (Figure 5A). In this particular study, directly 3D-printed conductive polymers could reach a resolution of 30 μm and could be used to prepare high-density flexible electronic circuits with soft nerve probes[121]. Tomaskovic-Crook *et al.* used 3D printing to construct a heart-on-a-chip platform that anchors tissue, evaluated continuous contraction force, and employed micropipettes to 3D-print PEDOT:PSS column electrodes in an array form, integrated with 3D printed flexible, quantum dots/TPE nanocomposite microwires (Figure 5B)[122]. The height-to-diameter aspect ratio of the PEDOT:PSS columns was ≈5.7, allowing for mechanical stability in cell culture media and biogels. Moreover, the conductivity of PEDOT:PSS columns was significantly better than that of PEDOT:PSS films, which facilitated *in situ* cell stimulation and promoted the growth of 3D tissues *in vitro*[122].

In addition to directly printing conductive polymer molding, mixing conductive polymers with stretchable hydrogels is also a common method to prepare conductive polymers-based flexible electrodes. For instance, Li et al. attempted to mix PEDOT:PSS, MXene, and ethylene glycol (EG) into a composite gel, which is targeted to be used as an ink for DIW 3D printing (Figure 5C). In the printable ink, uniformly distributed MXene nanosheets could improve the printability of the PEDOT:PSS solution and modulate the interconnected electronic structure of PEDOT:PSS to undergo a micelle-to-linear structure transition[95]. Conductive polymers-hydrogel electronics typically have well-organized mechanically compatible interfaces, which help in eliminating electrochemical instability caused by severe mechanical mismatches. However, the addition of hydrogels significantly reduces the overall conductivity, and increasing the content of conductive polymers will impair the mechanical properties of hydrogels[121,123,124]. In recent years, several studies have been conducted to improve the molding method or components of PEDOT:PSS ink to enhance the conductivity of conducting polymer-hydrogel composites and to maintain the mechanical properties of hydrogels. For example, as shown in Figure 5D, Xie *et al.* utilized the strong hydrophobicity of PEDOT:PSS to form an elastic film at the liquid-liquid interface by combining it with a

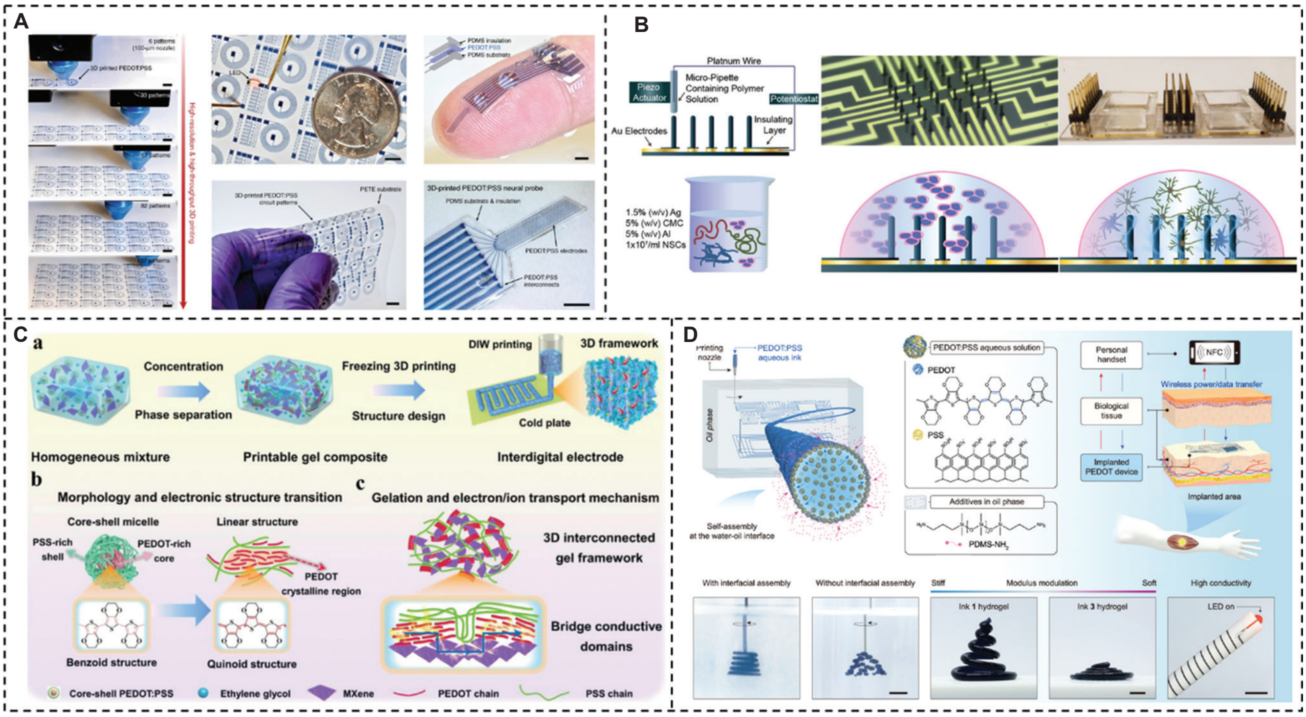

Figure 5. Conductive polymers for 3D-printed flexible electrodes. (A) A paste-like PEDOT:PSS ink for 3D printing[121]. Copyright © 2020 Springer Nature. Reprinted with permission of Springer Nature. (B) Printing of PEDOT:PSS column electrodes using micropipettes[122]. Copyright © 2019 Wiley-VCH. Reprinted with permission of Wiley-VCH. (C) PEDOT:PSS-MXene composite gel for direct ink writing 3D printing[95]. Copyright © 2023 Wiley-VCH. Reprinted with permission of Wiley-VCH. (D) PEDOT:PSS inks for liquid-liquid 3D printing formed in an oil environment[125]. Copyright © 2023 Springer Nature. Reprinted with permission of Springer Nature.

PDMS surfactant in an oil environment to prepare liquid-liquid 3D printable ink[125]. With an electrical conductivity of up to 301 S/m, the ink was formed by combining the light-curing hydrogel with ionic liquids that can enhance its stretchable properties and conductivity. The viscosity of the ink and the concentration of PEDOT:PSS can be adjusted to within a certain range, increasing the versatility of the ink in 3D printing technology. Zhou *et al.* reported a phase-separated ink consisting of an electrical phase (PEDOT:PSS) and mechanical phase (hydrophilic PU), which was prepared to obtain a bi-continuous conducting polymer hydrogel (BC-CPH). BC-CPH has high electrical conductivity (over 11 S/cm), elongation (over 400%), and fracture toughness (over 3300 J/m^2). It can be prepared as an all-hydrogel bioelectronic interface using extrusion 3D printing[126]. The viscosity of BC-CPH inks can also be adjusted to be used in electrostatic spinning technology for long-term stable electrophysiological recording and stimulation.

Despite the excellent properties of conductive polymers, the lack of stability still limits their application in daily life. In future research, there is a need to explore strategies to improve the conductivity of existing CPs and focus on ways to enhance their structural stability. At the same time, new types of conductive polymers with extended recycling life for flexible medical electrodes should be developed to cater to a broader range of applications.

5. Other materials

In addition to the aforementioned materials, an increasing number of novel material systems are being employed to 3D-print flexible medical electrodes, including ionic gels and composite hydrogels. In addition, conductive polymer-doped elastomers possess continuous conductive phases and excellent stretchability and transparency, attributes that facilitate more direct applications in flexible and wearable electronics.

Ionic gels are solid mixtures with ionic conductivity, usually a mixture of polymeric organic polymers and ionic liquids[127-129]. The polymer molecular chains are interconnected or entangled to form a spatial mesh structure, and the structural voids are filled with anions and cations that act as a dispersing medium, giving the ionic gel a continuous conductive phase[130-132]. To enable ionic gels to be used in 3D printing technology, Huang *et al.* designed a self-regulating ink consisting of poly (ionic liquid) networks, ionic liquid monomers, and free ionic liquid. By adjusting the ratio, the rheological properties of the ink can be modified, and the printability of the ionic gel can be increased to realize efficient DIW printing (Figure 6A)[133].

Increasing the content of ionic liquids is the primary approach to improving the electrical conductivity of ionic gels, often accompanied by a sharp decrease in the mechanical properties of the gels[134,135]. Liquid leaks can be toxic in the body, limiting the application of ionic gels[136-138]. Yao *et al.* utilized granular amphiphilic ionic particles to synthesize ionic gels, as shown in Figure 6B. The dissolved ionic particles increased the mechanical properties of the ionic gels due to electronic interactions or physical crosslinking, resulting in double-network ionic gels with high stretchability (>600%) and ultrahigh toughness (fracture energy >10 kJ/m^2)[139]. Zhang *et al.* used a phase separation strategy to improve the mechanical properties of the gels by doping lithium salt into the ionic gels[140]. The addition of lithium salts increased the electrical conductivity of the ionic gel and led to the formation of a phase-separated microstructure within the ionic gel. Lithium ions establish lithium bonds with hydroxyl groups present on the polymer network, which make up the rigid regions of the ionic gel and enhance the toughness of the ionic gel (mechanical strength in the range of 2.29 to 5.19 MPa). The polymer chains and ionic liquid form the soft region of the ionic gel, which improves the elongation of the gel (>1000%). Through DLP 3D printing, this ionic gel can be fabricated into microcircuits with complex structures and microarrays for self-powered tactile sensing, which has considerable potential for applications in the field of human-computer interaction[140] (Figure 6C).

Hydrogels are moisturizing, flexible, and biocompatible materials. However, due to the lack of an effective energy dissipation mechanism, hydrogels are prone to fracture or breakage during repeated stretching or compression. To satisfy the requirements for long-term applications of flexible electrodes, hydrogels with excellent mechanical properties (flexibility, resilience, *etc.*) and high stability need to be designed. Xiong *et al.* indicated that acrylated β-cyclodextrin could undergo precise host-guest recognition with bile acids and form polymerizable pseudorotaxane by self-assembling the two molecules[141]. Polymerizable pseudorotaxane can be mixed with photo-polymerizable acrylamide hydrogel to obtain conductive polymerizable rotaxane hydrogels (PR-Gel), as shown in Figure 6D. The topological network of pseudorotaxane enhances the mechanical properties of hydrogels, with a maximum tensile ratio of 830% and good flexibility in the temperature range of -20°C to 60°C. Furthermore, this method improved the poor fatigue resistance of the hydrogel, and no significant hysteresis was observed after 500 cycles at 300% strain. This report utilizes DLP 3D printing to fabricate PR-Gel into flexible sensors with complex geometries that can better adapt to the surface structure of the human body and can be used for real-time monitoring of human electrocardiographic signals[141].

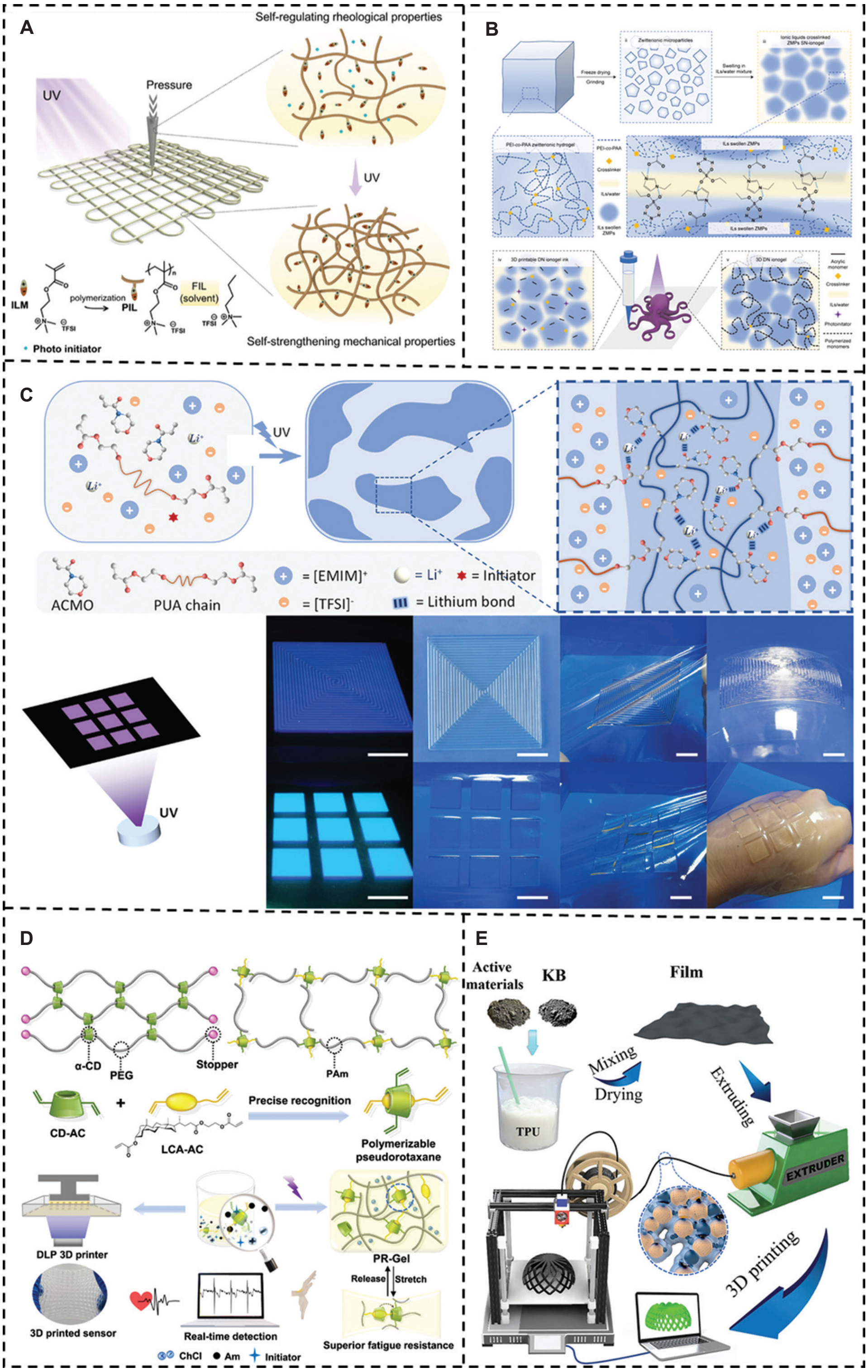

Figure 6. Other materials for 3D-printed flexible electrodes. (A) A self-regulating ink for direct ink writing printing[133]. Copyright © 2023 John Wiley and Sons. Reprinted with permission of John Wiley and Sons. (B) Granular ionogel particle inks for 3D printing[139]. Copyright © 2023 American Association for the Advancement of Science. Reprinted with permission of American Association for the Advancement of Science. (C) Digital light processing 3D-printable ionic gels for preparing conductive devices[140]. Copyright © 2022 Wiley-VCH. Reprinted with permission of Wiley-VCH. (D) Conductive polymerizable rotaxane hydrogels (PR-Gel) for 3D Printing[141]. Copyright © 2023 Springer Nature. Reprinted with permission of Springer Nature. (E) TPU-based electrode filaments that can be used for FDM printing[143]. Copyright © 2023 Wiley-VCH. Reprinted with permission of Wiley-VCH.

Hydrogels can be deformed and adhered to tissues. However, hydrogels are water-swellable crosslinked polymers, and the loss of water inevitably leads to deterioration of mechanical properties, making prolonged use in an anhydrous environment challenging. Elastomeric materials formed by crosslinking polymer chains exhibit better mechanical properties and environmental stability without relying on solvent swelling. Thus, elastomeric materials are more suitable for 3D printing technologies such as FDM, which rely on high-temperature conditions for printing and molding. Thermoplastic PU (TPU) is a common polymer used in FDM printing due to its excellent flexibility and stable melting temperature[142]. In Hu *et al.*'s study, TPU-based electrode filaments that can be used for FDM printing were prepared by mixing different active materials (lithium iron phosphate, lithium titanate, nickel cobalt manganese oxide, or graphite) with TPU and conductive additives in dimethylformamide (Figure 6E). The flexible electrodes with complex structures prepared by FDM printing exhibit excellent print stability and mechanical properties[143].

6. Conclusion and perspectives

Flexible electrodes serve diverse purposes in both medical research and clinical practice. Extracorporeal flexible medical electrodes enable the monitoring of human electrocardiographic signals for early diagnosis and risk prediction, allowing patients to receive timely cardiovascular interventions and reducing the occurrence of emergent cardiovascular events. Implantable flexible electrodes allow real-time transmission of electrical signals within the brain and are an important component of brain-computer interfaces. They serve diagnostic and therapeutic purposes and contribute to the study of functional brain regions. Furthermore, flexible electrodes have been explored in studies involving nerve conduit scaffolds to promote tissue repair and regeneration.

The continuous optimization of materials and improvement of manufacturing technology is significant for generating advanced medical flexible electrodes. In terms of materials, more comprehensive research on existing materials is required. For example, through doping, modification, and material composites, it is possible to enhance the conductivity and stability of electrically conductive materials or the flexibility and tensile properties of flexible materials. In addition, we need to improve the processability of materials and broaden the range of materials compatible with 3D printing technologies. At the same time, we also need to continually develop new conductive materials with excellent biocompatibility and cyclic stability, which can be used to create more flexible electrodes for *in vivo* implantation and prolong the lifespan of the electrodes. We believe that continuous explorations will give rise to flexible electrodes with higher resolutions and more channels, which can facilitate the delivery of precise and sensitive data.

In terms of technology, it is necessary to continuously improve the resolution and material compatibility with 3D printing technology to meet the growing demand for using 3D-printed flexible electrodes in various medical scenarios. In addition, combining 3D printing technology with photolithography and screen printing provides an impetus to the development of high-precision, multi-channel flexible electrodes, which are promising tools for acquiring and stimulating refined physiological signals. Future research could also consider optimizing the structural design of flexible electrodes to make 3D-printed flexible electrodes more personalized and compatible with clinical needs and applications.

In the future, clinical trials should be conducted to investigate innovative materials, technologies, and designs. It is also necessary to promote the adaptation of flexible electrodes into clinical use by improving the performance of flexible electrodes, expanding the function of electrodes, and reducing the production cost. These desirable features will also indirectly broaden their applications in the medical field.

Acknowledgments

The authors acknowledge the support received from Microsoft Bing's chat mode and BioRender.com. The middle image in Figure 1 was created using Microsoft Bing's chat mode, while other elements in Figures 1 and 2 were created using BioRender.com.

Funding

This work was financially supported by the National Key Research and Development Program of China (2021YFF1200800); Sichuan Science and Technology Program (2021JDTD0001); The National Natural Science Foundation (32271468); Natural Science Foundation of Sichuan Province (2022NSFSC1453); and Innovation Research Project of Sichuan University (2022SCUH0046).

Conflict of interest

The authors declare no conflict of interest.

Author contributions

Conceptualization: Maling Gou
Writing – original draft: Yiting Huang, Qi Zhu, Haofan Liu, Ya Ren
Writing – review & editing: Yiting Huang, Maling Gou, Li Zhang

Ethics approval and consent to participate

Not applicable.

Consent for publication

Not applicable.

Availability of data

Not applicable.

References

1. Metzger SL, Littlejohn KT, Silva AB, *et al.*, 2023, A high-performance neuroprosthesis for speech decoding and avatar control. *Nature*, 620:1037–1046.

   https://doi.org/10.1038/s41586-023-06443-4

2. Alagapan S, Choi KS, Heisig S, *et al.*, 2023, Cingulate dynamics track depression recovery with deep brain stimulation. *Nature*, 622:130–138.

   https://doi.org/10.1038/s41586-023-06541-3

3. Jang J, Kim J, Shin H, *et al.*, 2021, Smart contact lens and transparent heat patch for remote monitoring and therapy of chronic ocular surface inflammation using mobiles. *Sci Adv*, 7: eabf7194.

   https://doi.org/10.1126/sciadv.abf7194

4. Lee GH, Kang H, Chung JW, *et al.*, 2022, Stretchable PPG sensor with light polarization for physical activity-permissible monitoring. *Sci Adv*, 8: eabm3622.

   https://doi.org/10.1126/sciadv.abm3622

5. Li J, Liu Y, Yuan L, *et al.*, 2022, A tissue-like neurotransmitter sensor for the brain and gut. *Nature*, 606:94–101.

   https://doi.org/10.1038/s41586-022-04615-2

6. Yang Q, Yang S, Qiu P, *et al.*, 2022, Flexible thermoelectrics based on ductile semiconductors. *Science*, 377:854–858.

   https://doi.org/10.1126/science.abq0682

7. Hu H, Huang H, Li M, *et al.*, 2023, A wearable cardiac ultrasound imager. *Nature*, 613:667–675.

   https://doi.org/10.1038/s41586-022-05498-z

8. Flesher SN, Downey JE, Weiss JM, *et al.*, 2021, A brain-computer interface that evokes tactile sensations improves robotic arm control. *Science*, 372:831–836.

   https://doi.org/10.1126/science.abd0380

9. Pearre BW, Michas C, Tsang JM, *et al.*, 2019, Fast micron-scale 3D printing with a resonant-scanning two-photon microscope. *Addit Manuf*, 30:100887.

   https://doi.org/10.1016/j.addma.2019.100887

10. Trotter M, Juric D, Bagherian Z, *et al.*, 2020, Inkjet-printing of nanoparticle gold and silver ink on cyclic olefin copolymer for DNA-sensing applications. *Sensors*, 20:1333.

    https://doi.org/10.3390/s20051333

11. Im J, Trindade GF, Quach TT, *et al.*, 2022, Functionalized gold nanoparticles with a cohesion enhancer for robust flexible electrodes. *ACS Appl Nano Mater*, 5:6708–6716.

    https://doi.org/10.1021/acsanm.2c00742

12. Lin Z, Jiang T, Shang J, 2022, The emerging technology of biohybrid micro-robots: A review. *Biodes Manuf*, 5:107–132.

    https://doi.org/10.1007/s42242-021-00135-6

13. Adewole DO, Struzyna LA, Burrell JC, *et al.*, 2021, Development of optically controlled "living electrodes" with long-projecting axon tracts for a synaptic brain-machine interface. *Sci Adv*, 7: eaay5347.

    https://doi.org/10.1126/sciadv.aay5347

14. Steinmetz NA, Aydin C, Lebedeva A, *et al.*, 2021, Neuropixels 2.0: A miniaturized high-density probe for stable, long-term brain recordings. *Science*, 372: eabf4588.

    https://doi.org/10.1126/science.abf4588

15. Guo H, Wei Q, Wu Y, *et al.*, 2023, Enhanced nitrate removal from groundwater using a conductive spacer in flow-electrode capacitive deionization. *Chin Chem Lett,* 109325.

    https://doi.org/10.1016/j.cclet.2023.109325

16. Zhao ET, Hull JM, Mintz Hemed N, *et al.*, 2023, A CMOS-based highly scalable flexible neural electrode interface. *Sci Adv*, 9: eadf9524.

    https://doi.org/10.1126/sciadv.adf9524

17. Wang Z, Bai H, Yu W, *et al.*, 2022, Flexible bioelectronic device fabricated by conductive polymer-based living material. *Sci Adv*, 8: eabo1458.

    https://doi.org/10.1126/sciadv.abo1458

18. Larson NM, Mueller J, Chortos A, *et al.*, 2023, Rotational multimaterial printing of filaments with subvoxel control. *Nature*, 613:682–688.

    https://doi.org/10.1038/s41586-022-05490-7

19. Zeng C, Faaborg MW, Sherif A, *et al.*, 2022, 3D-printed machines that manipulate microscopic objects using capillary forces. *Nature*, 611:68–73.

    https://doi.org/10.1038/s41586-022-05234-7

20. Sanders SN, Schloemer TH, Gangishetty MK, *et al.*, 2022, Triplet fusion upconversion nanocapsules for volumetric 3D printing. *Nature*, 604:474–478.

    https://doi.org/10.1038/s41586-022-04485-8

21. Regehly M, Garmshausen Y, Reuter M, *et al.*, 2020, Xolography for linear volumetric 3D printing. *Nature*, 588:620–624.

    https://doi.org/10.1038/s41586-020-3029-7

22. Schmidt C, 2021, The rise of the assembloid. *Nature*, 597: S22–S23.

https://doi.org/10.1038/d41586-021-02628-x

23. Lawlor KT, Vanslambrouck JM, Higgins JW, *et al.*, 2021, Cellular extrusion bioprinting improves kidney organoid reproducibility and conformation. *Nat Mater*, 20:260–271.

    https://doi.org/10.1038/s41563-020-00853-9

24. Yi HG, Jeong YH, Kim Y, *et al.*, 2019, A bioprinted human-glioblastoma-on-a-chip for the identification of patient-specific responses to chemoradiotherapy. *Nat Biomed Eng*, 3:509–519.

    https://doi.org/10.1038/s41551-019-0363-x

25. Wang J, Lu T, Yang M, *et al.*, 2019, Hydrogel 3D printing with the capacitor edge effect. *Sci Adv*, 5: eaau8769.

    https://doi.org/10.1126/sciadv.aau8769

26. Browne MP, Mills A, 2018, Determining the importance of the electrode support and fabrication method during the initial screening process of an active catalyst for the oxygen evolution reaction. *J Mater Chem A*, 6:14162–14169.

    https://doi.org/10.1039/C8TA02908C

27. Benck JD, Pinaud BA, Gorlin Y, *et al.*, 2014, Substrate selection for fundamental studies of electrocatalysts and photoelectrodes: Inert potential windows in acidic, neutral, and basic electrolyte. *PLoS One*, 9: e107942.

    https://doi.org/10.1371/journal.pone.0107942

28. Song Y, Tay RY, Li J, *et al.*, 2023, 3D-printed epifluidic electronic skin for machine learning-powered multimodal health surveillance. *Sci Adv*, 9: eadi6492.

    https://doi.org/10.1126/sciadv.adi6492

29. Zeng L, Ling S, Du D, *et al.*, 2023, Direct ink writing 3D printing for high-performance electrochemical energy storage devices: A minireview. *Adv Sci* (*Weinh*), 10:2303716.

    https://doi.org/10.1002/advs.202303716

30. Huang H, Liao L, Lin Z, *et al.*, 2023, Direct ink writing of pickering emulsions generates ultralight conducting polymer foams with hierarchical structure and multifunctionality. *Small*, 19:2301493.

    https://doi.org/10.1002/smll.202301493

31. Kotlarz M, Ferreira AM, Gentile P, *et al.*, 2022, Droplet-based bioprinting enables the fabrication of cell-hydrogel-microfibre composite tissue precursors. *Biodes Manuf*, 5:512–528.

    https://doi.org/10.1007/s42242-022-00192-5

32. Lee J, So H, 2023, 3D-printing-assisted flexible pressure sensor with a concentric circle pattern and high sensitivity for health monitoring. *Microsyst Nanoeng*, 9:44.

    https://doi.org/10.1038/s41378-023-00509-z

33. Foster CW, Down MP, Zhang Y, *et al.*, 2017, 3D printed graphene based energy storage devices. *Sci Rep*, 7:42233.

    https://doi.org/10.1038/srep42233

34. Parra-Cabrera C, Achille C, Kuhn S, *et al.*, 2018, 3D printing in chemical engineering and catalytic technology: Structured catalysts, mixers and reactors. *Chem Soc Rev*, 47:209–230.

    https://doi.org/10.1039/C7CS00631D

35. Browne MP, Redondo E, Pumera M, 2020, 3D printing for electrochemical energy applications. *Chem Rev*, 120:2783–2810.

    https://doi.org/10.1021/acs.chemrev.9b00783

36. Tanzi MC, Farè S, Candiani G, 2019, Manufacturing technologies. In: Tanzi MC, Farè S, Candiani G, editors. Foundations of Biomaterials Engineering. Ch. 3. Cambridge: Academic Press. p. 137–196.

    https://doi.org/10.1016/B978-0-08-101034-1.00003-7

37. He Q, Wang Z, Wang Y, *et al.*, 2021, Electrospun liquid crystal elastomer microfiber actuator. *Sci Robot*, 6: eabi9704.

    https://doi.org/10.1126/scirobotics.abi9704

38. Cao F, Guo S, Ma H, *et al.*, 2011, Nickel oxide microfibers immobilized onto electrode by electrospinning and calcination for nonenzymatic glucose sensor and effect of calcination temperature on the performance. *Biosens Bioelectron*, 26:2756–2760.

    https://doi.org/10.1016/j.bios.2010.10.013

39. Wang X, Xiang H, Song C, *et al.*, 2020, Highly efficient transparent air filter prepared by collecting-electrode-free bipolar electrospinning apparatus. *J Hazard Mater*, 385:121535.

    https://doi.org/10.1016/j.jhazmat.2019.121535

40. Kim C, An K, Kang M, *et al.*, 2022, Facile fabrication of flexible metal grid transparent electrode using inkjet-printed dot array as sacrificial layer. *Sci Rep*, 12:1572.

    https://doi.org/10.1038/s41598-022-05312-w

41. Wei Z, Chen H, Yan K, *et al.*, 2014. Inkjet printing and instant chemical transformation of a CH3NH3PbI3/nanocarbon electrode and interface for planar perovskite solar cells. *Angew Chem Int Ed Engl*, 53:13239–13243.

    https://doi.org/10.1002/anie.201408638

42. Liu Z, Baluchová S, Brocken B, *et al.*, 2023, Inkjet printing-manufactured boron-doped diamond chip electrodes for electrochemical sensing purposes. *ACS Appl Mater Interfaces*, 15:39915–39925.

    https://doi.org/10.1021/acsami.3c04824

43. Yin J, Zhao D, Liu J, 2019, Trends on physical understanding of bioink printability. *Biodes Manuf*, 2:50–54.

    https://doi.org/10.1007/s42242-019-00033-y

44. Chen X, Sun M, Jaber F, *et al.*, 2023, A flexible wearable self-supporting hybrid supercapacitor device based on hierarchical nickel cobalt sulfide@C electrode. *Sci Rep*,

13:15555.

https://doi.org/10.1038/s41598-023-42278-9

45. Xu Y, Lin Z, Wei W, *et al.*, 2022, Recent progress of electrode materials for flexible perovskite solar cells. *Nanomicro Lett*, 14:117.

https://doi.org/10.1007/s40820-022-00859-9

46. Cabrera L, Sadle C, Purcell E, 2019, Neuroethical considerations of high-density electrode arrays. *Nat Biomed Eng*, 3:586–589.

https://doi.org/10.1038/s41551-019-0407-2

47. Bennett C, Álvarez-Ciara A, Franklin M, *et al.*, 2021, The complement cascade at the Utah microelectrode-tissue interface. *Biomaterials*, 268:120583.

https://doi.org/10.1016/j.biomaterials.2020.120583

48. Soscia DA, Lam D, Tooker AC, *et al.*, 2020, A flexible 3-dimensional microelectrode array for *in vitro* brain models. *Lab Chip*, 20:901–911.

https://doi.org/10.1039/C9LC01148J

49. Conway CR, Olin BD, Aaronson ST, *et al.*, 2021, A prospective, multi-center randomized, controlled, blinded trial of vagus nerve stimulation for difficult to treat depression: A novel design for a novel treatment. *Brain Stimul*, 14:1666.

https://doi.org/10.1016/j.brs.2021.10.247

50. Frederick RA, Meliane IY, Joshi-Imre A, *et al.*, 2020, Activated iridium oxide film (AIROF) electrodes for neural tissue stimulation. *J Neural Eng*, 17:056001.

https://doi.org/10.1088/1741-2552/abb9bf

51. Musk E, Neuralink, 2019, An integrated brain-machine interface platform with thousands of channels. *J Med Internet Res*, 21: e16194.

https://doi.org/10.2196/16194

52. Hui Y, Yao Y, Qian Q, *et al.*, 2022, Three-dimensional printing of soft hydrogel electronics. *Nat Electron*, 5:893–903.

https://doi.org/10.1038/s41928-022-00887-8

53. Ma S, Dahiya AS, Dahiya R, 2023, Out-of-plane electronics on flexible substrates using inorganic nanowires grown on high-aspect-ratio printed gold micropillars. *Adv Mater*, 35: e2210711.

https://doi.org/10.1002/adma.202210711

54. Saleh MS, Ritchie SM, Nicholas MA, *et al.*, 2022, CMU array: A 3D nanoprinted, fully customizable high-density microelectrode array platform. *Sci Adv*, 8: eabj4853.

https://doi.org/10.1126/sciadv.abj4853

55. Brown MA, Zappitelli KM, Singh L, *et al.*, 2023, Direct laser writing of 3D electrodes on flexible substrates. *Nat Commun*, 14:3610.

https://doi.org/10.1038/s41467-023-39152-7

56. Kamyshny A, Magdassi S, 2019, Conductive nanomaterials for 2D and 3D printed flexible electronics. *Chem Soc Rev*, 48:1712–1740.

https://doi.org/10.1039/c8cs00738a

57. Nayak L, Mohanty S, Nayak SK, *et al.*, 2019, A review on inkjet printing of nanoparticle inks for flexible electronics. *J Mater Chem C*, 7:8771–8795.

https://doi.org/10.1039/C9TC01630A

58. Fernandes IJ, Aroche AF, Schuck A, *et al.*, 2020, Silver nanoparticle conductive inks: Synthesis, characterization, and fabrication of inkjet-printed flexible electrodes. *Sci Rep*, 10:8878.

https://doi.org/10.1038/s41598-020-65698-3

59. Rahman MK, Lee JS, Kwon KS, 2023, Fine conductive line printing of high viscosity CuO ink using near field electrospinning (NFES). *Sci Rep*, 13:17668.

https://doi.org/10.1038/s41598-023-45083-6

60. Han E, Pan Y, Li L, *et al.*, 2023, Bisphenol a detection based on nano gold-doped molecular imprinting electrochemical sensor with enhanced sensitivity. *Food Chem*, 426:136608.

https://doi.org/10.1016/j.foodchem.2023.136608

61. Sadeghi M, Shabani-Nooshabadi M, 2022, Use of a nanoporous gold film electrode modified with chitosan/polypyrrole for electrochemical determination of metronidazole in the presence of acetaminophen. *Chemosphere*, 307:135722.

https://doi.org/10.1016/j.chemosphere.2022.135722

62. Tuleushova N, Amanova A, Abdellah I, *et al.*, 2023, Radiolysis-assisted direct growth of gold-based electrocatalysts for glycerol oxidation. *Nanomaterials* (*Basel*), 13:1713.

https://doi.org/10.3390/nano13111713

63. Ma B, Xu C, Chi J, *et al.*, 2019, A versatile approach for direct patterning of liquid metal using magnetic field. *Adv Funct Mater*, 29:1901370.

https://doi.org/10.1002/adfm.201901370

64. Neumann TV, Dickey MD, 2020, Liquid metal direct write and 3D printing: A review. *Adv Mater Technol*, 5:2000070.

https://doi.org/10.1002/admt.202000070

65. Saborio MG, Cai S, Tang J, *et al.*, 2020, Liquid metal droplet and graphene co-fillers for electrically conductive flexible composites. *Small*, 16: e1903753.

https://doi.org/10.1002/smll.201903753

66. Dickey MD, 2017, Stretchable and soft electronics using liquid metals. *Adv Mater*, 29:1606425.

https://doi.org/10.1002/adma.201606425

67. Wu Q, Zhu F, Wu Z, *et al.*, 2022, Suspension printing of liquid metal in yield-stress fluid for resilient 3D constructs with electromagnetic functions. *Npj Flex Electron*, 6:50.

https://doi.org/10.1038/s41528-022-00184-6

68. Lee W, Kim H, Kang I, *et al.*, 2022, Universal assembly of liquid metal particles in polymers enables elastic printed circuit board. *Science*, 378:637–641.

https://doi.org/10.1126/science.abo6631

69. An L, Jiang H, de Camargo Branco D, *et al.*, 2022, Self-packaged high-resolution liquid metal nano-patterns. *Matter*, 5:1016–1030.

https://doi.org/10.1016/j.matt.2022.01.004

70. Parker CJ, Krishnamurthi V, Zuraiqi K, *et al.*, 2023, Synthesis of planet-like liquid metal nanodroplets with promising properties for catalysis. *Adv Funct Mater*, 2304248.

https://doi.org/10.1002/adfm.202304248

71. Sheng A, Khuje S, Yu J, *et al.*, 2022, Copper nanoplates for printing flexible high-temperature conductors. *ACS Appl Nano Mater*, 5:4028–4037.

https://doi.org/10.1021/acsanm.2c00019

72. Wang F, Gosling JH, Trindade GF, *et al.*, 2021, Inter-flake quantum transport of electrons and holes in inkjet-printed graphene devices. *Adv Funct Mater*, 31:2007478.

https://doi.org/10.1002/adfm.202007478

73. E Silva EP, Huang B, Helaehil JV, *et al.*, 2021, *In vivo* study of conductive 3D printed PCL/MWCNTs scaffolds with electrical stimulation for bone tissue engineering. *Biodes Manuf*, 4:190–202.

https://doi.org/10.1007/s42242-020-00116-1

74. Kanoun O, Bouhamed A, Ramalingame R, *et al.*, 2021, Review on conductive polymer/CNTs nanocomposites based flexible and stretchable strain and pressure sensors. *Sensors*, 21:341.

https://doi.org/10.3390/s21020341

75. Shi Z, Meng L, Shi X, *et al.*, 2022, Morphological engineering of sensing materials for flexible pressure sensors and artificial intelligence applications. *Nanomicro Lett*, 14:141.

https://doi.org/10.1007/s40820-022-00874-w

76. Sun X, Wang C, Chi C, *et al.*, 2018, A highly-sensitive flexible tactile sensor array utilizing piezoresistive carbon nanotube-polydimethylsiloxane composite. *J Micromech Microeng*, 28:105011.

https://doi.org/10.1088/1361-6439/aaceb9

77. Zhao T, Li T, Chen L, *et al.*, 2019, Highly sensitive flexible piezoresistive pressure sensor developed using biomimetically textured porous materials. *ACS Appl Mater Interfaces*, 11:29466–29473.

https://doi.org/10.1021/acsami.9b09265

78. Park SJ, Kim J, Chu M, *et al.*, 2018, Flexible piezoresistive pressure sensor using wrinkled carbon nanotube thin films for human physiological signals. *Adv Mater Technol*, 3:1700158.

https://doi.org/10.1002/admt.201700158

79. Jia J, Huang G, Deng J, *et al.*, 2019, Skin-inspired flexible and high-sensitivity pressure sensors based on rGO films with continuous-gradient wrinkles. *Nanoscale*, 11:4258–4266.

https://doi.org/10.1039/C8NR08503J

80. Yu R, Xia T, Wu B, *et al.*, 2020, Highly sensitive flexible piezoresistive sensor with 3D conductive network. *ACS Appl Mater Interfaces*, 12:35291–35299.

https://doi.org/10.1021/acsami.0c09552

81. Jeong WY, Choi HE, Kim KS. Based Nanomaterials as Drug Delivery Carriers. SpringerLink. Available from: https://link.springer.com/chapter/10.1007/978-981-16-4923-3_6#sec7"graphene [Last accessed on 2023 Sep 11].

https://doi.org/10.1007/978-981-16-4923-3_6

82. Manikandan V, Lee NY, 2023, Reduced graphene oxide: Biofabrication and environmental applications. *Chemosphere*, 311:136934.

https://doi.org/10.1016/j.chemosphere.2022.136934

83. Chen Y, Li L, Zhang J, *et al.*, 2023, Tailored ionically conductive graphene oxide-encased metal ions for ultrasensitive cadaverine sensor. *Chin Chem Lett*, 109102.

https://doi.org/10.1016/j.cclet.2023.109102

84. Yang J, Zhang K, Yu J, *et al.*, 2021, Facile fabrication of robust and reusable PDMS supported graphene dry electrodes for wearable electrocardiogram monitoring. *Adv Mater Technol*, 6:2100262.

https://doi.org/10.1002/admt.202100262

85. Qian C, Xiao T, Chen Y, *et al.*, 2022, 3D printed reduced graphene oxide/elastomer resin composite with structural modulated sensitivity for flexible strain sensor. *Adv Eng Mater*, 24:2101068.

https://doi.org/10.1002/adem.202101068

86. Fang Y, Wang C, Liu Z, *et al.*, 2023, 3D printed conductive multiscale nerve guidance conduit with hierarchical fibers for peripheral nerve regeneration. *Adv Sci* (*Weinh*), 10: e2205744.

https://doi.org/10.1002/advs.202205744

87. Su T, Wang Y, Zhu Q, *et al.*, 2023, Multiple conductive network for KTi2(PO4)3 anode based on MXene as a binder for high-performance potassium storage. *Chin Chem Lett*, 109191.

https://doi.org/10.1016/j.cclet.2023.109191

88. Wang F, Yang C, Duan C, *et al.*, 2014, An organ-like titanium carbide material (MXene) with multilayer structure encapsulating hemoglobin for a mediator-free biosensor. *J Electrochem Soc*, 162: B16.

https://doi.org/10.1149/2.0371501jes

89. Amara U, Rashid S, Mahmood K, *et al.*, 2022, Insight into prognostics, diagnostics, and management strategies for SARS CoV-2. *RSC Adv*, 12:8059–8094.

https://doi.org/10.1039/D1RA07988C

90. Dos Santos CC, Lucena GN, Pinto GC, *et al.*, 2021, Advances and current challenges in non-invasive wearable sensors and wearable biosensors-a mini-review. *Med Devices Sens*, 4: e10130.

https://doi.org/10.1002/mds3.10130

91. Wang G, Park JM, Kang T, *et al.*, 2023, Anion storage of MXenes. *Small Methods*, 7: e2201440.

https://doi.org/10.1002/smtd.202201440

92. Elbadawi M, Ong JJ, Pollard TD, *et al.*, 2021, Additive manufacturable materials for electrochemical biosensor electrodes. *Adv Funct Mater*, 31:2006407.

https://doi.org/10.1002/adfm.202006407

93. Chen L, Eriksson A, Weström S, *et al.*, 2022, Ultra-sensitive monitoring of leukemia patients using superRCA mutation detection assays. *Nat Commun*, 13:4033.

https://doi.org/10.1038/s41467-022-31397-y

94. Cui T, Qiao Y, Li D, *et al.*, 2023, Multifunctional, breathable MXene-PU mesh electronic skin for wearable intelligent 12-lead ECG monitoring system. *Chem Eng J*, 455:140690.

https://doi.org/10.1016/j.cej.2022.140690

95. Li L, Meng J, Bao X, *et al.*, 2023, Direct-ink-write 3D printing of programmable micro-supercapacitors from MXene-regulating conducting polymer inks. *Adv Energy Mater*, 13:2203683.

https://doi.org/10.1002/aenm.202203683

96. Bubniene US, Ratautaite V, Ramanavicius A, *et al.*, 2022, Conducting polymers for the design of tactile sensors. *Polymers* (*Basel*), 14:2984.

https://doi.org/10.3390/polym14152984

97. Gaikar PS, Kadu KS, Tehare KK, *et al.*, 2022, Recent developments in polypyrrole/manganese oxide-based nanocomposites for thin film electrodes in supercapacitors: A minireview. *Nanoscale Adv*, 4:5245–5252.

https://doi.org/10.1039/d2na00654e

98. Chu X, Chen G, Xiao X, *et al.*, 2021, Air-stable conductive polymer ink for printed wearable micro-supercapacitors. *Small*, 17: e2100956.

https://doi.org/10.1002/smll.202100956

99. Gonzalez G, Nelson AC, Holman AR, *et al.*, 2023, Conductive electrospun polymer improves stem cell-derived cardiomyocyte function and maturation. *Biomaterials*, 302:122363.

https://doi.org/10.1016/j.biomaterials.2023.122363

100. Lim T, Kim M, Akbarian A, *et al.*, 2022, Conductive polymer enabled biostable liquid metal electrodes for bioelectronic applications. *Adv Healthc Mater*, 11: e2102382.

https://doi.org/10.1002/adhm.202102382

101. Tseng CP, Liu F, Zhang X, *et al.*, 2022, Solution-deposited and patternable conductive polymer thin-film electrodes for microbial bioelectronics. *Adv Mater*, 34: e2109442.

https://doi.org/10.1002/adma.202109442

102. Kayser LV, Lipomi DJ, 2019, Stretchable conductive polymers and composites based on PEDOT and PEDOT:PSS. *Adv Mater*, 31: e1806133.

https://doi.org/10.1002/adma.201806133

103. O'Neill SJ, Huang Z, Ahmed MH, *et al.*, 2023, Tissue-mimetic supramolecular polymer networks for bioelectronics. *Adv Mater*, 35: e2207634.

https://doi.org/10.1002/adma.202207634

104. Yang G, Zhang YM, Cai Y, *et al.*, 2020, Advances in nanomaterials for electrochromic devices. *Chem Soc Rev*, 49:8687–8720.

https://doi.org/10.1039/D0CS00317D

105. Li XG, Wang HY, Huang MR, 2007, Synthesis, film-forming, and electronic properties of o-phenylenediamine copolymers displaying an uncommon tricolor. *Macromolecules*, 40:1489–1496.

https://doi.org/10.1021/ma062463g

106. Huang X, Chen J, Xie H, *et al.*, 2022, Inkjet printing of 2D polyaniline for fabricating flexible and patterned electrochromic devices. *Sci China Mater*, 65:2217–2226.

https://doi.org/10.1007/s40843-022-2037-4

107. Shirakawa H, 2001, The discovery of polyacetylene film: The dawning of an era of conducting polymers (nobel lecture). *Angew Chem Int Ed Engl*, 40:2574–2580.

https://doi.org/10.1002/1521-3773(20010716)40::14<2574::AID-ANIE2574>3.0.CO;2-N

108. Luppi BT, Muralidharan AV, Ostermann N, *et al.*, 2022, Redox-active heteroatom-functionalized polyacetylenes. *Angew Chem Int Ed Engl*, 61: e202114586.

https://doi.org/10.1002/anie.202114586

109. Miao Z, Gonsales SD, Ehm C, *et al.*, 2021, Cyclic polyacetylene. *Nat Chem*, 13:792–799.

https://doi.org/10.1038/s41557-021-00713-2

110. Yang J, Cui N, Han D, *et al.*, 2022, A simple strategy for constructing hierarchical composite electrodes of PPy-posttreated 3D-printed carbon aerogel with ultrahigh areal capacitance over 8000 mF cm-2. *Adv Mater Technol*, 7:2101325.

https://doi.org/10.1002/admt.202101325

111. Li Q, Tang R, Zhou H, *et al*., 2023, A high-performance and flexible electrode film based on bacterial cellulose/polypyrrole/nitrogen-doped graphene for supercapacitors. *Carbohydr Polym*, 311:120754.

https://doi.org/10.1016/j.carbpol.2023.120754

112. Shi X, Sun L, Li X, *et al*., 2022, High-performance flexible supercapacitor enabled by polypyrrole-coated NiCoP@CNT electrode for wearable devices. *J Colloid Interface Sci*, 606:135–147.

https://doi.org/10.1016/j.jcis.2021.08.016

113. Zotti G, Vercelli B, Berlin A, 2008, Monolayers and multilayers of conjugated polymers as nanosized electronic components. *Acc Chem Res*, 41:1098–1109.

https://doi.org/10.1021/ar8000102

114. Ren SB, Ma W, Zhang C, *et al*., 2020, Exploiting polythiophenyl-triazine-based conjugated microporous polymer with superior lithium-storage performance. *ChemSusChem*, 13:2295–2302.

https://doi.org/10.1002/cssc.202000200

115. Memon MA, Bai W, Sun J, *et al*., 2016, Conjunction of conducting polymer nanostructures with macroporous structured graphene thin films for high-performance flexible supercapacitors. *ACS Appl Mater Interfaces*, 8:11711–11719.

https://doi.org/10.1021/acsami.6b01879

116. Liu Y, Li J, Song S, *et al*., 2020, Morphing electronics enable neuromodulation in growing tissue. *Nat Biotechnol*, 38:1031–1036.

https://doi.org/10.1038/s41587-020-0495-2

117. Fan X, Nie W, Tsai H, *et al*., 2019, PEDOT:PSS for flexible and stretchable electronics: Modifications, strategies, and applications. *Adv Sci* (*Weinh*), 6:1900813.

https://doi.org/10.1002/advs.201900813

118. Lipomi DJ, Vosgueritchian M, Tee BC, *et al*., 2011, Skin-like pressure and strain sensors based on transparent elastic films of carbon nanotubes. *Nat Nanotechnol*, 6:788–792.

https://doi.org/10.1038/nnano.2011.184

119. Nurazizah ES, Aprilia A, Risdiana R, *et al*., 2023, Different roles between PEDOT:PSS as counter electrode and PEDOT:Carrageenan as electrolyte in dye-sensitized solar cell applications: A systematic literature review. *Polymers* (*Basel*), 15:2725.

https://doi.org/10.3390/polym15122725

120. Sun Z, He Y, Xiong B, *et al*., 2021, Performance-enhancing approaches for PEDOT:PSS-Si hybrid solar cells. *Angew Chem Int Ed Engl*, 60:5036–5055.

https://doi.org/10.1002/anie.201910629

121. Yuk H, Lu B, Lin S, *et al*., 2020, 3D printing of conducting polymers. *Nat Commun*, 11:1604.

https://doi.org/10.1038/s41467-020-15316-7

122. Tomaskovic-Crook E, Zhang P, Ahtiainen A, *et al*., 2019, Human neural tissues from neural stem cells using conductive biogel and printed polymer microelectrode arrays for 3D electrical stimulation. *Adv Healthc Mater*, 8: e1900425.

https://doi.org/10.1002/adhm.201900425

123. Kappen J, Skorupa M, Krukiewicz K, 2022, Conducting polymers as versatile tools for the electrochemical detection of cancer biomarkers. *Biosensors* (*Basel*), 13:31.

https://doi.org/10.3390/bios13010031

124. Yuk H, Lu B, Zhao X, 2019, Hydrogel bioelectronics. *Chem Soc Rev*, 48:1642–1667.

https://doi.org/10.1039/C8CS00595H

125. Xie X, Xu Z, Yu X, *et al*., 2023, Liquid-in-liquid printing of 3D and mechanically tunable conductive hydrogels. *Nat Commun*, 14:4289.

https://doi.org/10.1038/s41467-023-40004-7

126. Zhou T, Yuk H, Hu F, *et al*., 2023, 3D printable high-performance conducting polymer hydrogel for all-hydrogel bioelectronic interfaces. *Nat Mater*, 22:895–902.

https://doi.org/10.1038/s41563-023-01569-2

127. Wong J, Gong AT, Defnet PA, *et al*., 2019, 3D Printing ionogel auxetic frameworks for stretchable sensors. *Adv Mater Technol*, 4:1900452.

https://doi.org/10.1002/admt.201900452

128. Zhou LY, Fu J, He Y, 2020, A review of 3D printing technologies for soft polymer materials. *Adv Funct Mater*, 30:2000187.

https://doi.org/10.1002/adfm.202000187

129. Cheng J, Wang R, Sun Z, *et al*., 2022, Centrifugal multimaterial 3D printing of multifunctional heterogeneous objects. *Nat Commun*, 13:7931.

https://doi.org/10.1038/s41467-022-35622-6

130. Ma X, Yu J, Hu Y, *et al*., 2023, Ionic liquid/poly(ionic liquid)-based electrolytes for lithium batteries. *Ind Chem Mater*, 1:39–59.

https://doi.org/10.1039/D2IM00051B

131. Fan X, Liu S, Jia Z, *et al*., 2023, Ionogels: Recent advances in design, material properties and emerging biomedical applications. *Chem Soc Rev*, 52:2497–2527.

https://doi.org/10.1039/D2CS00652A

132. Luo Z, Li W, Yan J, *et al*., 2022, Roles of ionic liquids in adjusting nature of ionogels: A mini review. *Adv Funct Mater*, 32:2203988.

https://doi.org/10.1002/adfm.202203988

133. Huang J, Yu Z, Wu P, 2023, 3D printing of ionogels with complementary functionalities enabled by self-regulating ink. *Adv Sci*, 10:2302891.

https://doi.org/10.1002/advs.202302891

134. Wang M, Lai Z, Jin X, *et al*., 2021, Multifunctional liquid-free ionic conductive elastomer fabricated by liquid metal induced polymerization. *Adv Funct Mater*, 31:2101957.

https://doi.org/10.1002/adfm.202101957

135. Yiming B, Han Y, Han Z, *et al*., 2021, A mechanically robust and versatile liquid-free ionic conductive elastomer. *Adv Mater*, 33: e2006111.

https://doi.org/10.1002/adma.202006111

136. Cao Y, Tan YJ, Li S, *et al*., 2019, Self-healing electronic skins for aquatic environments. *Nat Electron*, 2:75–82.

https://doi.org/10.1038/s41928-019-0206-5

137. Wang M, Zhang P, Shamsi M, *et al*., 2022, Tough and stretchable ionogels by in situ phase separation. *Nat Mater*, 21:359–365.

https://doi.org/10.1038/s41563-022-01195-4

138. Yu Z, Wu P, 2021, Underwater communication and optical camouflage ionogels. *Adv Mater*, 33: e2008479.

https://doi.org/10.1002/adma.202008479

139. Yao Y, Hui Y, Wang Z, *et al*., 2023, Granular ionogel particle inks for 3D printed tough and stretchable ionotronics. *Research* (*Wash D C*), 6:0104.

https://doi.org/10.34133/research.0104

140. Zhang M, Yu R, Tao X, *et al*., 2023, Mechanically robust and highly conductive ionogels for soft ionotronics. *Adv Funct Mater*, 33:2208083.

https://doi.org/10.1002/adfm.202208083

141. Xiong X, Chen Y, Wang Z, *et al*., 2023, Polymerizable rotaxane hydrogels for three-dimensional printing fabrication of wearable sensors. *Nat Commun*, 14:1331.

https://doi.org/10.1038/s41467-023-36920-3

142. Xiao J, Gao Y, 2017, The manufacture of 3D printing of medical grade TPU. *Prog Addit Manuf*, 2:117–123.

https://doi.org/10.1007/s40964-017-0023-1

143. Hu X, Chen Y, Xu W, *et al*., 2023, 3D-printed thermoplastic polyurethane electrodes for customizable, flexible lithium-ion batteries with an ultra-long lifetime. *Small*, 19: e2301604.

https://doi.org/10.1002/smll.202301604

Materials Science in Additive Manufacturing

ORIGINAL RESEARCH ARTICLE

Base shape generation and optimization for multi-axis hybrid additive manufacturing

Zhiping Wang[1], Zhen Hong[1], Sihao Deng[2], Yicha Zhang[3]*, and Alain Bernard[1]

[1]Ecole Centrale de Nantes, LS2N, CNRS UMR 6004, Nantes, 44321, France

[2]UTBM - Université de Technologie Belfort-Montbéliard, ICB-PMDM, CNRS UMR 6303, Sevenans, 90400, France

[3]UTBM - Université de Technologie Belfort-Montbéliard, ICB-CO2M, CNRS UMR 6303, Sevenans, 90400, France

Abstract

Hybrid additive manufacturing (HAM) processes combine the advantages of both additive and non-AM processing to achieve an improvement on quality, cost, and a good quality-cost balance. The non-additive manufacturing process is able to build the physical component of a computer-aided design model from zero or an existing relatively simple subvolume, called base shape in this paper. Hence, if the processing start point is an existing subvolume, how to determine an optimal base shape to save printing time, avoid manufacturing constraints and ensure component quality is an open question in the process planning. Nevertheless, this topic has rarely been investigated. Therefore, in this paper, we propose an optimization method using model skeleton-based decomposition and evolutionary computation. A set of generic evaluation criteria are defined for alternative evaluation. We also present two case studies in this paper for validating the proposed method and conclude that sequential HAM processes have a wide application potential.

Keywords: Base shape; Process planning; Hybrid additive manufacturing

***Corresponding author:**
Yicha Zhang
(yicha.zhang@utbm.fr)

Citation: Wang Z, Hong Z, Deng S, Zhang Y, Bernard A, 2023, Base shape generation and optimization for multi-axis hybrid additive manufacturing. *Mater Sci Add Manuf*, 2(4): 2103. https://doi.org/10.36922/msam.2103

Received: October 24, 2023

Accepted: November 13, 2023

1. Introduction

As the process and material development continues to advance, additive manufacturing (AM) emerges as a key technique in functional manufacturing[1]. Its capacity to manufacture parts with complex surface and internal geometries by adding layers of materials without the use of tooling or fixtures enables it to be a promising processing candidate for high-value component fabrication, and the non-linear relationship between its printing cost and the component complexity makes it an attractive avenue for manufacturing parts[2]. In addition, AM also provides freedom to design, offers mass personalization to consumers, removes the need for parts shipping and warehouse storage, and reduces waste and energy consumption[3,4]. However, compared with traditional processing technologies, limitations still exist in additive manufacturing processes, such as poorer dimensional accuracy and surface quality[5,6], limited materials, and relatively long printing time for some applications[7], especially for metallic AM processes. It is not realistic to use AM only for select attributes such as high accuracy and superior performance in fabrication while not considering the feasibility and high-cost problems this technique is tied to. For example, reducing the layer thickness to achieve a better surface quality may extend the printing time. On the contrary, the advantages of traditional manufacturing processes, such as high speed and high quality of finish surface, can greatly compensate for the disadvantages of AM[7]. In light of this, the combination of additive and subtractive manufacturing processes is regarded as a hybrid solution to compensate the limitations of both AM and traditional processes[8], spurring a variety of new applications[9]. The combined approach is now increasingly employed for producing or remanufacturing functional parts[6].

The term "hybrid" has been widely used in many areas of manufacturing[10]. It is used to describe several hybrid techniques: (i) hybrid processes; (ii) hybrid machines, which refer to the machine platform rather than the constituent processes; and (iii) hybrid materials, structures, or functions, combining one or more materials to yield a product with hybrid composition, structure, or function[11,12]. The definition of hybrid additive manufacturing (HAM) was proposed by Sealy *et al.*[10] as follows: "The use of AM with one or more secondary processes or energy sources that are fully coupled can synergistically affect part quality, functionality, and/or process performance." The authors also defined the three key features of HAM: (i) fully coupled processes, (ii) synergy, and (iii) part and/or process improvement. More descriptions and definitions have also been proposed in the literature[9,12,13]. In this paper, we consider HAM as a type of specific hybrid process, where AM is the principle process, and other processes, integrated in one machine with AM or separated as modular processing units, are assistive processes involved in shape formation procedure with AM working in a sequential, parallel, or iterative fashion.

Although the hybridization idea of the two types of processes seems simple, the process of combining them is more difficult than imagined since both of the existing constraints of AM and non-AM (NAM) processes are introduced and couple with each other. Therefore, the process planning for HAM is critical for the implementation of process combination. A few researchers noticed the importance of this and had already conducted a set of investigations as reviewed in Nassehi *et al.*[13]. However, a plethora of problems remain to be resolved, such as the selection of candidate process for combination, manufacturability analysis, processing from zero volume or existing volume, hybrid operation sequence planning, hybrid toolpath planning for AM, and NAM, *etc.* In this paper, we focus on the question of manufacturing from zero or an existing subvolume since this rarely discussed topic is important for the feasibility and efficiency of HAM. Based on the analysis of industrial application needs, we define this problem as the base shape generation and optimization for the process planning in HAM. At present, this problem is handled manually with many uncertainties, but there is no decision support tool to help automatically generating an optimal base shape for a given computer-aided design (CAD) model to be processed by a HAM process in the process planning. To solve this problem, this paper introduces a geometric computational method that automatically generates an optimal base shape, taking into account the processing cost, quality, and manufacturing constraints.

The contents of this paper are organized as follows: Section 2 reviews the related woks; Section 3 introduces the proposed method in detail; Section 4 demonstrates the method with computation examples; and Section 5 concludes the paper with perspectives on future work.

2. Related work

In the domain of manufacturing, the crux of process planning is about how to organize and make a full use of the existing processes and the corresponding machines with appropriate parameters[14]. In AM, there are some differences since the printing planning is usually done for one machine, the AM printer, if post-processing is not considered. The main function of the so-called process planning for AM is actually to transfer a design model, such as a CAD model, into a processing model, called the printing toolpath model, to complete the AM processing chain[15]. Four main planning tasks were defined as the model transformation steps for rapid prototyping, the initial form of AM[16]. Recently, with the rapid development of AM technologies and increased availability of material options, the process planning for AM has become widely explored. Some researchers proposed to include the manufacturability analysis, process selection, model clustering, and printing prediction as additional planning tasks to adapt to the AM evolution[15,17-19] since these tasks are critical for analyzing the feasibility and suitability of using AM before printing[15]. In general, these planning tasks are divided into two main classes: macroplanning and microplanning[19]. Microplanning not only includes the four classical planning tasks, namely, orientation determination[20], support structure design[21], slicing,[22] and toolpath planning[23] but also contains two additional new tasks, namely, part clustering/grouping and nesting, to meet the needs of simultaneous printing for group components[24-26].

In conjunction with the emergence of HAM, more NAM processing operations and machines are introduced in the processing chain. Hence, the process planning contents should be adjusted again. However, the current computer-aided process planning (CAPP) in AM domain is still focusing on the macro- and microplanning tasks as introduced above, but there are not so many systematic researches on CAPP for HAM in the past. HAM has been proposed and investigated for more than two decades. Karunakaran *et al.*[27,28] have conducted intensive research on the HAM process development, through which the concept of HAM processing chain has been implicitly mentioned, but the idea of adopting CAPP for HAM and the main challenges of adopting CAPP in HAM have never been formally discussed in their works. Later, after a research on HAM process development, Liou *et al.*, for the first time, proposed an integrated process planning for their developed multi-axis HAM process[23,29,30]. Kerbrat *et al.*[31] also conducted manufacturability analysis related to CAPP for HAM according to the two-level CAPP concept definition proposed in Zhang and Bernard[15]. Subsequently, Newman *et al.*[32,33] proposed systematic CAPP solutions for HAM process at a relative generic level. More recently, in face of the development of and increasing application demand for HAM processes, the research on CAPP for HAM is booming. A couple of researchers investigated how to connect AM with NAM process with automatic CAPP solutions[34,35]. These works mainly focused on how to decompose a CAD model into two processing sets of subvolumes, called features, for AM and NAM processing modules. They discussed more about the decomposition strategy, feature assignment scheme, and the processing sequence determination. There are also some researchers focusing solely on toolpath generation with consideration of AM or NAM constraints, for example, collisions, to obtain an automatic full HAM processing chain[36,37]. These studies focus more on the micro planning stage, where processing model transformation is the priority. Recently, a CAPP platform at a generic level that enables a more general planning for HAM has been proposed[38]. However, they are still situated in the micro processing chain level even though they added monitoring unit in their CAPP loop. In a very interesting work, Liu *et al.*[39] discussed a very microplanning task for iterative HAM, where the switch moments between the two processing modules need to be analyzed and optimized according to processing constraints, time and cost. Except for full CAPP solution development for HAM, some critical planning tasks in the macro or microstages also attracted research attention since they are important for the processing chain. How to plan for HAM starting from an existing part has also been extensively discussed[32,33], with a particular focus on how to reuse existing parts/legacy products to save cost for HAM process. Researchers applied HAM for remanufacturing existing physical components in adherence to this logic[6,40]. Gradually, the benefits of starting the HAM processing from an existing volume, called base, base plate or substrate, attracted the attention of a group of researchers. Eldakroury *et al.*[41] attempted to use primary shapes, cylinder, and cuboid to approach the initial CAD model's subvolume through a set of simple sequential rules to help process planners identifying optimal candidate substrate. However, they did not analyze the solution space of the substrate, nor applied any optimization tools to enable automatic searching. The results presented in the paper may not be comprehensive, covering only the local optimal candidate substrates. In addition, the word, "substrate," may cause confusion to the NAM processing module's planning. More recently, Chen and Frank[42] proposed a method to optimize the stock size for component families or groups and use the stock as the processing starting point for the following HAM processing. In their method, manufacturing begins with a base plate, where a set of subtractive steps will first create a portion of the design geometry. Next, the additive manufacturing process will be planned to create geometry on the machined base plate in two opposite directions, to minimize support structure, and build height. Finally, a secondary machining process is planned to produce finished surfaces on the additively manufactured near net shape geometry. However, there is no work about how to identify an optimal stock for a given CAD model in their paper. On the other hand, Reichler *et al.*[43] did a similar work, but they tried to extract a subvolume from the initial CAD model as starting base for incremental manufacturing, where AM is applied to add customized features for variant part. However, they did not explain how to obtain an optimal base volume automatically for the start point.

As reviewed above, research addressing the question about HAM processing starts from zero or existing volume is scarce. If the process starts from an existing volume, how to identify an optimal starting volume is a fundamental question to be solved. This study is aimed at filling this knowledge gap. We started from an existing volume and proposed a generic solution to automatically generate an optimal starting volume, called base shape, for HAM processing. The proposed method is expected to meet the needs of different multi-axis HAM processes by adapting related processing constraints as the boundary conditions of optimization. The following section gives a detailed explanation about our method. A CAD model of a relatively complex tree structure is adopted to illustrate each key step in the calculation procedure.

3. Proposed method

HAM processes combine the advantages of additive processing and subtractive processing or other traditional processing such as casting and stamping.

The hybrid processing can start from zero or an existing volume as discussed above. Processing from existing volume can help save material and processing time. The non-additive manufacturing process is able to build the physical component of a CAD model from existing relatively simple shapes, which could be subsections of the physical model, called base shape in this paper. However, how to determine an optimal base shape to save printing time, avoid manufacturing constraints, and ensure component quality is an open question for the process planning and has rarely been investigated. To address it, this paper proposes a model skeleton-based decomposition method to generate alternative base shapes. A set of generic evaluation criteria are defined for alternative evaluation. In this paper, we also present the application of the proposed method, together with cold spraying coupled to computer numerical control machining (as post-processing in a sequential way after printing), for the determination of base shape in a hybrid AM process. Certainly, the proposed method can be adopted for other hybrid AM processes after specific manufacturing constraints are taken into consideration.

3.1. Method overview

The proposed method includes three main steps, as shown in Figure 1:

(i) Voxelize a given CAD model in the format of STL to obtain a voxel model. Then, generate a skeleton, the medial axis, from the voxel model to represent the general topological relationship of the original CAD model. The skeleton allows defining the "material deposition directions," which is used when searching "decomposition" of basic volumes into "subparts."

(ii) Generate the optimal branch set, which has the largest volume of the corresponding volume of the original CAD model. Decompose the skeleton into a set of branches and the CAD model into original subparts using the intersection points on the skeleton. If necessary, remove a set of non-important sub-branches and extract the key branches, but all branches are kept in this research. The optimal branch set is a group of branches which are adjacent, and coplanar, as well as, with the largest volume of the corresponding subparts of the CAD model.

(iii) Generate alternative base shapes based on a set of pre-defined 2D cross-section profiles (primary shapes, *e.g.*, circles and polygons) sweeping along the optimal branch set to generate 3D volumes. Based on the various sizes of selected 2D cross-section profiles, generate numerous base shapes, which are known as "candidate base shapes." Search the "optimal candidate base shape" using evolutionary computational methods. The material use rate is used to obtain the optimal base shape.

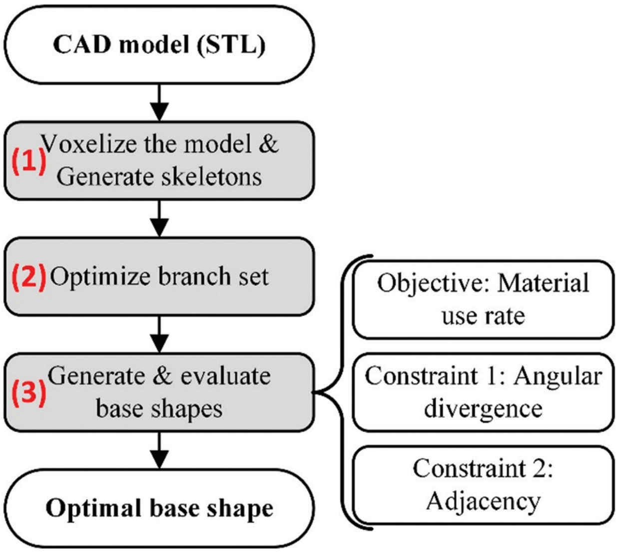

Figure 1. The proposed workflow of base shape generation.

3.2. Method implementation

The implementation details of the above-mentioned three steps entailed in the proposed global method are given below:

3.2.1. Step 1: Voxelization and skeleton generation

For voxelization, the method proposed in the literature[44] was adopted. This method allows efficient conversion of polygonal solid models into voxel format with a maximum resolution of 1000 (1 billion voxels) in <2 min. In this research, the voxelization algorithm was used to convert a solid model obtained from a CAD system in STL format. The voxel size is determined by dividing the maximum dimension of the bounding box of the STL model with a desired resolution. The voxelization process essentially passes rays along the X-axis in a preset order (increments along Y axis first, then along Z axis) and finds their intersections with the facets. The number of intersections for any ray is always even if the STL file is free of errors and the rays completely extend beyond the model on both sides, as shown in Figure 2. The voxelization process essentially passes rays along the X-axis in a preset order (increments along the Y-axis first, then along the Z-axis) to find their intersections with the facets. The process was carried out in a layer-by-layer fashion from the minimum to the maximum Z coordinate of the model, as depicted in Figure 3.

Figure 4 illustrates the examples of CAD models with complex tree shape structure. The tree structure was modeled using a parametric CAD tool called Rhino, a commercial parametric CAD software based on the NURBS mathematical model. To obtain a topology skeleton from a voxel model, we applied to this study a parallel 3D medial surface/axis thinning algorithm proposed in literature[45], which is an efficient 3D parallel thinning algorithm for extracting both the medial surfaces and the medial axes of a 3D object (given as a 3D binary image). Based on this method, the voxel model was processed by the adopted algorithm; the initial skeleton obtained is shown in Figure 4C. However, since the skeleton is generated by connecting the voxel centers, it does not have very smooth surface and the accuracy could be influenced by the voxel resolution. Therefore, the initial skeleton cannot be directly used for generating base shape as post-processing is required. In this research, slightly curved skeleton branches or small bent poly branches were simplified and replaced by straight line segments to facilitate the following base shape generation. The simplified skeleton of the tree structure is shown in Figure 4D.

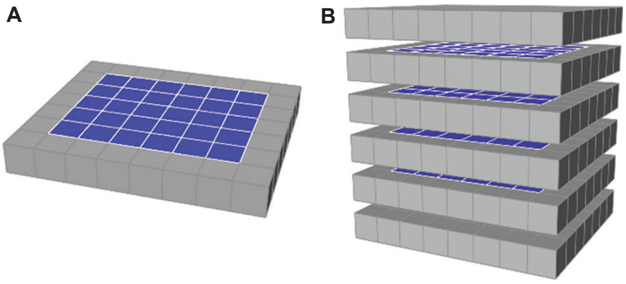

Figure 2. Solid model representation by voxel layers. (A) The selected voxel distribution for a solid model in one layer; (B) 3D voxel configuration for the solid model.

3.2.2. Step 2: Original subpart generation and branch set optimization

The base shape was generated by decomposing the skeleton and then sweeping some simple cross-sections like circles, along the selected branch set. Moreover, the corresponding volume of each branch was used to optimize the candidates; therefore, the model needs to be decomposed as well. The decomposition of original subparts, as shown in Figure 5, was based on the skeleton and CAD model, and the end

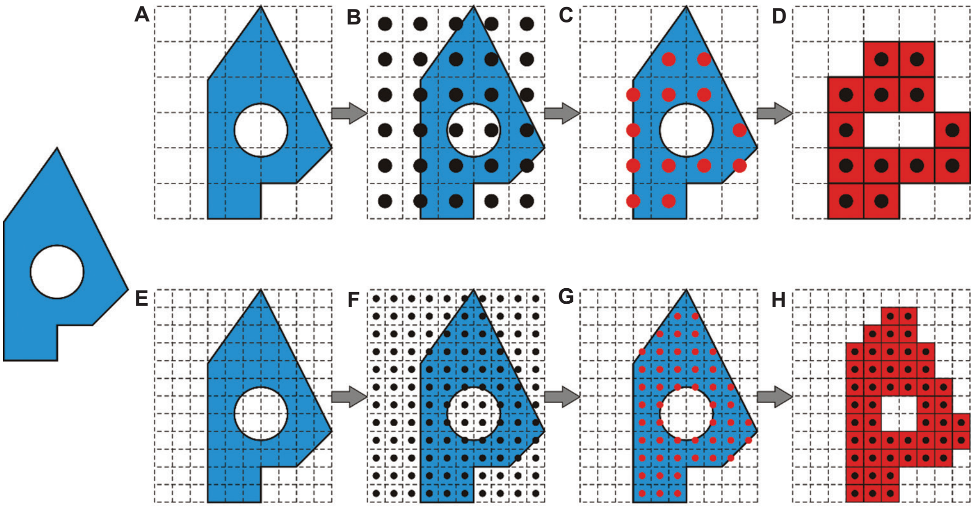

Figure 3. Voxelization by ray intersection for a model with different resolution. (A) Voxel meshing based on a bounding box; (B) center points generation; (C) internal point identification; (D) assembly of identified pixels; and (E-H) voxelization with a higher resolution.

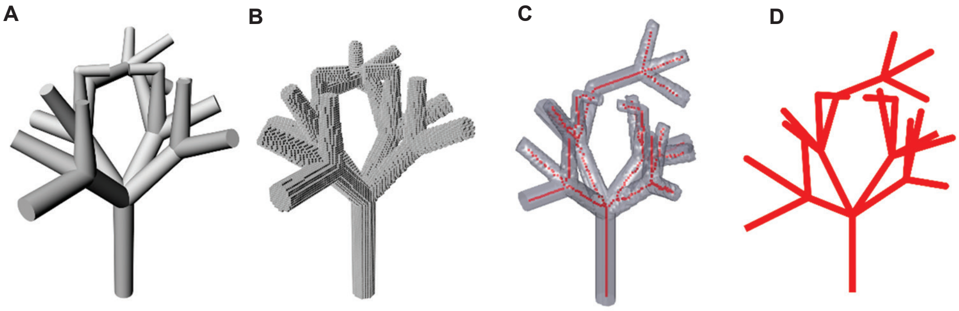

Figure 4. (A) CAD model of a tree structure; (B) a voxelized result; (C) initial generated skeleton; and (D) a post-processed skeleton replaced by straight line segments.

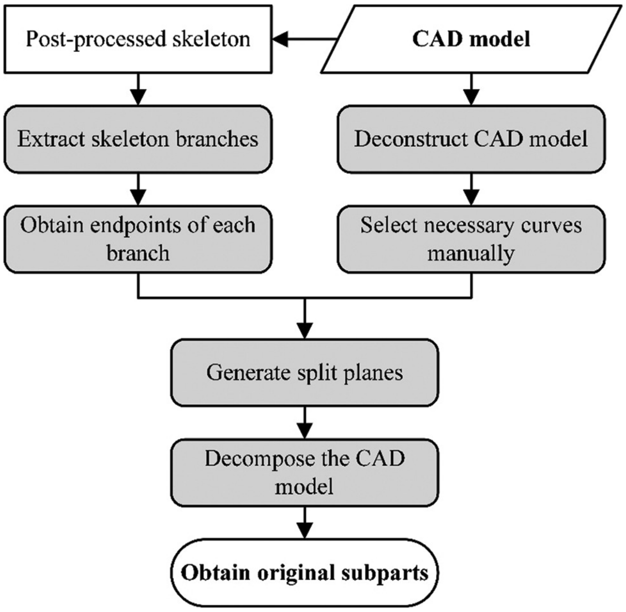

Figure 5. Workflow of the generation of original subparts based on the skeleton.

points of each extracted branch were obtained. Meanwhile, the CAD model was deconstructed in Grasshopper (GH), so the necessary curves could be selected manually in this research. With the branch end points and the points of selected curves, the split planes were determined and moved to the corresponding branch points, and then, the CAD model was decomposed into many original subparts by these split planes.

The tree structure with 25 skeleton branches presented in Figure 4A is taken as an example. The structure was decomposed into 25 original subparts, as illustrated in Figure 6. Figure 6A depicts the whole part which has been decomposed, and a partially enlarged structure was selected to show the generation process of split planes. The split planes were determined by the intersection point in the skeleton and the points manually selected on the surface of the entity (Figure 6C and E). The plane depicted in Figure 6D was obtained by one plugin called *plane fit* in Grasshopper and the planes were generated by three selected points, as shown in Figure 6F. All of these planes were translated through the intersection in the branches of these corresponding subparts. Then, these planes were used to cut the CAD model for the generation of original subparts. The branches of the skeleton and the original subparts were applied to generate and optimize base shapes in the next step.

3.2.3. Step 3: Base shape generation and evaluation

Genetic Algorithm (GA) is a typical evolutionary algorithm, which is a good choice for solving discrete combinatorial optimization problems. It is a stochastic optimization method that mimics natural evolution, whereby individuals in each generation go through the processes of crossover, mutation, and selection[46]. During the search, the branches can be randomly selected to form a combination. Hence, this is a discrete optimization problem since non-connected branches may be selected. In the encoding, if a branch is selected, a digital value, 1, is assigned; otherwise, another value, 0, is assigned. The objective function is the whole volumes of the subparts in a combination, which is randomly generated from the original branches.

$$V_g = \sum_{i=0}^{n} V_i \quad \text{(I)}$$

where V_g is the Boolean union sum of selected subparts, and V_i (i = 1, 2, 3…) is the volume of each subpart in a generated combination. Theoretically, selecting all the branches is the optimal solution, if we do not consider manufacturing constraints. However, to facilitate the manufacturing of the base shape, two generic constraints are set as examples in this research. We assume that the base shape should be a continuum volume, and less radiation of volume segments in different directions would be better for manufacturing since there should be fewer fixtures used and less reorientation required, if machining is applied to manufacture the base shape. A continuum volume also means less manufacturing operation. Hence, in the following subsections, we explain the proposed two constraints or criteria – angular divergence and adjacency – for consideration in the optimization process.

(A) Angular divergence

The first criterion is angular divergence, which is used to describe the coplanarity extent of different branches in a skeleton of a candidate base shape. The coplanarity extent can be calculated using the vectors of skeleton branches. For example, if given two branches, i and j, and their vectors, V_i and V_j, and their cross product V_{ij} is used to form dot product with the vectors of all other remained branches V_k (k = 1, 2, 3…) of the left skeleton. Theoretically, if there are more branches in a candidate base shape, it would be easier to fabricate the base shape and the subsequent AM or NAM processing would also be less challenging since collision detection is simplified and reorientation of the base shape is reduced in the processing. Hence, there is a need to define a coplanarity extent to describe the criterion of angular divergence. However, the size of the cross-sections of the original CAD model should also be paid attention to since branches with big volumes primarily affect the values of the waste material function

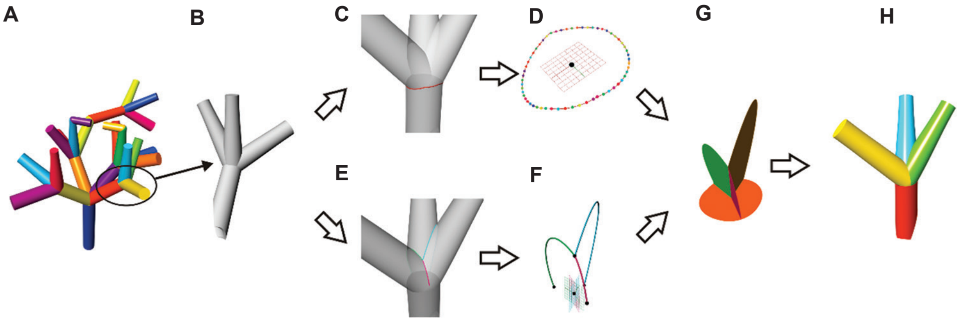

Figure 6. The decomposition process and the results of tree model decomposition. (A) 25 original subparts; (B) a partially enlarged structure; (C and E) intersection curves selected from the CAD model; (D and F) split planes; (G) cut sections; and (H) original subparts.

(to be introduced later below). Hence, we need to use a coefficient of these branch volumes, C_v, to differentiate the impact of each branch in the skeleton. The value of C_v can be assigned empirically or using a ranking scheme, where big branches gain bigger weights. Therefore, the degree of angular divergence can be described by *D,* as shown in Equations II and III.

$$V_{ij} = V_i \times V_j \ (i, j = 1,2,\ldots,n) \quad \text{(II)}$$

$$D = (V_{ij} \times V_k) \times C_v \ (i, j, k = 1,2,\ldots,n) \quad \text{(III)}$$

Hence, the mean of these *D* values can be used as an index value to describe the angular divergence of the skeleton combination of a candidate base shape.

$$\frac{\sum_{k=1}^{m} D_k}{m} (m = n-2, k = 1,2,\ldots,m) \quad \text{(IV)}$$

To simplify method demonstration, we only consider the coplanarity, except the size and volume of each branch. The branches are not only approximately coplanar but also need to connect to each other as discussed above, encapsulating an attribute known as adjacency.

(B) Adjacency

Since the candidate volume is generated using a GA operator to extract a random combination of branches, disconnected branches may occur sometimes. Disconnected branches will generate more than one base shape sections, increasing the complexity for the subsequent AM and NAM processing (more build orientations, assembly interfaces, fixtures, reorientations, *etc.*). Hence, an evaluation criterion called adjacency is proposed. It can be estimated using the number of common knots and the number of branches. If the number of knots and branches meet a formulation, $N_k - N_b \leq 1$, we can say that the branches are adjacent and connected. Skeletons with disconnected branches will be assigned penalty in the evaluation of individuals in the GA.

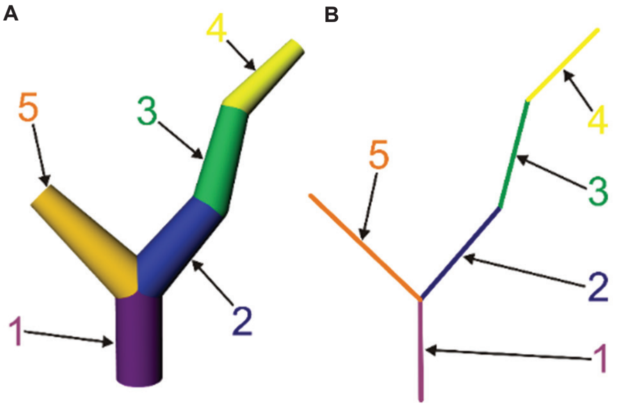

Figure 7. (A and B) A tree model and the position of its branches in a chromosome during encoding.

To illustrate the encoding, we used a simpler tree structure with only five branches, as shown in Figure 7A and B, for explanation. In the encoding, each branch takes a gene position in the chromosome. We used binary numbers to describe whether a branch was selected to generate a sub-skeleton set (already mentioned above). The value 0 (means the branch is not selected) and 1 (means the branch is selected) were used. Hence, a chromosome can be represented by five connected binary codes (Figure 8).

Based on the binary encoding scheme, we can design different GA operators. Figure 8 gives an example of crossover operation, where chromosomes are switched at a selected crossover point. The decoding of representative crossover operation results is shown in Figure 9.

According to the adopted encoding scheme, the chromosome length, indicated by the number of binary values, equals to the number of branches of a structure skeleton. For the tree structure model, the length of chromosome is 25 (Figure 10A). A representative decoding (implemented in a Rhino plugin, GH) with one candidate branch combination of the complex tree model is shown in Figure 10B.

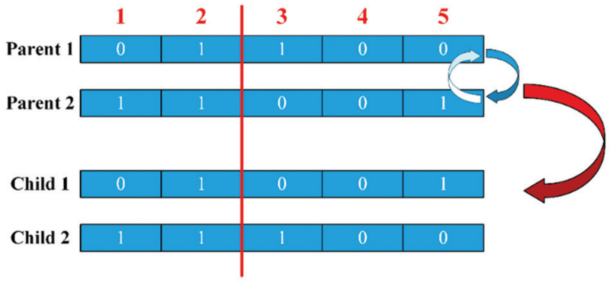

Figure 8. Chromosome and crossover operation.

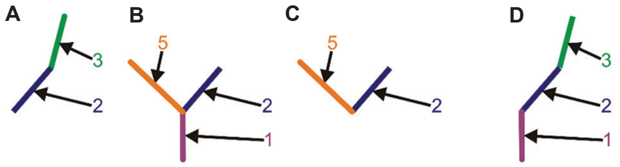

Figure 9. Decoding for the representative genetic algorithm chromosome in Figure 8: (A) Parent 1; (B) Parent 2; (C) Child 1; and (D) Child 2.

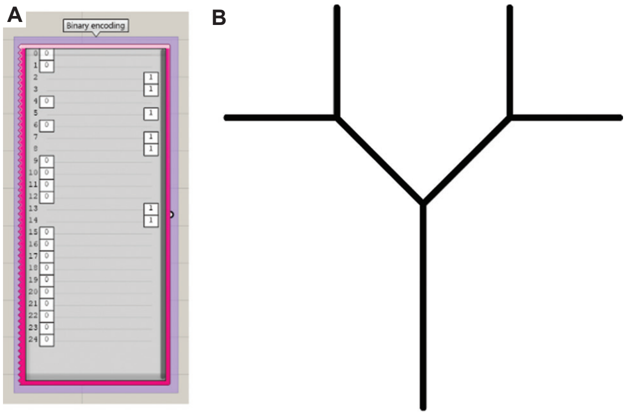

Figure 10. (A) Binary encoding in Galapagos and (B) the corresponding branches of tree structure.

With the defined fitness function and evaluation criteria, the implementation of GA was carried out in a CAD tool plugin called Grasshopper Galapagos editor. Table 1 shows the parameters for the initialization of algorithm. In detail, max. stagnant is 50, population is 50, initial boost is double, maintain is 5%, and inbreeding is 75%.

Once obtained, the equivalent cross-section profiles were used as reference to sweep along the corresponding optimal branch set to generate 3D volumes (Figure 11). The size and shape of profiles determined the final volume and the shape of the base shape. For this tree model, a base shape composed by a set of cylinder branches with different diameters was defined.

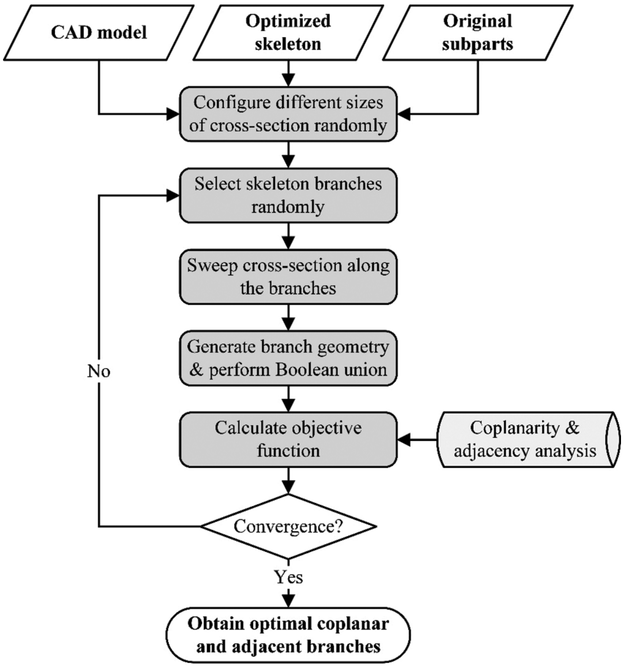

Figure 11. The workflow of base shape generation based on the coplanar and adjacent constraints.

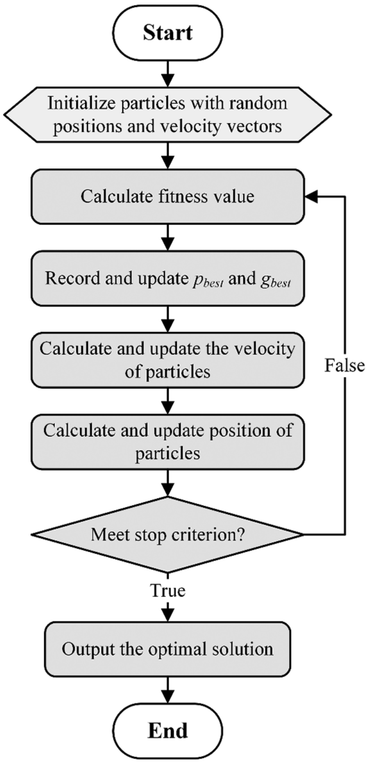

Figure 12. The basic steps of the Particle Swarm Optimization algorithm.

Since the basic GA is very slow for iterations, based on the results of coplanar branches, Particle Swarm Optimization algorithm (PSO)[47] was adopted to optimize the size of cross-sections. The flow chart of PSO is illustrated in Figure 12. This step is intended to evaluate and search for the optimal base shape. Since the material waste rate determined by volume could directly impact the AM and NAM processing time, we only focused on the volume of material in this research. To facilitate the searching process, an objective function concerning waste material volume is defined in Equation V:

$$\min: F_r = \omega_1 (f_i - f_p \cap f_i) + \omega_2 (f_p - f_p \cap fi) \tag{V}$$

where F_r is the material use rate, fi is the base shape (Figure 13A), and f_p is the volume of the finished part volume. Figure 13B shows the base shape after machining from the casting shown in Figure 13A. Figure 13C shows the subparts which need to be added through AM processing (CS spraying AM module is used as example in this research) to the qualified base shape. ω_1 and ω_2 are the weights assigned to the cost of AM and NAM processing, respectively, in terms of subtractive manufacturing processes and materials. Here, ω_1 and ω_2 are related in an equation, that is, $\omega_1 + \omega_2 = 1$. In this research, the weights were set at 0.95 and 0.05, respectively. This objective function could be directly used as fitness function in the PSO. In this research, we defined two main evaluation criteria for illustration and general application. In industrial application, different specific criteria can be defined according to HAM processing constraints and other objectives related to time, cost, and quality.

4. Case studies

In this section, we use two examples manufactured by a cold spraying-based HAM platform in different complexity levels to demonstrate the proposed method.

4.1. Case study 1

The model described in this case study was derived from a study on cold spraying process[48]. Using this method, the authors built the whole model from zero volume, causing wastage of many materials. After analyzing the CAD model, we learn that a quite large volume can be fabricated by traditional method easily and only very small complex structure, like the four feet, can be fabricated by iterative or sequential AM and NAM processes. Hence, we generated a base shape with an aim to save material and time for this case. The CAD model of this case is shown in Figure 14. It is a reproduction of the example CAD model used in Lynch *et al.*[48].

Based on the CAD model of the bracket, the voxelization and generation of skeleton were operated in accordance with the above-mentioned method in MATLAB, as illustrated in Figure 15A and B. A modified skeleton was adopted to replace the original one. The original subparts can be decided by the branches based on the joint points, similarly with the tree model. The subparts of the bracket are shown in Figure 16.

The selected branch combination after GA calculation is shown in Figure 18A. The following optimization is conducted by the mentioned PSO algorithm with consideration of the above-mentioned constraints and material use rate. The optimization procedure is depicted in Figure 17, which shows that the optimal solution is found after 32 iterations.

To simplify the whole process, circle was used as cross-section in this case study, and ball shapes were used as joints to connect the adjacent branches, as illustrated in

Table 1. Parameters for Genetic Algorithm (GA) in Galapagos editor

Option	Max. stagnant	Population	Initial boost	Maintain (%)	Inbreeding (%)
Description	50	50	2	5	75

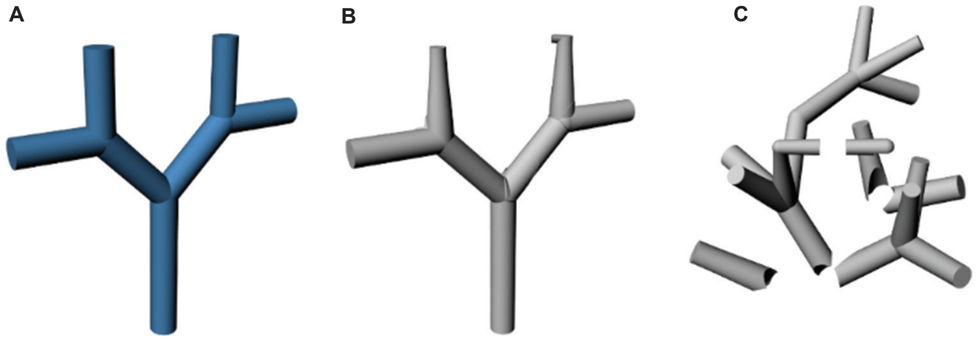

Figure 13. (A) Base shape of the tree structure; (B) qualified base shape after machining; and (C) cold-sprayed subparts.

Figure 18B. Then, a plane cutting and an extrusion cutting operations were performed as post-processing to make the base shape meet the coplanar criterion and approximate to the subpart shape of the original CAD model, as illustrated in Figure 18C. Figure 18D illustrates the subparts, which need to be deposited through the CS AM module onto the optimized base shape. For this case, it is obvious that if the CS deposition can start from the proposed optimal base shape, a lot of materials and much processing time could be saved.

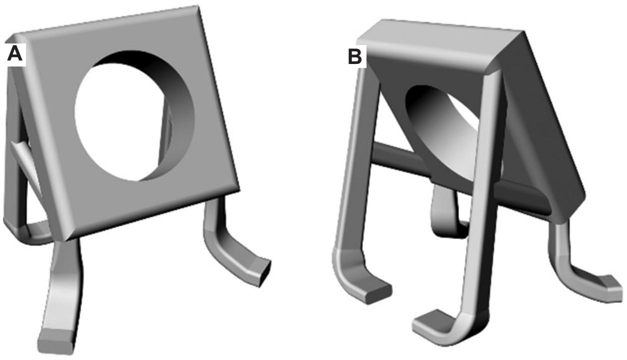

Figure 14. (A and B) Bracket computer-aided design model with different perspectives.

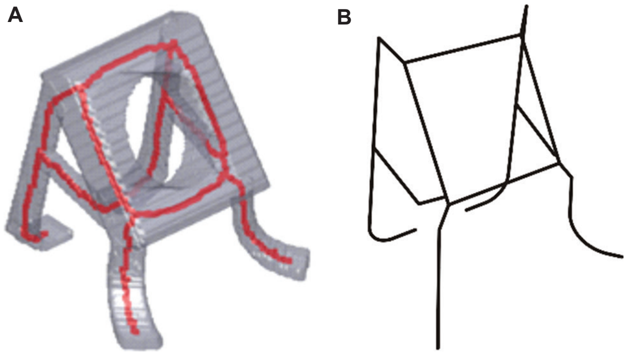

Figure 15. (A) Voxelization and original skeleton of the computer-aided design model and (B) modified skeleton.

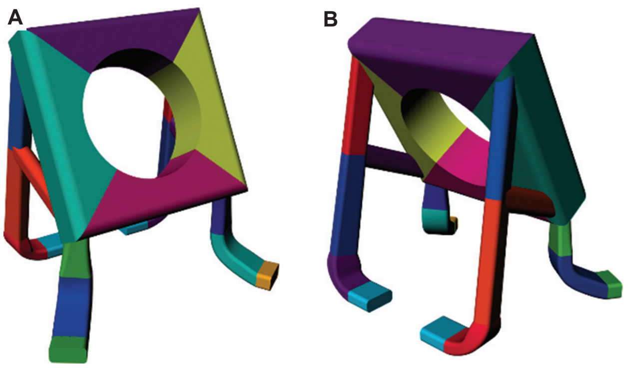

Figure 16. (A and B) Subparts of the bracket.

4.2. Case study 2

The CAD model described in the above case is not so complex that we can even identify the optimal base shape based on our experiences. However, HAM is usually used in complex and high-value manufacturing, through which complex models are often made. In this case, we used a more complex CAD model to demonstrate the

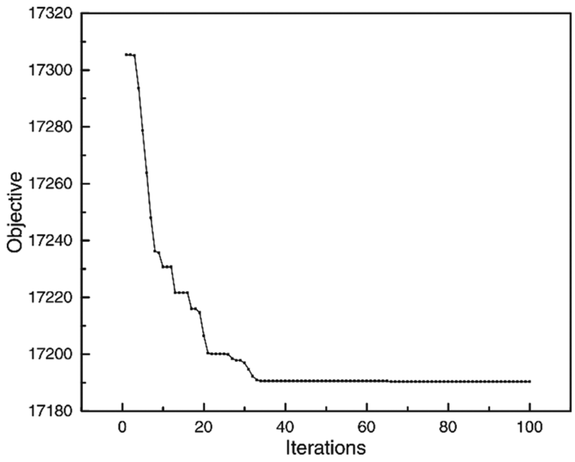

Figure 17. The optimization process of base shape with Particle Swarm Optimization.

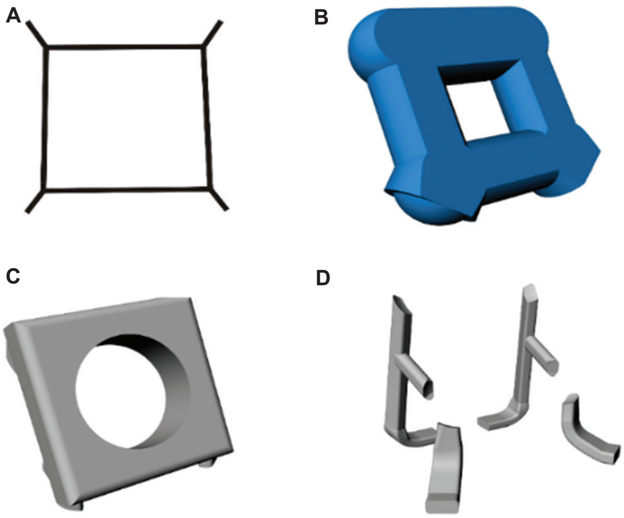

Figure 18. (A) Optimal initial skeleton; (B) optimal base shape; (C) optimal base shape; and (D) remaining subparts for CS AM module.

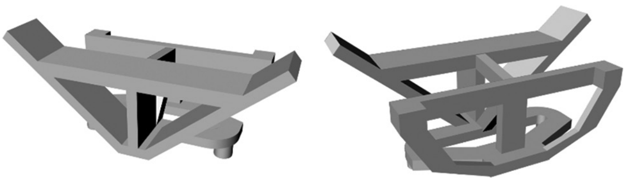

Figure 19. The computer-aided design model of case study 2.

validity and necessity of the proposed method. The model has many features and no obvious bases as well as many radial subvolumes in different directions (Figure 19). Similarly, the CAD model in STL file was voxelized and a coarse skeleton was obtained (Figure 20A). After simplification, the approximate skeleton was generated (Figure 20B).

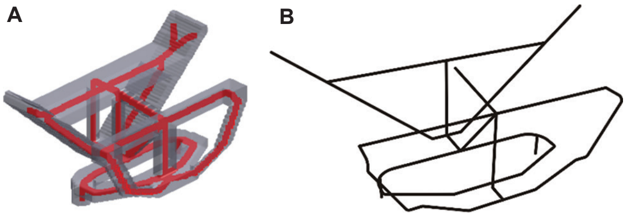

Figure 20. (A) Voxelization and skeleton in MATLAB; (B) modified skeleton.

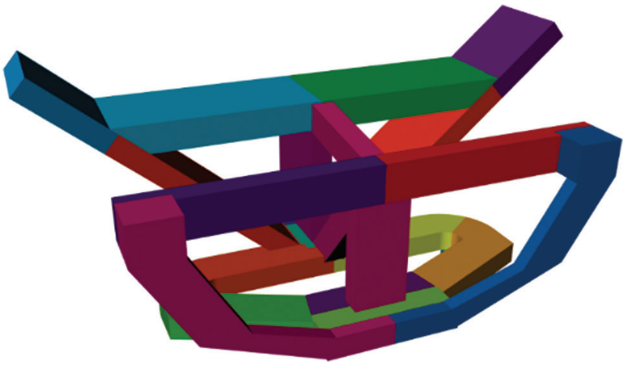

Figure 21. The subparts of case study 2.

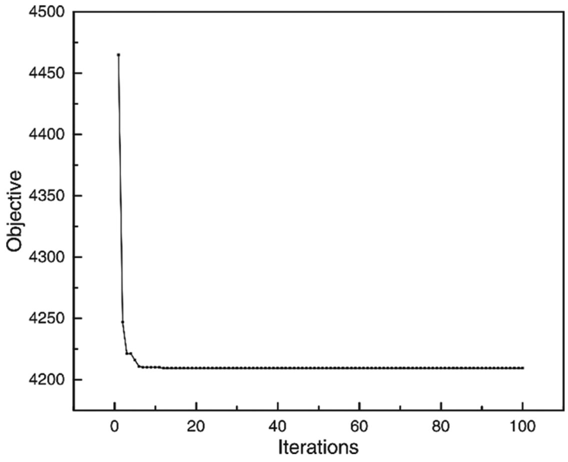

Figure 22. The optimization process of base shape with Particle Swarm Optimization.

In this case, all the branches are important since they have similar volumes. Hence, the subparts of the original CAD model, as shown in Figure 21, were generated using the joint points of branches of the simplified skeleton (only smoothing process applied). The optimization calculation of base shape considers the constraints mentioned above and the material use rate as the objective function is calculated using the PSO algorithm in Silvereye, one plugin of Grasshopper. The result of each iteration was obtained, as shown in Figure 22. It can be found that the convergence occurred at the 7th iteration (Figure 22). The optimization results of case study 2 are presented in Figure 23.

5. Conclusion

In this research, we analyzed a key process planning problem, called base shape generation and optimization, for the CAPP of HAM. This problem is important for the industrial application, although it has rarely been investigated. For sequential HAM processes, where there is no iterative AM and NAM processing, the determination of an optimal base shape directly affects the final manufacturing complexity, time, cost, and quality. To address the problem at the generic level, this paper introduces an optimization method and presents two examples for demonstration purposes. The case studies show that the proposed optimization method can well resolve the base shape determination problem for complex geometries, for example, the tree model and bracket model in the paper. The expected advantages are obvious, especially in terms of material saving in the CS HAM process. It is can also be adopted for other similar sequential HAM processes, such as wire arc AM and cladding-based HAM process. However, the method still has room for improvement. For instance, the skeleton generation and CAD model decomposition algorithms can be improved with more consideration of the constraints of manufacturing the base shape, which are not discussed in this paper. We intend to address this gap by developing a CS HAM platform to further verify the proposed method and its application value.

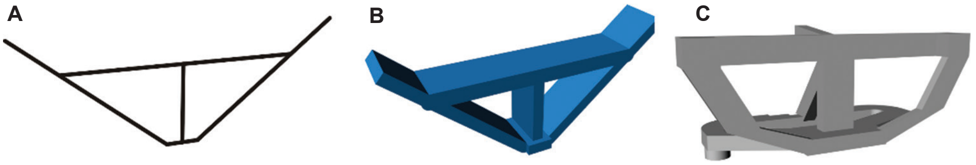

Figure 23. (A) Optimized skeleton by genetic algorithm; (B) optimized base shape by Particle Swarm Optimization; and (C) remaining subparts for CS AM module.

Acknowledgments

The authors would like to express their appreciation for the support provided by Hongjian Wu from UTBM.

Funding

None.

Conflict of interest

The authors declare no conflicts of interest.

Author contributions

Conceptualization: Yicha Zhang, Zhen Hong, Zhiping Wang
Formal analysis: Zhiping Wang, Zhen Hong
Funding acquisition: Alain Bernard
Investigation: Sihao Deng
Methodology: Zhiping Wang, Zhen Hong
Writing – original draft: Zhen Hong, Zhiping Wang
Writing – review & editing: Yicha Zhang, Alain Bernard

Ethics approval and consent to participate

Not applicable.

Consent for publication

Not applicable.

Availability of data

Raw data are available from the corresponding author on reasonable request.

References

1. Wohlers TT, Wohlers Associates, Campbell I, *et al.*, 2020, Wohlers Report 2020: 3D Printing and Additive Manufacturing State of the Industry. United States: Wohlers Associates.
2. Zhang Y, Wang Z, Zhang Y, *et al.*, 2020, Bio-inspired generative design for support structure generation and optimization in additive manufacturing (AM). *CIRP Ann*, 69: 117–120.

   https://doi.org/10.1016/j.cirp.2020.04.091
3. Esmaeilian B, Behdad S, Wang B, 2016, The evolution and future of manufacturing: A review. *J Manuf Syst*, 39: 79–100.

   https://doi.org/10.1016/j.jmsy.2016.03.001
4. Gao W, Zhang Y, Ramanujan D, *et al.*, 2015, The status, challenges, and future of additive manufacturing in engineering. *Comput Aided Des*, 69: 65–89.

   https://doi.org/10.1016/j.cad.2015.04.001
5. Vayre B, Vignat F, Villeneuve F, 2012, Metallic additive manufacturing: State-of-the-art review and prospects. *Mech Ind*, 13: 89–96.

   https://doi.org/10.1051/meca/2012003
6. Le VT, Paris H, Mandil G, 2017, Process planning for combined additive and subtractive manufacturing technologies in a remanufacturing context. *J Manuf Syst*, 44: 243–254.

   https://doi.org/10.1016/j.jmsy.2017.06.003
7. Ramaswami K, 1997, *Process Planning for Shape Deposition Manufacturing.* [Doctoral dissertation]. Stanford, CA: Stanford University.
8. Flynn JM, Shokrani A, Newman ST, *et al.*, 2016, Hybrid additive and subtractive machine tools-research and industrial developments. *Int J Mach Tools Manuf*, 101: 79–101.

   https://doi.org/10.1016/j.ijmachtools.2015.11.007
9. Zhu Z, Dhokia VG, Nassehi A, *et al.*, 2013, A review of hybrid manufacturing processes -state of the art and future perspectives. *Int J Comput Integr Manuf*, 26: 596–615.

   https://doi.org/10.1080/0951192x.2012.749530
10. Sealy MP, Madireddy G, Williams RE, *et al.*, 2018, Hybrid processes in additive manufacturing. *J Manuf Sci Eng*, 140: 060801.

    https://doi.org/10.1115/1.4038644
11. Kickelbick G, 2006, Introduction to hybrid materials. In: Hybrid Materials: Synthesis, Characterization, and Applications. Hoboken: Wiley.
12. Lauwers B, Klocke F, Klink A, *et al.*, 2014, Hybrid processes in manufacturing. *CIRP Ann*, 63: 561–583.

    https://doi.org/10.1016/j.cirp.2014.05.003
13. Nassehi, A., Newman, S., Dhokia, V, *et al.*, 2011, Using formal methods to model hybrid manufacturing processes. In: Enabling Manufacturing Competitiveness and Economic Sustainability. Berlin, Heidelberg: Springer.
14. Ham I, Lu SC, 1988, Computer-aided process planning: The present and the future. *CIRP Ann*, 37: 591–601.

    https://doi.org/10.1016/s0007-8506(07)60756-2
15. Zhang Y, Bernard A, 2018, A KBE CAPP framework for qualified additive manufacturing. *CIRP Ann*, 67: 467–470.

    https://doi.org/10.1016/j.cirp.2018.04.045
16. Kulkarni P, Marsan A, Dutta D, 2000, A review of process planning techniques in layered manufacturing. *Rapid Prototyp J*, 6: 18–35.

    https://doi.org/10.1108/13552540010309859
17. Zhang Y, Bernard A, 2014, AM Feature and Knowledge Based Process Planning for Additive Manufacturing in Multiple Parts Production Context. In: Proceedings of 25th Annual International Solid Freeform Fabrication Symposium.

18. Zhang Y, Bernard A, 2014, An integrated decision-making model for multi-attributes decision-making (MADM) problems in additive manufacturing process planning. *Rapid Prototyp J*, 20: 377–389.

    https://doi.org/10.1108/rpj-01-2013-0009

19. Zhang Y, Bernard A, Gupta RK, *et al*., 2014, Evaluating the design for additive manufacturing: A process planning perspective. *Procedia CIRP*, 21: 144–150.

    https://doi.org/10.1016/j.procir.2014.03.179

20. Zhang Y, Bernard A, Harik R, *et al*., 2015, Build orientation optimization for multi-part production in additive manufacturing. *J Intell Manuf*, 28: 1393–1407.

    https://doi.org/10.1007/s10845-015-1057-1

21. Hussein A, Hao L, Yan C, *et al*., 2013, Advanced lattice support structures for metal additive manufacturing. *J Mater Process Technol*, 213: 1019–1026.

    https://doi.org/10.1016/j.jmatprotec.2013.01.020

22. Byun HS, Lee KH, 2005, Determination of optimal build direction in rapid prototyping with variable slicing. *Int J Adv Manuf Technol*, 28: 307–313.

    https://doi.org/10.1007/s00170-004-2355-5

23. Ruan J, Eiamsa-Ard K, Liou FW, 2005, Automatic process planning and toolpath generation of a multiaxis hybrid manufacturing system. *J Manuf Process*, 7: 57–68.

    https://doi.org/10.1016/s1526-6125(05)70082-7

24. Zhang Y, Bernard A, 2014, Grouping parts for multiple parts production in additive manufacturing. *Procedia CIRP*, 17: 308–313.

    https://doi.org/10.1016/j.procir.2014.01.096

25. Zhang Y, Gupta RK, Bernard A, 2016, Two-dimensional placement optimization for multi-parts production in additive manufacturing. *Robot Comput Integr Manuf*, 38: 102–117.

    https://doi.org/10.1016/j.rcim.2015.11.003

26. Zhang Y, Bernard A, Harik R, *et al*., 2018, A new method for single-layer-part nesting in additive manufacturing. *Rapid Prototyp* J, 24: 840–854.

    https://doi.org/10.1108/rpj-01-2017-0008

27. Akula S, Karunakaran KP, 2006, Hybrid adaptive layer manufacturing: An intelligent art of direct metal rapid tooling process. *Robot Comput Integr Manuf*, 22: 113–123.

    https://doi.org/10.1016/j.rcim.2005.02.006

28. Karunakaran KP, Suryakumar S, Pushpa V, *et al*., 2009, Retrofitment of a CNC machine for hybrid layered manufacturing. *Int J Adv Manuf Technol*, 45: 690–703.

    https://doi.org/10.1007/s00170-009-2002-2

29. Ren L, Sparks T, Ruan J, *et al*., 2010, Integrated process planning for a multiaxis hybrid manufacturing system. *J Manuf Sci Eng*, 132(2):021006.

    https://doi.org/10.1115/1.4001122

30. Liou F, Slattery K, Kinsella M, *et al*., 2007, Applications of a hybrid manufacturing process for fabrication of metallic structures. *Rapid Prototyp J*, 13: 236–244.

    https://doi.org/10.1108/13552540710776188

31. Kerbrat O, Mognol P, Hascoet JY, 2010, Manufacturing complexity evaluation at the design stage for both machining and layered manufacturing. *CIRP J Manuf Sci Technol*, 2: 208–215.

    https://doi.org/10.1016/j.cirpj.2010.03.007

32. Newman ST, Zhu Z, Dhokia V, *et al*., 2015, Process planning for additive and subtractive manufacturing technologies. *CIRP Ann,* 64: 467–470.

    https://doi.org/10.1016/j.cirp.2015.04.109

33. Zhu Z, Dhokia V, Newman ST, 2014, A novel decision-making logic for hybrid manufacture of prismatic components based on existing parts. *J Intell Manuf*, 28: 131–148.

    https://doi.org/10.1007/s10845-014-0966-8

34. Rossi A, Lanzetta M, 2020, Integration of hybrid additive/subtractive manufacturing planning and scheduling by metaheuristics. *Comput Ind Eng*, 144: 106428.

    https://doi.org/10.1016/j.cie.2020.106428

35. Xiao X, Joshi S, 2020, Process planning for five-axis support free additive manufacturing. *Addit Manuf*, 36: 101569.

    https://doi.org/10.1016/j.addma.2020.101569

36. Leite M, Cunha J, Sardinha M, *et al*., 2018, Tool path generation for hybrid additive manufacturing. In: Proceedings of the 29th Annual International Solid Freeform Fabrication Symposium-an Additive Manufacturing Conference.

37. Chen L, Lau TY, Tang K, 2020, Manufacturability analysis and process planning for additive and subtractive hybrid manufacturing of Quasi-rotational parts with columnar features. *Comput Aided Des*, 118: 102759.

    https://doi.org/10.1016/j.cad.2019.102759

38. Dewitte LN, Saldana CJ, Feldhausen TA, *et al*., 2020, Initial Process Planning of a Hybrid Multi-Tasking Platform. In: ASME 2020 15th International Manufacturing Science and Engineering Conference.

39. Liu B, Shen H, Deng R, *et al*., 2020, Research on a planning method for switching moments in hybrid manufacturing processes. *J Manuf Process*, 56: 786–795.

    https://doi.org/10.1016/j.jmapro.2020.05.039

40. Zheng Y, Ahmad R, 2020, Feature extraction and process planning of integrated hybrid additive-subtractive system for remanufacturing. *Math Biosci Eng*, 17: 7274–7301.

    https://doi.org/10.3934/mbe.2020373

41. Eldakroury MA, Chen N, Frank MC, 2018, A new method for locating candidate substrates for multi axis hybrid manufacturing systems. *Rapid Prototyp J*, 24: 237–248.

    https://doi.org/10.1108/rpj-12-2016-0213

42. Chen N, Frank M, 2019, Process planning for hybrid additive and subtractive manufacturing to integrate machining and directed energy deposition. *Procedia Manuf*, 34: 205–213.

    https://doi.org/10.1016/j.promfg.2019.06.140

43. Reichler AK, Gerbers R, Falkenberg P, *et al*., 2019, Incremental manufacturing: Model-based part design and process planning for hybrid manufacturing of multi-material parts. *Procedia CIRP*, 79: 107–112.

    https://doi.org/10.1016/j.procir.2019.02.020

44. Patil S, Ravi B, 2005, Voxel-based representation, display and thickness analysis of intricate shapes. In: Ninth International Conference on Computer Aided Design and Computer Graphics (CAD-CG'05), Hong Kong, China: IEEE.

45. Lee TC, Kashyap RL, Chu CN, 1994, Building skeleton models via 3-D medial surface axis thinning algorithms. *CVGIP Graph Models Image Process*, 56: 462–478.

    https://doi.org/10.1006/cgip.1994.1042

46. Schmitt LM, 2001, Theory of genetic algorithms. *Theor Comput Sci*, 259: 1-61.

    https://doi.org/10.1016/S0304-3975(00)00406-0

47. Cichocka JM, Migalska A, Browne WN, *et al*., 2017, SILVEREYE-the Implementation of particle swarm optimization algorithm in a design optimization tool. In: Computer-Aided Architectural Design. Future Trajectories. Singapore: Springer. p. 151–169.

48. Lynch ME, Gu W, El-Wardany T, *et al*., 2013, Design and topology/shape structural optimisation for additively manufactured cold sprayed components. *Virtual Phys* Prototyp, 8: 213–231.

    https://doi.org/10.1080/17452759.2013.837629

ACCSCIENCE PUBLISHING

Materials Science in Additive Manufacturing

ORIGINAL RESEARCH ARTICLE

An exploratory study on biocompatible Ti-6Mn-4Mo alloy manufactured by directed energy deposition

Roman Savinov[1], Yachao Wang[2], and Jing Shi[1]*

[1]Department of Mechanical and Materials Engineering, University of Cincinnati, Cincinnati, Ohio, United States of America

[2]Department of Mechanical Engineering, University of North Dakota, Grand Forks, North Dakota, United States of America

Abstract

Titanium is a widely used metal in biomedical applications due to its low toxicity, but its mechanical properties need to be tailored for different applications. Efforts are called for to search for effective and yet non-toxic elements to be alloyed with Ti to improve its strength. Fitting in this category, Mn and Mo are two such alloying elements. In this study, Ti-6Mn-4Mo alloy was manufactured by laser-directed energy deposition (DED) through *in situ* alloying of Ti, Mn, and Mo elemental powders. This study was intended to not only demonstrate for the first time the printability of the Ti-Mn-Mo ternary system by laser DED but also investigate the basic mechanical properties and corrosion resistance of the obtained alloy. Under the as-built condition, the alloy consisted mainly of ß phase, while after heat treatment it was transformed into α phase. The average ultimate tensile strength under as-built condition was 706.0 MPa, lower than similar alloys from conventional methods. However, the average hardness reached 421.1 HV for the as-built condition, much higher than the similar alloys made through conventional methods. On the other hand, the corrosion resistance of the obtained alloy was found to be relatively low compared to similar alloys produced with traditional methods. In addition, heat treatment was not able to significantly change the tensile properties or the corrosion resistance. In essence, the exploratory study indicates that the DED-produced Ti-Mn-Mo alloy could be deposited without cracks and major voids, and shows that its high hardness and modulus are attractive to applications for high wear resistance. However, further investigation is needed to improve strength, ductility, and corrosion resistance of the alloy.

Keywords: Ti-Mn-Mo alloys; Laser-directed energy deposition; Tensile properties; Hardness; *In situ* alloying

***Corresponding author:**
Jing Shi
(jing.shi@uc.edu)

Citation: Savinov R, Wang Y, Shi J, 2023, An exploratory study on biocompatible Ti-6Mn-4Mo alloy manufactured by directed energy deposition. *Mater Sci Add Manuf*, 2(4): 2180.
https://doi.org/10.36922/msam.2180

Received: November 6, 2023

Accepted: November 24, 2023

1. Introduction

To be suited for biomedical applications, metal alloys should possess certain properties. The alloys should be nontoxic, non-carcinogenic, and ideally highly resistant to wear and corrosion. To date, the most used metallic biomaterials have been stainless steels, Co-Cr alloys, and Ti-based alloys[1]. Stainless steels are often used due to their corrosion resistance and relatively low price. Co-Cr alloys are hard and wear-resistant metals and are often used as knee and hip replacements. However, those materials exhibit certain weaknesses when implanted in the human body. For instance, despite its corrosion resistance, SUS316L steel has been reported to suffer from localized corrosion. Furthermore, austenitic stainless steels contain a significant amount of Ni known to cause allergic problems. Implants made of Co-Cr alloys may release ions of Co, Cr, and Mo, which increase the risk of inflammatory reactions and other complications[2]. Ti alloys, on the other hand, have better suitability due to their lower toxicity and balanced properties. Commercially, pure titanium (CP-Ti) and Ti-6Al-4V were originally designed to be used as structural materials and now are among the most used Ti-based biomaterials[3]. However, the mechanical strength of CP-Ti is relatively low compared to other alloys such as Co-Cr alloys, thus limiting its applications where intensive wear use or high strength is expected[4]. Ti-6Al-4V has much better mechanical performance than CP-Ti, but it is known to release cytotoxic elements such as V and Al which may cause health issues[5,6]. Some new Ti alloys with good biocompatibility and no toxic elements, as well as improved performance, have been investigated[7], but these alloys often contain expensive elements, such as Nb and Ta.

Ti-based alloys exist in two allotropic forms. Below 882.3°C, hexagonal-close-packed (HCP) α phase is stable; above this allotropic transformation temperature, body-centered-cubic (BCC) β phase is formed. The temperature at which either α or β phase is stable can be modified by addition of interstitial and substitutional elements. Therefore, phase composition and thus mechanical properties of Ti alloys can be controlled by the addition of alloying elements. The β phase Ti alloys generally have higher strength and lower elastic modulus compared to the Ti alloys with α or α + β alloys. For that reason, the research in Ti-based biocompatible alloys has paid close attention to β-stabilizing elements, such as Nb, Ta, Mo, and Mg[4]. Another strong β-stabilizer is Mn which is also not expensive and has low toxicity compared to other β-stabilizers[8,9]. Ti-Mn alloys with Mn concentrations between 8% and 13% were found to possess not only mechanical properties similar to Ti-6Al-4V but also cytotoxicity and cell viability close to CP-Ti[10]. The addition of a third element with weaker β-stabilizing effect can simplify the control of Mn addition[11]. For this reason, the previous studies investigated the effect of Mo addition to Ti-Mn alloy[9,12]. Mo is a trace element found in the human body and less cytotoxic than V, Fe, and Co. The addition of Mo to Ti-Mn system may also activate twinning, thus improving balance between strength and ductility.

Until recently, biocompatible metallic alloys have been fabricated by traditional fabrication methods, such as forging, casting, hot rolling, and machining. However, additive manufacturing methods offer an alternative method for producing biocompatible parts[13]. Industry can benefit from additive manufacturing technology due to its distinctive advantages, such as customized small batch production, simplification of the manufacturing process, capability of handling complex geometries, as well as waste and cost reduction. As a result, many biomedical products can benefit from implementing additive manufacturing technology to obtain products of novel and complex shapes and with functionally graded compositions. Various additive manufacturing technologies are available for obtaining metal components. The predominant processes are powder bed fusion (PBF) such as selective laser melting (SLM), and directed energy deposition (DED) techniques such as powder-blowing laser DED[14,15]. The majority of additive manufacturing studies on biocompatible Ti alloys are based on PBF processes. Such processes are usually better controlled and thus more accurate. However, DED processes are more efficient and often less costly compared with PBF processes. More importantly, DED processes are more potent in terms of material synthesis capability based on the *in situ* alloying mechanism[16]. This is because many DED systems are able to dynamically adjust the alloy composition through multi-channel powder feed control, while the alloy composition is generally fixed in PBF processes.

In recent years, numerous studies have employed PBF processes to obtain Ti-6Al-4V materials to address various research issues. A major goal of those studies has been on how to control the elastic modulus and cell adhesion of printed parts by induced porosities[17-19]. For instance, Tseng *et al.*[20] used a PBF method to produce Ti-6Al-4V lattice structures suitable for the growth of bone cells. Furthermore, the corrosion behaviors of Ti-6Al-4V produced by PBF[21] as well as the effects of PBF process parameters on corrosion resistance of the resultant Ti-6Al-4V[17,22] were investigated. Other biocompatible Ti-based alloys produced by PBF methods have been widely investigated. For instance, binary alloys such as Ti-Nb synthesized by laser PBF were studied for mechanical properties[23,24], and the effects of pore size on mechanical and shape memory properties were studied on porous NiTi scaffolds[25]. Furthermore, next-generation biomaterials such as Ti-Nb-Ta[26-28] and Ti-Nb-Zr[29] were evaluated for biocompatibility, printability, and possibility to tailor elastic modulus by build orientation[30].

Researchers have also employed DED methods to study the biocompatible Ti-based alloys. For Ti-6Al-4V, investigations in recent years were focused on the mechanical properties[31,32], the influence of thermal cycling on microstructure evolution[33], the biocompatibility,[1] as well as the evolution of electrochemical properties[34]. More importantly, DED techniques have been also adopted to study other Ti-based alloy systems, but the efforts have been limited. In this regard, Gong *et al.*[35] evaluated Ti-Mn alloy for laser DED technique using a high throughput method. Yang *et al.*[36] studied the Ti-20 wt% Mo by coating prepared by *in situ* alloying of pure Ti and Mo powders during laser cladding. Kang *et al.*[37] investigated the effect of the thermal cycle during the *in situ* DED production of a Ti-Mo alloy with functionally varied composition.

Based on the literature survey, we learned that while additive manufacturing-produced Ti-6Al-6V has been extensively studied, the investigation of AM-produced new Ti alloys with Mn or Mo additions is still in the infancy stage. To date, very limited research has been conducted on using additive manufacturing methods to produce Ti-Mn or Ti-Mo binary systems, while the Ti-Mn-Mo ternary system has not been fabricated by either PBF or DED methods to the best of our knowledge. As such, this study intends to bridge the gap, by investigating the feasibility of using laser DED technique to synthesize a Ti-Mn-Mo ternary alloy through *in situ* alloying of elemental powders, and exploring the mechanical properties and corrosion resistance of the obtained alloy.

2. Materials and methods

2.1. DED experiment

Elemental titanium (Ti), manganese (Mn), and molybdenum (Mo) powders with particle size ranges from 50 to 150 µm were used in this study. Ti and Mo powders were spherical while Mn powder was of an irregular shape. Elemental powders of Ti, Mn, and Mo were mixed in 90:6:4 proportion, respectively, in a low-energy ball milling machine for 2 h. This composition was chosen due to the promising mechanical properties (such as high strength) reported in literature[5,11], in which conventional manufacturing processes were employed. The powder mixture was dried in an oven for 90 min at 110°C immediately before use. Figure 1 shows the scanning electron microscopy (SEM) images of the resultant powder mixture. The diameter of powder particles is in the range of 30 to 150 µm. While most particles are spherical, some irregular shape particles are present in the mixture, and they are identified as Mn particles. Ti-6Mn-4Mo deposits were obtained using the InssTek MX-Lab AM system equipped with a CNC 3-axis stage, a fiber laser with maximum power of 300 W and spot size of 0.4 mm. The powder mixture was loaded into the hopper and deposited on a Ti-6Al-4V substrate through a coaxial powder feeding nozzle together with argon as a shielding gas.

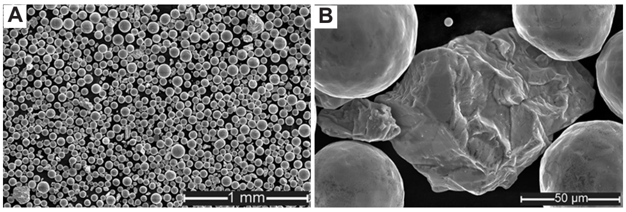

Figure 1. Micrographs of Ti-6Mn-4Mo powder mixture for directed energy deposition experiment. (A) Low-magnification scanning electron microscopy image at 50×; (B) close-up view for the minor irregular Mn particles at ×800.

Pilot trials were conducted to determine the optimal parameters for the DED process, involving variations in laser power and scanning speed. A summary of the different combinations of laser power and scanning speeds is presented in Table 1. Basically, the laser power was systematically increased from 200 W to 300 W (the highest possible level for the DED machine) in 50 W increments while maintaining a constant scanning speed of 500 mm/min. The final test run (Condition 4) was performed at the highest available laser power of 300 W but with an increased scanning speed of 1000 mm/min. Evaluation of the deposited material from each condition included an assessment of porosity, supported by optical micrograph images of cross-sections as illustrated in Figure 2. Both Conditions 2 and 3 exhibited notable pores and voids, while Conditions 1 and 4 displayed significantly lower porosity. Ultimately, Condition 1, with the least void content, was chosen for all subsequent experiments.

The selected process parameters used for producing Ti-6Mn-4Mo are listed in Table 2. Samples were deposited in two shapes: (i) rectangular blocks of 12 × 60 × 4 mm and (Figure 3A–3D) (ii) disks with a diameter of 25 mm and a height of 2.5 mm (Figure 3E–3F). For the scanning strategy, a unidirectional scan with 180°-layer rotation was utilized during deposition for the blocks (Figure 3A), while a spiral strategy was used for disk specimens. The deposited materials were separated from the build plate using a wire electrical discharge machine. Tensile test samples were cut out of the rectangular blocks such that their tensile axis was aligned with the scanning direction (Figure 3B). Half of the samples were heat-treated in an induction furnace with Ar atmosphere by heating with a rate of 10°C/min up to 1000°C, which was maintained for 1 h before furnace cooling with the rate of 10°C/min. The heat treatment strategy was directly adopted from the literature[8,11] for similar Ti alloys and is summarized in Figure 4.

2.2. Material characterization

The specimens for optical and SEM observations were first ground using silicon carbide sandpaper with granulation down to 1200. Ground samples were then polished with

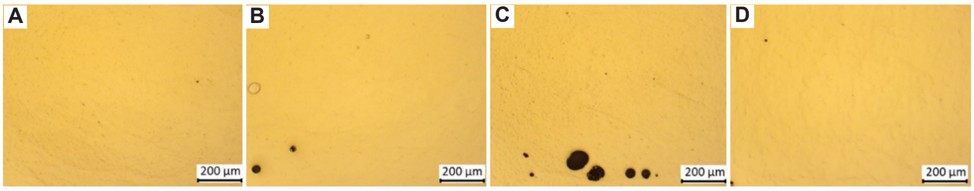

Figure 2. Porosity observation of Ti-6Mn-4Mo deposits for process parameters selection: (A) Condition 1, (B) Condition 2, (C) Condition 3, and (D) Condition 4.

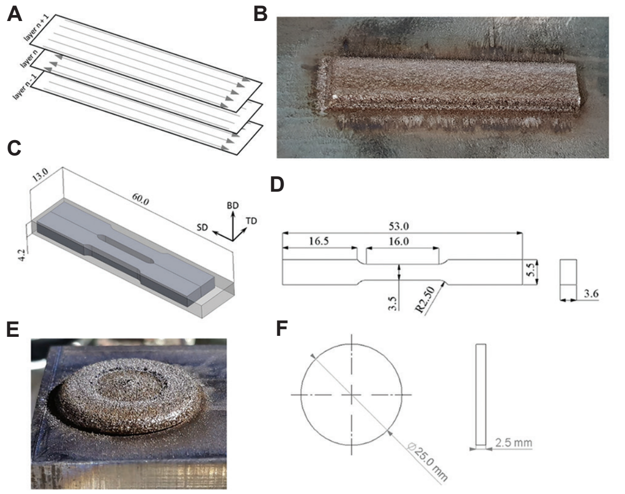

Figure 3. Directed energy deposition-produced Ti-6Mn-4Mo deposits. (A) Scanning strategy used for all deposited samples; (B) orientation of the tensile samples relative to build direction; (C) image of an as-deposited rectangular block before tensile samples were extracted (mm); (D) dimensional specifications of the tensile samples (mm); (E) an as-built disk for corrosion test; and (F) dimensional specification of the disk samples.

Table 1. Process parameters used in the DED test runs

Process parameter	Condition 1	Condition 2	Condition 3	Condition 4
Laser power (W)	200	250	300	300
Scanning speed (mm/min)	500	500	500	1000

DED: Directed energy deposition

Table 2. Selected laser DED process parameters used for making Ti-6Mn-4Mo samples

Process parameter	Description
Laser power	200 W
Scanning speed	500 mm/min
Hatch spacing	300 µm
Scan strategy	Unidirectional, 180° rotation
Shield gas flow rate	0.8 L/min
Powder flow rate	0.70 g/min
Substrate	Ti-6Al-4V

DED: Directed energy deposition

A_2O_3 suspension with 1 µm and 0.3 µm. The microstructure was obtained by etching with Kalling's #2 solution (2 g $CuCl_2$ 40 ml HCl 60 ml C_2H_6O) for 60 seconds. The surface morphology and chemical composition of deposited samples were studied using an optical microscope (AMScope ME400TA-FMA050) and a SCIOS dual-beam SEM (Thermo Fisher Scientific) equipped with energy dispersive spectroscopy (EDS). Phases present in the deposited materials were identified with X-ray diffraction (XRD) using Rigaku Smartlab with Cu-Kα source of wavelength 1.54056 Å. XRD analysis was performed with tube voltage and current of 40 kV and 44 mA, respectively, using the step size of 0.01° in the 2θ range of 25 – 100°. Tensile test was performed by a Shimadzu AGS-X 50 kN material testing system at a rate of 0.5 mm/min. Elongation was measured using an axial extensometer (model 3542-025M-100-ST, Epsilon Tech), which meets ASTM E83 class B-1 accuracy requirements. The density of the printed parts was measured in accordance with ASTM B926-15. The specimens were first weighed in air using an electronic balance with accuracy of 0.1 mg and then reweighed when immersed in water, and its density was calculated based on Archimedes' principle.

For corrosion resistance test, disk samples were first ground by 600 grit silicon carbide sandpaper and, then, exposed to the 3.5 wt% NaCl saline media at room temperature using a three-electrode cell. The cell consists of a silver chloride (Ag/AgCl) reference electrode, a Ti wire as the counter electrode, and a disk sample as the working electrode. Electrolyte was exposed to an area of 2.85 cm^2. Open circuit potential test was conducted for 60 min to ensure a steady-state potential. Tafel potentiodynamic polarization curves were obtained with a scan rate of 5 mV/s using by a potentiostat (Pine WaveDriver 100 EIS).

3. Results and discussion

3.1. Density of obtained Ti-6Mn-4Mo

The density of deposited materials was measured using Archimedes' principle before and after heat treatment. The results are shown in Table 3 in terms of absolute values and

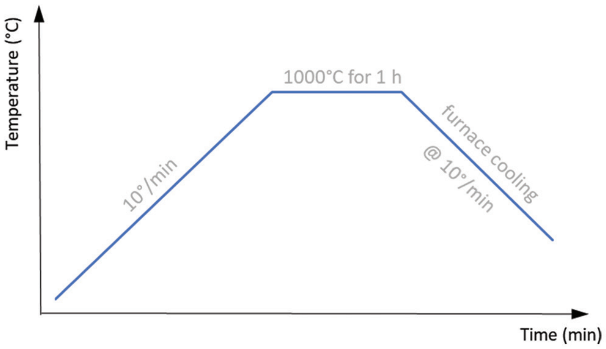

Figure 4. Heat treatment scheme for Ti-6Mn-4Mo samples.

relative values normalized to the theoretical density for Ti-6Mn-4Mo alloy. The theoretical density was calculated using the rule of mixture for the given alloy composition. As can be seen, DED deposition with the chosen process parameters resulted in dense materials. The density values of the as-built and heat-treated samples were measured to be above 99.2%. Since the as-built material already has high density close to the theorectical value, it is not a surprise that the effect of heat treatment in densifying the as-built material was not observed.

3.2. Microstructure analysis

Figure 5 shows the XRD spectra of the powder mixture as well as additively manufactured Ti-6Mn-4Mo samples before and after heat treatment. In the case of the powder mixture, the pattern corresponds to simple mechanical mixture of elemental Ti, Mn, and Mo phases. The peaks of Mn and Mo have low intensity which agrees with a low concentration of these elements in the mixture. On the other hand, the two cases of deposited samples demonstrate the mixture of α and β phases. The as-built Ti-6Mn-4Mo consists mainly of β phase. Very small peaks that correspond to α phase can also be seen. This suggests that a small amount of α phase was also formed during the cooling stage of DED process. In the literature, similar XRD spectra were observed in Ti6554 consisting of α and β phases[38]. By contrast, the XRD pattern of the heat-treated Ti-6Mn-4Mo contains strong peaks that correspond to α phase while some small β phase peaks are still present. Besides α and β phases, the heat-treated Ti-6Mn-4Mo contains intermetallic $Ti_{0.75}Mo_{0.25}$ phase (ICDD # 04-013-0263). Although XRD peaks of this phase are close to those of β-Ti, it has a very good fit with the following three peaks: 39.44°, 57.16°, and 71.70°, which match the locations of $Ti_{0.75}Mo_{0.25}$ phase peaks with the strongest intensity. Note that the homogeneity of the powder mixture could be implied from the presence of Mn and Mo peaks in XRD observation on the powder mixture. Since the peaks were detected in the small samples (1 – 2 g) randomly taken from the prepared mixture before deposition, it is believed that both Mn and Mo elements were homogeneously distributed in resultant powder mixture.

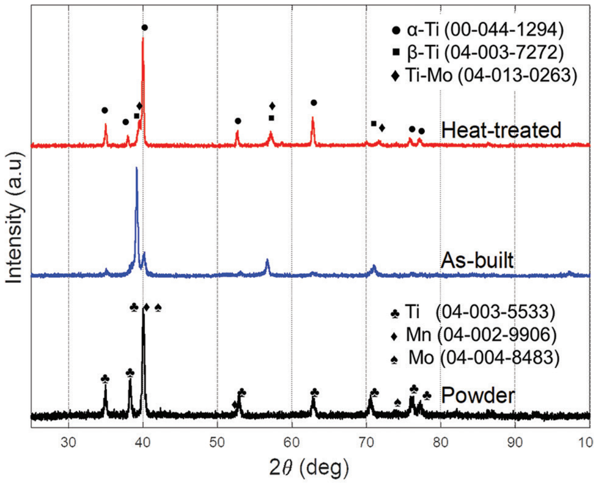

Figure 5. X-ray diffraction analysis of powder mixture and additively manufactured Ti-6Mn-4Mo before and after heat treatment. The corresponding PDF card numbers are included in parentheses.

Table 3. Density of DED-produced Ti-6Mn-4Mo materials under as-built and heat-treated conditions

Condition	Density (g/cm³)	Relative density (%)
As-built	4.596±0.05	99.27±0.02
Heat-treated	4.593±0.05	99.20±0.02

DED: Directed energy deposition

While DED deposition ensures β phase in Ti-6Mn-4Mo alloy under the as-built condition, high cooling rates associated with the DED process may also lead to formation of the metastable phases in Ti-alloys[39]. As the study by Kang *et al.*[37] suggests, metastable phases form initially during cooling. During layer-by-layer manufacturing, however, the previous layers experience reheating cycles as new layers are being deposited. This leads to an "*in situ*" heat treatment, causing the unstable phases to transform into α and β phases. In the present study, combination of high cooling rate, "*in situ*" heat treatment, and the presence of a given amount of Mn and Mo in Ti matrix result in the formation of Ti-6Mn-4Mo alloy. The alloy predominantly consists of *β* phase with a small amount of α phase. After the as-built sample was heat-treated, β phase partially transformed into α phase such that α phase became the dominant one.

The microstructure analysis of the deposited Ti-6Mn-4Mo alloy reveals the presence of long grains oriented along the build direction, as shown in Figure 6A. In this figure, several boundaries of such long grains are indicated by dashed lines. The existence of long grains along the build direction is supported by the similar observations in the literature, such as DED-produced Ti-6Al-4V by Tan *et al.*[33], and DED-produced Ti-Mo alloy by Kang *et al.*[37] Some partially melted powder particles can be found in the bulk of material, as shown in Figure 6. As seen from the figure, as-built alloy is composed of predominantly β phase grains. However, α + β lamellar microstructure is also present mostly near the bottom of melt pools (Figure 6C). This observation agrees with the XRD results, which show that β phase is the dominant phase while a small amount of α phase is also present. Alshammari *et al.*[40] indicated that the number of α + β lamellar microstructure present in Ti-Mn alloy depends on the amount of Mn. As Mn increases from 1 to 5%, the amount of β phase becomes more abundant. At 10% Mn, the microstructure is entirely composed of β phase rather than α + β lamellar microstructure. An increase in the volume fracture of β phase along with an increase of Mn was also reported for Ti-Mn produced by laser DED[35]. From these observations, it can be assumed that as-built Ti-6Mn-4Mo consists of mostly β phase, but a small amount of α phase is also present.

Several elongated patches of about 100 μm long can be visible at the bottom of melt pools (Figure 6B). The microstructure within these patches is different from the matrix. It consists of a long and fine-needle-like structure. The presence of such patches is a sign of inhomogeneous distribution of alloying elements. Depletion of alloying elements in certain regions can be explained by the unmelted or partially melted powder particles. This is especially relevant for Mo, which is hard to melt due to its very high melting temperature. In addition, the deposited Ti-6Mn-4Mo samples are overall free of apparent cracks and only a few micropores can be found in the cross-section. This, further, confirms the soundness of the selected DED process parameters.

After the heat treatment, the microstructure undergoes a noticeable change (Figure 7). A dual-phase α + β lamellar microstructure was formed within the primary phase grains. A similar microstructure was observed in Ti-5.8wt% Mn produced by laser DED[35]. In such a microstructure, darker lamella is an HCP α-Ti while brighter lamella is BCC β-Ti (Figure 7D). This observation is consistent with XRD results, which show that heat-treated Ti-6Mn-4Mo consists mainly of α phase. As beta alloy with metastable β phase undergoes heat treatment, α phase starts to precipitate from the β matrix. Such transformation from β to α + β during aging is a slow process, during which α plates grow in β matrix through a diffusion-controlled mechanism.

3.3. Elemental composition analysis

Figure 8 shows the EDS mapping results for a region of 550 × 550 μm on the cross-section of as-built Ti-6Mn-4Mo. It is evident that Ti and Mn elements are distributed homogeneously. Although there is a distinct segregation of Mn from melt pool boundaries

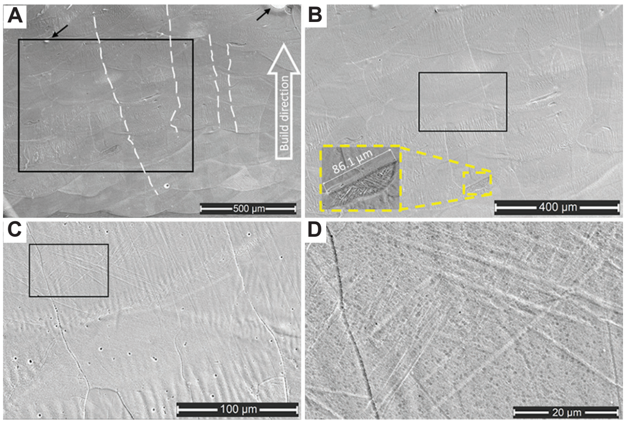

Figure 6. Scanning electron microscopy micrographs of the microstructure of as-built Ti-6Mn-4Mo alloy. (A) Observation at ×65 magnification. Arrows point at the partially melted Mo powder particles, and the black box represents the close-up view area for the next higher magnification level; (B) observation at ×120 magnification. The black box represents the close-up view area for the next higher magnification level; (C) observation at ×500 magnification. Black box represents the close-up view area for the next higher magnification level; and (D) observation at ×2000 magnification.

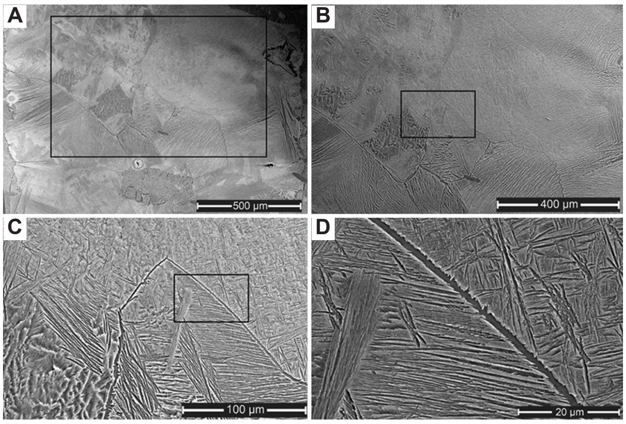

Figure 7. Scanning electron microscopy micrographs of the microstructure of directed energy deposition-produced Ti-6Mn-4Mo after heat treatment. (A) Observation at 65× magnification. Black box represents the close-up view area for the next higher magnification level; (B) observation at 120× magnification. The black box represents the close-up view area for the next higher magnification level; (C) observation at 500× magnification. The black box represents the close-up view area for the next higher magnification level; (D) observation at 2000× magnification.

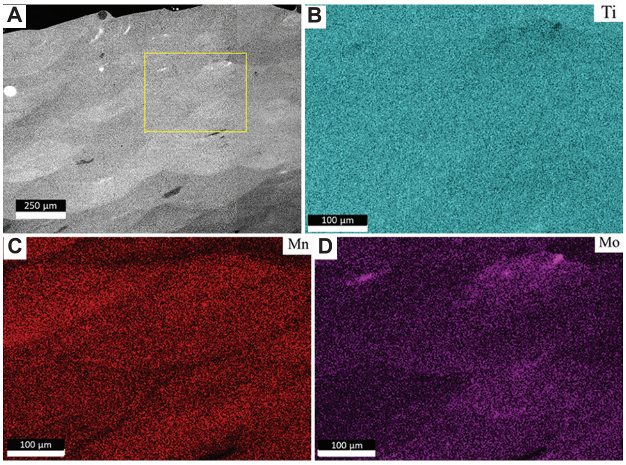

Figure 8. Energy dispersive spectroscopy mapping directed energy deposition-produced Ti-6Mn-4Mo alloy. (A) Backscattering scanning electron microscopy image; (B-D) distributions of Ti, Mn and Mo, respectively, portrayed within the yellow box in (A).

(Figure 8C), no apparent change in the concentration of Mn is visible within melt pools. Mo, on the other hand, shows a tendency to accumulate in certain regions (Figure 8D). These regions with a higher amount of Mo are visible in backscattering images as white areas (Figure 8A). As seen in Figure 8D, some melt pools have a distinctively lower amount of Mo (bottom left), while other melt pools are richer in Mo (top right). The dark elongated features in the backscattering image of Figure 8A are regions of pure Ti. One such region is shown in higher magnification, as shown in Figure 6B. Microstructure in this region consists of fine-needle-like plates, and its composition is pure Ti. Such regions are formed due to insufficient concentration of alloying elements in a melt pool. This might be a consequence of inhomogeneous distributions of Mn and Mo powder particles in the mixture.

3.4. Electrochemical corrosion

The corrosion resistance performance of Ti-6Mn-4Mo under both as-built and heat-treated conditions is presented in Figure 9 in terms of open circuit potential and linear sweep voltammetry curves. Open circuit potential decreases first and approaches the minimum value between 15 and 20 min for both conditions. Thereafter, it starts to gradually increase toward a steady state value of −225 mV and −230 mV for as-built and heat-treated conditions, respectively. The initial decrease in open circuit potential curve is due to removal of the oxide formed in air, while the subsequent increase indicates the formation and growth of a new passive oxide layer[41]. Tafel potentiodynamic polarization curve is shown in Figure 9B. There is a very small difference in polarization curves of the two conditions. Cathodic branches are in the potential range between −1250 mV and −500 mV. Anodic branches are in the range of −500 – 100 mV. A short plateau of passivity is observed in the range from 100 mV to 200 mV. After the plateau, a breakdown starts where current density increases exponentially. Such a breakdown indicates the formation of pits[34]. The system stability was evaluated by the value of potential denoted as corrosion potential (E_{corr}) at the dip of the curve in this figure. Corrosion susceptibility in the corrosion medium is lower when E_{corr} is higher (or less negative)[42]. The obtained E_{corr} values are −528.1 ± 8.9 mV and −520.6 ± 10.6 mV for the as-built and heat-treated conditions, respectively. Note that the biocompatible Ti alloys obtained by conventional manufacturing methods usually have higher corrosion resistance in terms of E_{corr}. However, metallic materials from additive manufacturing processes such as PBF and DED processes usually exhibit lower corrosion resistance. For instance, corrosion potentials of Ti-6Al-4V were reported to be in the wide range of -474

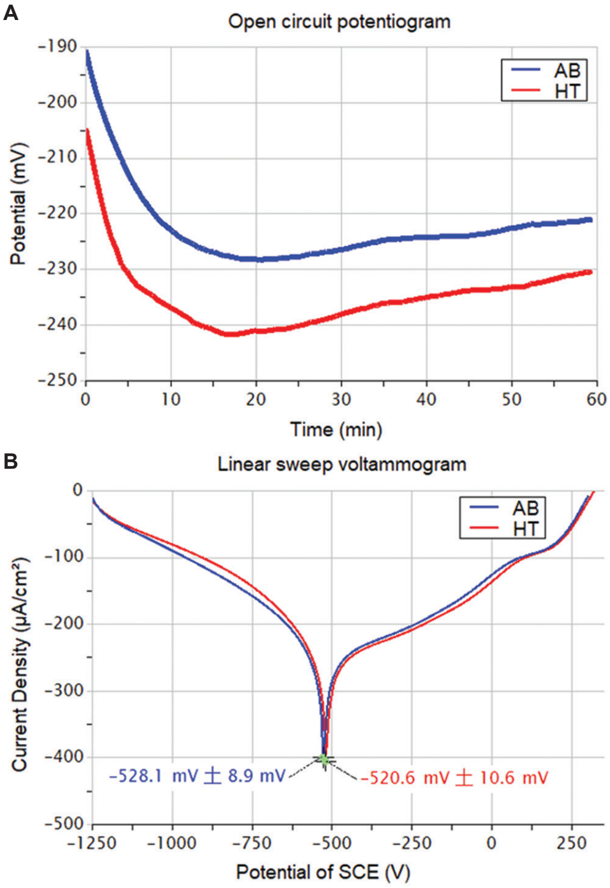

Figure 9. Corrosion resistance performance of Ti-6Mn-4Mo. (A) open circuit potential and (B) linear sweep voltammetry.
Abbreviation: SCE: Saturated calomel electrode.

mV to −116.2 mV, depending on many factors such as the selection of process parameters[17,21,22,34,43,44].

Figures 10 and 11 show the SEM observations and EDS mapping results after corrosion test for the sample surfaces of as-built and heat-treated conditions, respectively. At the low magnification, although the difference in corrosion morphology is not apparent, the as-built sample surface contains a slightly higher number of corrosion products as indicated by arrows. The higher-magnification images (Figures 10B and 11B) reveal the flake-like corrosion products of about 60 μm accumulating on sample surface. The EDS mapping images suggest that these features are oxides formed after the corrosion test.

3.5. Mechanical properties

3.5.1. Tensile properties

Figure 12A shows the representative tensile stress-strain curves of the as-built and heat-treated Ti-6Mn-4Mo samples. Figure 12B shows the corresponding values of ultimate tensile strength (UTS) and yield strength (YS). Figure 12C shows

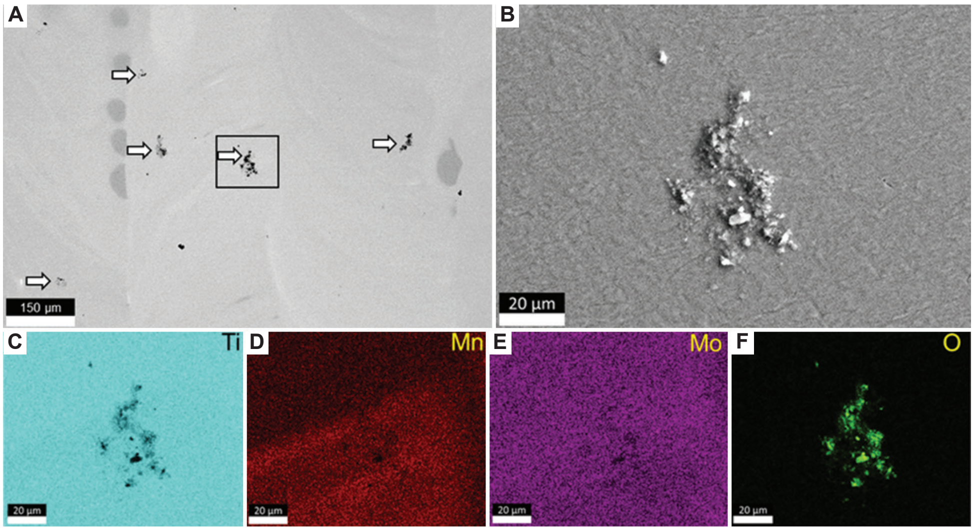

Figure 10. Micrographs of the as-built sample surface after corrosion test. (A) Backscattering scanning electron microscopy image; (B) close-up view of a selected area of energy dispersive spectroscopy mapping; and (C, D, E, F) elemental distributions of Ti, Mn, Mo, and O, respectively.

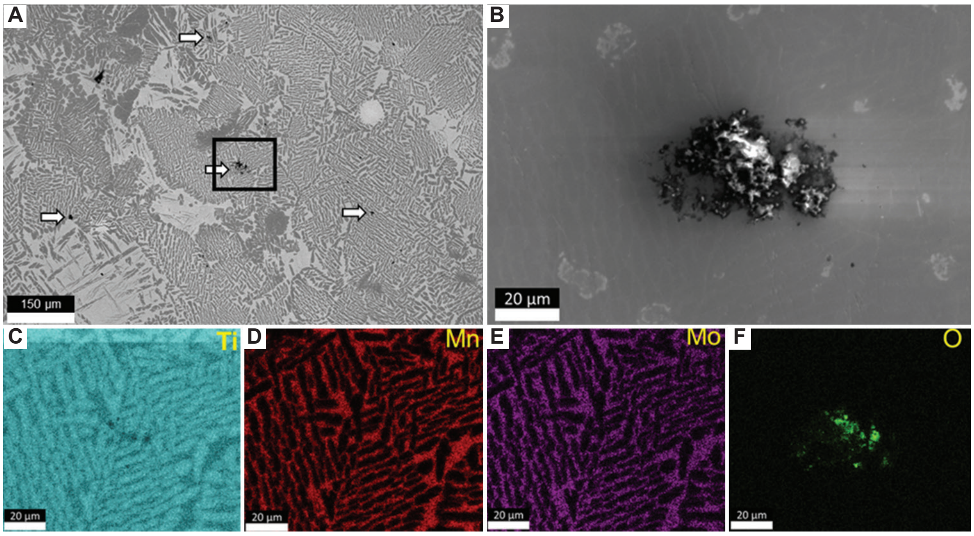

Figure 11. Micrographs of the heat-treated sample surface after corrosion test. (A) backscattering scanning electron microscopy image; (B) close-up view of a selected area of energy dispersive spectroscopy mapping; (C, D, E, F) elemental distributions of Ti, Mn, Mo, and O, respectively.

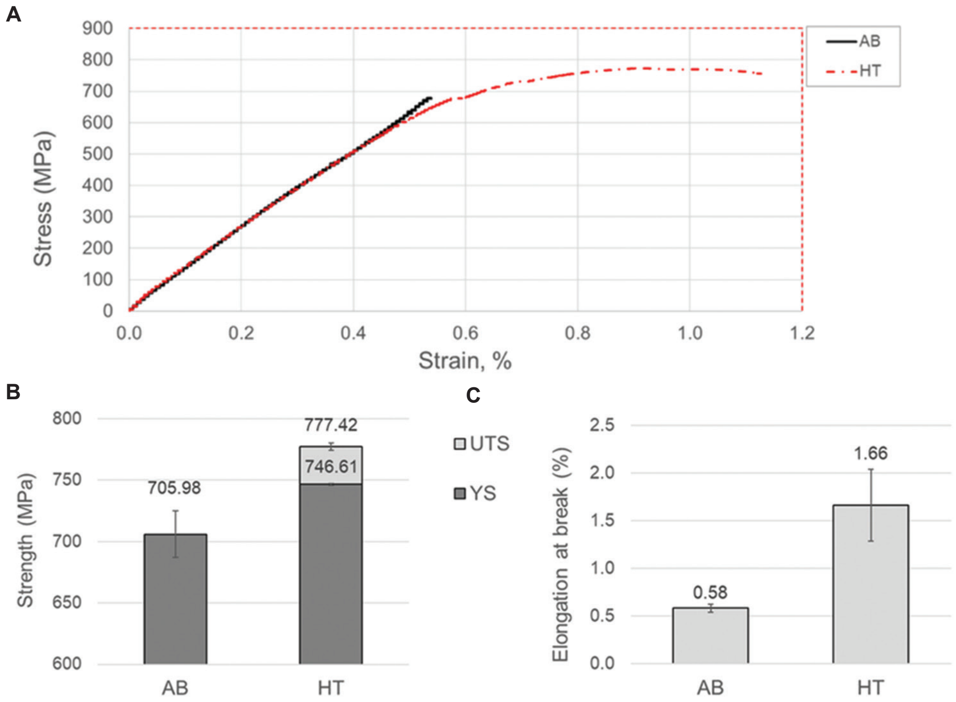

Figure 12. Tensile properties of the as-built and heat-treated Ti-6Mn-4Mo materials. (A) Representative tensile stress-strain curves; (B) comparison of ultimate tensile strength; and (C) comparison of elongation at break.
Abbreviations: AB: As-built; HT: Heat-treated.

elongation at break. The UTS of as-built material is 705.98 ± 18.92 MPa, but the material appears to be brittle because the as-built tensile samples fractured before even reaching 1% elongation. Since premature failure of as-built samples happened before plastic deformation was reached, YS and UTS for the as-built condition were measured to be at the same level. The UTS of the heat-treated material was found to be at 777.42 ± 3.09 MPa, which was also not significantly higher than its YS at 746.61 ± 0.73 MPa. However, the elongation improved slightly and reached around 1.66 ± 0.38%, as compared to 0.58 ± 0.04% for the as-built condition. In addition, limited influence of the heat treatment on Young's modulus of Ti-6Mn-4Mo was observed.

In this study, the average UTS of DED-produced Ti-6Mn-4Mo appears to be relatively low, as compared to the UTS of alloys made by other fabrication methods reported in literature. For example, metal injection molding (MIM) and plasma arc manufacturing produce Ti-6Mn-4Mo with high UTS values of 1093 MPa[8] and about 900 MPa[9], respectively. It is commonly believed that higher concentration of Mn and Mo increases the solid solution strengthening effect, which enhances UTS of the obtained ternary alloy. Thus, unmelted Mo particles in the deposits are likely a contributing factor to the reduction of UTS for the present study. Furthermore, many conventional methods achieved higher elongation-at-break values than methods used in this study. It is worth noticing that similar low elongation at break (2 – 5%) was observed in Ti-Mn-Mo alloys produced by MIM[8], in which elongation improved with higher concentration of Mn and Mo elements. In fact, the absence of Mo leads to a significant decrease in elongation compared to Ti-Mn-Mo alloy[9]. Therefore, the lower concentration of alloying elements due to unmelted Mo particles in this study is believed to be responsible for the lower ductility. Moreover, Ti-Mn-Mo alloys with lower concentration of alloying elements also exhibit a brittle-like behavior. This was attributed to a high amount of athermal ω phase[5]. While this detrimental phase was not observed in the present study, the presence of such phase cannot be ruled out. This is because ω phase is difficult to detect by XRD. On the other hand, the Young's modulus values obtained in the present study range between 130 and 147 GPa, which are significantly higher than those of Ti-Mn-Mo alloys obtained by cold crucible levitation melting (CCLM) and MIM[5,8]. Furthermore, the Ti-Mn alloys produced by laser DED demonstrated that the modulus values varied between 100 and 130 GPa (with 2 – 12 wt% Mn content)[35], which are closer to the values observed in the present study. It is suspected that the existence of unmelted Mo in the resultant alloy in the present study weakened the β stabilizing effect and lead to higher modulus. In addition, lower concentration of Mo element might contribute to formation of ω phase, which also increases Young's modulus. The microstructures of the Ti-Mn-Mo alloys produced by MIM and CCLM consist of equiaxed grains, which vary in size from 37 µm to 165 – 216 µm, respectively[5,8,11]. The average grains in the current study are much less equiaxed and highly elongated, and can reach as long as 500 µm (Figure 6). It is believed that this grain morphology contributes to the low UTS compared to that of Ti-Mn-Mo produced by MIM and CCLM reported in the literature.

3.5.2. Hardness analysis

Figure 13 shows the Vickers hardness obtained on the vertical cross-sections of the AB and HT Ti-6Mn-4Mo samples. The hardness of as-built sample is 421.1±8.8 $HV_{0.1}$. Compared with the wrought Ti-6Al-4V (325 HV)[8], the as-built Ti-6Mn-4Mo is significantly harder. Hardness of other Ti-Mn-Mo alloy compositions produced by CCLM and MIM methods vary from 312 to 392 HV[8,11]. In comparison, the hardness of the as-built Ti-6Mn-4Mo in the present study is significantly higher. Hardness in Ti-Mn-Mo alloys depends on a few factors, such as presence of carbides, pores, ω phase, and solid solution hardening effect of alloying elements. Hardness tends to decrease in Ti alloys with lower amount of ω phase[45]. Consequently, as mentioned earlier, unmelted Mo particles in the present study could lead to higher amount of ω phase, which, in turn, increases the hardness. The unusually high hardness of as-built Ti-6Mn-4Mo provides potential benefits in biomedical applications where wear resistance is desired. On the other hand, the heat treatment resulted in a noticeable decrease in hardness to 348.14±9.0 $HV_{0.1}$. The lower hardness value compared to that of the as-built condition can be explained by higher amount of α phase, as was demonstrated by XRD and SEM observations. Hardness of α phase is typically lower than that of β phase[46,47].

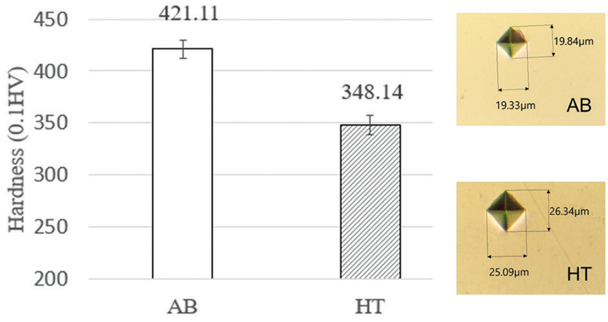

Figure 13. Vickers hardness of as-built and heat-treated Ti-6Mn-4Mo samples, and indentation images.
Abbreviations: AB: As-built; HT: Heat-treated.

3.6. Fracture surface analysis

To gain a deep understanding of tensile fracture mechanism, fracture surfaces of both as-built and heat-treated samples were analyzed using SEM and EDS, as shown in Figure 14. Figure 14A indicates that the fracture surface of the as-built material is dominated by large areas with smooth surface and large cleavage-like facets. The higher-magnification SEM image reveals that the smooth surface is covered with a river pattern (Figure 14C). Such fracture morphology suggests a brittle fracture, which agrees with the observed low elongation of the as-built sample. The fracture surface of the heat-treated samples contains large cleavage-like facets as well. However, its area contains more dimples compared to the fracture surface of the as-built sample. This explains the slight improvement of ductility after heat treatment for Ti-6Mn-4Mo. However, the elongation value of 1.6 % is still low in comparison to other Ti-Mn-Mo alloys reported in the literature. This can be explained by the lower concentration of Mo element and potential presence of embrittling ω phase in Ti-6Mn-4Mo samples. The third factor might be the presence of intermetallic phases formed during solidification. An example of such intermetallic phase is shown in the inset of Figure 14B. It shows a large, fractured particle of about 100 µm with smooth flat facets. EDS analysis revealed that it consists of only Ti and Mn. The presence of Ti-Mo compound (T_3Mo) in the heat-treated sample was also confirmed by XRD in this study. Similarly, intermetallic compound of T_3Mo was previously observed in Ti–Zr–Hf–Mo high entropy alloy[48].

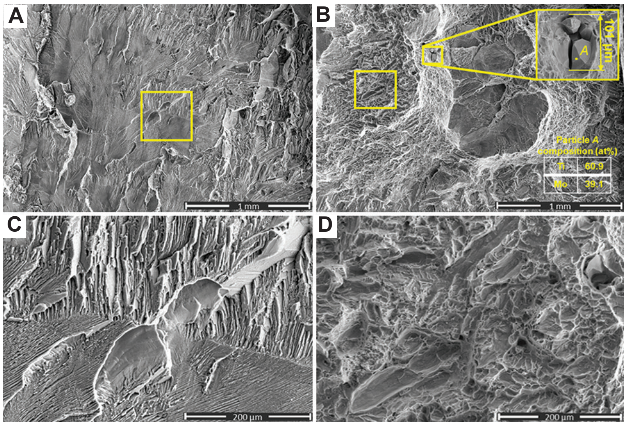

Figure 14. Scanning electron microscopy fracture surface images of (A and C) as-built and (B and D) heat-treated Ti-6Mn-4Mo. Yellow boxes in (A) and (B) are the areas to be magnified, with the higher-magnification images shown in (C) and (D), respectively.

4. Conclusions

In this study, Ti-6Mn-4Mo alloy was successfully synthesized by *in situ* alloying of elemental powders using laser DED technique. Both as-built and heat-treated materials were analyzed for resultant density, tensile properties, hardness, microstructure, elemental distribution, and corrosion resistance. The key findings are summarized in the following:

(i) As-built Ti-6Mn-4Mo consisted mainly of β phase, while there were signs of α phase presence in a small quantity. In contrast, the heat-treated material mostly consisted of α phase with traces of β phase still present. EDS mapping revealed that the distributions of elements were overall uniform.

(ii) The densities of both as-built and heat-treated Ti-6Mn-4Mo were close to the theoretical density for this composition, which was calculated by the rule of mixture. Furthermore, no cracks or major voids were detected, while some Mo powder particles failed to melt completely.

(iii) The difference in corrosion resistance between the as-built and heat-treated materials was insignificant. However, the corrosion resistance of both conditions was lower than the reported performance for Ti-6Al-4V alloys obtained through additive manufacturing techniques.

(iv) The DED-produced Ti-6Mn-4Mo materials appeared to be hard and brittle. It is possible that the high hardness and modulus were caused by the low concentration of alloying elements and the presence of ω phase.

Acknowledgments

None.

Funding

None.

Conflicts of interest

The authors declare that they have no competing interests.

Author contributions

Conceptualization: Jing Shi
Data curation: Roman Savinov
Formal analysis: Roman Savinov
Investigation: Roman Savinov, Yachao Wang, Jing Shi
Methodology: Yachao Wang, Jing Shi
Supervision: Jing Shi
Visualization: Roman Savinov
Writing – original draft: Roman Savinov
Writing – review & editing: Yachao Wang, Jing Shi

Ethics approval and consent to participate

Not applicable.

Consent for publication

Not applicable.

Availability of data

The data used in this study have been included in the paper.

References

1. Trevisan F, Calignano F, Aversa A, *et al.*, 2017, Additive manufacturing of titanium alloys in the biomedical field: Processes, properties and applications. *J Appl Biomater Funct Mater*, 16: 57–67.

   https://doi.org/10.5301/jabfm.5000371

2. Fu W, Liu S, Jiao J, *et al.*, 2022, Wear resistance and biocompatibility of Co-Cr dental alloys fabricated with CAST and SLM techniques. *Materials*, 15: 3263.

   https://doi.org/10.3390/ma15093263

3. Niinomi M, 2002, Recent metallic materials for biomedical applications. *Metallurgical Mater Trans A*, 33: 477–486.

   https://doi.org/10.1007/s11661-002-0109-2

4. Li Y, Yang C, Zhao H, *et al.*, 2014, New developments of Ti-based alloys for biomedical applications. *Materials*, 7: 1709–1800.

   https://doi.org/10.3390/ma7031709

5. Santos P, Niinomi M, Cho K, *et al.*, 2016, Development of New Ti-Mn-Mo Alloys for Use in Biomedical Applications. In: Proceedings of the 13th World Conference on Titanium. John Wiley & Sons, Inc., pp. 1741–1745.

6. Maitra V, Shi J, Lu C, 2022, Robust prediction and validation of as-built density of Ti-6Al-4V parts manufactured via selective laser melting using a machine learning approach. *J Manuf Processes*, 78: 183–201.

   https://doi.org/10.1016/j.jmapro.2022.04.020

7. Kuroda D, Niinomi M, Morinaga M, *et al.*, 1998, Design and mechanical properties of new β type titanium alloys for implant materials. *Mater Sci Eng A*, 243: 244–249.

   https://doi.org/10.1016/S0921-5093(97)00808-3

8. Santos PF, Niinomi M, Cho K, *et al.*, 2017, Effects of Mo addition on the mechanical properties and microstructures of Ti-Mn alloys fabricated by metal injection molding for biomedical applications. *Mater Trans*, 58: 271–279.

   https://doi.org/10.2320/matertrans.m2016286

9. Morioka R, Cho K, Yasuda HY, 2018, Effects of Mo addition on deformation behavior of metastable beta-type Ti-Mn single crystals. *Mater Sci Forum*, 941: 1360–1365.

   https://doi.org/10.4028/www.scientific.net/MSF.941.1360

10. Tanji A, Gapsari F, Syahrom A, *et al*., 2021, Effect of Mo addition on the pitting resistance of TiMn alloys in Hanks' solution. *J Alloys Compds*, 871: 159582.

https://doi.org/10.1016/j.jallcom.2021.159582

11. Santos P, Niinomi M, Liu H, *et al*., 2016, Improvement of microstructure, mechanical and corrosion properties of biomedical Ti-Mn alloys by Mo addition. *Mater Des*, 110: 414–424.

https://doi.org/10.1016/j.matdes.2016.07.115

12. Lourenço ML, Cardoso GC, Sousa K, *et al*., 2020, Development of novel Ti-Mo-Mn alloys for biomedical applications. *Sci Rep*, 10: 6298.

https://doi.org/10.1038/s41598-020-62865-4

13. Maitra V, Shi J, 2023, Evaluating the predictability of surface roughness of Ti–6Al–4V alloy from selective laser melting. *Adv Eng Mater*, 25: 2300075.

https://doi.org/10.1002/adem.202300075

14. Shi J, Wang Y, 2020, Development of metal matrix composites by laser-assisted additive manufacturing technologies: A review. *J Mater Sci*, 55: 9883–9917.

https://doi.org/10.1007/s10853-020-04730-3

15. Savinov R, Wang Y, Shi J, 2020, Microstructure and properties of CeO2-doped CoCrFeMnNi high entropy alloy fabricated by laser metal deposition. *J Manuf Processes*, 56: 1245–1251.

https://doi.org/10.1016/j.jmapro.2020.04.018

16. Wang J, Wang Y, Su Y, *et al*., 2022, Evaluation of in-situ alloyed Inconel 625 from elemental powders by laser directed energy deposition. *Mater Sci Eng A*, 830: 142296.

https://doi.org/10.1016/j.msea.2021.142296

17. Kosec T, Bajt Leban M, Ovsenik M, *et al*., 2022, Estimation of the corrosion properties for titanium dental alloys produced by SLM. *Mater Technol*, 56: 429–435.

https://doi.org/10.17222/mit.2022.519

18. Suresh S, Sun CN, Tekumalla S, *et al*., 2021, Mechanical properties and *in vitro* cytocompatibility of dense and porous Ti–6Al–4V ELI manufactured by selective laser melting technology for biomedical applications. *J Mech Behav Biomed Mater*, 123: 104712.

https://doi.org/10.1016/j.jmbbm.2021.104712

19. Wang N, Dheen ST, Fuh JYH, *et al*., 2022, Biocompatibility and mechanical properties evaluation of Ti-6Al-4V lattice structures with varying porosities. *Key Eng Mater*, 923: 21–29.

https://doi.org/10.4028/p-64o0e4

20. Tseng SF, Wang IH, Chang CM, *et al*., 2022, Mechanical characteristic comparison of additively manufactured Ti-6Al-4V lattice structures in biocompatible bone tissue growth. *Mater Sci Eng A*, 857: 144045.

https://doi.org/10.1016/j.msea.2022.144045

21. Zadeh MK, Yeganeh M, Shoushtari MT, *et al*., 2022, Microstructure, corrosion behavior, and biocompatibility of Ti-6Al-4 V alloy fabricated by LPBF and EBM techniques. *Mater Today Commun*, 31: 103502.

https://doi.org/10.1016/j.mtcomm.2022.103502

22. Xiang S, Yuan Y, Zhang C, *et al*., 2022, Effects of process parameters on the corrosion resistance and biocompatibility of Ti6Al4V parts fabricated by selective laser melting. *ACS Omega*, 7: 5954–5961.

https://doi.org/10.1021/acsomega.1c06246

23. Vonavkova I, Vojtech D, Palousek D, 2020, Characterization of β-Ti alloy prepared by SLM method. *Manuf Technol*, 20: 690–696.

https://doi.org/10.21062/mft.2020.091

24. Zhao D, Han C, Li J, *et al*., 2020, *In situ* fabrication of a titanium-niobium alloy with tailored microstructures, enhanced mechanical properties and biocompatibility by using selective laser melting. *Mater Sci Eng C*, 111: 110784.

https://doi.org/10.1016/j.msec.2020.110784

25. Lu HZ, Ma HW, Luo X, *et al*., 2021, Microstructure, shape memory properties, and *in vitro* biocompatibility of porous NiTi scaffolds fabricated via selective laser melting. *J Mater Res Technol*, 15: 6797–6812.

https://doi.org/10.1016/j.jmrt.2021.11.112

26. Batalha RL, Batalha WC, Deng L, *et al*., 2020, Processing a biocompatible Ti–35Nb–7Zr–5Ta alloy by selective laser melting. *J Mater Res*, 35: 1143–1153.

https://doi.org/10.1557/jmr.2020.90

27. Ishimoto T, Ozasa R, Nakano K, *et al*., 2021, Development of TiNbTaZrMo bio-high entropy alloy (BioHEA) super-solid solution by selective laser melting, and its improved mechanical property and biocompatibility. *Scr Mater*, 194: 113658.

https://doi.org/10.1016/j.scriptamat.2020.113658

28. Luo JP, Huang YJ, Xu JY, *et al*., 2020, Additively manufactured biomedical Ti-Nb-Ta-Zr lattices with tunable Young's modulus: Mechanical property, biocompatibility, and proteomics analysis. *Mater Sci Eng C Mater Biol Appl*, 114: 110903.

https://doi.org/10.1016/j.msec.2020.110903

29. Chakkravarthy V, Jose SP, Lakshmanan M, *et al*., 2022, Additive manufacturing of novel Ti-30Nb-2Zr biomimetic scaffolds for successful limb salvage. *Mater Today Proc*, 64: 1711–1716.

https://doi.org/10.1016/j.matpr.2022.05.469

30. Challis VJ, Xu X, Halfpenny A, *et al*., 2023, Understanding the effect of microstructural texture on the anisotropic

elastic properties of selective laser melted Ti-24Nb-4Zr-8Sn. *Acta Mater*, 254: 119021.

https://doi.org/10.1016/j.actamat.2023.119021

31. Wolff S, Lee T, Faierson E, *et al.*, 2016, Anisotropic properties of directed energy deposition (DED)-processed Ti–6Al–4V. *J Manuf Processes*, 24: 397–405.

    https://doi.org/10.1016/j.jmapro.2016.06.020

32. Ivanov S, Gushchina M, Artinov A, *et al.*, 2021, Effect of elevated temperatures on the mechanical properties of a direct laser deposited Ti-6Al-4V. *Materials*, 14: 6432.

    https://doi.org/10.3390/ma14216432

33. Tan H, Guo M, Clare AT, *et al.*, 2019, Microstructure and properties of Ti-6Al-4V fabricated by low-power pulsed laser directed energy deposition. *J Mater Sci Technol*, 35: 2027–2037.

    https://doi.org/10.1016/j.jmst.2019.05.008

34. Shalnova SA, Gushchina MO, Strekalovskaya DA, *et al.*, 2022, Electrochemical properties of the heat-treated Ti-6Al-4V alloy manufactured by direct energy deposition. *J Alloys Compds*, 899: 163226.

    https://doi.org/10.1016/j.jallcom.2021.163226

35. Gong X, Yabansu YC, Collins PC, *et al.*, 2020, Evaluation of Ti-Mn alloys for additive manufacturing using high-throughput experimental assays and Gaussian process regression. *Materials* (*Basel*), 13: 4641.

    https://doi.org/10.3390/ma13204641

36. Yang R, Liu Z, Yang G, *et al.*, 2012, Study of the Ti-20 wt. % Mo composite coating prepared by laser cladding. *Procedia Eng*, 36: 355–359.

    https://doi.org/10.1016/j.proeng.2012.03.052

37. Kang N, Lin X, Mansori ME, *et al.*, 2020, On the effect of the thermal cycle during the directed energy deposition application to the *in-situ* production of a Ti-Mo alloy functionally graded structure. *Addit Manuf*, 31: 100911.

    https://doi.org/10.1016/j.addma.2019.100911

38. Zhan H, Ceguerra AV, Wang G, *et al.*, 2018, Precipitation of string-shaped morphologies consisting of aligned α phase in a metastable β titanium alloy. *Sci Rep*, 8: 2038.

    https://doi.org/10.1038/s41598-018-20386-1

39. Wang CH, Liu M, Hu P, *et al.*, 2017, The effects of α″ and ω phases on the superelasticity and shape memory effect of binary Ti-Mo alloys. *J Alloys Compd*, 720: 488–496.

    https://doi.org/10.1016/j.jallcom.2017.05.299

40. Alshammari Y, Yang F, Bolzoni L, 2019, Mechanical properties and microstructure of Ti-Mn alloys produced via powder metallurgy for biomedical applications. *J Mech Behav Biomed Mater*, 91: 391–397.

    https://doi.org/10.1016/j.jmbbm.2018.12.005

41. Salahinejad E, Hadianfard MJ, Macdonald DD, *et al.*, 2013, *In vitro* electrochemical corrosion and cell viability studies on nickel-free stainless steel orthopedic implants. *PLoS One*, 8: e61633.

    https://doi.org/10.1371/journal.pone.0061633

42. Savinov R, Wang Y, Shi J, 2023, Evaluation of microstructure, mechanical properties, and corrosion resistance for Ti-doped inconel 625 alloy produced by laser directed energy deposition. *Mater Sci Eng A*, 884: 145542.

    https://doi.org/10.1016/j.msea.2023.145542

43. Chandramohan P, Bhero S, Obadele BA, *et al.*, 2017, Laser additive manufactured Ti-6Al-4V alloy: Tribology and corrosion studies. *Int J Adv Manuf Technol*, 92: 3051–3061.

    https://doi.org/10.1007/s00170-017-0410-2

44. Zhou X, Xu D, Geng S, *et al.*, 2021, Mechanical properties, corrosion behavior and cytotoxicity of Ti-6Al-4V alloy fabricated by laser metal deposition. *Mater Characterization*, 179: 111302.

    https://doi.org/10.1016/j.matchar.2021.111302

45. Coakley JA, Vorontsov VA, Jones N, *et al.*, 2015, Precipitation processes in the Beta-Titanium alloy Ti-5Al-5Mo-5V-3Cr. *J Alloys Compd*, 646: 946–953.

    https://doi.org/10.1016/j.jallcom.2015.05.251

46. Kao YH, Tu GC, Huang CA, *et al.*, 2005, A study on the hardness variation of α- and β-pure titanium with different grain sizes. *Mater Sci Eng A*, 398: 93–98.

    https://doi.org/10.1016/j.msea.2005.03.004

47. Jadhav S, Powar A, Patil S, *et al.*, 2017, Effect of volume fraction of alpha and transformed beta on the high cycle fatigue properties of bimodal Ti6Al4V alloy. *IOP Conf Ser*, 201: 012035.

    https://doi.org/10.1088/1757-899x/201/1/012035

48. Iijima Y, Nagase T, Matsugaki A, *et al.*, 2021, Design and development of Ti-Zr-Hf-Nb-Ta-Mo high-entropy alloys for metallic biomaterials. *Mater Des*, 202: 109548.

    https://doi.org/10.1016/j.matdes.2021.109548

ACCSCIENCE PUBLISHING

Materials Science in Additive Manufacturing

ORIGINAL RESEARCH ARTICLE

An experimental study on 3D-printed continuous fiber-reinforced composite auxetic structures

Peiqing Liu[1,2] and Jikai Liu[1,2]*

[1]Center for Advanced Jet Engineering Technologies (CaJET), Key Laboratory of High Efficiency and Clean Mechanical Manufacture (Ministry of Education), School of Mechanical Engineering, Shandong University, Jinan, Shandong, China

[2]Key National Demonstration Center for Experimental Mechanical Engineering Education, Shandong University, Jinan, Shandong, China

***Corresponding author:**
Jikai Liu
(jikai_liu@sdu.edu.cn)

Citation: Liu P, Liu J, 2023, An experimental study on 3D-printed continuous fiber-reinforced composite auxetic structures. *Mater Sci Add Manuf*, 2(4): 2159. https://doi.org/10.36922/msam.2159

Received: November 2, 2023

Accepted: November 29, 2023

Abstract

Auxetic structures have negative Poisson's ratios (NPR). Due to the unique deformation mechanism, auxetic structures possess extraordinary mechanical properties, such as indentation resistance, shear resistance, fracture toughness, and energy absorption capability. However, the stiffness and load-bearing capacity are the weak points for auxetic structures. 3D printing of continuous fiber-reinforced composite enables the fabrication of lightweight and highly stiff complex structures, providing a perfect manufacturing method to remedy the shortcomings of auxetic structures. This work investigated the mechanical properties of 3D-printed continuous fiber-reinforced composite auxetic structures. In this study, we utilized continuous fiber-reinforced composite 3D printing to fabricate two types of auxetic structures. The fiber path configurations were varied among the test specimens to explore the effect of fiber distribution on mechanical properties. A uniaxial tensile test was performed to evaluate the tensile properties and Poisson's ratio of continuous fiber-reinforced composite auxetic structures. Results showed that the tensile modulus and strength have been dramatically improved with a minor mass increase. The auxetic behavior can be strengthened by properly allocating the reinforcing fibers. However, the addition of continuous fiber led to different performances on the selected auxetic structures. In summary, two out of the five specimens demonstrated simultaneous improvements in stiffness, strength, and auxeticity across the conducted tests.

Keywords: Auxetic structures; Continuous fiber-reinforced composites; Additive manufacturing

1. Introduction

Auxetic materials are materials that have a negative Poisson's ratio (NPR). Applying stretching (compressive) load on the auxetic material results in a lateral expansion (contraction). The unusual deformation mechanism gives them excellent mechanical properties, such as resistance of indentation[1], resistance to shear[2], fracture toughness[3,4] and energy absorption capability[5]. Due to its superior properties, auxetic materials have potential applications in different fields, such as aerospace[6], sports[1], medicine[7], and energy absorbers[8,9]. It has been found that skins[10], ceramics, graphite, zeolite, metals, and other natural auxetic materials exhibit natural auxetic behaviors[11]. Inspired by natural architectures, several types of artificial auxetic structures have been designed, which can be classified into three types: re-entrant type, chiral type, and rotating rigid type[8]. With the advancement of additive manufacturing, auxetic structures are fabricated as mechanical metamaterials endowed with fascinating physical properties[12-15].

Due to the porosity and deformability, auxetic structures generally have lower stiffness and load-bearing capacity. To enhance the mechanical properties of auxetic materials, auxetic composites are developed. The auxetic chiral structure can be 3D-printed with thermoplastic polyurethane elastomer (TPU) and then filled with polyurethane (PU) foam, producing a foam-filled chiral structure that is significantly reinforced in terms of stiffness and specific energy absorption capacity[5]. A study by Xue *et al.*[16] showed that the composites fabricated by combining aluminum-based auxetic lattice structure with polymer fillers exhibited higher elastic modulus, compressive strength, and energy absorption capacity, as verified in the compressive experiment. Another study showed that the printed auxetic chiral structures fabricated from high-performance composites added with chopped carbon fibers manifested enhanced tensile modulus, strength, and energy absorption[17].

Continuous fiber-reinforced composites encompass several desirable advantages, such as lightweight, high strength, and stiffness. They have been widely used in the fields of automobile, aircraft, and space[18-20]. 3D printing of continuous fiber-reinforced composites provides a feasible avenue to bridge the gap between advanced materials and innovative structures. Hou *et al.* have demonstrated the design and fabrication of a novel corrugated structure and discussed the correlations among the process parameters, structure parameters, density, fiber content, and final performance of the printed specimens[21]. Besides that, the manufacture of sandwich structures in different shapes using a continuous carbon fiber 3D printer has also been attempted[22]. Considering the requirement on path continuity, Liu *et al.*[23] proposed a path-driven design method to generate lattice structures with designable anisotropy and close-to-zero mean curvatures for 3D printing of continuous fiber-reinforced composites. In addition to improving mechanical properties, accentuating the multi-functional properties of continuous fibers such as sensing[24], shape morphing,[25,26] and electromagnetic interference shielding[27] provides a new direction for developing smart structures.

The 3D-printed continuous fiber-reinforced composite auxetic structures possess the unified advantages of both continuous fibers and auxetic structures. Given these desirable benefits, Dong *et al.* developed continuous fiber-reinforced auxetic composite structures for reusable energy absorption applications[28]. Another study fabricated continuous fiber-reinforced re-entrant auxetic honeycomb structures through the 3D printing technology by tailoring the printing path to ensure better fiber path continuity[29], and concluded that adding continuous fibers led to dramatic increases in compressive stiffness, energy absorption, and smaller NPR. As disclosed earlier, the auxetic behaviors come from different types of deformation mechanisms, and due to the high and anisotropic stiffness/strength of continuous fibers, their addition would not result in consistent performance on different types of auxetic structures.

This study aimed to investigate the mechanical properties of 3D-printed continuous fiber-reinforced composite auxetic structures. Auxetic test specimens with different topology and fiber path configurations were fabricated and evaluated for mechanical properties, including tensile modulus, tensile strength, and Poisson's ratio, using uniaxial tensile test. The effect of adding continuous fibers on the properties of the structures is discussed.

2. Materials and methods

To investigate the mechanical properties of continuous fiber-reinforced composite auxetic structures, we designed and fabricated a group of test specimens and evaluated their mechanical properties through a uniaxial tensile test.

2.1. Design of specimens

Three types of structures are selected as test specimens (Figure 1). Two of them are auxetic structures: the rotating rigid[30] and the re-entrant types[31]. The other is a structure with a positive Poisson's ratio named rhombus. The dimensions of the unit cell of the three specimens are 16 × 16 mm. The rotation angle of a single square in a rotating rigid structure is 15°. The width of rods in re-entrant and rhombus structures is 2 mm.

Figure 2 displays the dimensions of the test specimen. The test specimen is composed of a 4 × 7 array of unit cells and two holders. To capture a more obvious auxetic behavior and shorten the manufacturing cycle, the thickness of specimens was set as 2 mm. The test specimen was fixed on the test machine through holders, and the uniaxial tensile loads were applied along the y direction.

Due to the property anisotropy of continuous fibers, the distribution of fiber paths has a great impact on the

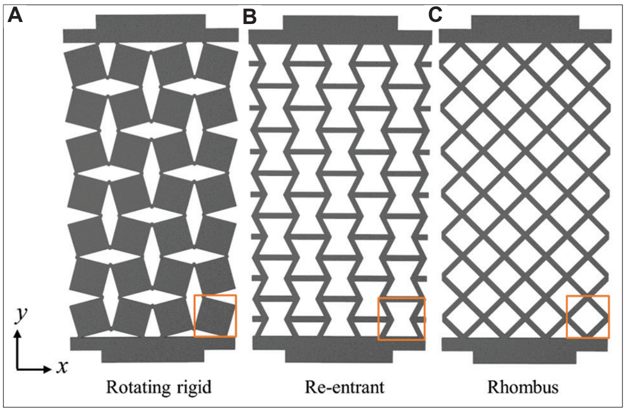

Figure 1. (A-C) Tree types of auxetic structures.

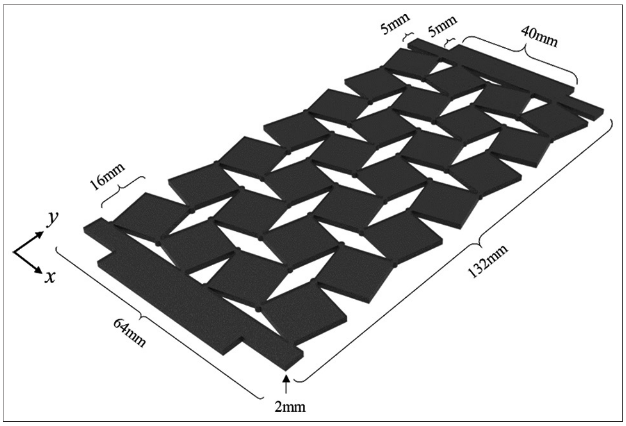

Figure 2. Dimensions of the test specimen.

mechanical properties of composites. As shown in Figure 3, different types of fiber distributions were designed for each type of specimen. To better differentiate between the staggered fiber paths, the continuous fiber paths, as shown in Figure 3, were colored orange or blue. For rotating rigid, the first distribution contains fiber paths along the x direction and y direction (Figure 3A). In the second design (Figure 3B), only fibers along the y direction will infill the structure. The third design (Figure 3C) contains only fibers along the x direction. The fiber paths in re-entrant FR1 (Figure 3D) are distributed along the y direction, and the fiber paths in re-entrant FR2 (Figure 3E) are distributed along the x direction. The rhombus FR is designed with fiber paths along the y direction.

2.2. Fabrication of specimens

The test specimens were fabricated using the Anisoprint[32] A4 3D printer (Figure 4A). There are two nozzles in the printer; the plastic nozzle extrudes Smooth PA, which is a thermoplastic polymer material filled with chopped carbon fibers, whereas the other nozzle simultaneously feeds thermoplastic polymer called CFC PA and continuous fiber-reinforced composite into the nozzle. As shown in Figure 4, the left nozzle is used for fabricating the plastic external shell (Figure 4B) and the right nozzle is used to extrude continuous fiber composites (Figure 4D). The reinforcing fiber is a 1.5K composite carbon fiber with a diameter of 0.36 mm and a tensile strength of 2130 ± 230 MPa. Smooth PA, CFC PA, and composite carbon fiber were obtained from Anisoprint[32]. The mechanical properties of the printing materials are listed in Table 1. The printing temperature of both nozzles is 240°C, and the building plate temperature is 60°C.

Figure 5 illustrates the printing layers of the specimen during fabrication. For the composite specimen (Figure 5B), there are 15 layers in total. The height of the first layer is 0.2 mm, while the height of other layers fabricated with Smooth PA is 0.12 mm. The layer height of continuous fiber-reinforced composite is three times that of the external shell, i.e., 0.36 mm. It should be noted that there are interlaced and overlapping regions in the designed fiber path (*e.g.*, Figure 3A and E). The 3D printer is capable of handling local overlaps of fibers. As shown in Figure 4D, the composite extruder presses the fiber composites to fill the matrix. The local overlaps are compacted for controlling layer height (Figure 4E). Due to the high stiffness of fibers and the excessive force from the nozzle[33], the 3D-printed fiber bundles cannot build sharp corners, as shown in Figure 4C. The specimens without reinforcing fibers utilize the same path pattern for the plastic nozzle but lack the fiber composite extruder, thereby transforming the fiber space into a void (Figure 5A). The 3D-printed test specimens are displayed in Figure 6. Compared with specimens fabricated by Smooth PA, there was a minor increase in the weight of the continuous fiber-reinforced composite structures.

2.3. Evaluation of mechanical properties

Uniaxial tensile tests were performed on the WDW-20M universal test machine with a maximum 20 kN load (Figure 7A). The loading speed was set to 5 mm/min. The load and displacement data derived from the test machine were used to plot the stress-strain curves. The tensile modulus E_y was extracted from the linear stage of stress-strain curve using Equation I:

$$E_y = \frac{\sigma}{\varepsilon_y} \tag{I}$$

where σ is the stress calculated by $\frac{F}{A}$ in which A is the cross-section area. The peak stress of the stress-strain curve is regarded as tensile strength.

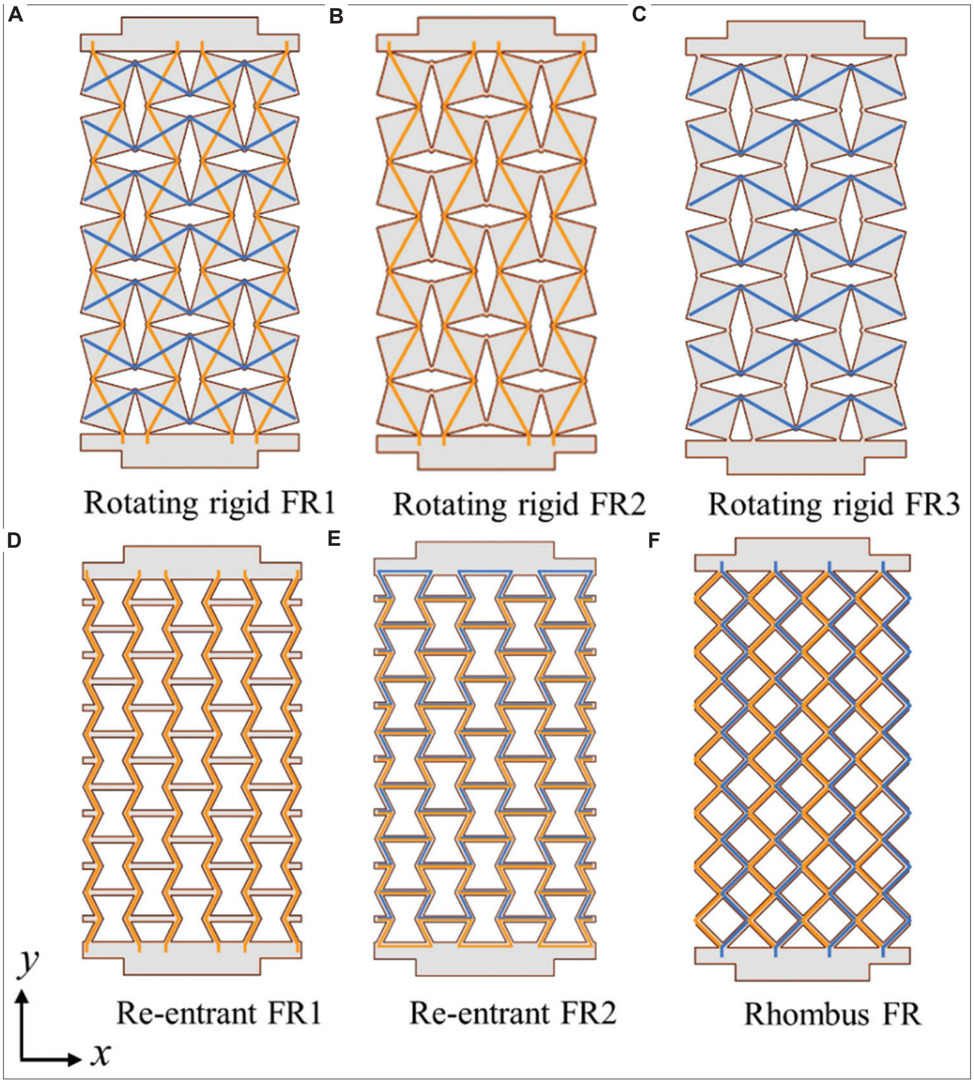

Figure 3. (A-F) Design of fiber paths.

A digital camera was used to record the deformation during the tensile test. The axial and lateral strains (ε_y and ε_x, respectively) can be derived from the images (Figure 7B). The Poisson's ratio v_{yx} was calculated using Equation II:

$$v_{yx} = -\frac{\varepsilon_x}{\varepsilon_y} \tag{II}$$

3. Results and discussion

3.1. Deformation behaviors of structures

The test specimens were evaluated in uniaxial tensile tests. The deformation behaviors were captured by the digital camera. It was shown that the topology of the structure had a great impact on the deformation behaviors and the mechanical properties. Figure 8 displays the deformations of the test specimens under tension. All the specimens depicted in Figure 8 were fabricated using only Smooth PA, allowing for the characterization of mechanical properties in the absence of reinforcing fibers.

Due to the difference in topology, the deformation mechanism varies between structures, thus leading to different values of Poisson's ratio. The observed deformations of the three types of specimens are shown in Figure 8A. The rotating rigid structure consists of a group of squares with different angles, which are connected with each other by the intersection of vertices. When the tensile loads were applied, the movements of individual vertices drove the rotation of all squares. Afterward, the rotation enlarged the space between the squares, and the whole structure started to exhibit auxetic behavior. The re-entrant structure has a different way of exhibiting auxetic behavior. When the structures were under tension, the re-entrant struts stretched out and pushed the horizontal ribs nearby outward, leading to the extension of the whole structure. Different from the other two auxetic structures, the rhombus structure has a positive Poisson's ratio. When the tensile loads were applied, the rhombus structure was elongated and transversely contracted. In summary, the test specimens undergo two types of deformation, namely tensile deformation and mechanism-type deformation. The latter involves rotation in the rotating rigid and angle change of struts in the re-entrant and rhombus structures. Of note, the Poisson's ratio of the structures exhibits a broad range of variation mainly due to the mechanism-type deformation.

Table 1. Mechanical properties of printing materials

Materials	Young's modulus (MPa)	Tensile strength (MPa)
Smooth PA	5.82×10^3	15.2
CFC PA	1251.45±282.43	41.05±1.20
Reinforcing fiber	$135\pm15\times10^3$	2130±230

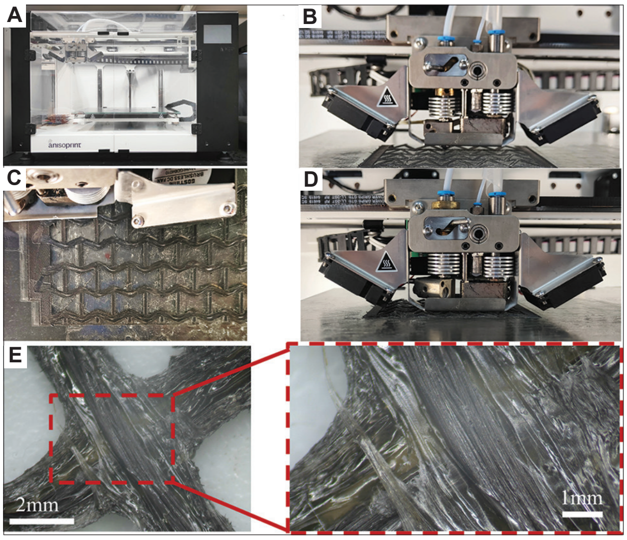

Figure 4. Fabrication of test specimens. (A) Continuous fiber-reinforced composite 3D printer. (B) Plastic extruder. (C) Display of fiber layer. (D) Composite extruder. (E) A close view of continuous fiber composite.

The difference in the deformation mechanism leads to different values of Poisson's ratio. In this study, the tensile tests were terminated when failure occurred. The Poisson's ratios under different strains were calculated and summarized in Figure 8C. The rotating rigid and re-entrant structures have a similar Poisson's ratio at the initial stage of the tensile test. However, because of the different deformation mechanisms, they have opposite variation tendencies. The auxetic behavior of the rotating rigid structure was induced by the rotation of squares. Along with the increase of tensile strain, the rotation angles also increased, continuously enlarging the spaces between squares until the rotation angle reached 45°. The failure occurred before the rotation angle reached the critical degree. Therefore, the rotating rigid structure presented a continuous decreasing trend of Poisson's ratios. As for the re-entrant structure, the application of tensile loads on the structure led to less obvious re-entrant characteristics along the stretching. Thus, the lateral extension slowed down while the longitudinal extension remained, leading to an increasing Poisson's ratios along with an increase in tensile strain.

The stress-strain curves of three specimens are shown in Figure 8B. It can be observed that the re-entrant structure has the maximum tensile modulus and tensile strength. As shown in the von Mises distribution (Figure 9B), the vertical struts are the major load-bearing components. The stress-strain curve of the re-entrant structure can be divided into three stages: linear elastic stage, plateau stage, and plastic stage. In the linear elastic stage, the stress increased proportionally with the strain. Plastic deformations or small fractures occurred at some locations, especially the stress-concentrated areas (Figure 9B). Such behaviors led to mechanism-type deformation, marked by the angle change of the re-entrant struts. In theory, the mechanism-type deformation produces lateral displacement output. The stress-strain curve was said to be in the plateau stage when the stress ceased to increase. In the plastic stage, both tensile deformation and mechanism-type deformation happened. Both the rotating rigid and rhombus structures lack components to directly bear the tensile loads and the stress concentration at the joints. Thus, they were underperforming in terms

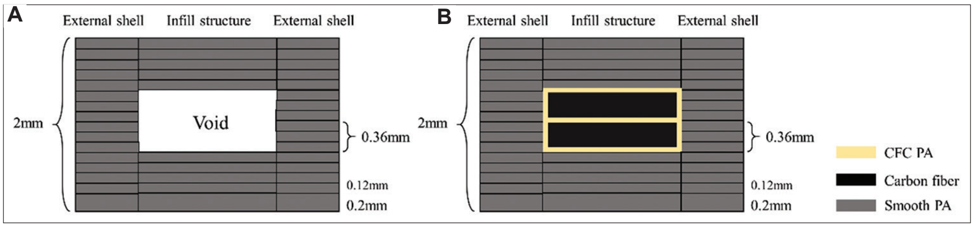

Figure 5. Illustration of printing layers. (A) Specimens without reinforcing fibers. (B) Specimens infilled with reinforcing fibers.

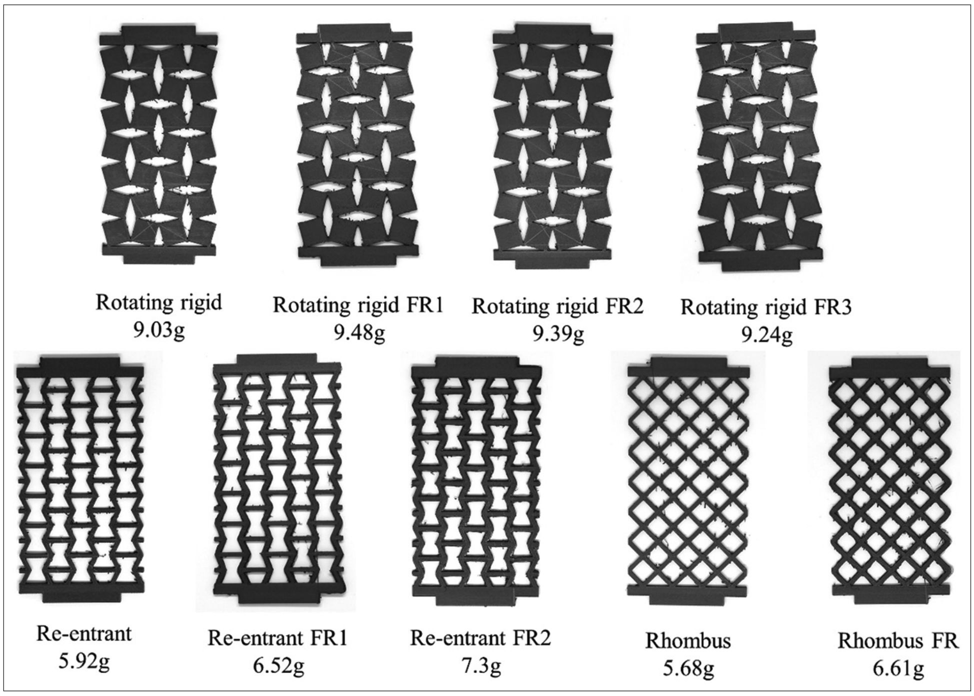

Figure 6. Display of printed test specimens.

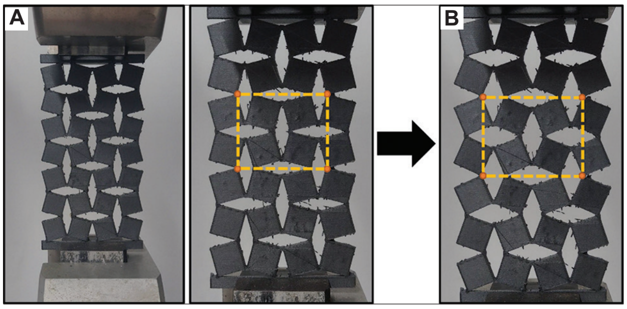

Figure 7. Evaluation of Poisson's ratio via tensile test. (A) Uniaxial tensile test. (B) Images of deformation of the test specimen, from which we can obtain the axial and lateral strain.

of tensile modulus and strength. As shown in Figure 10, the location of failure is consistent with the layout of stress concentrations.

3.2. Effect of continuous fibers on tensile behavior

The continuous carbon fiber has prominent performance in stiffness and strength. In this work, only two layers of continuous carbon fibers were infilled in the auxetic structures. The tensile modulus and tensile strength were calculated based on stress-strain curves (Figure 11B, Figure 12B, Figure 13B) and summarized in Table 2. Results showed that a weight increase of less than 20% resulted in a significant increase in tensile modulus and tensile strength. The reinforcing effect was conspicuous, especially for rotating rigid and rhombus structures, which had weak regions at joints. With a 4.75% increase in weight, rotating rigid FR1 was endowed with 2.69 times tensile modulus and 2.77 times tensile strength, compared with the specimen without reinforcing fibers. Similar improvements can also be found in rotating rigid FR2 and rhombus FR.

Due to the anisotropy of carbon fiber, the printing direction has a great impact on the tensile properties of specimens. This can be illustrated by the comparison between re-entrant FR1 and re-entrant FR2. Although re-entrant FR2 was infilled with a higher percentage of fibers, the tensile strength of re-entrant FR2 was lower than that of re-entrant FR1 because the fiber direction in re-entrant FR2 was perpendicular to the loading direction, while the fiber direction in re-entrant FR1 was parallel with the loading direction. On the other hand, the tensile modulus was weakly correlated to the printing direction. The addition of fiber composites increased the tensile modulus of re-entrant FR2, which had the highest tensile modulus of 189.25MPa among the specimens since it has the highest fiber composite content. A similar trend also happened to rotating rigid FR3. Although infilled with 2.27% fiber composites, the rotating rigid FR3 achieved a tensile strength increase of only 13%, which is much lower than the strength improvements observed in the other two reinforcing specimens.

The continuous reinforcing fibers significantly improved the tensile properties of test specimens.

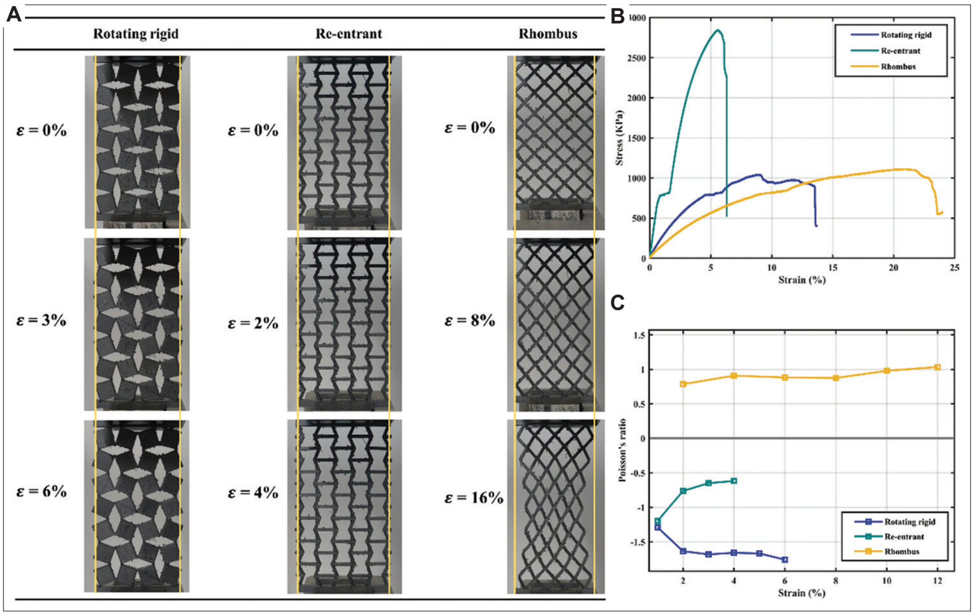

Figure 8. Test results of three types of lattice structures without reinforcing fibers. (A) Deformation of test specimens. (B) Stress-strain curves of three specimens under tensile loads. (C) Plots of Poisson's ratio versus strain of three specimens.

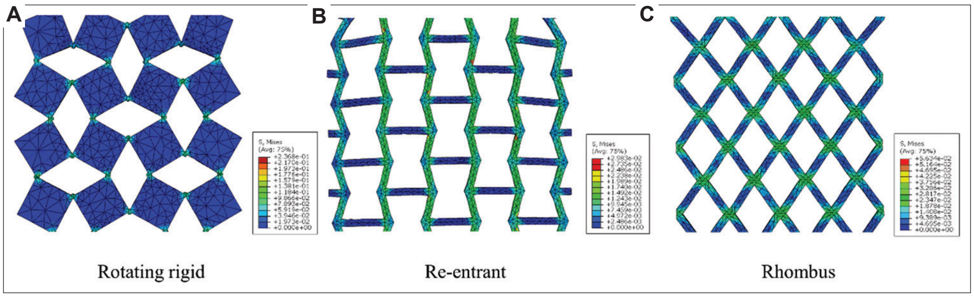

Rotating rigid Re-entrant Rhombus

Figure 9. (A-C) von Mises distributions of three types of structures. The finite element analysis was conducted using the commercial FE software called Abaqus. The boundary condition used in this analysis aligned with the conditions set in the physical experiment. The upper holder was fixed, and a displacement-load boundary condition was applied to the bottom holder. Homogeneous nylon materials, with Young's modulus of 5.82GPa and a Poisson's ratio of 0.3, were adopted as the finite element model.

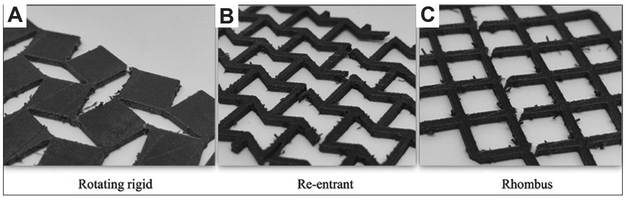

Rotating rigid Re-entrant Rhombus

Figure 10. (A-C) Fractures in three types of structures.

Moreover, the addition of fibers also successfully prevented the sudden failure of the test specimens. Our results showed several sudden drops in the stress-strain curves of fiber-reinforced specimens (Figure 11B, Figure 12B, Figure 13B). Since the composite fiber is composed of 1.5K carbon monofilaments, a small portion of the failed fibers will not lead to the failure of the whole structure unless the fiber bundle is broken. Nevertheless, the stress curve will fluctuate within a certain range.

3.3. Effect of continuous fibers on auxetic behavior

The auxetic behaviors of different types of structures varied because they were deformed by different deformation mechanisms. The addition of fiber composites had discrepant effects on structures formed by different deformation mechanisms. In addition, the distribution of reinforcing fibers also contributes to such a difference. The test results comparison between different auxetic structures and fiber reinforcement patterns is shown in Figures 11 and 12.

As shown in Figure 11C, the changes in Poisson's ratio of the fiber-reinforced specimens share similar trends with the specimens fabricated with pure Smooth

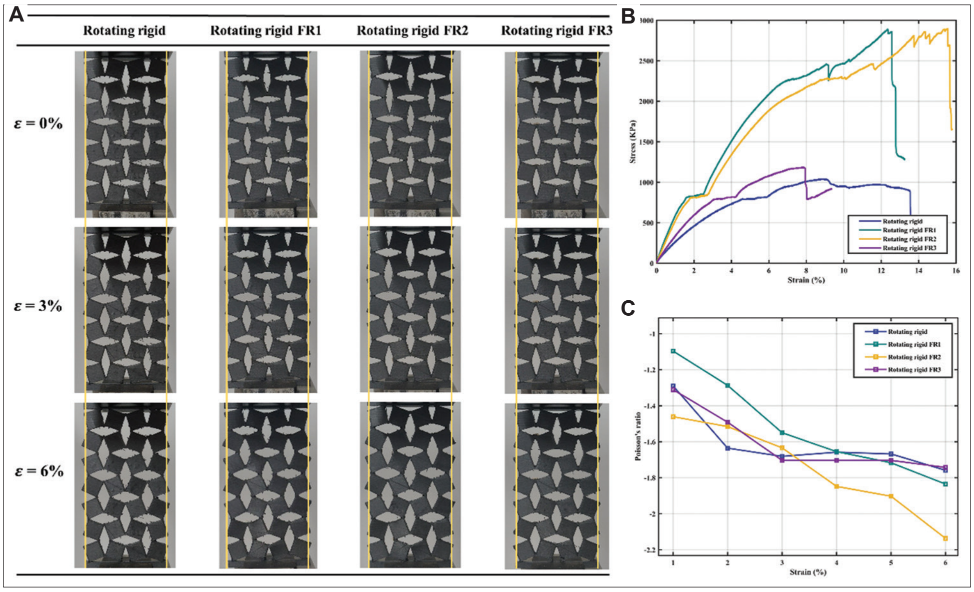

Figure 11. Test results of rotating rigid structures. (A) Deformation of test specimens. (B) Stress-strain curves of three specimens under tensile loads. (C) Plots of Poisson's ratio versus strain of three specimens.

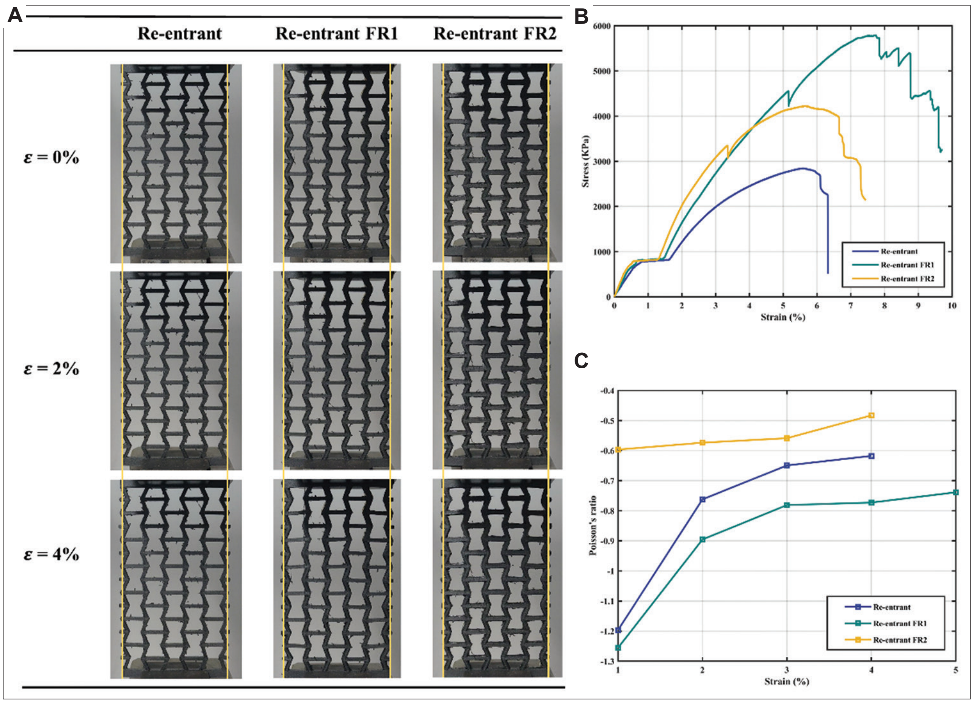

Figure 12. Test results of re-entrant structures. (A) Deformation of test specimens. (B) Stress-strain curves of three specimens under tensile loads. (C) Plots of Poisson's ratio versus strain of three specimens.

PA. The auxetic behavior of rotating rigid structure was engendered by the rotation of squares, and the addition of fibers has little influence on such deformation. Despite the similar trends, Poisson's ratios of the fiber-reinforced specimens and the specimens fabricated with pure Smooth PA were inherently different, a disparity caused by the different patterns of fiber reinforcement. Rotating rigid FR2, which was infilled with four continuous fibers along the axial direction (Figure 3), had the smallest Poisson' ratio. Due to the high stiffness, the reinforcing fibers limited the tensile deformation of the structure, causing a decrease in Poisson's ratio (according to

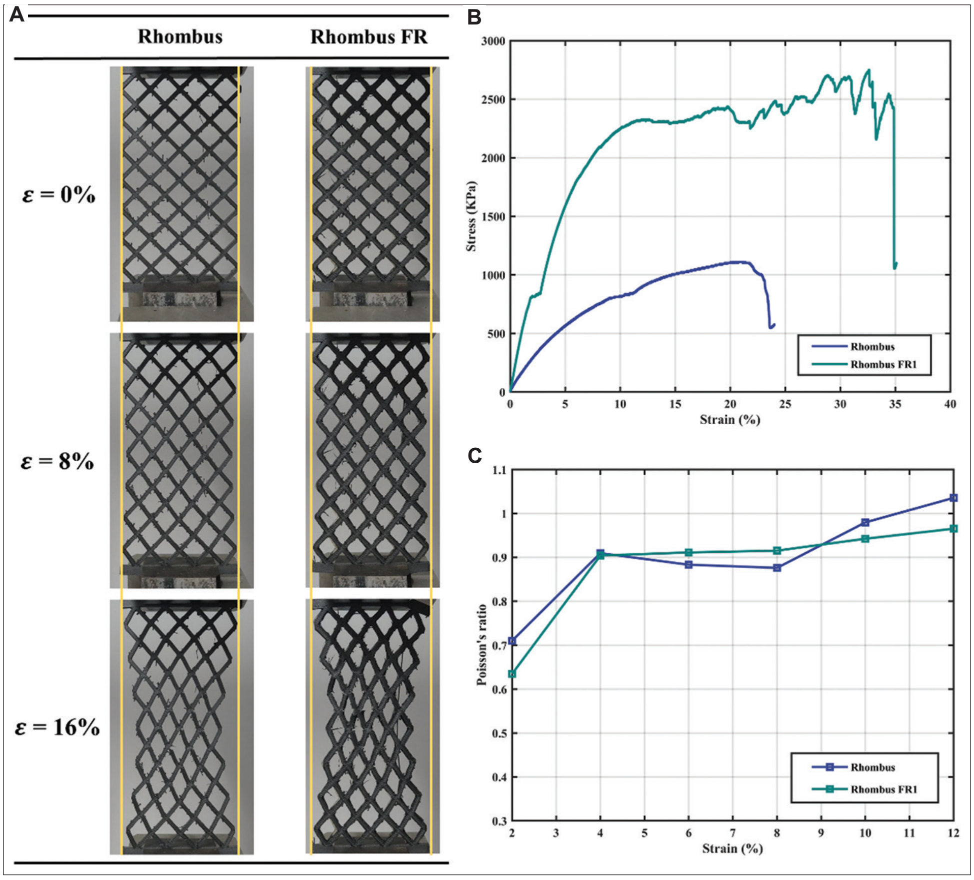

Figure 13. Test results of rhombus structures. (A) Deformation of test specimens. (B) Stress-strain curves of three specimens under tensile loads. (C) Plots of Poisson's ratio versus strain of three specimens.

Equation II). Rotating rigid FR3 was infilled with lateral fibers that had little influence on the auxetic behavior, and thus, the Poisson's ratio of rotating rigid FR3 was roughly the same as that of rotating rigid. The rotating rigid FR1 was reinforced by both axial and lateral continuous fibers. The fiber composites (highest percentage) increased the rigidity of joints in rotating rigid FR1, whose rotating deformation at the initial stage was less pronounced than that of other specimens. This illustrates the reason why rotating rigid FR1 had the highest Poisson's ratio under low strain.

When rotating rigid FR2 was stretched and horizontally expanded, warpage (out of plane) deformation occurred due to the squeezing of the squares (Figure 14B). In contrast, fracture occurred in the test specimens without infilled continuous fiber (Figure 14A) before stretching to warpage. Both of the above-mentioned failures can lead to degradation of the auxetic behavior.

As shown in Figure 12C, the re-entrant FR2 infilled with lateral continuous reinforcing fibers (Figure 3E) exhibited less auxetic effect than the other two specimens as a consequence of the weakened mechanism-type deformation. There were some overlaps in the fiber paths of re-entrant FR2 (Figure 3E). The overlapped fibers and excessive binding materials (CFC PA) increased the rigidity of joints, thus weakening the mechanism-type deformation of the re-entrant structure. For re-entrant FR1, the infilled reinforcing fibers along the axial direction had little effect on lateral deformation but had a constraining impact on axial deformation. This led to a lower Poisson's ratio in re-entrant FR1 as compared with specimens without fibers.

A structure named rhombus, having a positive Poisson' ratio, was also evaluated as a supplement to other test specimens through the tensile test. As shown in Figure 13C, the Poison's ratio of rhombus FR is similar to rhombus without fiber. The existence of axial reinforcing fibers in rhombus FR limited the axial deformation, which gives the structure a greater inclination toward rotation. On the other side, the intersections of fiber paths increased the rigidity of joints, thus restricting the rotation-dominated deformation. Since these two factors mutually negate each other, rhombus FR and rhombus ended up with similar

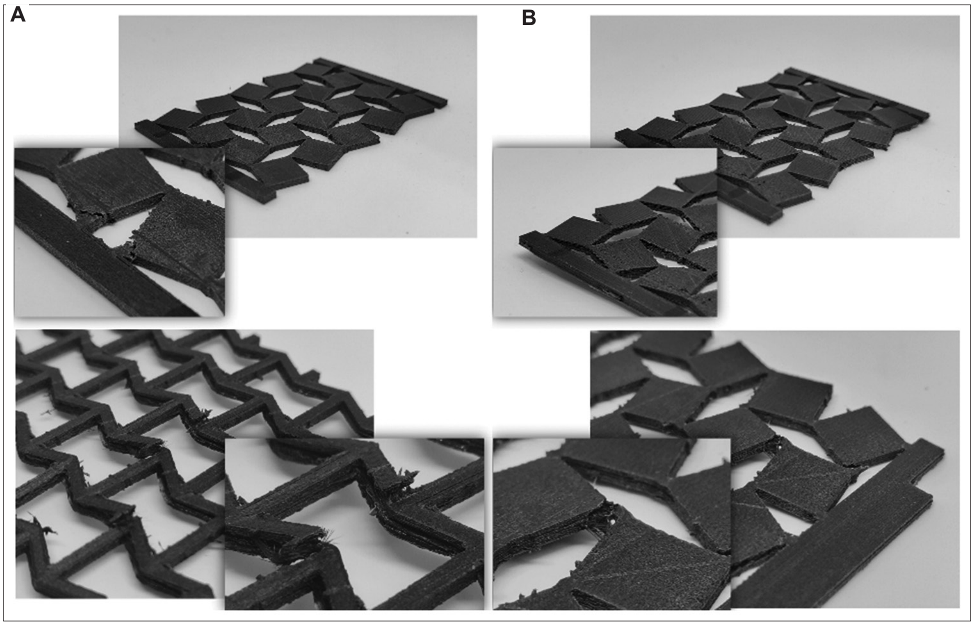

Figure 14. Failures in test specimens. (A) The fracture occurred in the test specimens without infilled continuous fiber. (B) The warpage deformation occurred in the fiber-reinforced test specimens.

Table 2. Properties of test specimens

Structures	Tensile modulus (MPa)	Tensile strength (MPa)	Weight (g)	Carbon fiber ratio (%)
Rotating rigid	22.45	1.039	9.03	0.00
Rotating rigid FR1	60.55	2.883	9.48	4.75
Rotating rigid FR2	51.68	2.891	9.39	3.83
Rotating rigid FR3	30.65	1.180	9.24	2.27
Re-entrant	114.19	2.836	5.92	0.00
Re-entrant FR1	150.02	5.781	6.52	9.20
Re-entrant FR2	189.25	4.229	7.30	18.90
Rhombus	13.64	1.109	5.68	0.00
Rhombus FR	49.58	2.742	6.61	14.07

Poison's ratios. Along with the increase in tensile strain, the fibers were found to straighten and separate from the base material, as shown in Figure 13A.

In summary, the addition of fibers does influence the auxetic behavior of both rotating rigid and re-entrant structures. The auxetic behavior can be strengthened by allocating axial fibers to limit axial deformation, thereby making the mechanism-type deformation the dominant form of deformation. On the other hand, the inappropriate addition of continuous fibers may weaken the auxetic behavior as a result of the accumulation of too many materials at the joints, causing high rigidity that blocks mechanism-type deformation.

4. Conclusion

In this work, we successfully investigated the mechanical properties of 3D-printed continuous fiber-reinforced composite auxetic structures in the uniaxial tensile test. The major highlight of this study is that the addition of continuous fiber can significantly enhance the tensile properties of auxetic structures. With only a 3.83% mass increase, the tensile modulus and tensile strength of rotating rigid FR2 almost tripled as compared with the specimens without infill fibers. Owing to the anisotropy of continuous fibers, the direction of the fiber path plays a key role in the tensile properties. The auxetic behavior can be strengthened by limiting axial deformation caused by axial reinforcing fibers. Our findings also showed that rotating rigid FR2 and re-entrant FR1 similarly achieve improvements in stiffness, strength, and auxeticity following the addition of continuous fibers. However, the inappropriate addition of continuous fibers can weaken the auxeticity behavior due to the increasing rigidity of joints.

Acknowledgments

None.

Funding

The authors would like to acknowledge the support from Shandong Provincial Key Research and Development Program (Major Scientific and Technological Innovation Project) (2021CXGC010206).

Conflict of interest

The authors declare they have no competing interests.

Author contributions

Conceptualization: Jikai Liu, Peiqing Liu
Formal analysis: Peiqing Liu
Investigation: Peiqing Liu
Methodology: Peiqing Liu, Jikai Liu
Writing – original draft: Peiqing Liu
Writing – review & editing: Peiqing Liu, Jikai Liu

Ethics approval and consent to participate

Not applicable.

Consent for publication

Not applicable.

Availability of data

Data will be made available upon request.

References

1. Sanami M, Ravirala N, Alderson K, *et al.*, 2014, Auxetic materials for sports applications. *Procedia Eng*, 72: 453–458.

   https://doi.org/10.1016/j.proeng.2014.06.079

2. Choi JB, Lakes RS, 1995, Nonlinear analysis of the poissons ratio of negative poissons ratio foams. *J Compos Mater*, 29: 113–128.

   https://doi.org/10.1177/002199839502900106

3. Lakes R, 1987, Foam structures with a negative poisson's ratio. *Science*, 235: 1038–1040.

   https://doi.org/10.1126/science.235.4792.1038

4. Donoghue JP, Alderson KL, Evans KE, 2009, The fracture toughness of composite laminates with a negative Poisson's ratio. *Phys Status Solidi*, 246: 2011–2017.

   https://doi.org/10.1002/pssb.200982031

5. Zhang XG, Ren X, Jiang W, *et al.*, 2022, A novel auxetic chiral lattice composite: Experimental and numerical study. *Compos Struct*, 282: 115043.

   https://doi.org/10.1016/j.compstruct.2021.115043

6. Wang Z, Zulifqar A, Hu H, 2016, Auxetic composites in aerospace engineering. In: Advanced Composite Materials for Aerospace Engineering. Netherlands: Elsevier, pp. 213–240.

   https://doi.org/10.1016/B978-0-08-100037-3.00007-9

7. Bhullar SK, 2013, Influence of negative poisson's ratio on stent applications. *Adv Mater*, 2: 42.

   https://doi.org/10.11648/j.am.20130203.14

8. Saxena KK, Das R, Calius EP, 2016, Three decades of auxetics research - materials with negative poisson's ratio: A review. *Adv Eng Mater*, 18: 1847–1870.

   https://doi.org/10.1002/adem.201600053

9. Novak N, Vesenjak M, Ren Z, 2016, Auxetic cellular materials - a review. *Strojniški Vestn J Mech Eng*, 62: 485–493.

   https://doi.org/10.5545/sv-jme.2016.3656

10. Pissarenko A, Yang W, Quan H, *et al.*, 2019, Tensile behavior and structural characterization of pig dermis. *Acta Biomater*, 86: 77–95.

    https://doi.org/10.1016/j.actbio.2019.01.023

11. Balan PM, Mertens AJ, Bahubalendruni MVAR, 2023, Auxetic mechanical metamaterials and their futuristic developments: A state-of-art review. *Mater Today Commun*, 34: 105285.

    https://doi.org/10.1016/j.mtcomm.2022.105285

12. Kolken HMA, Zadpoor AA, 2017, Auxetic mechanical metamaterials. *RSC Adv*, 7: 5111–5129.

    https://doi.org/10.1039/C6RA27333E

13. Jin Y, Xie C, Gao Q, *et al.*, 2021, Fabrication of multi-scale and tunable auxetic scaffolds for tissue engineering. *Mater Des*, 197: 109277.

    https://doi.org/10.1016/j.matdes.2020.109277

14. Zheng X, Guo X, Watanabe I, 2021, A mathematically defined 3D auxetic metamaterial with tunable mechanical and conduction properties. *Mater Des*, 198: 109313.

    https://doi.org/10.1016/j.matdes.2020.109313

15. Fozdar DY, Soman P, Lee JW, *et al.*, 2011, Three-dimensional polymer constructs exhibiting a tunable negative poisson's ratio. *Adv Funct Mater*, 21: 2712–2720.

    https://doi.org/10.1002/adfm.201002022

16. Xue Y, Wang W, Han F, 2019, Enhanced compressive mechanical properties of aluminum based auxetic lattice structures filled with polymers. *Compos B Eng*, 171: 183–191.

    https://doi.org/10.1016/j.compositesb.2019.05.002

17. Hu C, Dong J, Luo J, *et al.*, 2020, 3D printing of chiral carbon fiber reinforced polylactic acid composites with negative Poisson's ratios. *Compos B Eng*, 201: 108400.

    https://doi.org/10.1016/j.compositesb.2020.108400

18. Tian X, Todoroki A, Liu T, *et al.*, 2022, 3D printing of continuous fiber reinforced polymer composites: Development, application, and prospective. *Chin J Mech Eng Addit Manuf Front*, 1: 100016.

    https://doi.org/10.1016/j.cjmeam.2022.100016

19. Cheng P, Peng Y, Li S, *et al.*, 2023, 3D printed continuous fiber reinforced composite lightweight structures: A review

and outlook. *Compos B Eng*, 250: 110450.

https://doi.org/10.1016/j.compositesb.2022.110450

20. van de Werken N, Tekinalp H, Khanbolouki P, *et al*., 2020, Additively manufactured carbon fiber-reinforced composites: State of the art and perspective. *Addit Manuf*, 31: 100962.

    https://doi.org/10.1016/j.addma.2019.100962

21. Hou Z, Tian X, Zhang J, *et al*., 2018, 3D printed continuous fibre reinforced composite corrugated structure. *Compos Struct*, 184: 1005–1010.

    https://doi.org/10.1016/j.compstruct.2017.10.080

22. Sugiyama K, Matsuzaki R, Ueda M, *et al*., 2018, 3D printing of composite sandwich structures using continuous carbon fiber and fiber tension. *Compos A Appl Sci Manuf*, 113: 114–121.

    https://doi.org/10.1016/j.compositesa.2018.07.029

23. Liu P, Lu L, Liu J, 2023, Path-driven shell lattices designed for continuous fiber composite 3D printing. *Addit Manuf*, 78: 103838.

    https://doi.org/10.1016/j.addma.2023.103838

24. Luan C, Yao X, Zhang C, *et al*., 2019, Large-scale deformation and damage detection of 3D printed continuous carbon fiber reinforced polymer-matrix composite structures. *Compos Struct*, 212: 552–560.

    https://doi.org/10.1016/j.compstruct.2019.01.064

25. Cheng Y, Li J, Qian X, *et al*., 2021, 3D printed recoverable honeycomb composites reinforced by continuous carbon fibers. *Compos Struct*, 268: 113974.

    https://doi.org/10.1016/j.compstruct.2021.113974

26. Dong K, Ke H, Panahi-Sarmad M, *et al*., 2021, Mechanical properties and shape memory effect of 4D printed cellular structure composite with a novel continuous fiber-reinforced printing path. *Mater Des*, 198: 109303.

    https://doi.org/10.1016/j.matdes.2020.109303

27. Yin L, Tian X, Shang Z, *et al*., 2019, Characterizations of continuous carbon fiber-reinforced composites for electromagnetic interference shielding fabricated by 3D printing. *Appl Phys A*, 125: 266.

    https://doi.org/10.1007/s00339-019-2566-0

28. Dong K, Wang Y, Wang Z, *et al*., 2023, Reusability and energy absorption behavior of 4D printed continuous fiber-reinforced auxetic composite structures. *Compos A Appl Sci Manuf*, 169: 107529.

    https://doi.org/10.1016/j.compositesa.2023.107529

29. Quan C, Han B, Hou Z, *et al*., 2020, 3d printed continuous fiber reinforced composite auxetic honeycomb structures. *Compos B Eng*, 187: 107858.

    https://doi.org/10.1016/j.compositesb.2020.107858

30. Xue X, Lin C, Wu F, *et al*., 2023, Lattice structures with negative Poisson's ratio: A review. *Mater Today Commun*, 34: 105132.

    https://doi.org/10.1016/j.mtcomm.2022.105132

31. Larsen UD, Sigmund O, Bouwstra S, 1997, Design and fabrication of compliant micromechanisms and structures with negative poisson's ratio. *J Microelectromechanical Syst*, 6: 99–106.

32. Antonov F, 2015, Anisoprint. Available from: https://anisoprint.com [Last accessed on 2023 Sep 30].

33. Zhang H, Chen J, Yang D, 2021, Fibre misalignment and breakage in 3D printing of continuous carbon fibre reinforced thermoplastic composites. *Addit Manuf*, 38: 101775.

    https://doi.org/10.1016/j.addma.2020.101775

ACCSCIENCE
PUBLISHING

OUR JOURNALS

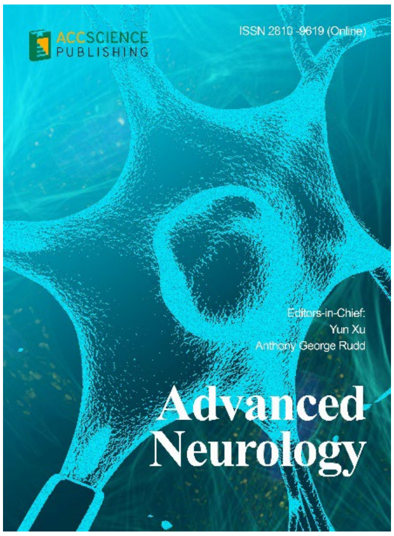

ACCSCIENCE PUBLISHING
ISSN 2810-9619 (Online)
Editors-in-Chief:
Yun Xu
Anthony George Rudd
Advanced Neurology

Advanced Neurology is a peer-reviewed and open-access journal that aims to publish and disseminate novel research in the breadth of neurology and neuroscience. The journal aims to advance our understanding in the nervous system and provide a platform to neuroscientists and physicians to showcase their findings in original fundamental and clinical research as well as to present new ideas that highlight the changes in the neurological clinical practice.

Advanced Neurology covers subject areas, including but not limited to the following:

- Neurological disorders
- Neurodegenerative disease
- Cerebrovascular disease
- Epilepsy and movement disorders
- Neuroimmune disease
- Neurological infections
- Muscle disease
- Molecular and cellular neuroscience
- Systems neuroscience
- Cognitive neuroscience
- Computational modeling of nervous system

Gene & Protein in Disease publishes rigorously peer-reviewed and high quality original articles and authoritative reviews that focus on the latest development in multidisciplinary areas in biology and biomedicine, with an emphasis on gene and protein research. The journal has worldwide authorship, and a broad scope in basic and translational biomedical research of genetics, biochemistry, biophysics, oncology, immunology, cell biology, molecular biology, developmental biology, microbiology, neuroscience, stem cell, protein science, structural biology, regenerative medicine and translational medicine.

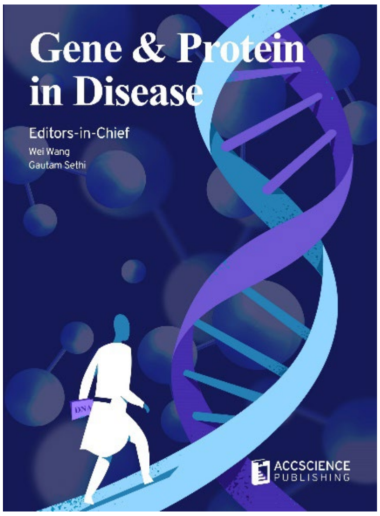

Gene & Protein in Disease
Editors-in-Chief
Wei Wang
Gautam Sethi
ACCSCIENCE PUBLISHING

Start a new journal

Write to us via email if you are interested to start a new journal with AccScience Publishing. Please attach your CV, professional profile page and a brief pitch proposal in your email. We shall inform you of our decision whether we are interested to collaborate in starting a new journal.

Contact: info@accscience.com

ACCSCIENCE
PUBLISHING

Access Science Without Barriers

Contact

www.accscience.com
8 Burn Road, #15-03 Trivex, Singapore 369977
Email: editorial@accscience.com
Phone: +65 8182 1586